OPERATION AND CONTROL OF SMART TRANSFORMER BASED MESHED HYBRID MICROGRID

A THESIS

submitted by

DWIJASISH DAS

for the award of the degree

of

DOCTOR OF PHILOSOPHY

DEPARTMENT OF ELECTRONICS AND ELECTRICAL ENGINEERING

INDIAN INSTITUTE OF TECHNOLOGY GUWAHATI, GUWAHATI, INDIA

FEBRUARY 2023

To Science

THESIS CERTIFICATE

This is to certify that the thesis entitled **"OPERATION AND CONTROL OF SMART TRANSFORMER BASED MESHED HYBRID MICROGRID"** submitted by **DWIJASISH DAS** to the Indian Institute of Technology Guwahati, Guwahati, India for the award of the degree of Doctor of Philosophy is a bonafide record of the research work done by him under my supervision. The contents of this thesis, in full or in parts, have not been submitted to any other Institute or University for the award of any degree or diploma.

Place: Guwahati
Date: 01.02.2023

Dr. Chandan Kumar
Research Guide
Associate Professor
Department of Electronics and Electrical Engineering
IIT Guwahati, 781039

DECLARATION

I certify that:

1. The work contained in this thesis is original and has been done by me under the guidance of my supervisor.
2. The work has not been submitted to any other Institute for any degree or diploma.
3. I have followed the guidelines provided by the Institute in preparing the thesis.
4. I have conformed to the norms and guidelines given in the Ethical Code of Conduct of the Institute.
5. Whenever I have used materials (data, theoretical analysis, figures, and text) from other sources, I have given due credit to them by citing them in the text of the thesis and giving their details in the references.

Place: Guwahati
Date: 01.02.2023

Dwijasish Das

ACKNOWLEDGEMENTS

I take this opportunity to acknowledge my heartfelt gratitude to all those people who directly or indirectly helped me to carry out this research work successfully.

I am heartily thankful to my supervisor, Dr. Chandan Kumar, for the encouragement, guidance and support during my research work. I express my gratitude for his willingness to help and timely advice on the issues I faced during the doctoral studies.

I also acknowledge Ministry of Education, formerly the Ministry of Human Resource Development (MHRD) for supporting me financially. I express my gratitude to the Science and Engineering Research Board (SERB), Department of Science and Technology, India for the grant "ECR/2017/001564", and Intel India for providing technical and financial support during my research days.

I would like to acknowledge the financial, academic and technical support of the Indian Institute of Technology Guwahati for this research. I am thankful to the Heads of the Department during the course of my study. I am sincerely grateful to Dr. Praveen Tripathy, Dr. Sanjib Ganguly, and Dr. Ravindranath Adda, for assessing the work and giving invaluable suggestions as members of Doctoral Committee. I also thank Prof. Marco Liserre for his technical advice on the various issues.

I would like to express gratitude to the services being offered by Mr. Paban Bujor Barua, Mr. Rakesh Singha, staff of power electronics laboratory and Mr. Mukut Baruah, Mr. Dasarath Das, Late Mr. Uday Shankar Uzir and Mr. Sundeep Borah, office staff of Electronics and Electrical Engineering department.

The Smart Energy Conversion group members have contributed immensely to my personal and professional time during my stay in the Institute. I especially thank Dr. Hrishikesan VM, Dr. Manojkumar Rampelli, Sourav Kumar Ghosh, Anup Kumar Deka, Dr. Arunima Dutta, Devendra Kumar and Anand N for their valuable help during my research. I am extremely thankful for the support extended by my friends from the power group Abhishek Paikray, Dr. Bikash Shah, Dr. Gayatri Nayak, Pramit Nandi, Dr.

Rajendra Kumar, Tako Nama and all my other friends from Power and Control Lab II.

Since the time I had started my education in nursery, right up to doctoral research, I have shared my journey with numerous people. It's wonderful how some people come near you and never leave your side. A big thank you my friends Abubakkar Siddique Farooque, Arindom Shyam, Ayushman Gogoi, Bibek Baruti, Dr. Chandana Deka, Chandasmita Barman, Dhananjay Sinha, Dr. Halim Hussain, Momi Das, Raj Nasim, Rupjyoti Barman, Swatah Siddha Borkotoky, Dr. Uddipana Dowerah, Vaishali Sharma and Yubaraj Boro.

Lastly, as they say, "family gives you the roots to stand strong and tall", I would like to thank my parents, Pramod Chandra Das, Dr. Manjula Das, my sister Dr. Seujee Das and brother in law Dipankar Nath for always encouraging me to pursue my dreams and offering immense love and support all these years. And of course a big "thank you" to my greatest support not just during PhD but throughout life, a long-time friend and currently my wife, Dr. Dhriti Mahanta.

Dwijasish Das

ABSTRACT

KEYWORDS: Smart transformer (ST); solid-state transformer (SST); power management; meshed hybrid microgrid.

The excessive use of fossil fuels for power generation in the previous decades has led to various environmental concerns. Moreover, such fuels are also with limited availability. These factors have encouraged engineers and scientists to look for alternate renewal energy sources (RES) for power generation. Various RES like solar photo-voltaic (PV), wind, geothermal, etc., have been used for power generation and injection into the electric grid. However, such changing trends come with their own limitations. RES are generally intermittent in nature with widely varying levels of availability throughout the day and round the year. In addition to that, such sources also need power electronic interface for power injection into the electric grid. These factors give rise to various challenges like voltage variations, faults, harmonics in voltages and currents, islanded operation, complexity of control, etc. Various power electronic equipments such as distribution static compensator (DSTATCOM), dynamic voltage restorer (DVR), unified power quality conditioner (UPQC), static transfer switch, static current limiter, etc., are used in the electric grid to address such challenges.

In recent times, solid state transformer (SST) has received considerable research interest for improving performance of electric grid in presence of RES. It is a distribution transformer realized with the help of power electronic converters. In addition to ac voltage transformation and isolation, similar to conventional transformer, SST also provides dc voltage connection which can be used for realizing dc distribution system or interfacing RES to the electric grid. Therefore, the SST is a very attractive solution for the changing power distribution scenario. An SST can be integrated with intelligent control strategies and communication features for voltage control, power quality improvement and power management. Such an SST is termed as a smart transformer (ST).

Many RES generate power in the form of dc. Moreover, modern day loads are also shifting towards the dc side. This has led to the existence of both ac and dc grids in the

distribution system, and such grids are termed as hybrid grids. With multiple ports at different ac and dc levels, the ST has the capacity to provide multiple features in hybrid distribution grids.

This thesis investigates the operation and control of ST based hybrid microgrid and explores the various power management as well as control strategies facilitated by the ST to achieve improved and efficient operation in both the ac and dc grids. A meshed hybrid microgrid with ac and dc grid interconnection enabled by ST is proposed. This is realized by extending the LVdc bus of the ST in the distribution grid and connecting it to the dc buses of the distributed generation (DG) converters already presented in the system. Multiple power flow paths are realized in such a configuration which helps in reducing the line losses. Compared to the ac line, line losses in the proposed LVdc line reduces to 22%. Moreover, reverse power flow efficiency increases by 6%.

Further, the operation of the proposed meshed hybrid microgrid is explored in islanded mode. Islanded operation is achieved by maintaining the LVdc voltage with the help of a battery energy storage system (BESS) and the LVac grid voltage is maintained by the ST LV converter. The multiple power flow paths offered by the meshed hybrid microgrid are exploited to achieve optimal power flow management in the islanded mode of operation. This helps in reducing the line losses in the system and consequently increases the operation time of the islanded system. It was observed that while in a particular case, the conventional method incurred 1.337 kW losses, the proposed method was able to reduce the line losses to 1.0487 kW. This shows a 22% reduction in line losses with proposed method as compared to conventional method.

The stability of the ST based islanded meshed hybrid microgrid is also investigated while catering to sudden high power demands from electric vehicle (EV) loads. Since a BESS maintains the LVdc voltage in islanded mode, any disturbance or sudden high power demand has to be handled by the BESS. However, owing to the presence of right half plane zero in the transfer function of the BESS converter, the converter's ability to cater to sudden loads is limited. This issue is addressed by exploiting the meshed hybrid configuration. The ST is used to execute an LVac voltage control strategy which reduces the total load on the BESS during EV load transients, and ensures that the system remains stable.

Finally, to establish the reconnection of the ST based islanded meshed hybrid microgrid

to the MVac grid, a step-by-step partial start-up procedure is proposed. Since in the islanded operation, ST LV converter is already operational, the partial start-up procedure helps to start the non-operational converters namely the ST isolated dc-dc converter and the ST MV converter without disturbing the operation of the LV grid.

The thesis presents and explores the operation of an ST-based meshed hybrid microgrid and proposes various methods for power management, loss minimization, stability and overall operation of the system in islanded and grid connected mode.

TABLE OF CONTENTS

LIST OF TABLES

LIST OF FIGURES

ABBREVIATIONS

ac	Alternating Current
ADC	Analogue to Digital Converter
BESS	Battery Energy Storage System
CCM	Current Control Mode
CPT	Conventional Power Transformer
DAB	Dual Active Bridge
dc	Direct Current
DG	Distributed Generation
DSTATCOM	Distribution Static Compensator
DVR	Dynamic Voltage Restorer
EV	Electric Vehicle
GA	Genetic Algorithm
GHI	Global Horizontal Irradiance
IEEE	Institute of Electrical and Electronics Engineers
IGBT	Insulated Gate Bipolar Transistor
LV	Low Voltage
MV	Medium Voltage
MPP	Maximum Power Point
MPPT	Maximum Power Point Tracking
NPC	Neutral Point Clamped
OLTC	On-Load Tap Changer
PET	Power Electronic Transformer
PI	Proportional Integral
PSCAD	Power System Computer Aided Design
PV	Photo-voltaic
RES	Renewable Energy Source
rms	Root Mean Square
SoC	State of Charge

SST	Solid-State Transformer
ST	Smart Transformer
THD	Total Harmonic Distortion
UPQC	Unified Power Quality Conditioner
VCM	Voltage Control Mode

NOTATIONS

C_f	Per phase capacitance of ST LV converter filter
C_{fm}	Per phase capacitance of DG converter filter
C_{MVdc}	Capacitance of MVdc capacitor
D_i	Distance between the i^{th} and $(i+1)^{th}$ bus in kilometers
f_{DAB_sw}	Switching frequency of DAB converter
G_{BESS}	Control to output transfer function of BESS in discharging mode
$G_{PV}(s)$	Control to inductor current transfer function of PV dc-dc converter
G_h^{DG}	DG converter hysteresis gain transfer function
$G_d^{DG}(s)$	DG converter digital delay transfer function
G_h^{STLV}	ST LV converter hysteresis gain transfer function
$G_d^{STLV}(s)$	ST LV converter digital delay transfer function
$G_{DG\_conv}(s)$	Open loop transfer function of DG converter
$G_{STLV\_conv}(s)$	Open loop transfer function of ST LV converter
$H_{LC}(s)$	LC filter transfer function
$H_{LCL}(s)$	LCL filter transfer function
H_{load}	Harmonic power component of the total load
$I_1, I_2 \ldots I_n$	rms currents drawn from the LVac buses 1, 2 ... n, respectively
I_{ac}^a	rms current flowing through ac line
I_{dc}^b	Current flowing through dc line
I_{dc_i}	Current drawn by the i^{th} DG converters from the LVdc line
i_{mi_a}, i_{mi_b} and i_{mi_c}	i^{th} DG converter output currents for phase a, b and c, respectively
L_f	Per phase inductance of ST LV converter filter
L_{fm}	Per phase converter side inductance of DG converter LCL filter

L'_{fm}	Per phase grid side inductance of DG converter LCL filter
L_r	Leakage inductance of isolation transformer
n	Isolation transformer turns ratio
n_{acl}	Number of ac lines
n_{dcl}	Number of dc lines
$P_{3\phi\_Loss}$	Total power loss in three phase lines
$P_{ac\_load_i}$	Load at the i^{th} LVac bus
$P_{dc\_load_j}$	Load at the j^{th} LVdc bus
P_{DG_k}	Power injected by the k^{th} DG plant
P_{EV_l}	Power injected by the l^{th} EV
P_{BESS_r}	Power injected by the r^{th} BESS
$P_{DG\_Conv_k}$	Reference power for the k^{th} DG converter
$P^c_{EV_l}(t)$	Charging power of EV
$P^c_{BESS_0}(t)$	Charging power of BESS
$P^{c,max}_{EV_l}(t)$	Maximum charging power limit of EV
$P^{c,max}_{BESS_0}(t)$	Maximum charging power limit of BESS
$P^d_{EV_l}(t)$	Discharging power of EV
$P^d_{BESS_l}(t)$	Discharging power of BESS
$P^{d,max}_{EV_l}(t)$	Maximum discharging power limit of EV
$P^{d,max}_{BESS_0}(t)$	Maximum discharging power limit of BESS
$P_{i(avbl)}$	Renewable power available for injection at the i^{th} DG converter
$P^*_{i(inj)}$	Reference power injection for the i^{th} DG converter
P_{load}	Active power component of total load
P_{LVac}	LVac load active power
P^*_{MVac}	Reference MVac active power
P_{MVac}	MVac active power
P_{dc_Loss}	Total power loss in LVdc line
P_{DAB}	Power transfer through DAB
P^{max}_{DAB}	Maximum load capacity of DAB
Q_{load}	Reactive power component of total load
R^{charge}_{MVdc}	MVdc capacitor charging resistor
R^a_{ac}	Resistance of ac line

R^b_{dc}	Resistance of dc line
$R_{dc\_1}, R_{dc\_2} ... R_{dc\_n}$	Resistances of various sections in the LVdc line
$R_1, R_2 ... R_n$	Resistances of various sections in the LVac lines
R_{ac}	Per kilometer resistance in each conductor of ac distribution line
R_{dc}	Per kilometer resistance in each conductor of dc distribution line
R_f	Per phase resistance of ST LV converter filter
R_{fm}	Per phase damping resistance of DG converter LCL filter
$S_{i(rated)}$	Converter rating of the i^{th} DG converter
$S^{rated}_{DG\_Conv}$	Rating of DG converter
S_{load}	Total load
$SoC^{min}_{EV_l}$	Minimum SoC limit of EV
$SoC^{max}_{EV_l}$	Maximum SoC limit of EV
$SoC^{min}_{BESS_0}$	Minimum SoC limit of BESS
$SoC^{max}_{BESS_0}$	Maximum SoC limit of BESS
$SoC^{critical}_{BESS_0}$	Critical SoC limit of $BESS_0$
SoC_{EV_l}	SoC of EV
SoC_{BESS_0}	SoC of $BESS_0$
t^{min}_{rise}	Minimum rise time od BESS duty ratio for stable operation
v_{fc}	Voltage across ST LV converter filter capacitor
V^{nom}_{LVac}	Nominal LVac voltage
V_{LVac}	LVac per phase rms voltage
V^{min}_{LVac}	Minimum limit of load bus voltage magnitude specified by grid code
V^{max}_{LVac}	Maximum limit of load bus voltage magnitude specified by grid code
V^{i}_{LVac}	Magnitude of ac load voltage
V^{j}_{LVdc}	Magnitude of dc load voltage
V^{nom}_{MVdc}	Nominal MVdc voltage
V_{MVdc}	MVdc voltage
V_{LVdc}	LVdc voltage
V_{C_MVdc}	Voltage across MVdc capacitor

$X_1, X_2 ... X_n$	Reactances of various sections in the LVac lines
Z_{ac}	Per kilometre impedance of the ac distribution line

Greek Symbols

δ	Firing angle delay between the primary and secondary sides of isolated dc-dc converter
η_{STMV}	Efficiency of the ST MV converter
$\eta_{STdc-dc}$	Efficiency of the ST dc-dc converter
η_{STLV}	Efficiency of the ST LV converter
η_{DG_i}	Efficiency of the i^{th} DG converter

CHAPTER 1

INTRODUCTION

1.1 Overview of Present Power Scenario

Over the years, electric power has been generated mainly in coal thermal power plants for distribution to the consumers [1]. Even though a significant amount of power is generated in hydro-electric power generating stations, setting up such plants need huge pre-requisites and favourable conditions [2]. Therefore, power generation from such sources is limited. Fig. 1.1 shows the global power production growth as well as share of various sources from 1985 to 2021 [3]. It can be observed that the major share of production has always been dominated by coal. A comparison between the amount of power generated from various sources in India upto March 2022 is given in Fig. 1.2 [4].

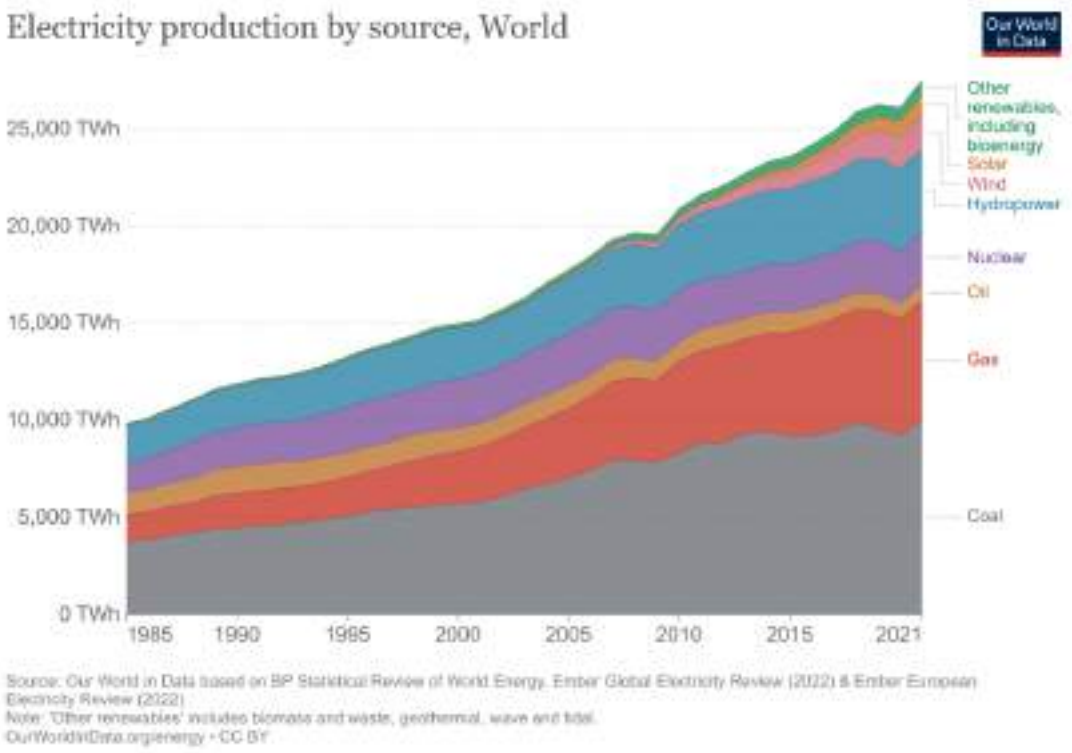

Fig. 1.1 Global electricity production by source [3].

Similar to the global scenario, in India too, coal is leading the chart by a huge margin. However, such generation has its limitations. In addition to environmental hazards,

the fast depletion of available natural resources has led mankind to search for other alternatives [5]. Therefore, the importance of green energy is increasing rapidly and several types of renewable energy sources (RES) are being explored. This has led to a significant change in the power generation and distribution scenario. A breakup of the renewable power installed in India upto March 2022 is also given in Fig. 1.2 [4]. Solar power is the most popular RES, which is closely followed by large hydro and wind power plants.

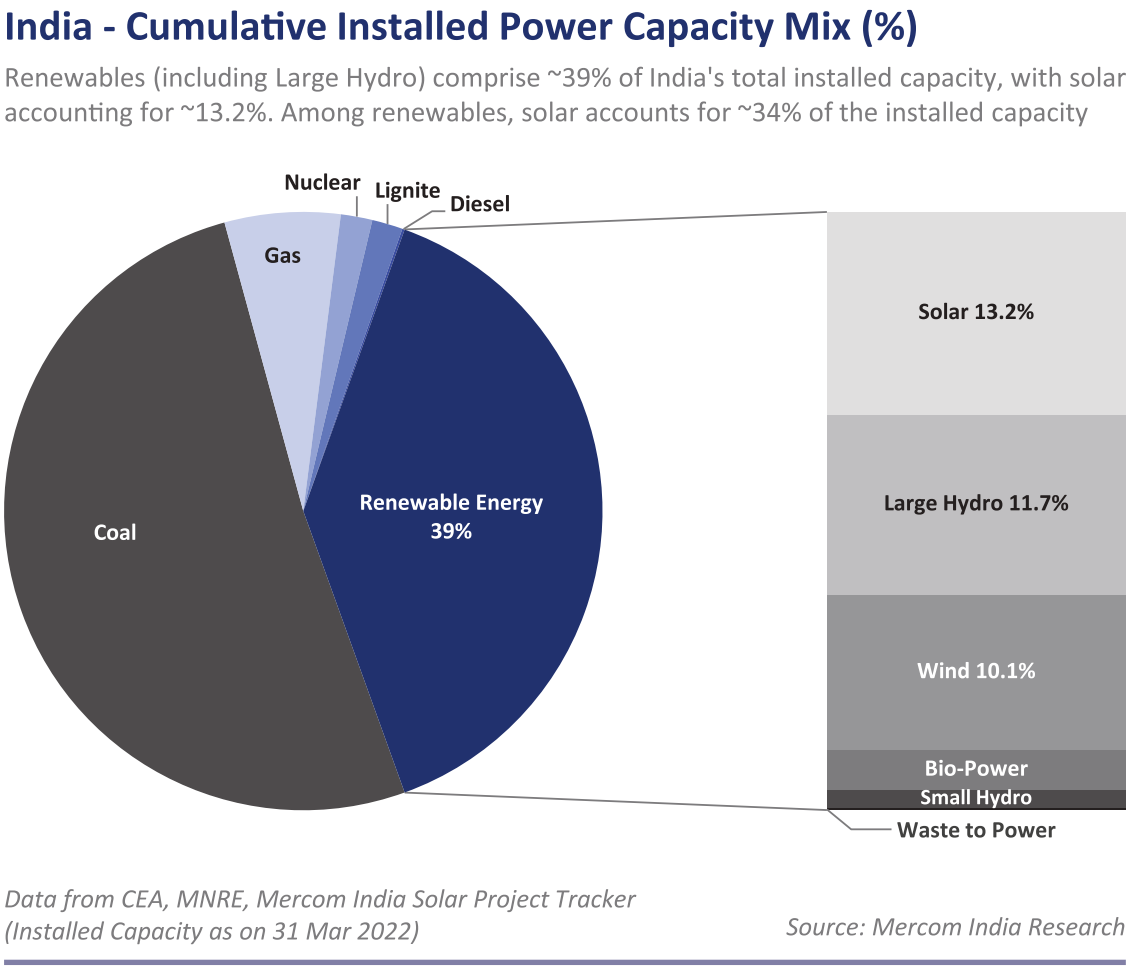

Fig. 1.2 India's cumulative installed power capacity upto March 2022 [4].

Owing to the tremendous potential in RES like solar energy and wind, an exponential growth has appeared in the installation of such plants [6]. In the long run, such plants are not only environment friendly, but also cheap. Fig. 1.3 shows the growth of global renewable power share over the past 20 years [7]. It has risen to over 80% in 2019 in comparison to a share of about 23% in 2001. With such a growth curve, it is expected that the coming years will see increased renewable energy penetration.

Such a changing trend will lead to the production of cheap and environment friendly

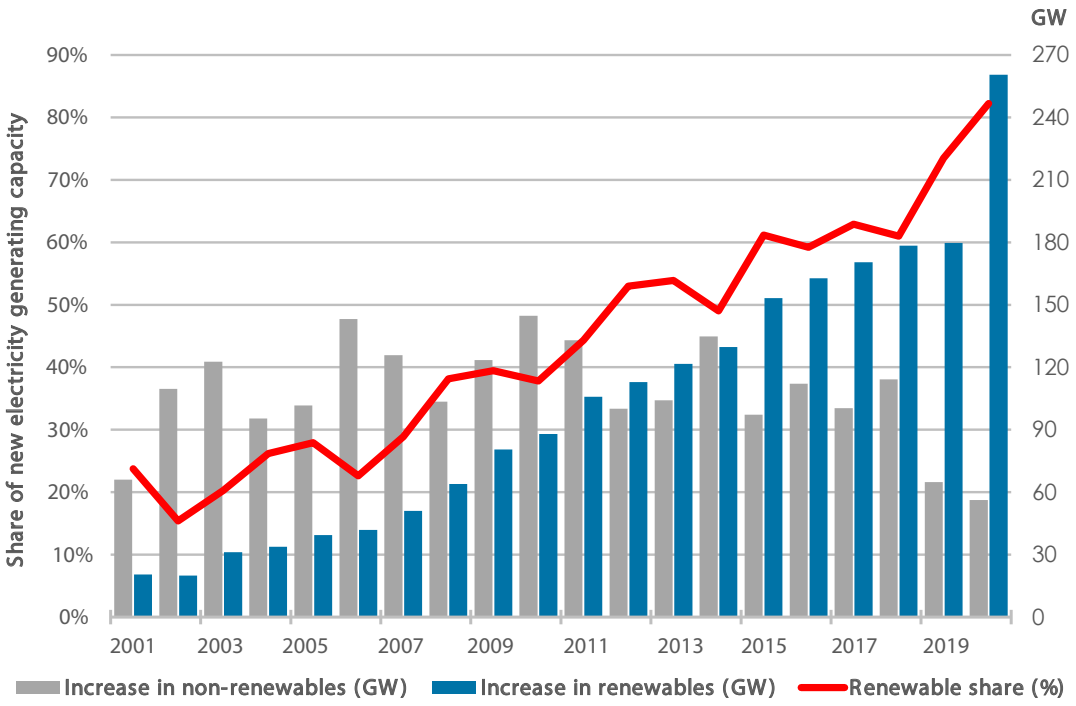

Fig. 1.3 Global renewable share of annual power capacity expansion [7].

power. However, this also demands change in the existing grid structures [8], [9]. There are many issues that seep in along with the penetration of renewable power, and the conventional grids were not designed to cope up with such demands [9]. This has brought about a need to change the existing grid structure and components. Moreover, as RES are not reliable sources for drawing power as per need, there is also the need of measures to provide backup power at times when renewable power generation is not possible. This incorporates more challenges and complexities into the grid. Many such issues have appeared along with the integration of RES.

To address the issues in the modern and upcoming grid, researchers have suggested various power electronics based solutions. However, the need for improved, efficient and flexible solutions still exists. This thesis explores the capabilities of a smart transformer (ST) to address multiple issues that the electric grids are currently facing.

1.2 Organization of the Thesis

Chapter 1 initially gives an overview of the present power scenario and the recent trends that have shifted the power generation to environment friendly and renewable sources.

In **Chapter 2**, the issues that come along with such renewable energy integration have been presented along with some conventional approaches that are currently being adopted to address such issues. The ST is introduced along with some of its applications, which make it a promising solution to address the modern grid issues. The typical ST based LV distribution grid that has been considered for this thesis work is explained along with the possible research gaps. This is followed by the problem statements and objectives of the research work.

In **Chapter 3**, ST based meshed hybrid microgrid is proposed. This is realized by extending the ST LVdc link in the distribution grid and connecting to the dc buses of the DG converters already present in the system. The features and advantages of such a meshed hybrid microgrid have been analytically explained and experimentally verified.

Chapter 4 presents the islanded operation of the proposed ST-based meshed hybrid microgrid. The islanded operation is explored and improved power management strategies for optimal power loss reduction are proposed. Genetic algorithm is used to determine optimal power references for the converters. This results in minimum line losses which improves the operation time of the islanded system. The operation of the system is verified in simulation as well as experimentally.

The issue of EV charging transients is discussed in **Chapter 5**. Transients pose a threat to system stability, especially in islanded mode of operation when the grid is maintained by power electronic converters. Stability studies have been carried out for the islanded ST-based meshed hybrid microgrid. A control algorithm is proposed to ensure that such an islanded system does not lose stability during EV charging transients. The efficacy of the proposed scheme is verified both in simulation and experiments.

Chapter 6 proposes a step-by-step start-up procedure to reconnect an islanded ST based meshed hybrid microgrid back to the MVac grid. The start-up mechanism ensures proper reconnection while maintaining the capacitor inrush currents during starting within safe limits. This is achieved without disturbing the system operation on the LV side. The start-up method has been validated in simulation and also demonstrated in the laboratory prototype.

Chapter 7 highlights the important contributions of the research work that have been carried out along with some suggestions for future research in the area.

The details of the experimental setup with photographs and the procedure for development of some of the components have been given in the **Appendix**.

CHAPTER 2

LITERATURE REVIEW

2.1 Renewable Power Integration and Challenges

There are various challenges that are introduced to the electric grid along with the integration of renewable power sources. These are discussed as follows.

2.1.1 Intermittency and Unpredictability

Photovoltaic (PV) sources have a very high variance in the power injection throughout the day. Moreover, the effective solar hours vary from region to region. At peak times, the PV plant may provide a very high amount of power and the power injection goes down to zero during the night time. Even during the day time, factors like solar elevation, clouds moving over the sky, pollutants, etc., also significantly affect the swell and dip of injected power [10].

Power injected by wind energy systems vary not only throughout the day but also throughout the year along with the season. Moreover, power can only be generated when the wind speed remains between the cut-in speed and the cut-out speed [11]. Therefore, renewable energy systems need effective ways of harnessing the intermittent and time varying power in an optimum and maximum possible manner. Such intermittency also affects the net load on the conventional power sources in the system [12]. The net load is the power difference between the total load and the renewable power generation. This is the power that the utility grid has to supply. Fig. 2.1 shows the impact on net load by increased use of renewables. Such high variation of net load needs faster ramping requirement and fast responding generation on the utility side. Consequently, predictability of net load becomes necessary.

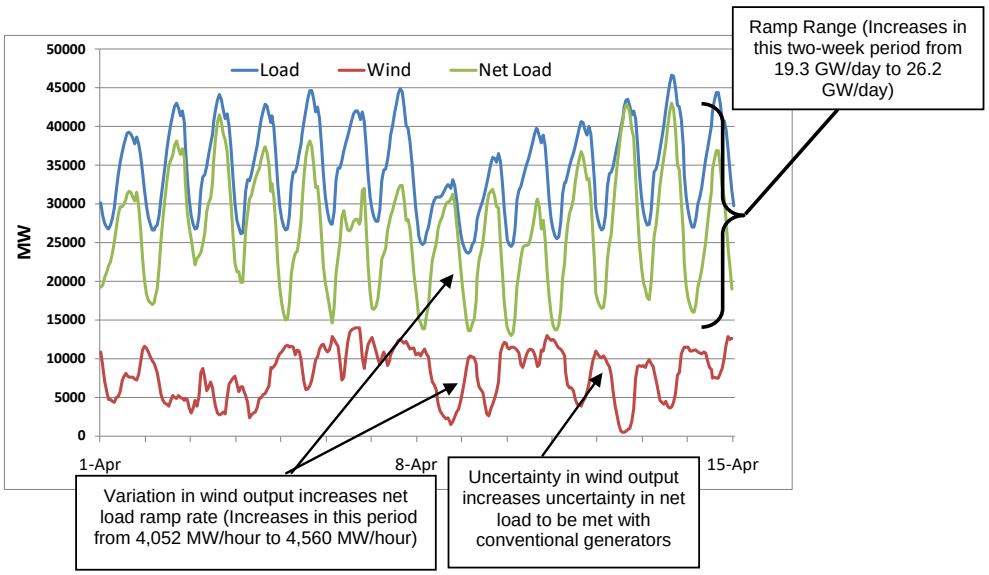

Fig. 2.1 Impact on the net load from increased use of renewable energy [12].

2.1.2 Harmonics Injection

With the increase in RES, voltage and current harmonics are on the rise as RES generally need power electronic converters for power injection [13]–[15]. Broadly two types of harmonics are associated with such renewable integration. The first type is due to the switching in power electronic converters which are used to interface the distributed generation (DG) sources. These are in the ranges of multiples of the switching frequencies. Fig. 2.2(a) shows the waveforms of such switching frequency harmonics. It is observed that instead of a smooth sinusoidal wave, the waveform is composed of a band of high frequency oscillations. The second type is the grid frequency harmonics which are due to non-linear loads like rectifiers. Such harmonics are present in the multiples of grid frequency. Fig. 2.2(b) shows such harmonic frequencies that may be injected into the grid and the resultant waveform is the overall waveform. The fundamental wave shown is the ideal waveform. The components like the third and fifth harmonics add up to form the resultant as shown in the figure. It is observed that the resultant waveform is no longer a sinusoidal wave.

In both the types of harmonics mentioned above, the overall current and voltage waveform is distorted which leads to various issues like increased transformer losses, increased skin effect, etc. In addition to the power converters and loads, various conditions like irradiance profile of a particular day can also contribute to the harmonics in a PV system as cloudy days generally result in higher total harmonic distortion

(THD) [16].

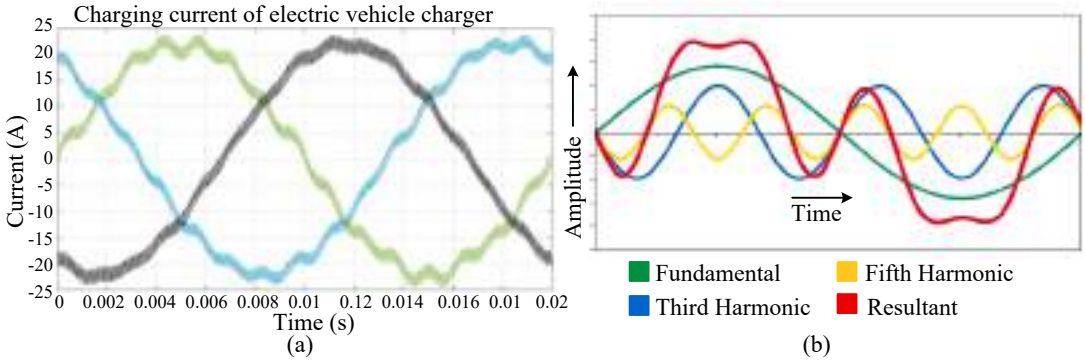

Fig. 2.2 (a) Waveforms showing switching harmonics [17]. (b) Waveforms showing grid frequency harmonics [18].

2.1.3 Voltage and Frequency Fluctuations

The active and reactive power flow, respectively determine the frequency and voltage magnitudes in a power system [20], [21]. The amount of reactive power generated by wind farms changes with the change in wind speed. Such reactive power fluctuations lead to voltage magnitude fluctuations in addition to frequency variations due to the variations in injected real power. Fig. 2.3 shows the effect of increasing wind power penetration on the frequency of the system [19]. It is observed that the deviation in frequency increases as the wind power injection increases. A PV system generally does not inject reactive power [22]. However, as PV power is varying throughout the day, the active power injection varies accordingly. The total solar electromagnetic radiation incident on any horizontal surface at a given time and location is known as the global horizontal irradiance (GHI) [23]. This is the most useful metric for estimating the

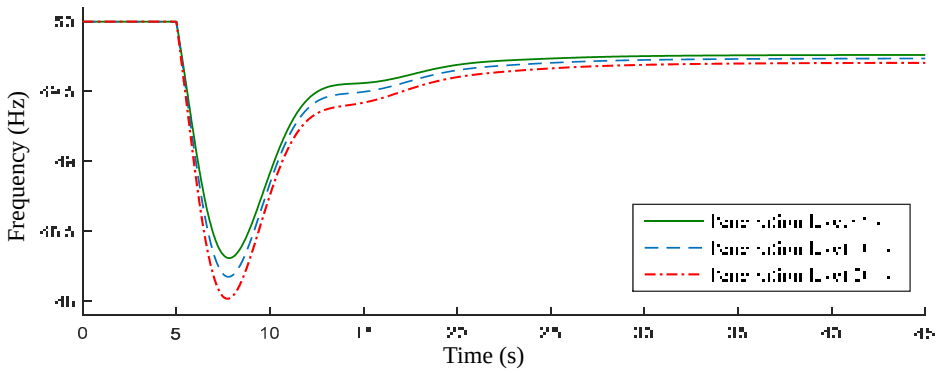

Fig. 2.3 Frequency variation with increasing wind power penetration [19].

PV power output from solar panels. Fig. 2.4 shows a typical 1-minute GHI data for one complete day [24]. Such variations in irradiation results in a varying active power injection which can lead to frequency fluctuations in the grid. Thus, it is important to address such issues that can otherwise lead to varying power quality issues.

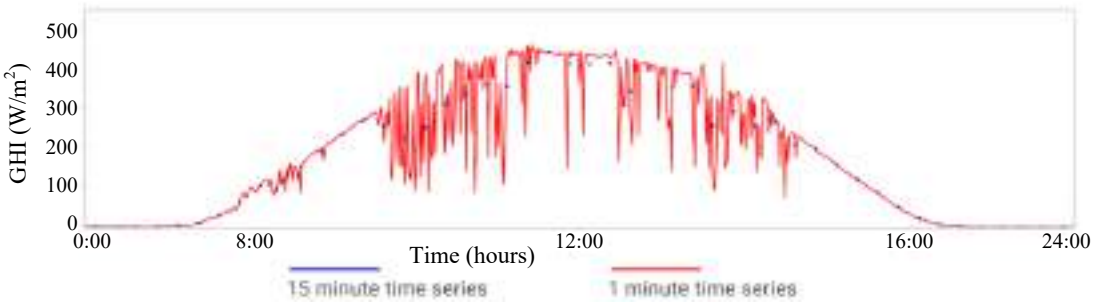

Fig. 2.4 1-minute solar radiation GHI data [24].

2.1.4 Issues with Islanding and Reclosure

The U.S. Department of Energy defines a microgrid as "a group of interconnected loads and distributed energy resources within clearly defined electrical boundaries that acts as a single controllable entity with respect to the grid. A microgrid can connect and disconnect from the grid to enable it to operate in both grid-connected or islanded mode" [25]. Microgrids enhance the integration of RES. Such decentralized generation from RES also reduces power losses by generating power near the load points. With islanded operation, the microgrid can avail continuous power from RES even when there is some fault in the utility grid. However, such benefits come along with its challenges. During faults, even when the main grid gets separated, the system remains energized due to the availability of distributed generation in the microgrid. This becomes a hazard for the operators who are involved in fault clearance [26]–[29]. Moreover, synchronizing becomes an issue during re-closure. Hence, quality of service is not guaranteed [30]. Fig. 2.5 depicts a similar scenario where the control mode change can have a considerably large clearing time, and in that duration the voltages and currents can vary uncontrollably [31].

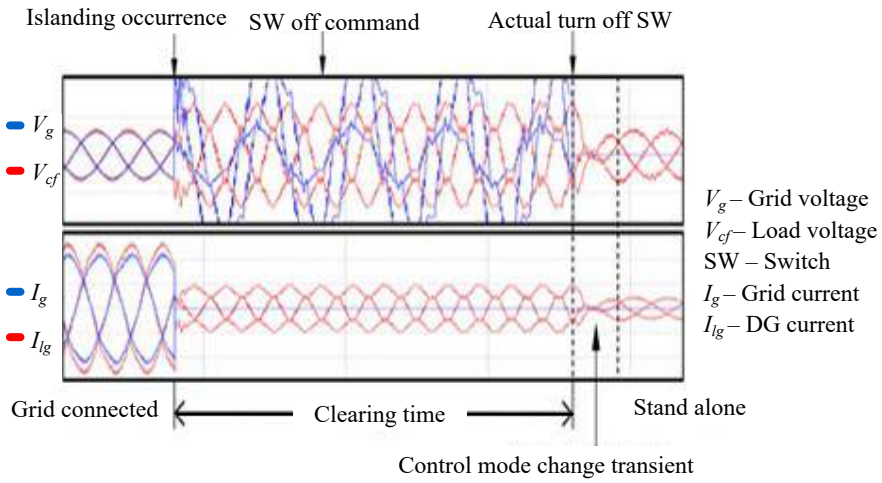

Fig. 2.5 Voltage and current waveforms during islanding [31].

2.2 Conventional Approach to Address Challenges in the Grid

There are various conventional technologies present to handle the issues highlighted in the previous section. Control systems, both mechanical and electrical, along with power electronics, have been implemented to deal with such issues. Some of the technologies already being utilized are discussed as follows.

2.2.1 On Load Tap Changer Transformer

In a conventional power transformer (CPT), voltage regulation is achieved with the help of on load tap changer (OLTC) method [32]. The tap changer technology allows the change of effective number of turns in a transformer without the interruption of power flow. Fig. 2.6 shows the principle of tap change that is applied for each winding of a three phase mechanical tap changer. The neutral terminal can be mechanically connected to terminals A or B and one of the individual switches from 1 to 8 can be closed to change the effective number of turns as desired.

Over the years, several methods have been proposed to obtain improved operation of OLTCs to address grid issues arising from renewable energy penetration. In [33], a coordinated control of storage systems along with OLTCs and step voltage regulators is proposed to handle the issue of voltage rise due to PV penetration. Moreover, features like peak load shaving, reduced losses and increased life cycle is also achieved. A method for intelligent control of OLTCs is proposed in [34]. The equivalent impedance

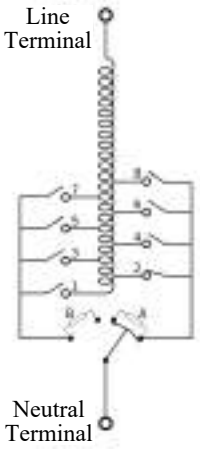

Fig. 2.6 A mechanical OLTC.

of the supply system is estimated with the help of the changes observed in the primary side voltage and current. These are used to keep track of the OLTC stability by estimating a simple tap changer stability index, which is the ratio of the per unit change in primary side current and the per unit change in primary side voltage of the OLTC. The use of power electronics for the automatic operation of OLTCs to achieve improved voltage regulation is proposed in [35], [36]. Such techniques help to achieve arc free tap changing operation along with higher accuracy of voltage sag or swell correction. There are several studies on OLTC which specifically deal with the grid issues arising out of high PV penetration [37], [38]. In [37], a reactive power control method along with OLTC transformer is used to enhance PV penetration in LV networks. Fig. 2.7(a) shows a comparison of the voltage profile in a grid with high PV penetration for fixed tap and OLTC transformer. It is observed that improved voltage profile is obtained with OLTC. Further, the comparison with the proposed reactive power control scheme is shown in Fig. 2.7(b). It is seen that the use of OLTC with reactive power control is most effective in keeping the voltage near the nominal value. Such studies suggest the consideration of PV planning during the design of LV network. Design of transformer OLTC along with the coordinated control of PV inverters can make the distribution systems more PV friendly. In spite of such functions, OLTCs have their limitations. In addition to high implementation costs, OLTCs also have the issues of arcing, carbonization of contact points, faster degradation of insulation oil, need for regular maintenance, etc. [39].

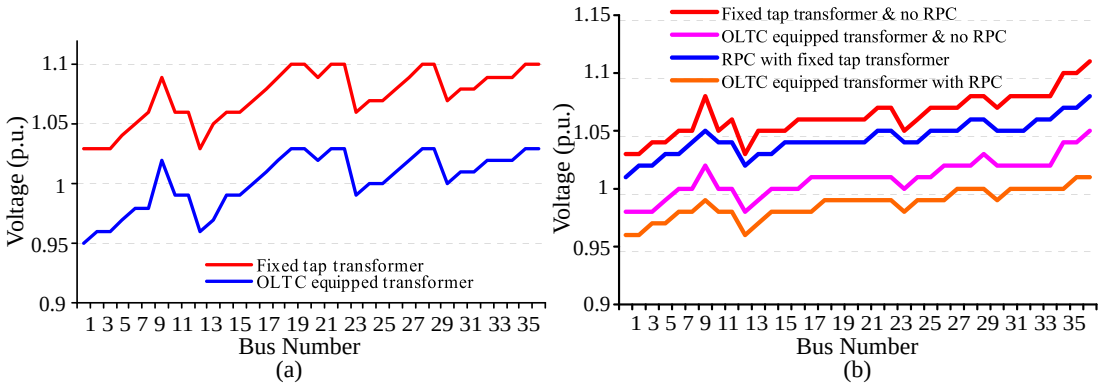

Fig. 2.7 Comparison of voltage profile with high PV penetration for fixed tap and OLTC transformer. (a) Without reactive power control. (b) With reactive power control [37].

2.2.2 Distribution Static Compensator

A distribution static compensator (DSTATCOM) is a shunt connected power electronic device utilized in the distribution grid for voltage regulation, power factor correction, load balancing and harmonic filtering. These are achieved by injecting appropriate reactive and harmonic power at the point of common coupling (PCC). In the current control mode (CCM), it can mitigate issues of harmonics and imbalance. Moreover, in voltage control mode (VCM), it acts as a voltage regulator [40]. A schematic diagram of the DSTATCOM is shown in Fig. 2.8. A capacitor is interfaced to the LVac grid through a dc-ac converter and a filter.

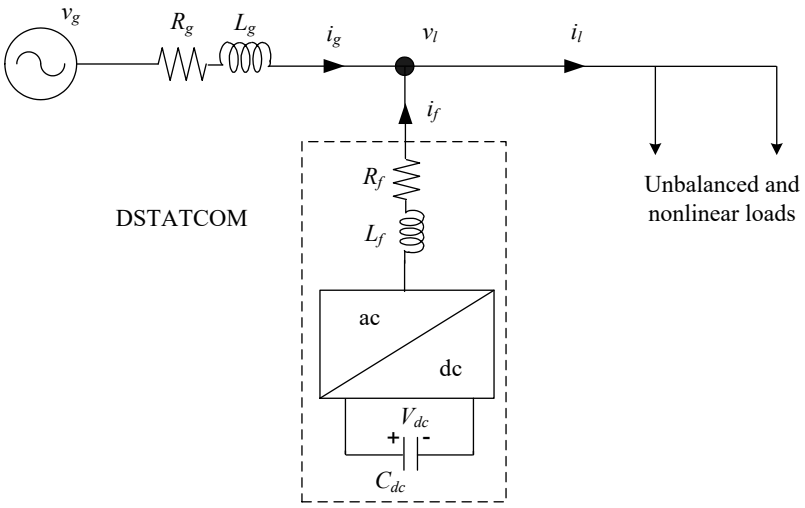

Fig. 2.8 Schematic diagram of DSTATCOM [41].

There are various studies in the literature which utilize DSTATCOM for power quality improvement in electric grids with RES. In [42], a bi-level coordinated planning model

is presented which determines the optimal integration of RES and DSTATCOM in the upper level and protection devices are incorporated in the lower level. Studies like [43], [44] present various control and optimization techniques specifically for grids with PV injection with DSTATCOM integration. A DSTATCOM however, has limited application as it is generally used only to exchange reactive power for improvement in voltage or current waveform. Moreover, when used to inject active power from RES or storage device, additional transformer is needed to provide galvanic isolation with the distribution grid.

2.2.3 Dynamic Voltage Restorer

Dynamic voltage restorer (DVR) is another power electronic device used to mitigate voltage disturbances in the distribution grid [45]. To improve the voltage profile, a DVR injects ac voltage in series to the distribution grid. The schematic of a DVR is shown in Fig. 2.9. It consists of a dc power source, a dc to ac converter and an injection transformer in series with the load. Any sag/swell in the distribution voltage is detected by the DVR and power is injected/absorbed through the transformer to compensate for the sag/swell such that the loads receive voltages as per grid standards. In [46], the use of DVR to improve power quality is demonstrated. It is shown that the DVR compensates third and fifth harmonic components of the voltage.

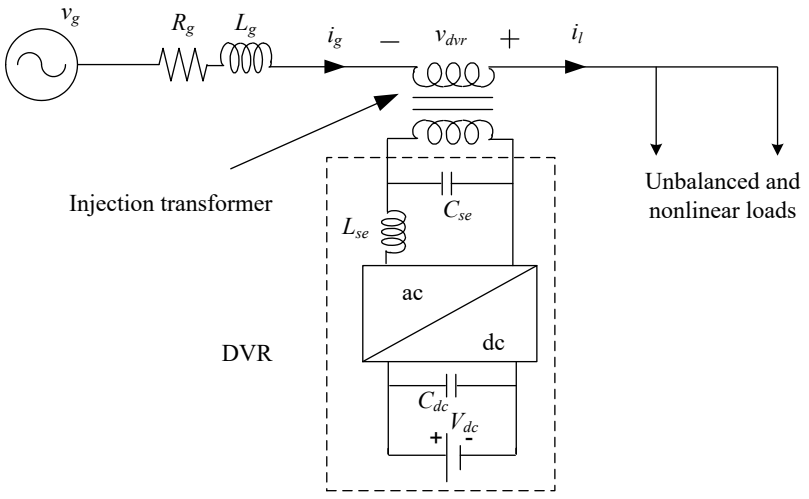

Fig. 2.9 Schematic diagram of DVR [46].

2.2.4 Unified Power Quality Conditioner

A unified power quality conditioner (UPQC) is a device which combines the functions of both DSTATCOM and DVR [47]. A schematic is shown in Fig. 2.10. Two back-to-back converters are connected to a common dc bus. One converter is interfaced to a transformer in series with the grid, while the other converter is shunt connected. The series compensator addresses the grid side issues like voltage sag/swell, flicker, and imbalance. The shunt compensator can inject real power from a DG source connected to the dc bus. It also provides reactive and harmonic power which isolates the grid from reactive and harmonic power demand [48]. With the capability to address both current and voltage issues in the distribution grid, the UPQC is considered as one of the most powerful solutions to the loads which are sensitive to supply voltage flicker or imbalance.

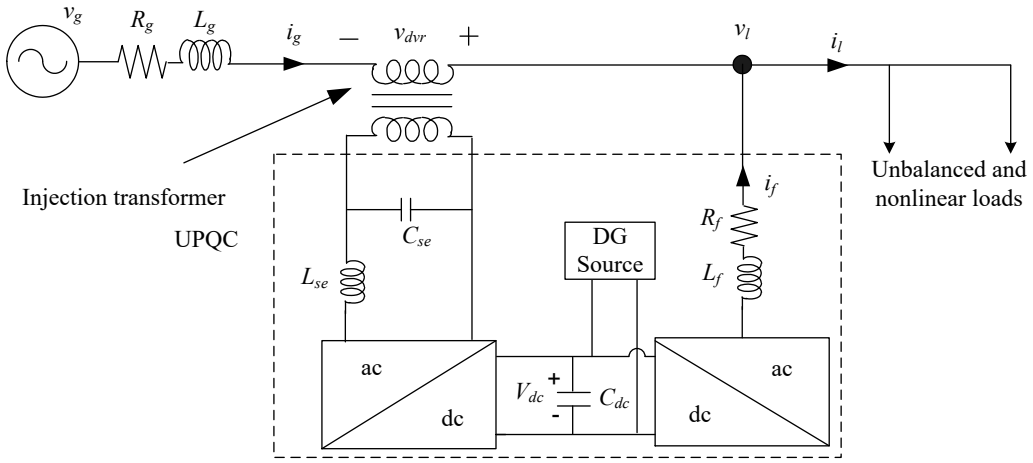

Fig. 2.10 Schematic diagram of UPQC [47].

2.2.5 Static Transfer Switches and Current Limiters

Static transfer switches and current limiters are power electronics based custom power devices utilized to cut or limit the power flow in the distribution system [49]–[51]. The schematic diagrams are shown in Fig. 2.11. In [49], the operation of a 15 kV, 600 A static transfer switch is analysed to improve system reliability by isolating it from disturbances. Static current limiters are gate turn-OFF thyristor (GTO) based static devices used to limit and even interrupt fault currents. Two GTOs are connected in anti-parallel mode as shown in Fig. 2.11(b). The GTOs are connected in parallel to a current limiting reactor and a voltage arrester. On detecting a fault, the GTOs turn OFF and the

fault current is diverted through the reactor which provides impedance for the current. The voltage arrester limits the transient rate of rise of the voltage across the switches. This enables the GTO pair to block forward and reverse voltages upto their ratings.

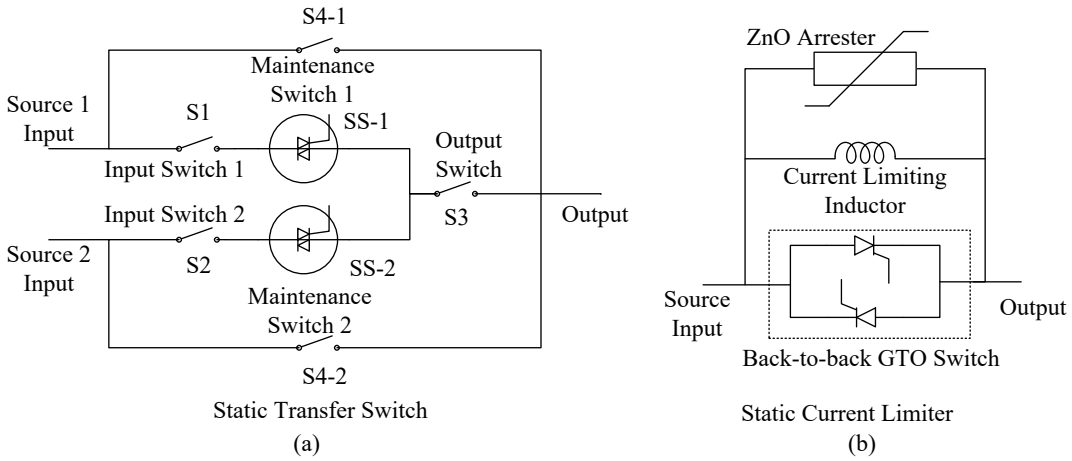

Fig. 2.11 Schematic diagram. (a) Static switch [49]. (b) Static current limiter [51].

2.2.6 Hybrid Grids

The RES uses power electronics based interconnection for integration to the ac system since major portion of these sources generate power in form of dc or require a dc link for the interconnection with ac grid. As most of the loads are still ac, pure dc microgrid requires all the loads to change to dc load. This is not possible in the immediate future due to their economic impact [52], [53]. Moreover, for dc distribution system, finding a voltage standard is challenging as various types of load require different levels of voltages. Also, these voltage levels require power conversion stages at various levels resulting in further loss and greater control complexity [54], [55].

A hybrid grid incorporates the benefits of both ac and dc grids, and avoids the drawbacks of a pure dc system. The loads and sources are connected to either ac or dc microgrids and this improves the overall efficiency due to the reduction of number of power conversion stages. This also leads to cost reduction of electronic products. Moreover, the hybrid configuration provides various power flow paths while controlling power flow and voltage in the ac and dc lines. Therefore, it is expected that the future distribution system will be a combination of ac and dc grids to harness the advantages of both [52]–[55].

In [56], the structures of hybrid microgrid are classified into ac-coupled, dc-coupled

and ac-dc coupled microgrids. The structures of ac-coupled and dc-coupled hybrid microgrids are shown in Fig. 2.12(a) and (b), respectively. In the ac-coupled hybrid microgrid, the various RES and storage elements are connected to a common ac bus through their individual interfacing converters. For the dc-coupled hybrid microgrid, the sources are connected to a common dc bus and then an interfacing converter connects the dc and ac buses. In the ac-dc coupled hybrid microgrid, the sources are connected to the ac and dc buses as per convenience and interlinking converters (IC) are used to connect the ac and dc buses. The structure of such a grid is shown in Fig. 2.13.

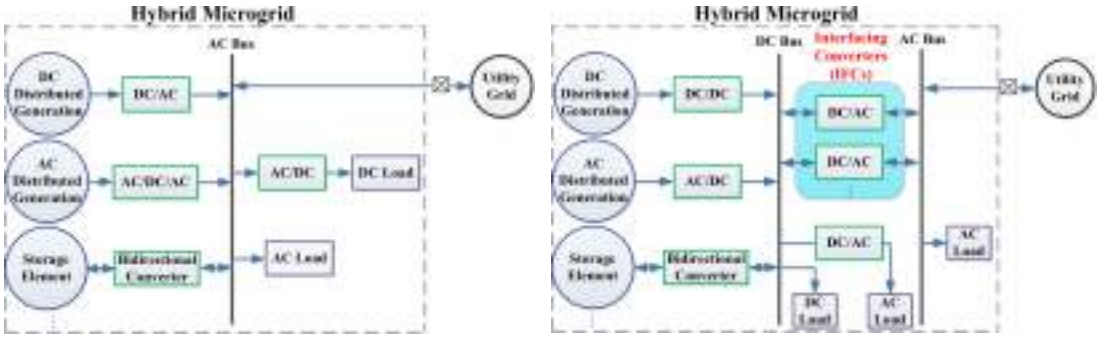

(a) (b)

Fig. 2.12 Structures of hybrid microgrid. (a) ac-coupled. (b) dc-coupled [56].

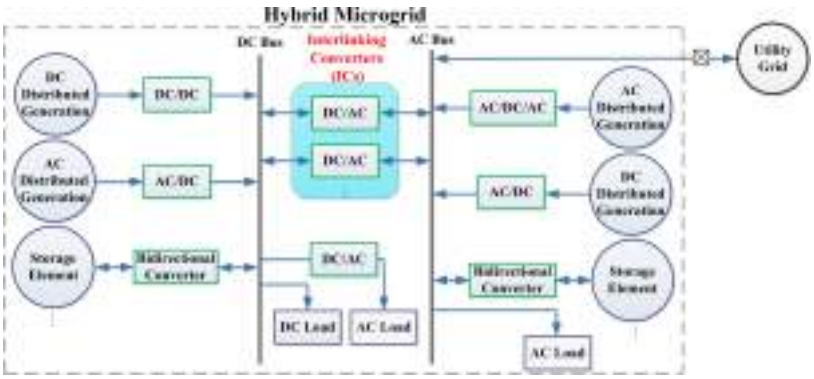

Fig. 2.13 Structure of ac-dc coupled hybrid microgrid [56].

2.2.7 Interlinking Converters

Interlinking converters (ICs) are used to interlink the ac and dc grids [57], [58]. Primary task of IC is to ensure appropriate power flow between the ac and dc grids. Generally, ICs in parallel are made to imitate the synchronous droop control method for power management. Due to line resistances, such methods also pose the issues of circulating currents. In [58] the issue of circulating current is addressed and an autonomous control scheme is presented to achieve maximum utilization of the IC with proper power

sharing. Two ICs, IC1 and IC2 are considered. IC1 is rated at twice the value of IC2. In Fig. 2.14(a), the power sharing with conventional voltage based droop is shown. It is seen that the power sharing is not as per the ratings due to voltage drops at line resistances. With the proposed method, proper power sharing is observed between IC1 and IC2. This is shown in Fig. 2.14(b).

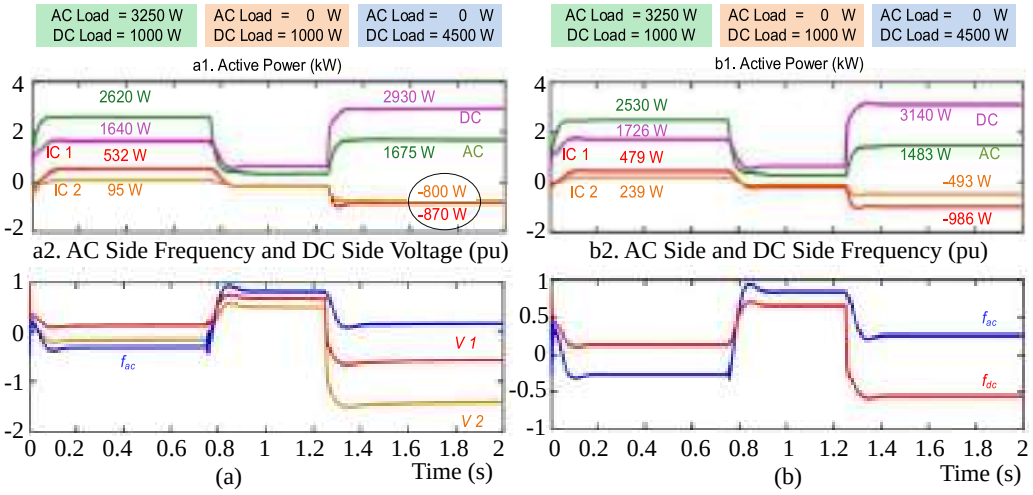

Fig. 2.14 Illustration of over-stressing of ICs. (a) Voltage based droop method. (b) Proposed droop control [58].

Table 2.1 summarizes the various technologies that have been discussed above for addressing issues in the modern grid.

Table 2.1 Summary of conventional solutions for modern grid issues.

Technology	Features
On Load Tap Changer Transformer	Voltage regulation
Distribution Static Compensator	Voltage regulation, power factor correction, load balancing, harmonic filtering
Dynamic Voltage Restorer	Mitigate voltage disturbances
Unified Power Quality Conditioner	Combines the functions of both DSTATCOM and DVR
Static Transfer Switches and Current Limiters	Cut or limit the power flow with power electronic switches
Hybrid Grids	Incorporates benefits of both ac and dc grids
Interlinking Converters	Interlink ac and dc grids

2.3 Smart Transformer (ST)

2.3.1 History

The technologies discussed in the previous section can address most of the issues of the present day electric grid. However, such technologies are application specific and can only deal with limited issues. As the modern power system is undergoing change with time, need has aroused to incorporate devices which can efficiently handle several issues of the modern grid. As the grids get increasingly complicated, a "one stop solution" is very much necessary to reduce the overall costs and complexity of the systems. With such goals in mind, researchers have explored the scope of power electronics for an alternative to the CPT to meet the new challenges of the modern grid. Considerable attempts have been made by researchers worldwide to come up with a power electronic device possessing not just the features of a conventional transformer, but also with many added functionalities.

The concept of such a power electronic device with the functionalities of a conventional transformer dates back to 1968 when William McMurray filed a patent named "Power converter circuits having high frequency link" [59]. A device based on solid state switches with high frequency isolation behaving like a conventional transformer was proposed. Many researches have been conducted ever since on this new power electronic device which got popular by the name of "solid state transformer (SST)". Researchers have also frequently referred to such a device as a "power electronic transformer (PET)". Along with more functionalities, an SST can also contribute significantly in weight and volume reduction. Such a feature, being a great attraction to the traction industry, made researchers to explore the capabilities of an SST in the traction industry. Recently, ABB group installed the world's first ever power electronic traction transformer and it is presently in use by Swiss Federal Railways [60].

The use of an SST has significant potential in smart grid functionalities for a distribution system. The voltage transformation in an SST is realized in stages and most topologies of SST have one or more intermediate dc links. The availability of a dc link adds the possibility of dc power transfer to and from the grid, enabling integration of RES and storage systems. In fact, an SST can also act as an energy router by communicating with the different sources and loads. Such control and communication functionalities make

the SST a smart device and is referred as a “smart transformer (ST)” in literature [61].

2.3.2 Structure of a Smart Transformer

In an ST, the grid power is converted into dc power with an ac-dc converter. With the help of high frequency dc/dc converter, the power is brought down to LV level. A transformer is added in between for galvanic isolation. The presence of a high frequency transformer contributes significantly to the reduction in weight and size. The power is again converted to ac power with the help of dc-ac converter to support the load.

Depending on the number of stages and the output type, the ST architecture can be broadly classified into four categories [62] as shown in Fig. 2.15.

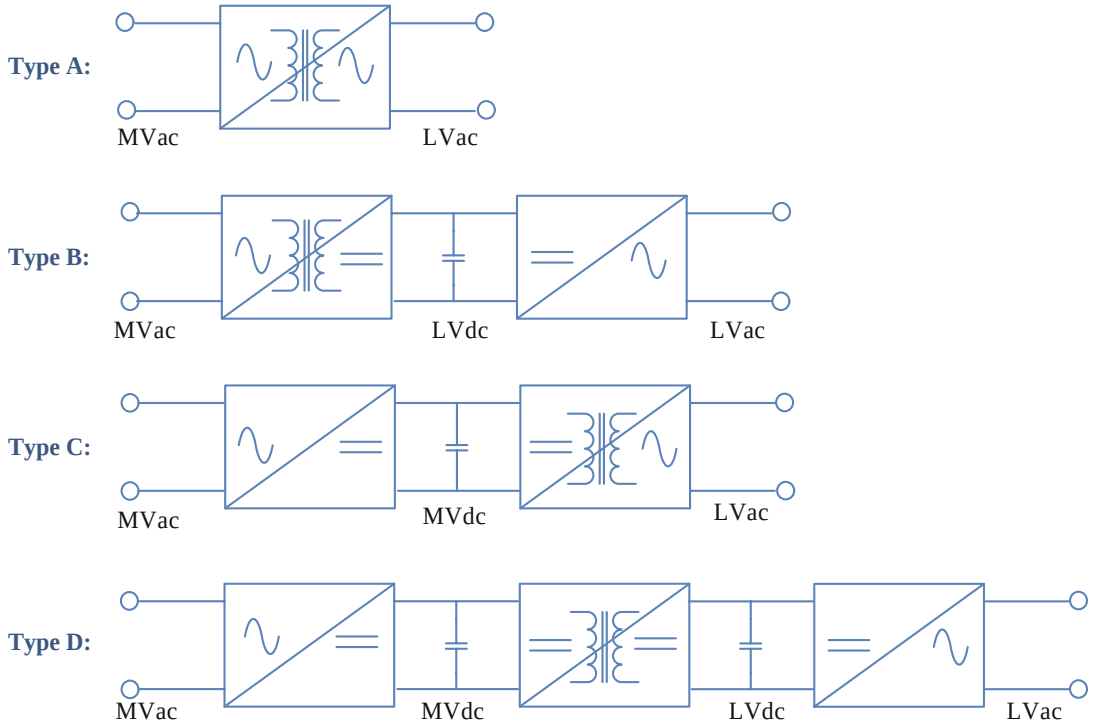

Fig. 2.15 Topology classification of ST [63].

Type A has no dc link and thus has no possibility of integrating dc sources and loads. Type B has an LVdc link while Type C has a medium voltage (MV) dc link as the galvanic isolation is done in the dc/ac stage. Type D has three stages and both MV and LVdc links are available. This offers the possibility to interface RES at MVdc and LVdc level. Moreover, interface to MVdc and LVdc grid is also possible. Therefore, type D is evidently the most feasible and convenient architecture for electric grid application [63]. The different components of a three stage ST are discussed as follows.

2.3.3 ac/dc Conversion Stage

The primary task of the ac/dc conversion stage is to absorb active power from the MVac grid based on the load requirement in the distribution grid along with the converter losses [61]. This converter is referred to as the ST MV converter. It is a controlled rectifier which converts ac power into dc. As the converter operates at MV level, it is essential to have series-connected switches to achieve the blocking voltage requirement. Fig. 2.16 shows some topologies used for the ST MV converter. In Fig. 2.16(a), a three-level neutral point clamped (NPC) configuration is shown. The circuit uses clamping diodes to ensure proper voltage sharing among the power switches. This circuit topology is relatively simple and is already adopted in industry. The availability of dc link is another advantage. However, this structure has lesser levels which results in bulkier filters, and high switching frequency which decreases the overall efficiency of the system. Moreover, each device should have fault detection and isolation mechanism that come into action in case of failure.

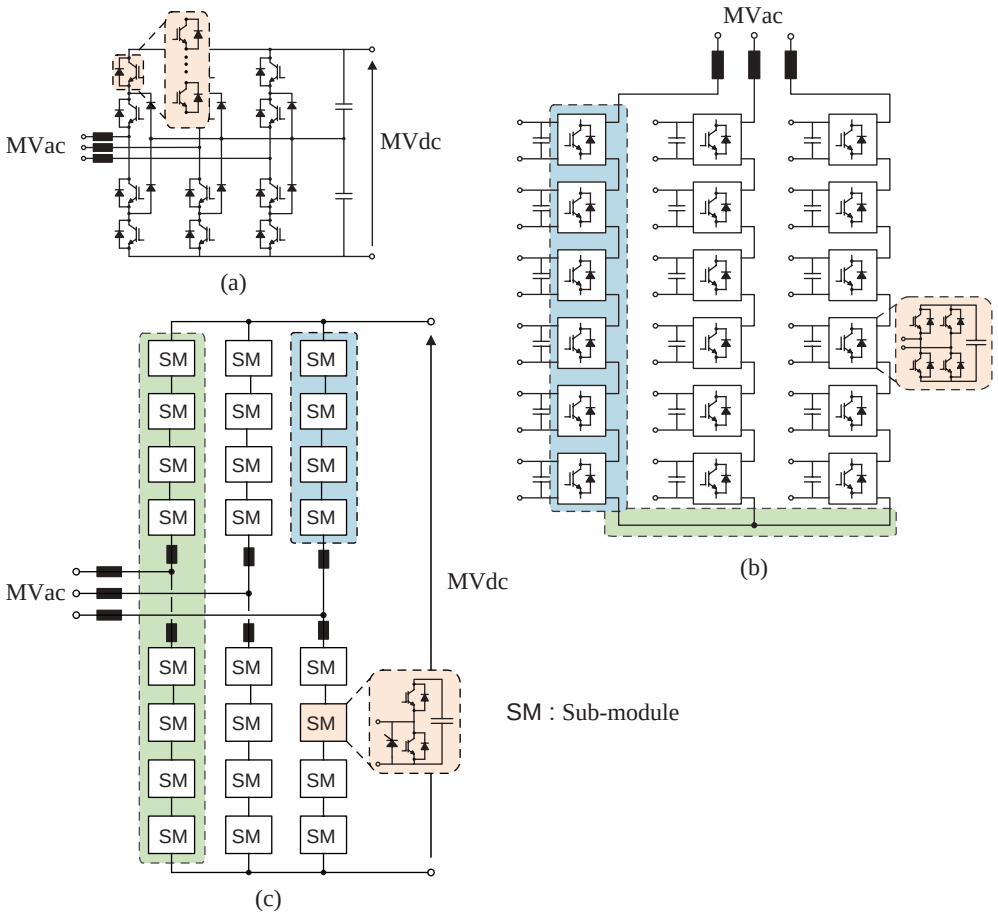

Fig. 2.16 Various topologies for ac/dc conversion stage. (a) Three-level NPC configuration. (b) Modular configuration. (c) Modular multi-level converter configuration [61].

Fig. 2.16(b) shows a modular approach for the ST MV converter realized with cascaded H-bridge configuration. The main idea of such a configuration is to reach higher voltage levels with devices having lower voltage ratings [64]. The topology has lower control complexity, offers good performance with lower switching frequencies and has been widely used in MV drives. However, there is absence of dc link which is a main drawback. Moreover, each cell will need an isolated supply.

In Fig. 2.16(c), the ST MV converter is realized with a modular multi-level converter. This configuration satisfies the requirements of both modular structure and low frequency operation. The main advantage of a modular structure is that advanced control actions can be performed with internal power routing. This can be useful for removing modules with faults or the ones which show signs of degradation [61]. There is also the availability of dc link. But such a structure needs bulky dc link capacitors, and they also require complex control.

2.3.4 dc/dc Conversion Stage

In this stage, the MVdc power is stepped down to LVdc power with a dc/dc converter along with a high frequency isolation transformer [61]. The converter maintains the LVdc voltage and allows power transfer between the MVdc and LVdc links of the ST. Therefore, it needs a high voltage (HV) capability on the MV side and a high current capability on the LV side. The dual active bridge (DAB) converter is considered most suitable for the ST isolated dc-dc converter [65]. One of the primary goals is to reduce core size of the isolation transformer and reduce losses at the same time. A high frequency operation can reduce the required core size of the transformer and soft switching techniques can reduce losses significantly. However, high frequency operation increases hysteresis and Eddy current losses to a great extent. This requires the core to be made of materials producing low losses like amorphous (metglas, vitrovac) or nano-crystalline (fixemet, vitroperm) materials for ST operation [63].

The ST isolated dc-dc converter can either be a single phase DAB or a 3 phase DAB. Fig. 2.17(a) shows the structure of a single phase DAB. This converter actively controls the transferred power and is therefore advantageous when output voltage or power flow control is necessary. However, such a converter may face the issue of transformer sat-

uration. To prevent this and to allow reduced rms transformer currents, a capacitor can be inserted in series with the transformer. This configuration is called a series resonant DAB and shown in Fig. 2.17(b). The converter can help to achieve reduced switching losses. Moreover, while operating in discontinuous conduction mode, it can provide a well regulated output voltage for a wide range of loads. This is possible without the need of additional control loops and sensors.

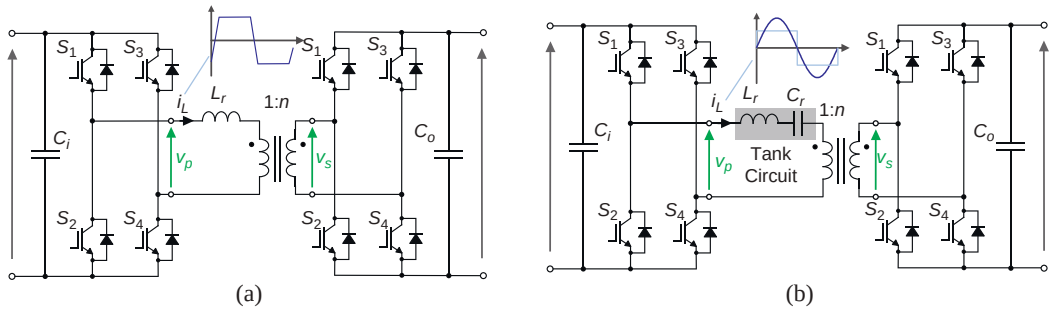

Fig. 2.17 Circuit diagram for isolated dc-dc converter. (a) DAB converter. (b) Series resonant DAB converter [61].

Fig. 2.18 shows the circuit diagram of a three phase DAB. Compared to a single phase DAB, this converter has lower filter size, reduced transformer rating, and lesser current stress [66].

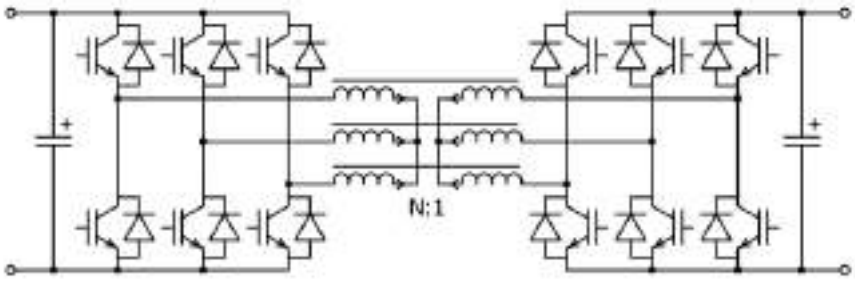

Fig. 2.18 Three phase DAB [63].

Another possible configuration for the ST isolated dc-dc converter is the multi active bridge (MAB) converter. In such a converter, more number of active bridges can be integrated into a single high frequency transformer. Therefore, multiple dc voltage levels are present both at the input and output, which can be used to integrate multiple RES, loads or BESS [67]. The circuit diagram is shown in Fig. 2.19. The control of MAB is challenging due to inherent coupling between the power flow ports.

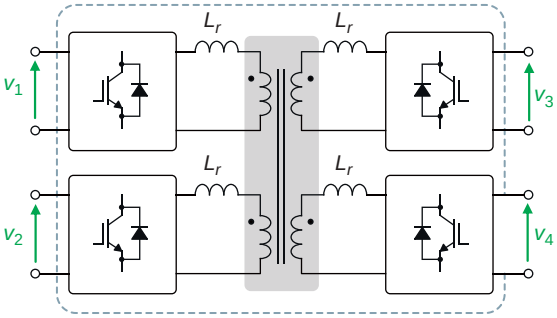

Fig. 2.19 Circuit diagram of MAB converter [61].

2.3.5 dc/ac Conversion Stage

In this stage the power conversion from LVdc to LVac takes place. This is the inverter stage which is referred to as the ST LV converter. Its primary task is to maintain the LVac grid voltage and frequency. A standard CPT offers a 3-phase 4-wire connection at the distribution grid. These are the three phases and the neutral. Since the ST is targeted to be used as an alternative to the CPT, the neutral connection is important for the ST LV converter [61]. The neutral can be connected to the mid-point of the LVdc link which is divided into two levels with two capacitors in series. To ensure accurate voltage distribution amongst the capacitors, additional dc-dc converters can also be used. Due to lower voltage levels, a wide choice of devices and topologies are available for this converter. A two-level converter or a three-level NPC configuration are the most commonly used converters for this stage. Fig. 2.20(a) and (b) shows the circuit diagrams of two-level, 3-leg and 4-leg converters, respectively. The three-level topology allows the use of 600 V devices which improves the output waveform along with efficiency. Thus, it is a prevalent choice for industry. A standard or T-type configuration of three-level NPC are most commonly used. The circuit diagrams are shown in Fig. 2.20(c) and (d), respectively.

2.3.6 Smart Transformer Features

The key features of an ST are as follows:

1. It performs the action of the CPT by providing isolation and voltage transformation.
2. It can act as a power management node.

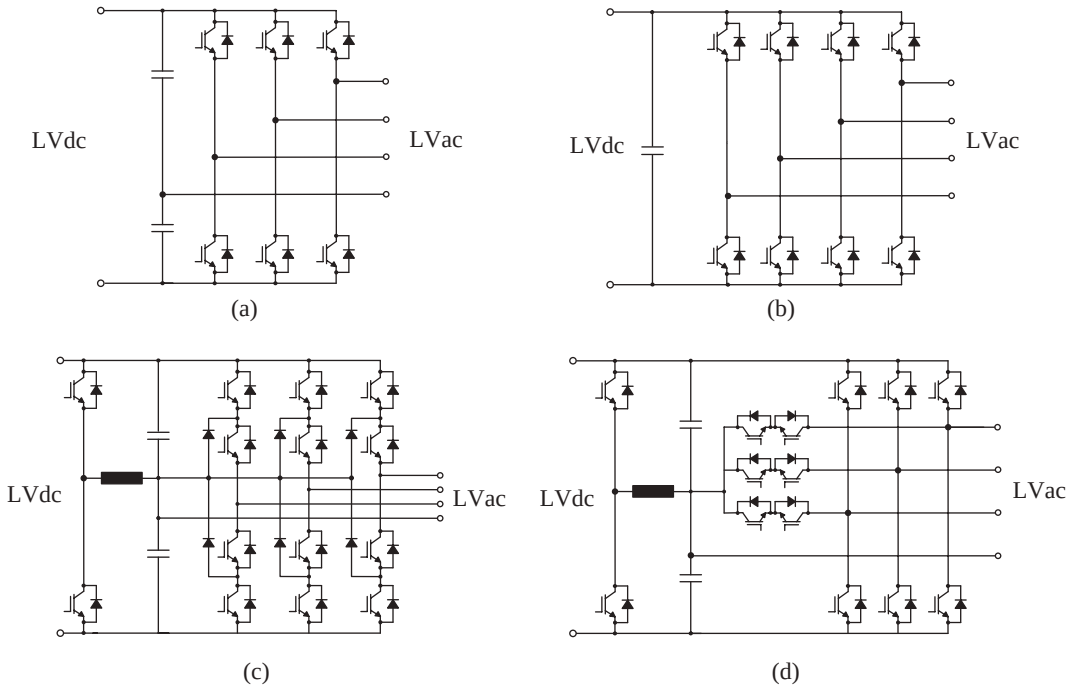

Fig. 2.20 Various configurations for the dc-ac converter stage. (a) Two-level 3-leg converter. (b) Two-level 4-leg converter. (c) Three-level NPC converter. (c) Three-level T-type NPC converter. [61].

3. It can serve as a link to different ac and dc infrastructures acting as sources or loads.
4. It can act as a link to other energy sources or plants.
5. It can also act as a support for EV infrastructure.

The availability of MV and LVdc buses enable an ST to exchange power with a variety of renewable sources and dc loads. Fig. 2.21 shows the schematic for such interfacing. The MVdc bus is used to interface large wind farms operating at MVdc voltage level. The LVdc bus is used to interface RES like PV and wind. It can also be used to interface EVs, BESS and dc loads. The LVac grid consists of LVac loads, turbine generator, BESS, etc. With such interfacing, most of the grid issues like voltage swell or sag, load balancing, reactive power compensation, fault isolation and limitation can be handled by the ST itself without the need of other conventional power quality improvement technologies.

Table 2.2 shows a comparison between a CPT and an ST. The ST lags behind the CPT in terms of cost, life cycle and efficiency. However, it offers superior features in terms of power quality, fault management, flexibility, energy management and dc connectivity. Therefore, more research and development is needed to realize the potential of ST in

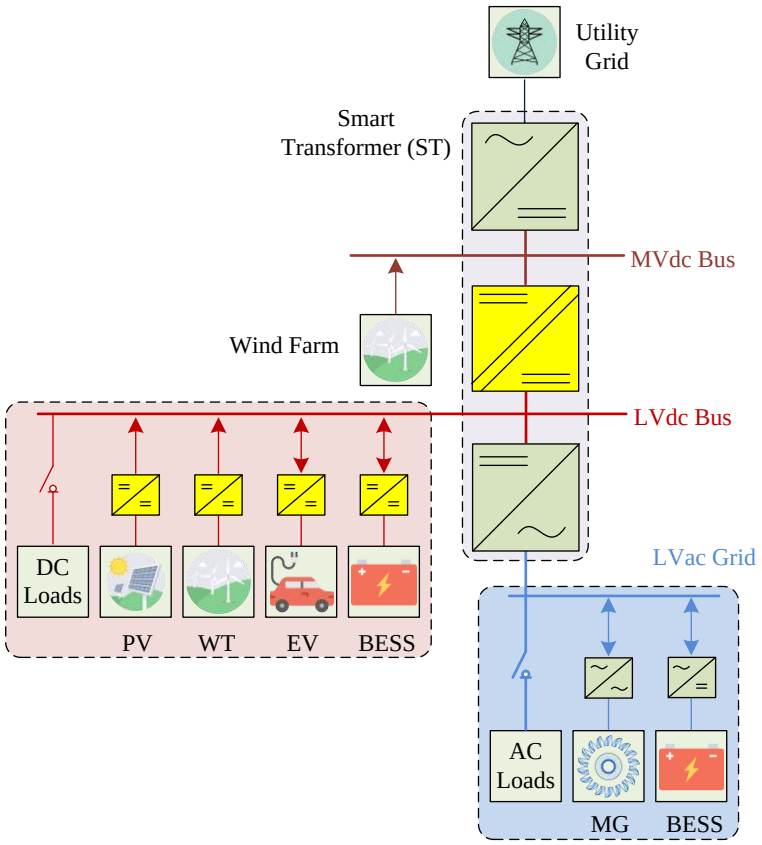

Fig. 2.21 ST interfacing multiple sources and loads in the electric grid.

distribution grid.

Table 2.2 Comparison of CPT with ST.

Factor	Traditional Transformer	ST
Life cycle	Higher	Lower
Cost (incl. maintenance)	Lower	Higher
Volume/weight	Higher	Lower
dc-connectivity	No	Yes
Power quality	Lower	Higher
Fault management	No	Yes
Optimal energy management	No	Yes
Flexibility	Lower	Higher
Hybrid grid operation	No	Yes
Meshed grid operation	Only in ac grids	In both ac and dc grids
Stability enhancement	No control	Yes

2.4 Smart Transformer Applications

In recent times, performance of ST is extensively explored in the distribution grid. There have been applications of ST for grid operations, control and management. Some

of the applications are broadly classified and explained as follows.

2.4.1 ST for Interfacing Renewable Energy Sources

Researchers in [68], [69] have presented the system integration issues of a PMSG wind energy conversion system with an SST, along with wind turbine level control methods. Fig. 2.22(a) shows the conventional integration strategy where the wind PMSG is interfaced to the grid through a back to back converter and an isolated ac-ac converter. Fig. 2.22(b) shows the proposed integration strategy, which utilizes the SST to integrate the wind PMSG to the grid. Simulation and experimental results for wind speed variation and step change in load have been presented and the results show good system performance. Fig. 2.23 shows the simulation results for a step change in load at t = 4 sec. As the wind system is not able to provide the additional power, SST switches into grid supply mode to support the load. The result given in Fig. 2.23(f) shows that the power drawn from the wind system remains constant. Some transients appear at the HV and LVdc buses but they recover quickly to the steady-state. The proposed power management strategy highlights the SST's capability to establish a coordination among the wind energy system, distribution grid and the loads.

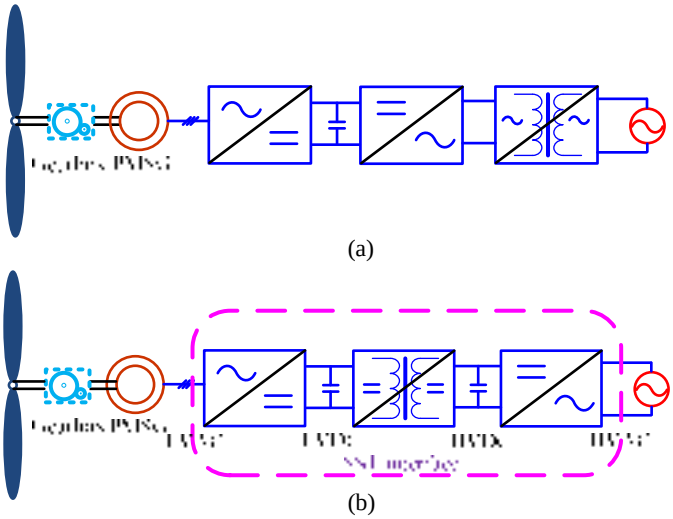

(a)

(b)

Fig. 2.22 PMSG wind system PCC integration configuration. (a) Conventional integration strategy. (b) Proposed integration strategy [68].

A high efficiency control strategy for 10-kV/1-MW SST to be utilized for PV application is presented in [70]. An SST composed of DAB and cascaded H-bridges as shown in Fig. 2.24 is considered for the PV system. To improve the efficiency, a model for

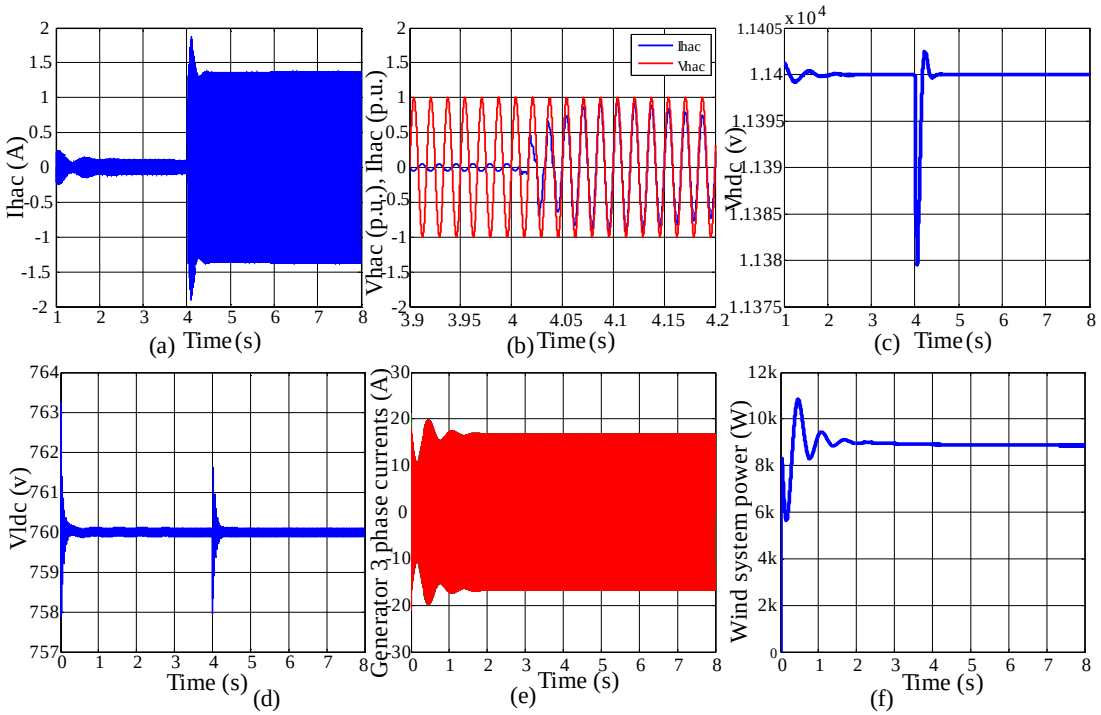

Fig. 2.23 Simulation results for PMSG wind system integration with SST under load step change. (a) Distribution line side input current. (b) Distribution line side input voltage and current. (c) HVdc bus voltage. (d) Low voltage dc bus voltage. (e) Generator 3-phase currents. (f) Wind turbine system output power [68].

calculating the losses in the DAB is derived under frequency domain analysis, and the switching turn ON and turn OFF losses are plotted against the switching current as shown in Fig. 2.25. Such loss analysis is useful for the efficiency optimization of the proposed SST-based PV system.

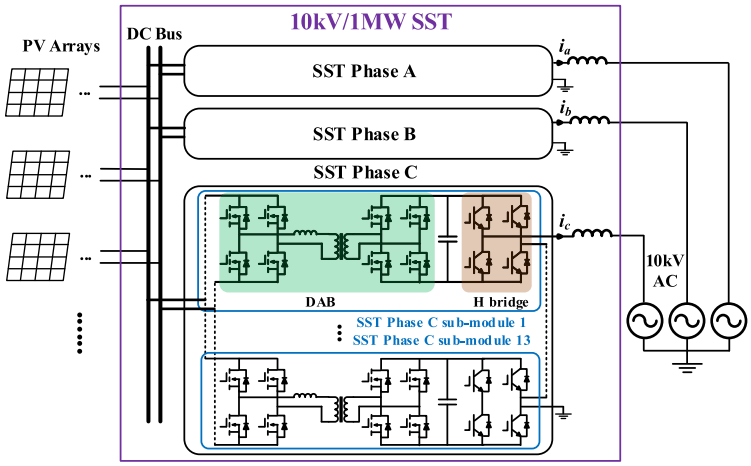

Fig. 2.24 Circuit scheme of SST in PV application [70].

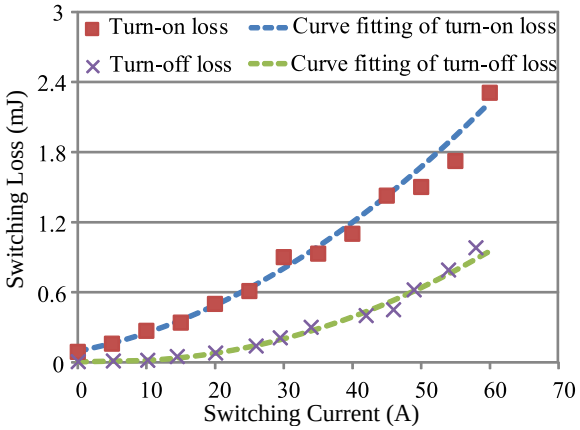

Fig. 2.25 Switching loss of DAB power switch [70].

2.4.2 ST for Zonal Microgrids

The concept of a zonal microgrid consisting of a smart and sustainable building or a group of buildings has been presented in [71]. They have focused on investigating a new microgrid architecture that integrates the solid state transformer with zonal dc grids. Fig. 2.26 shows the dc microgrid architecture considered. Different modes of operation of the system considered are given and a centralized power management algorithm is developed for functioning of the SST as an energy router in the 10 different modes. The modes consist of permutations like failure of the storage system or its charging or discharging modes, along with the varying behaviour of the various sources and loads. The algorithm dictates the ST to work efficiently and appropriately in all these scenarios.

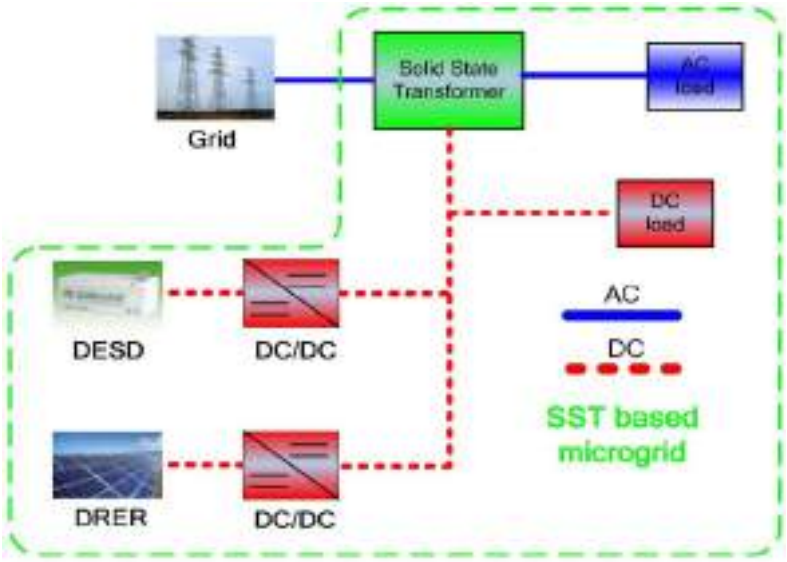

Fig. 2.26 dc microgrid architecture [71].

Fig. 2.27 shows the results for the passive grid interaction mode where PV operates in MPPT mode, battery balances the power within zonal dc microgrid, and SST only supplies power for ac load. With the change in the solar irradiation curve, the battery charges accordingly drawing power from the PV system. The ac and dc load powers remain constant throughout. The LV terminal waveforms are well regulated. The in-phase SST input voltage and current waveforms verify the unity power factor operation.

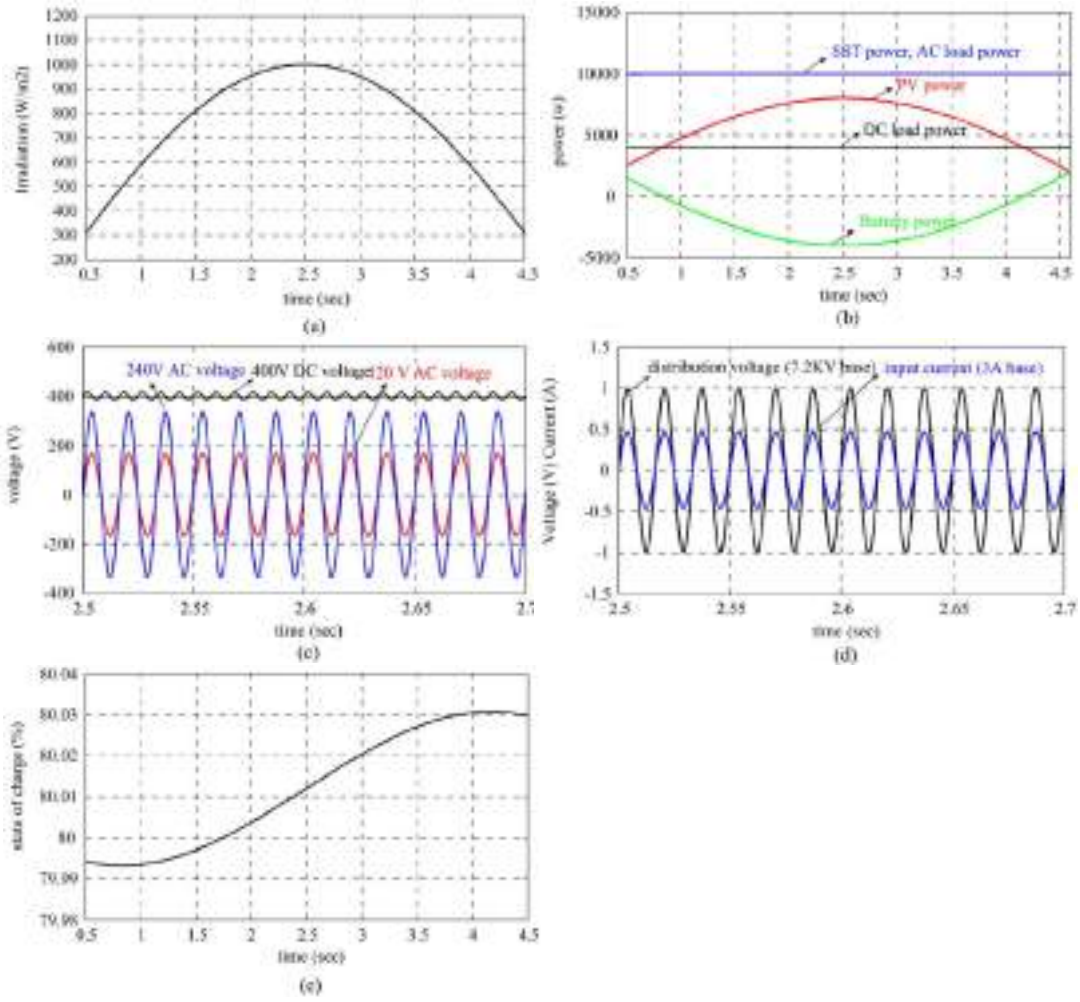

Fig. 2.27 (a) Irradiation of PV panel. (b) Power distribution of the system. (c) Low voltage terminal waveforms. (d) HV terminal waveforms. (e) Battery SoC [71].

In another study, the operation of hybrid dc-ac zonal microgrid enabled by ST is explored [72]. The system considered is shown in Fig. 2.28. The zonal microgrid is considered similar to the structure of large individual buildings in smart cities. An energy storage system is considered which is interfaced to the LVdc bus of the ST through a DAB for higher power transfer and improved performance. Modes of operation like the grid interaction and islanded mode of operation are discussed and the control strategies are explained.

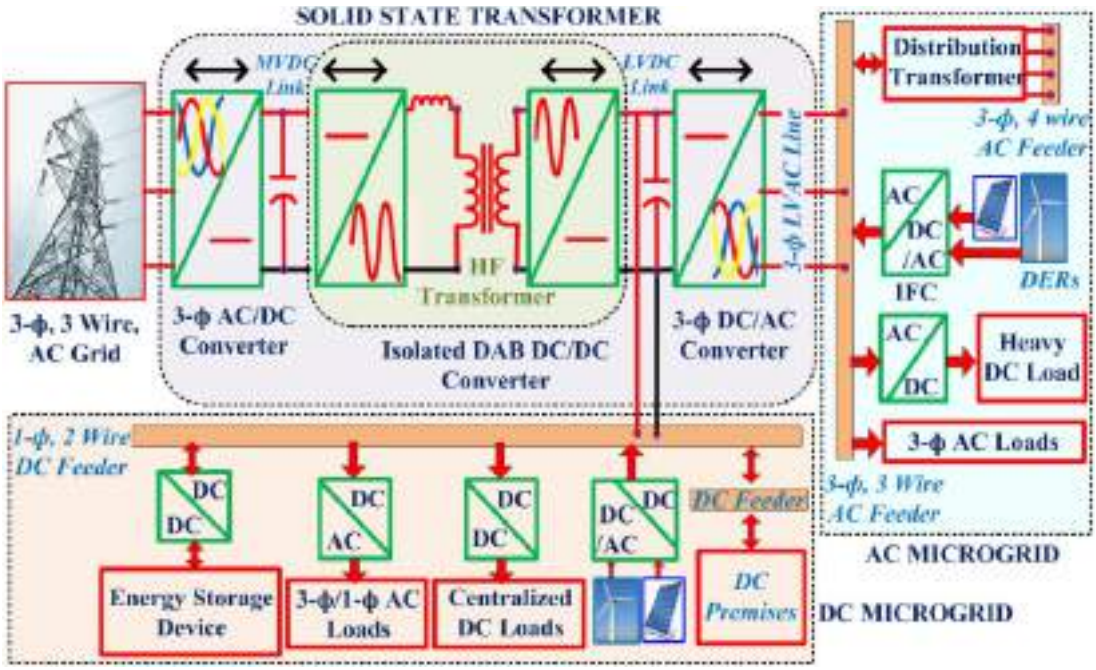

Fig. 2.28 ST enabled hybrid dc-ac zonal microgrid architecture [72].

2.4.3 ST as an Energy Router

The potential of an SST as an energy router has been explored in [73]. An economic energy routing strategy is introduced which utilizes energy storage to reduce consumption of grid power. A dispatch algorithm has been developed from a rule based list that schedules charging and discharging of energy storage for the entire day, depending on utility energy prices, generation and load forecasting. A case was simulated considering a typical 3 kW peak load curve for a single home, a typical 1.5 kW peak solar curve, and a 1.5 kWh battery with a power limit of 1.5 kW. The initial state of charge (SoC) and final desired SoC were set to 40%, with the lower limit and upper limit at 30% and 70%, respectively. The prices during the different periods of the day were considered. The simulation results showed that an intelligent scheduling of battery storage and dispatch can substantially reduce the grid demand during the mid-peak and on-peak time blocks, thus reducing the consumer's electricity bill [73]. The power curve results for the various connected sources and loads, obtained from simulation are shown in Fig. 2.29. Such power routing can be considered an as important aspect and capability of an SST.

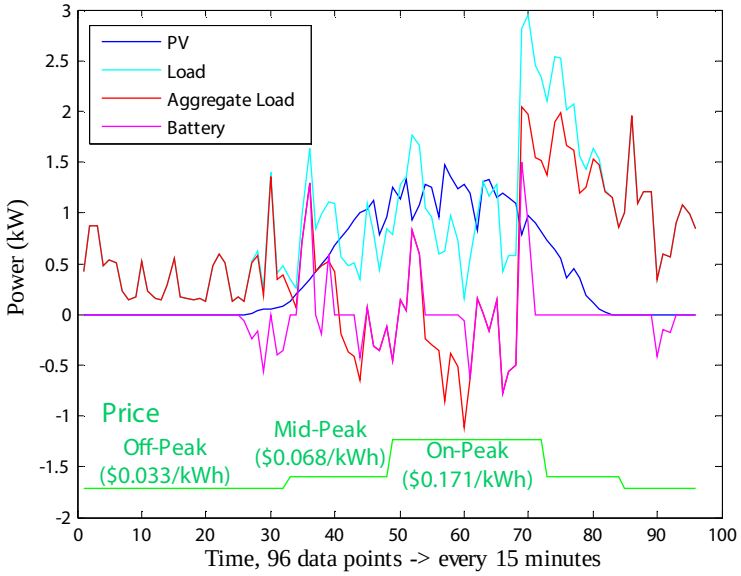

Fig. 2.29 Power curve [73].

2.4.4 ST for Grid Frequency Interactions

Unlike the CPT, the ST has the capability to interact with the frequency of the grid. This feature has been exploited by researchers to control the grid frequency and various control techniques have been proposed to obtain improved power quality in the distribution grid. In [74], [75], a frequency adaptive ST based grid is presented for overload management that acts in coordination with the droop controller of DG systems. Power semiconductor devices can withstand overloads for only a few micro seconds while in distribution grid scenarios, the grid components might require to bear such over-currents for several seconds. Existing distribution grids are designed for passive operation. However, these are subjected to increasing power transients caused mainly due to the integration of distributed generation. Adding to that, non-conventional loads like EVs and battery storage systems are also being incorporated. Existing technologies like load tap changer or hybrid solutions via power electronics are not able to meet the requirements of such transient optimization.

An ST can solve such an overloading problem by modifying the grid frequency and activating the distributed generation droop controller. As the current approaches the hard limit and exceeds the set security threshold, the ST lowers the frequency and lets the DG increase the injected active power to compensate the frequency drop. An emergency situation is considered in [74] when the load demand exceeds the ST capacity and the LV grid is sustained with the help of diesel engine and wind turbine as shown

in Fig. 2.30. When the power from wind turbine decreases, load on the ST increases. The ST, in such a condition, reduces the frequency and allows the diesel generator to pump more active power. Consequently, it prevents the ST from shutdown. Without control, the current exceeds the hard limit which will cause the ST to turn OFF. This is demonstrated in Fig. 2.31.

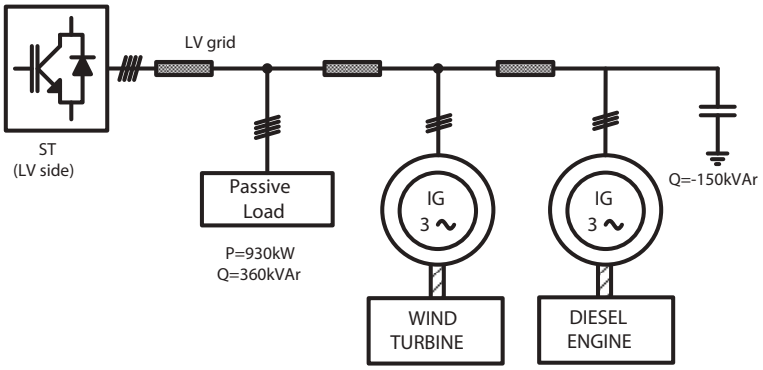

Fig. 2.30 Grid connected with diesel engine and wind turbine [74].

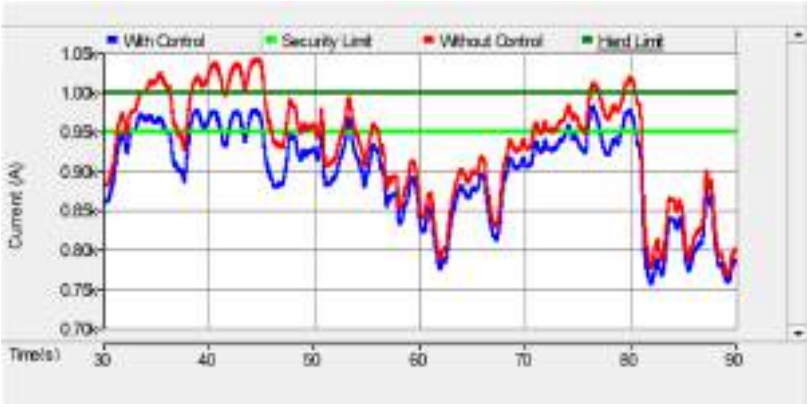

Fig. 2.31 Current waveforms for the considered system with and without control [74].

2.5 ST Fed LV Distribution Grid

Fig. 2.32 shows a CPT fed LV distribution grid with RES, EV and BESS integration [76]. The CPT steps down the MVac grid voltage from 11 kV to 0.4 kV and 0.4 kV distribution lines carry the power to the various LVac buses in the distribution grid. Some of the LVac buses are interfaced with systems like PV, BESS and EV. The PV systems inject power as per the availability of PV power and the power is either consumed in the distribution grid or in case of surplus generation, fed back to the MVac grid through the CPT. Maximum power is extracted from the PV panels by a dc-dc converter. A DG converter maintains the dc bus voltage and converts the power from dc

to ac for injection into the LVac grid. The BESS and EV also charge or discharge by drawing power from or injecting into their corresponding LVac bus. These are operated with dc-dc converters for charge/discharge operation and DG converters enable power exchange with the LVac grid.

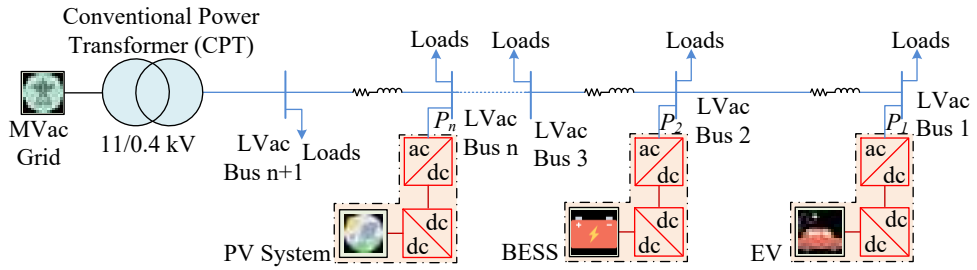

Fig. 2.32 Typical configuration of a CPT fed LV distribution grid with RES.

When the CPT is replaced with a three stage ST, the structure of the LV distribution grid is as shown in Fig. 2.33. Here, the ST replaces the CPT for voltage transformation and power exchange between the MVac and LVac grid. The ST offers the availability of MVdc and LVdc bus which were absent in case of the CPT. Moreover, as the converters of the ST can be individually controlled, they can be used to ensure regulated voltages at the MVdc, LVdc and LVac buses with the help of closed loop control. This is not possible with the CPT as it is a passive device.

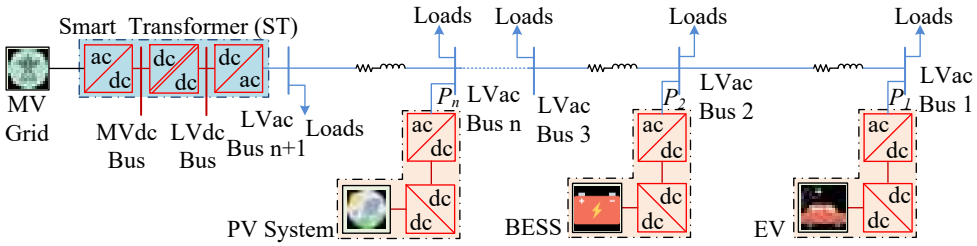

Fig. 2.33 Typical configuration of ST in the LV distribution grid.

Many researches have already been conducted on ST based systems similar to the one shown in Fig. 2.33. Some of these have been discussed in the previous section. However, there are quite a few research gaps that have been identified. There is limited study on such ST based systems which deals with meshed grids. The interaction of the ST with the DG converters present in the system has not been discussed. Moreover, there is the scope of islanded operation of the LV grid which also has not been explored much in the literature. Such research gaps have led to the motivations for this thesis work and they are discussed in the following section.

2.6 Problem Statements

The present power system scenario discussed in Chapter 1 clearly indicates that the future grids will be rich in RES as well as widely varying loads. The loads comprise of active, reactive as well as harmonic components. Moreover, with both ac and dc power being generated and consumed, hybrid grids will get more popular with time [56]. Researchers have already presented the ST as a promising solution to several issues posed by the modern grid [77]. Nevertheless, owing to higher costs and lesser efficiency as compared to the CPT, the use of ST can only be justified if the overall functionalities exceed than that of the CPT. While a CPT cannot contribute much to a hybrid grid, the ST is very suitable owing to its multiple ac and dc links [78].

Power distribution systems can be classified into radial, parallel, ring and meshed type systems [79]. Out of these, the meshed type distribution has received recent focus due to improved redundancy as many power flow paths between any two points. Meshed HVdc grids have also been substantially discussed in the literature. Studies like [80]–[82] focus on improved power flow control in meshed dc grids. [83] discusses circulating net currents that can appear in meshed dc grids, similar to the residual ground currents in ac systems. Derivations of net circulating currents are presented for unipolar and bipolar dc distribution grids along with a discussion on measurement and protection devices for such circulating currents. In [84], an investigation has been carried out on impact of wind systems on the cost and stability of a meshed dc/ac grid. However, there is limited study available on such meshed hybrid grids. Moreover, with the attractive features being offered by the ST, the potential to cater to a meshed hybrid grid is an interesting area of research which has still not been explored.

A meshed hybrid grid enabled by ST will have features of a meshed system, hybrid system and ST. These will include, ac/dc grid interactions, multiple power flow paths, RES integration, etc. as discussed in the previous sections. Considering all these in one system will unveil multiple functionalities as well as challenges. There will be improved possibility of line loss reduction, optimal power management, renewable integration, EV integration, better power quality and stability improvement. With multiple sources integrated together along with multiple power flow paths, there will also be the possibility to improve the voltage profile in both ac and dc grids.

Owing to renewable energy penetration, microgrids are also receiving increased importance. One of the key features of a microgrid is the ability to operate in islanded mode, disconnected from the main grid. The ST can provide various functions in such renewable based islanded microgrids which have still not been explored in the literature. With the global trends shifting towards EVs, vehicle to grid technologies are also seeing increased focus [85]. The ST is also very useful for such EV to grid integrations. EVs generally draw a high amount of power for charging. The grids have to cater to such high demands without voltage disturbances or stability issues. This is a challenge which needs more research.

There are studies in the literature which discuss the islanding and re-closure mechanism of microgrids where CPTs are present [86]. When the CPT is replaced with ST, the islanding and re-closure mechanisms will be much different. Especially for re-closure, there needs to be specific start-up schemes that have to be designed and implemented to ensure controlled inrush current during starting and smooth transition from islanded to grid connected mode. With the integration of ST, new techniques and control strategies have to be devised.

2.7 Objectives

Based on the literature and motivations, the objectives of this research work are summarized as follows:

1. To explore the operation of ST in a hybrid microgrid where both ac and dc distribution are present.
2. To develop power management strategies of ST based islanded microgrids for line loss minimization.
3. To investigate the stability aspects of the ST based islanded meshed microgrids during EV charging transients.
4. To propose a reconnection procedure for the ST based islanded microgrid back to the MVac grid for smooth transition from islanded to grid connected mode with seamless operation of the LV grid.
5. To validate the proposed algorithms and control strategies on laboratory prototypes.

CHAPTER 3

SMART TRANSFORMER ENABLED MESHED HYBRID DISTRIBUTION GRID

In Chapter 2, the issues arising out of RES integration in the modern electric grid are highlighted along with currently available and utilized solutions. The current need of hybrid grids is also discussed. Further, the ST is introduced along with emphasis on its various features that make it suitable for a hybrid grid which consists of ac and dc loads along with DG converters. The DG converters are used to inject power from various sources into the electric grid.

The ST provides features of CPT in a distribution grid, and also other benefits such as voltage control, frequency control, load compensation, interfacing link for various ac and dc infrastructures, thus improving the flexibility of the system [61]. Various ST configurations are proposed in the literature [62], [87], [88]. For electric grid applications, the ST with three power conversion stages is considered the most suitable choice due to availability of two dc links [62]. The ST has been explored for various services in electric grid. In [89], a power management strategy for an ST based dc microgrid consisting of fuel cells, PV system and energy storage is presented. With seamless power transfer between charging and discharging modes, a dc microgrid, ac loads and a distribution grid are interfaced. [90] proposes a hierarchical power management strategy for an ST interfaced dc microgrid. In [91], [92], investigation on the integration and power management of ST interfaced ac microgrids along with issues like RES integration, energy storage, reverse power flow and voltage regulation are explored.

As explained in Chapter 1, since modern distributed sources can either be ac or dc, hybrid microgrid with parallel existence of dc and ac microgrids are proposed in literature [56]. Such hybrid microgrids combine the benefits of both ac and dc systems. [57], [93] focus on the interlinking power electronic converters between ac and dc grids, and various control strategies for such converters are proposed. In [94], [95], hybrid ac-dc microgrids have been investigated, and planning and power flow algorithms have been proposed. Moreover, to inject active power into distribution grid, RES are first

connected through either dc-dc or ac-dc converter and then to a dc-ac converter (DG converter). Since RES have intermittent active power production, the DG converters do not operate at their rated capacity at all times [96]. For realizing such hybrid microgrids with improved utilization of DG converters, ST with availability of LVdc link can be a promising solution. With presence of both ac and dc interface options, the ST not only eliminates the need of interlinking converters connecting various ac and dc sub-grids [93], but also enables various power flow paths and power management strategies.

In this chapter, an ST enabled meshed hybrid LVac and LVdc interconnected distribution grid is proposed. An LVdc line is proposed which connects the ST LVdc link with the dc bus of DG converters. This introduces various power flow paths to support the loads. The DG converters supply active power near the load points which ensures that the line losses are reduced significantly while achieving improved voltage regulation as compared to conventional microgrid. Moreover, the DG converters can draw active power from ST LVdc link during absence of RES to support the load resulting in improved utilization of these converters. The control complexity of the DG converters is reduced as the ST controls both the LVac and LVdc line voltages. Further, the newly developed power flow path allows reverse power flow from DG plants more efficiently. Performance of the proposed system is verified with simulation and experimental results.

3.1 Description of Conventional and Proposed Systems

Fig. 3.1(a) shows a conventional distribution system [76]. The LVac grid is connected to medium voltage (MV) ac grid through a CPT. An n bus LVac grid is considered each having an RES and loads. $R_1 + jX_1$, $R_2 + jX_2$... $R_n + jX_n$ denote impedance of various sections in the LVac lines. Renewable sources like PV and EVs are connected to the LVac grid through DG converters. The DG converters supply power to LVac grid based on availability of RES.

Fig. 3.1(b) shows the proposed ST-based meshed hybrid microgrid. The CPT is replaced with an ST. The ST consists of a MV converter, DAB converter and LV converter. The MV converter converts MVac grid supply into MVdc. The DAB converter

steps down the MVdc to LVdc. The LV converter maintains a constant voltage and frequency on the LVac side of the grid. The LVdc link of the ST is extended to supply dc buses of the DG converters. R_{dc_1}, R_{dc_2}... R_{dc_n} denote resistances of various sections in the LVdc line. The DG converters draw power directly from the ST LVdc bus when sufficient DG power is not present, and supply to ac loads. This ensures that the utilization of DG converters is improved. On the other hand, the proposed LVdc line facilitates reverse power flow when the load is less than the total DG power available. Moreover, the DG converters need not maintain the dc bus voltage as the LVdc line voltage is regulated by ST.

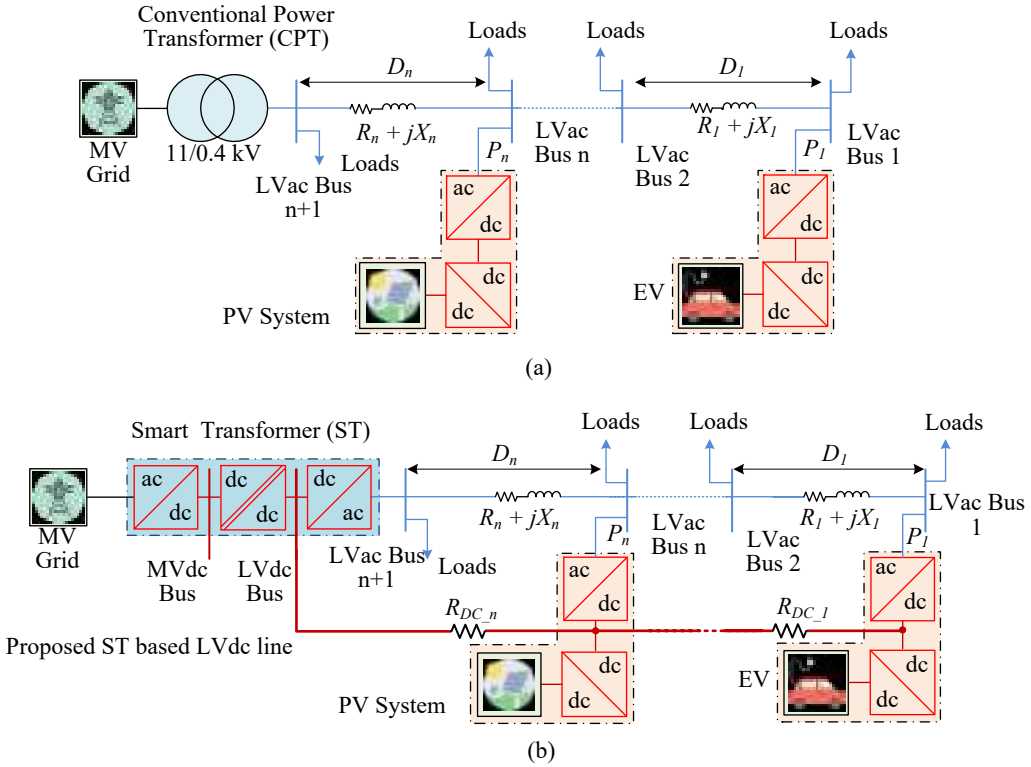

Fig. 3.1 Single-line diagram. (a) Conventional hybrid system [76]. (b) Proposed ST-based meshed hybrid system.

3.2 Power Management in the Proposed Scheme

The power management algorithm determines the reference powers for the various power converters present in the system. These are calculated based on the total loads, the available renewable power and the ratings of the DG converters. The power management also ensures that the available RES power and DG converters are utilized to their full potential.

Let total load requirement at the LVac side in the proposed system is S_{load} and given as

$$S_{load} = \sqrt{P_{load}^2 + Q_{load}^2 + H_{load}^2} \tag{3.1}$$

where P_{load} is fundamental active power component, Q_{load} is fundamental reactive power component and H_{load} is harmonic power component of the total load. In this study, it is considered that the DG converters only inject active power, while the reactive and harmonic components of the loads are supplied by the ST LV converter.

The DG converters are rated for maximum installed capacity of the renewable energy systems. However, they are under utilized most of the time due to variable power generation through renewable sources. Let for the i^{th} DG converter, $S_{i(rated)}$ and $P_{i(avbl)}$ are the converter rating and the renewable power available for injection at any given time, respectively. A load demand exceeding the total rating of the DG converters means that each of them have to supply power at their rated value. In cases when the DG converters are not delivering power at their rated value, the power is shared amongst the DG converters. A centralized controller is designed which generates the reference power injection for each DG converter in proportion to their ratings [97]. The reference power injection for the i^{th} DG converter will be calculated as

$$P^*_{i(inj)} = \begin{cases} \dfrac{P_{load} \times S_{i(rated)}}{\sum_{r=1}^{n} S_{r(rated)}} & \text{if} \quad P_{load} < \sum_{r=1}^{n} S_{r(rated)} \\ S_{i(rated)} & \text{otherwise} \end{cases} \tag{3.2}$$

where r is the numbering index for the DG units varying from 1 to n, connected to the corresponding LVac bus.

The total power rating of the DG converters and the load demand together determine the active power demand from the ST LV converter. This is summarized in Table 3.1. The flowchart for power management of the proposed system is shown in Fig. 3.2. In Mode I, where load demand is higher than the total DG converter ratings, the DG converters inject active power to the LVac grid at their rated capacity. Moreover, the ST LV converter supplies the remaining part of the load power. In case the power generation from the renewable sources is not sufficient to meet the rating of the corresponding DG converter, the DG converter draws extra power from the proposed LVdc line such

that it operates at its rated capacity. In mode II, load is higher than total renewable power but lower than total DG converter ratings. Here, the DG converters share the total load amongst them as per (3.2) and the excess renewable power is fed back to the ST through the proposed LVdc line. Moreover, ST LV converter supplies reactive and harmonic component of the load. In mode III, load is lower than available renewable power. In this case, the additional DG power is directly fed back to the ST LVdc bus through the LVdc line. The total load is shared among DG converters as per (3.2).

Table 3.1 Active Power Demand from ST LV Converter.

Mode of Operation	System Condition	ST LV Converter Active Power Demand
I	$P_{load} > \sum_{r=1}^{n} S_{r(rated)}$	$P_{load} - \sum_{r=1}^{n} S_{r(rated)}$
II	$\sum_{r=1}^{n} P_{r(avbl)} < P_{load} < \sum_{r=1}^{n} S_{r(rated)}$	0
III	$P_{load} < \sum_{r=1}^{n} P_{r(avbl)}$ (reverse power flow case)	0

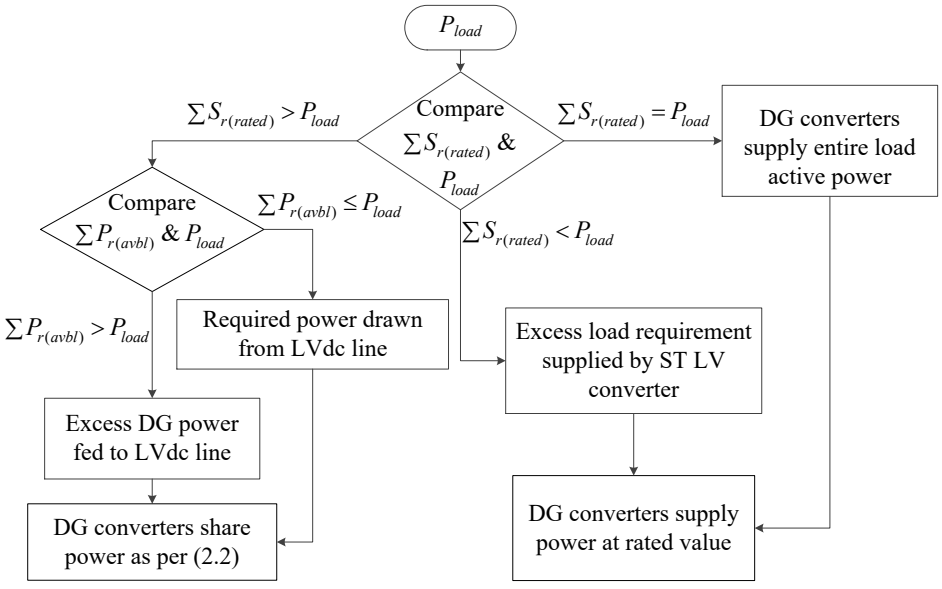

Fig. 3.2 Flowchart for power management of the proposed system.

3.3 Control Strategies for Power Converters

The overall control block diagram is shown in Fig. 3.3. The converters present in the system are the ST MV converter, ST isolated dc-dc converter, ST LV converter, DG con-

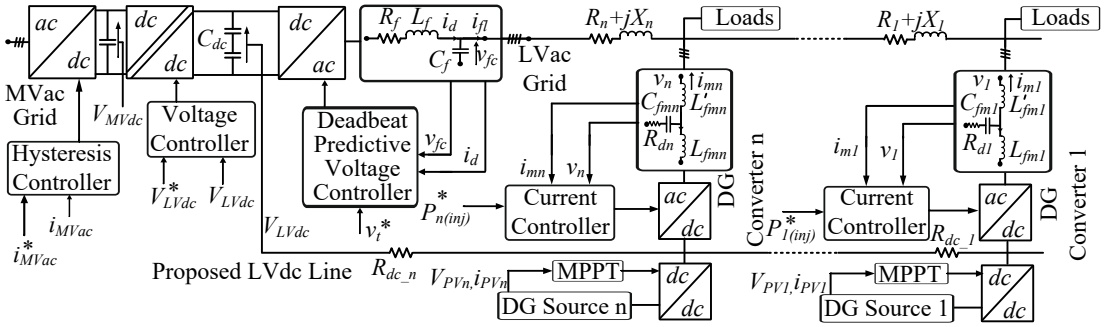

Fig. 3.3 Overall control block diagram of the proposed system.

verters, and dc-dc converters for PV system. The control strategies ensure satisfactory operation of the power converters. These are explained as follows.

3.3.1 Control of ST MV Converter

Fig. 3.4 shows the detailed circuit diagram of the ST MV converter. This converter exchanges power between the MVac and LV sides as per the demand or supply from the LV side, denoted by P_{LV_demand}. In addition to that, it also draws the power from the MVac side to compensate the converter losses (P_{MV_Loss}). Compensation of the converter losses maintains the MVdc bus voltage. The actual voltage is compared to the reference voltage (V^*_{MVdc}) and the error obtained (e_{MVdc}) is passed through a proportional integral (PI) controller with proportional and integral constants K_p and K_i, respectively. This is expressed as:

$$P_{MV\_Loss} = K_p e_{MVdc} + K_i \int e_{MVdc}\, dt. \tag{3.3}$$

The total reference power that the ST MV converter has to draw from the MVac side is given by:

$$P^*_{MVac} = P_{MV\_Loss} + P_{LV\_demand}. \tag{3.4}$$

P^*_{MVac} is used as the power reference to generate the reference currents using the instantaneous symmetric component theory [98]. The theory is explained as follows.

As the ST MV converter draws balanced sinusoidal current from the MVac grid, the

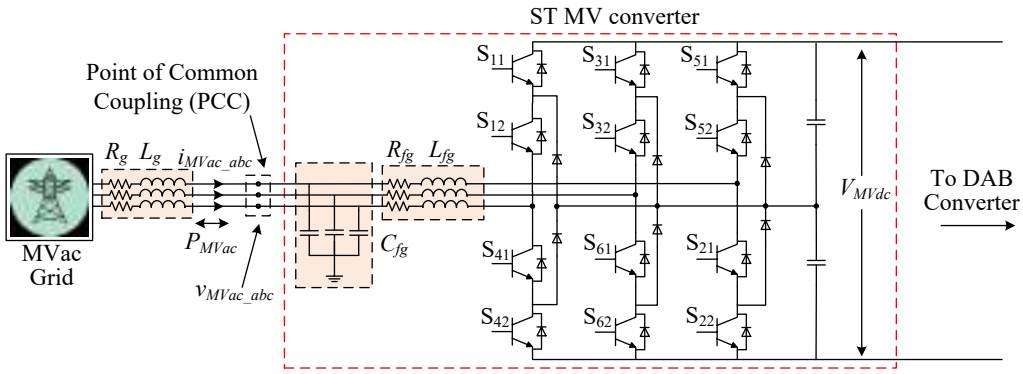

Fig. 3.4 Circuit diagram of ST MV converter.

sum of three phase ac currents is zero. Therefore,

$$i_{MVac\_a} + i_{MVac\_b} + i_{MVac\_c} = 0 \tag{3.5}$$

where i_{MVac_abc} are the three phase ac currents drawn from the MVac grid.

The ST MV converter operates at unity power factor. This implies that the phase angle of the currents will be same as the corresponding phase voltages. Therefore,

$$\angle v^{+}_{MVac\_abc1} = \angle i^{+}_{MVac\_abc1}. \tag{3.6}$$

Further, as the ST MV converter draws a constant power (P^{*}_{MVac}) from the MVac grid,

$$v^{+}_{MVac\_a1} i^{+}_{MVac\_a1} + v^{+}_{MVac\_b1} i^{+}_{MVac\_b1} + v^{+}_{MVac\_c1} i^{+}_{MVac\_c1} = P^{*}_{MVac}. \tag{3.7}$$

The reference currents are obtained by solving (3.5)-(3.7). These are as follows:

$$\begin{aligned} i^{*}_{MVac\_a} &= \frac{v^{+}_{MVac\_a1}}{\Delta} P^{*}_{MVac} \\ i^{*}_{MVac\_b} &= \frac{v^{+}_{MVac\_b1}}{\Delta} P^{*}_{MVac} \\ i^{*}_{MVac\_c} &= \frac{v^{+}_{MVac\_c1}}{\Delta} P^{*}_{MVac} \end{aligned} \tag{3.8}$$

where $\Delta = (v^{+}_{MVac\_a1})^2 + (v^{+}_{MVac\_b1})^2 + (v^{+}_{MVac\_c1})^2$.

A hysteresis current controller is utilized to ensure that the actual MVac currents are as per the reference currents given by (3.8). The actual and reference currents are compared and based on a hysteresis band, switching pulses are generated for the ST MV

converter. These pulses are used to operate the ST MV converter and maintain the reference currents. The schematic block diagram of the control strategy for the ST MV converter is shown in Fig. 3.5.

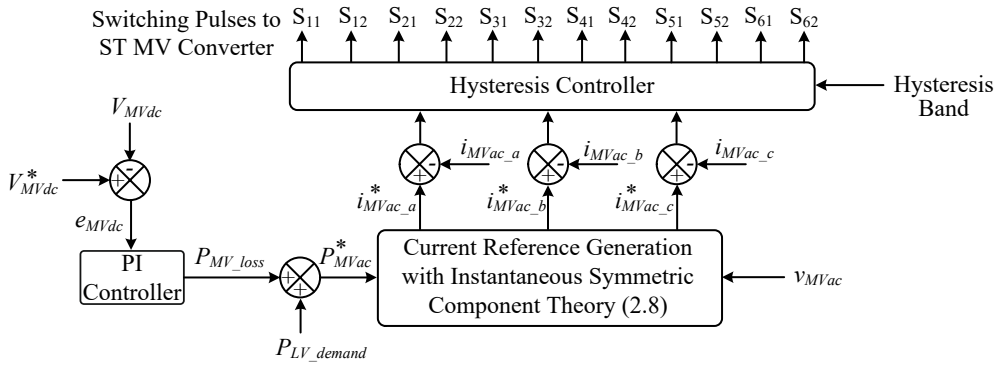

Fig. 3.5 Control diagram of ST MV converter.

3.3.2 Control of ST Isolated dc-dc Converter

Fig. 3.6 shows the complete circuit diagram of the ST isolated dc-dc converter. It consists of two H-bridge converters one at the MVdc side and the other at the LVdc side with a high frequency isolation transformer in between for galvanic isolation. Moreover, this converter maintains the LVdc bus voltage constant. With appropriate control, this converter can also mitigate second order oscillations in LVdc dc link voltage appearing due to unbalance in LVac grid [99].

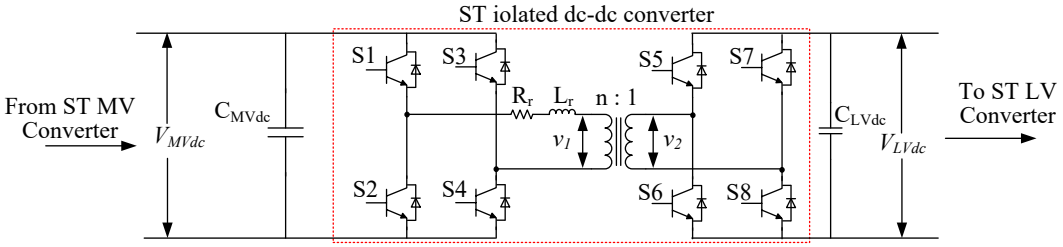

Fig. 3.6 Circuit diagram of ST isolated dc-dc converter.

The ST isolated dc-dc converter maintains the LVdc voltage by controlling the firing angle delay (δ) between the primary and secondary bridges of the ST isolated dc-dc converter. The actual LVdc voltage is compared with the reference and the error is fed to a PI controller which generates the delay for firing pulses between the two H-bridges

of the converter [100]. Thus, the delay in firing pulses is given by

$$\delta = K_{pd}\, e_{LVdc} + K_{id} \int e_{LVdc}\, dt \tag{3.9}$$

where e_{LVdc} is the voltage error between the actual and reference LVdc voltage, K_{pd} is the constant of proportionality and K_{id} is the integral constant of the PI controller. A square wave of the required switching frequency with 50% duty ratio is used to the fire the primary side H-bridge of the ST isolated dc-dc converter. A NOT gate is used to give complimentary pulses to the switch of each leg. The square wave is delayed by δ and the secondary side H-bridge is fired in a similar manner. The complete control block diagram is shown in Fig. 3.7.

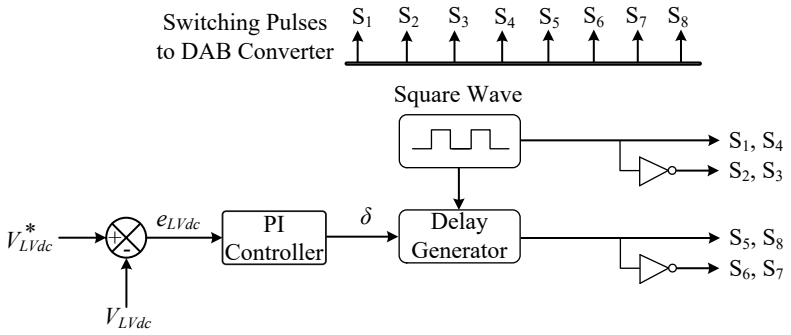

Fig. 3.7 Control diagram of ST isolated dc-dc converter.

3.3.3 Control of ST LV Converter

The ST LV converter circuit diagram is shown in Fig. 3.8. This converter's primary task is to maintain the LVac grid voltage and frequency. A two level converter is used with an *LC* filter. This converter draws power from the LVdc bus which is maintained by the DAB and delivers it to the LVac loads. The mid-point of the two dc link capacitors provides the neutral connection for the LVac side.

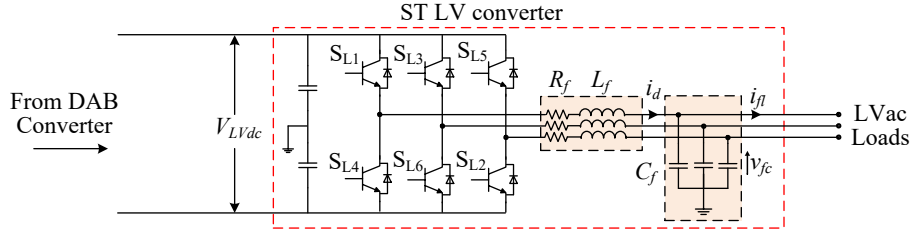

Fig. 3.8 Circuit diagram of ST LV converter.

The ST LV converter maintains constant voltage at LVac side using deadbeat control strategy [98]. A state space equation for capacitor and inductor dynamics is written in the form of $\dot{\mathbf{x}} = \mathbf{A}\mathbf{x} + \mathbf{B}\mathbf{z}$, where

$$\mathbf{A} = \begin{bmatrix} 0 & \frac{1}{C_f} \\ \frac{1}{L_f} & -\frac{R_f}{L_f} \end{bmatrix}, \quad \mathbf{B} = \begin{bmatrix} 0 & \frac{1}{C_f} \\ \frac{V_{LVdc}}{L_f} & 0 \end{bmatrix}, \mathbf{x} = [v_{fc} \quad i_d]^T \text{ and } \mathbf{z} = [u_c \quad i_{fl}]^T.$$

The terms v_{fc}, i_d, and i_{fl} denote the capacitor voltage, inductor current and filter output current, respectively. u_c is a switching control variable having value $+V_{LVdc}$ or $-V_{LVdc}$. The time domain state space equation is converted into discrete domain for a sampling instant of k and a relation for v_{fc} at the $(k+1)^{th}$ instant is derived as

$$v_{fc}(k+1) = G_{11}v_{fc}(k) + G_{12}i_d(k) + H_{11}u_c(k) + H_{12}i_{fl}(k) \tag{3.10}$$

where $\mathbf{G} = e^{\mathbf{A}T_d}$, $\mathbf{H} = \int_0^{T_d} e^{\mathbf{A}t}\mathbf{B}dt$ and T_d is the sampling time.

A deadbeat controller is designed for a reference voltage of v_t^* (230 V per phase at 50 Hz) and the following cost function is considered:

$$J = \{v_{fc}(k+1) - v_t^*(k+1)\}^2. \tag{3.11}$$

The cost function represented by (3.11) is minimized by differentiating with respect to $u_c(k)$ and equating it to zero. This gives

$$v_{fc}(k+1) = v_t^*(k+1). \tag{3.12}$$

Equation (3.12) is used in (3.10) and the control law for the converter is generated as follows:

$$u_c^*(k) = \frac{v_t^*(k+1) - G_{11}v_{fc}(k) - G_{12}i_{fl}(k) - H_{12}i_d(k)}{H_{11}}. \tag{3.13}$$

$u_c^*(k)$ is maintained around a hysteresis band to generate switching pulses for the ST LV converter with a hysteresis controller. The complete control schematic is shown in Fig. 3.9.

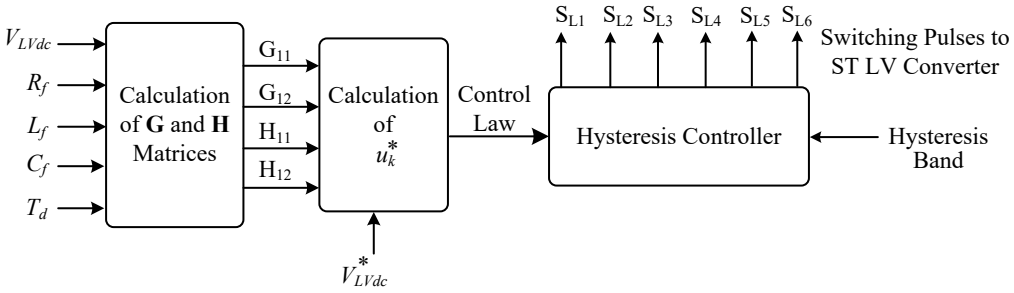

Fig. 3.9 Control diagram of ST LV converter.

3.3.4 Control of DG Converters

The circuit diagram of a DG converter is shown in Fig. 3.10. It is a two level dc-ac converter which uses an *LCL* filter. The DG converters inject active power to the LVac grid by operating in CCM based on $P^*_{i(inj)}$ obtained from (3.2).

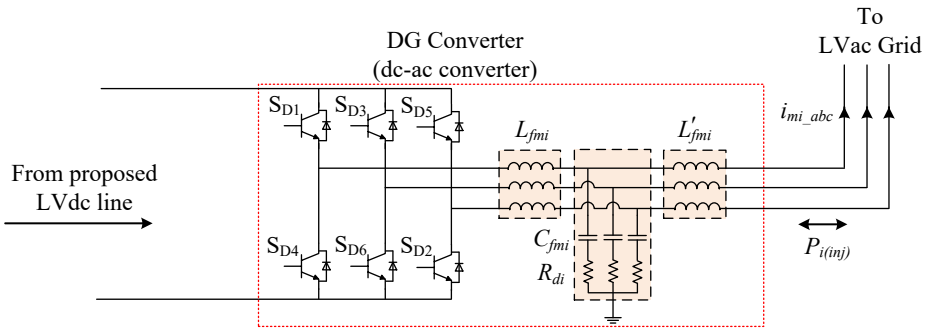

Fig. 3.10 Circuit diagram of DG converter.

After computing reference power for the i^{th} DG converter ($P^*_{i(inj)}$), the reference currents for that particular DG converter is calculated based on instantaneous symmetrical components theory [98] and explained as follows.

It is considered that the currents injected by the DG converters are balanced. Thus, for the i^{th} DG converter, the sum of the three phase DG currents will be zero

$$i_{mi\_a} + i_{mi\_b} + i_{mi\_c} = 0 \tag{3.14}$$

where i_{mi_a}, i_{mi_b} and i_{mi_c} are i^{th} DG converter output currents for phase a, b and c, respectively.

As the DG converters inject power to the LVac grid at unity power factor, the phase angle of the LVac voltages and DG converter currents will be same. Therefore, for the i^{th} DG converter, the angle relation between the positive sequence components of LVac

voltage and DG converter currents is given by

$$\angle v^{+}_{i\_abc1} = \angle i_{mi\_abc}. \tag{3.15}$$

A constant power has to be injected from the DG converter. The expression for power injection for the i^{th} DG converter can be written as

$$v^{+}_{i\_a1} i_{mi\_a} + v^{+}_{i\_b1} i_{mi\_b} + v^{+}_{i\_c1} i_{mi\_c} = P^{*}_{i(inj)}. \tag{3.16}$$

Solving (3.14)-(3.16), reference currents for the i^{th} DG converter are given as follows:

$$\begin{aligned}
i^{*}_{mi_a} &= \frac{v^{+}_{i_a1}}{(v^{+}_{i_a1})^2 + (v^{+}_{i_b1})^2 + (v^{+}_{i_c1})^2} P^{*}_{i(inj)} \\
i^{*}_{mi_b} &= \frac{v^{+}_{i_b1}}{(v^{+}_{i_a1})^2 + (v^{+}_{i_b1})^2 + (v^{+}_{i_c1})^2} P^{*}_{i(inj)}. \\
i^{*}_{mi_c} &= \frac{v^{+}_{i_c1}}{(v^{+}_{i_a1})^2 + (v^{+}_{i_b1})^2 + (v^{+}_{i_c1})^2} P^{*}_{i(inj)}
\end{aligned} \tag{3.17}$$

The reference currents obtained from (3.17) are compared with actual currents. A hysteresis controller is used to control the firing pulses of the DG converter which ensures that the actual currents stay within a specified hysteresis band. The control block diagram of the DG converter is shown in Fig. 3.11.

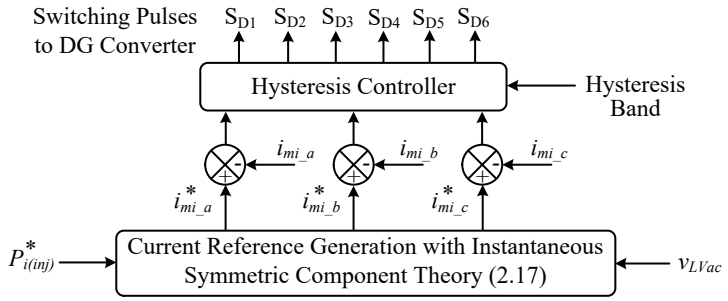

Fig. 3.11 Control diagram of DG converter.

3.3.5 Control of PV dc-dc Converters

Power from the PV panels is fed to the LVdc line through dc-dc converters. The circuit diagram of such a converter is shown in Fig. 3.12.

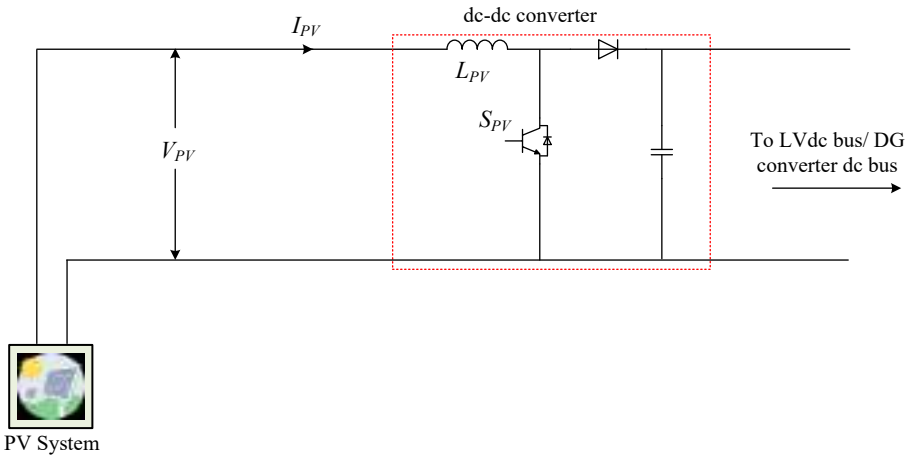

Fig. 3.12 Circuit diagram of PV dc-dc converter.

The PV dc-dc converters ensure that maximum power is drawn from the PV panels with the help of a maximum power point tracking (MPPT) algorithm. The incremental conductance MPPT algorithm is used to determine the maximum power point (MPP) and accordingly a reference voltage of PV array is generated [101]. This reference voltage is compared with the actual PV array voltage to generate an error signal. The error signal is given to a PI controller and the output of the PI controller is compared with a triangular wave to generate pulses for the dc-dc converter [102]. This ensures that the dc-dc converter operates at MPP. A detailed block diagram of PV MPPT controller is given in Fig. 3.13.

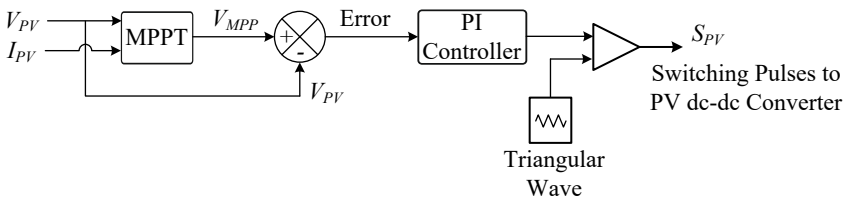

Fig. 3.13 Block diagram of PV MPPT controller.

3.4 Performance of the Proposed System

This section presents comparative power loss analysis and voltage regulation of proposed system with conventional system.

3.4.1 Loss Analysis

In the proposed system, three power converters are involved to deliver power to the loads connected to LVac buses. The ST MV converter and dc-dc converter are common and third converter is either DG converter or ST LV converter. The DG converters are structurally similar to the ST LV converter. Therefore, the operating losses of the DG converters and the ST LV converter are comparable as both operate at similar power and voltage levels. Thus, the device losses in the proposed configuration equals losses in ST, which is currently lower than CPT.

In this section, firstly, a comparison is carried out between the conventional and proposed systems for losses in the distribution line. Then, converter losses in reverse power flow in the proposed system is also compared with an ST-based system.

Power Loss in Distribution Line

Fig. 3.14 shows conventional distribution system with n LVac buses. $I_1, I_2 \ldots I_n$ are the rms currents drawn from the LVac buses 1, 2 ... n, respectively and D_i is the distance between the i^{th} and $(i+1)^{th}$ bus in kilometers ($1 \leq i \leq n-1$). For a fixed amount of active power transfer, the losses in an ac system increase with a decrease in power factor. It is considered that active power is flowing through the LVac lines at unity power factor. In this case, the total power loss is given by [103]

$$\begin{aligned} P_{3\phi\_Loss} = \quad & 3I_1^2 R_{ac} D_1 + 3(I_1+I_2)^2 R_{ac} D_2 + \ldots \\ & + 3(I_1+I_2+\ldots+I_n)^2 R_{ac} D_n \end{aligned} \tag{3.18}$$

where R_{ac} is the per kilometer resistance in each conductor of the distribution line. After simplification, (3.18) can be written as

$$P_{3\phi\_Loss} = 3\sum_{i=1}^{n}\left[\left(\sum_{j=1}^{i} I_j\right)^2 R_{ac} D_i\right]. \tag{3.19}$$

Fig. 3.15 shows the dc power flow in the proposed system assuming that the entire power is supplied through the proposed LVdc line. The LVac buses are considered to be at the same locations like the ones shown in Fig. 3.14 and each bus is considered to be fed by a DG converter. $I_{dc\_1}, I_{dc\_2} \ldots I_{dc\_n}$ are currents drawn by the corresponding DG

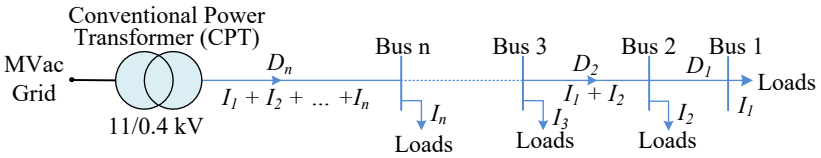

Fig. 3.14 Power flow path in conventional hybrid microgrid.

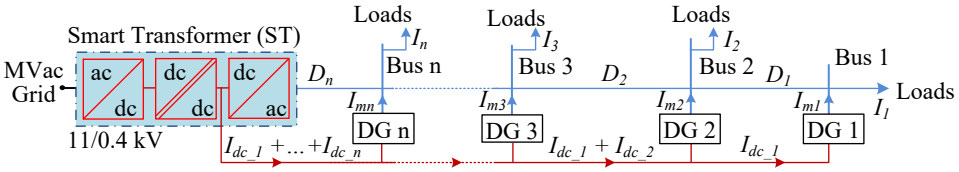

Fig. 3.15 Power flow path in proposed meshed hybrid microgrid.

converters. Here, the total power losses in the LVdc line is given by

$$P_{dc\_Loss} = 2\sum_{i=1}^{n}\left[\left(\sum_{j=1}^{i} I_{dc\_j}\right)^2 R_{dc} D_i\right] \tag{3.20}$$

where R_{dc} is the per kilometer resistance in each conductor of the dc distribution line.

Dividing (3.20) by (3.19) gives the ratio between the dc and ac losses which can be obtained as

$$\frac{P_{dc\_Loss}}{P_{3\phi\_Loss}} = \frac{2\sum_{i=1}^{n}\left[\left(\sum_{j=1}^{i} I_{dc\_j}\right)^2 R_{dc} D_i\right]}{3\sum_{i=1}^{n}\left[\left(\sum_{j=1}^{i} I_j\right)^2 R_{ac} D_i\right]}. \tag{3.21}$$

Let $P_{3\phi}$ and P_{dc} denote the power flow in an ac and dc system, respectively. These are expressed as follows:

$$P_{3\phi} = 3VI\cos\theta, \quad P_{dc} = V_{dc} I_{dc}. \tag{3.22}$$

In ac system, V is the per phase rms voltage, I is the per phase rms current and θ is the power factor angle. V_{dc} and I_{dc} are the voltage and current, respectively of the dc system.

For an equal amount of power flow in both the ac and dc systems while considering unity power factor operation in ac grid, the ratio of the currents in the two systems will be obtained from (3.22) as

$$\frac{I_{dc}}{I} = \frac{3V}{V_{dc}}. \tag{3.23}$$

We consider a case where the current injections at all the LVac buses are equal, i.e., the

load at LVac buses are equal and they are supplied by equally rated DG converters connected at that bus. Then, using (3.23) in (3.21), and considering that the per kilometer line resistance in the ac and dc systems are of same value,

$$\frac{P_{dc\_Loss}}{P_{3\phi\_Loss}} = 6\left(\frac{V}{V_{dc}}\right)^2. \tag{3.24}$$

In this study, LVac rms phase voltage V is 230 V. For the LVdc distribution grid, IEC 60038 standards have set the limit for maximum LVdc voltage as 1500 V [104], [105]. The dc link voltage is varied from 700 V to 1500 V in steps of 100 V and the graph from (3.24) is plotted as shown in Fig. 3.16. It is seen that the ratio of dc to ac losses is inversely proportional to the square of dc link voltage. This suggests a higher efficiency with increase in dc link voltage. Moreover, the higher voltage at dc link is also needed to keep the THD in voltages and currents within IEEE limits, supply reactive power and to operate the system satisfactorily during load changes. Considering the requirements of a three-phase four-wire converter and the IEC 60038 standards, the LVdc voltage of 1200 V is chosen in this system [106], [107].

From Fig. 3.16, it is seen that the line losses in the proposed LVdc line is 22% of that of the LVac lines of conventional system at 1200 V dc bus voltage. This comparison is done for unity power factor operation of the LVac system. However, for more realistic scenario where the power factor is less than unity, the losses in the LVac system will further increase. In this case, the proposed system will have better efficiency as compared to the conventional system.

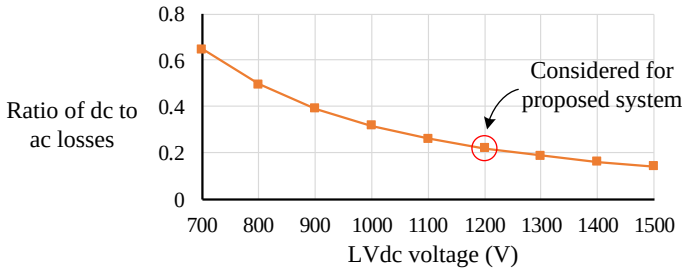

Fig. 3.16 Ratio of dc to ac losses against LVdc voltage.

Converter Losses for Reverse Power Flow

Reverse power flow occurs when the DG power generated is higher than the LVac load demand, and the additional power is fed from LVac to MVac grid through the ST [92]. The efficiency at the MVac side in such power flow depends on the efficiency of all the converters involved. Consider η_{STMV} as the efficiency of the ST MV converter, $\eta_{STdc-dc}$ as the efficiency of the ST dc-dc converter, η_{STLV} as the efficiency of the ST LV converter, and η_{DG_i} as the efficiency of the i^{th} DG converter. The overall efficiency during reverse power flow as shown in Fig. 3.17, at the MVac side, is given by

$$\eta = (\eta_{STMV}) \times (\eta_{STdc-dc}) \times (\eta_{STLV}) \times (\eta_{DG\_i}). \tag{3.25}$$

In the proposed system, when there is excess DG power available, the power is directly fed to the ST LVdc bus through the proposed LVdc line as shown in Fig. 3.17. This eliminates two power converter stages, one at the DG converter and the other at ST LV converter. This removes the converter losses completely during reverse power flow from DG sources to the ST LVdc bus. Neglecting line losses, the efficiency during reverse power flow for the proposed system at the MVac side, is given by

$$\eta_{proposed} = (\eta_{STMV}) \times (\eta_{STdc-dc}). \tag{3.26}$$

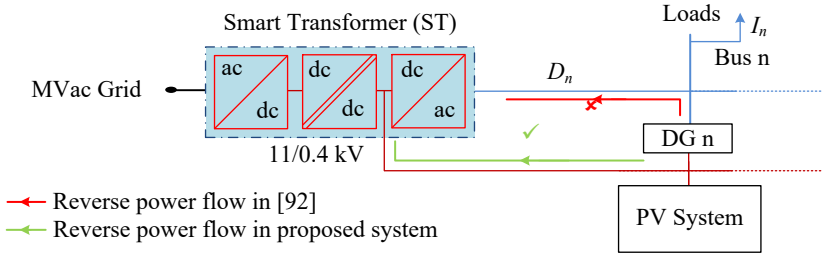

Fig. 3.17 Reverse power flow in the proposed system.

The efficiencies of the three stages of an ST and DG converter at different load are taken from [91], [108] and the overall efficiency obtained from (3.25) and (3.26) is shown in Fig. 3.18. It can be observed that in the proposed system, the efficiency at the MVac side for reverse power flow is increased by approximately 6%. Thus, the overall losses are reduced and better utilization of DG power is achieved.

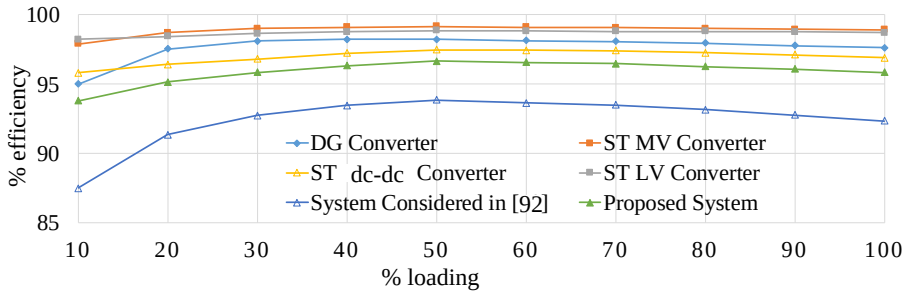

Fig. 3.18 Efficiency variation for reverse power flow in [92] and the proposed system.

3.4.2 Voltage Regulation Performance

In the proposed system, a portion of the power is transferred to the load points through the LVdc line. The LVdc line is also used for reverse power flow. These factors affect the voltage at the LVac and LVdc buses. An analysis for the voltage regulation in the LVac and LVdc buses of the proposed system is given as follows.

LVac Grid Voltage Regulation

In Fig. 3.14, per phase voltage at the i^{th} LVac bus is given by

$$\begin{aligned}\overline{V}_i = \quad & \overline{V}_n - (\bar{I}_1 + \bar{I}_2 + ... + \bar{I}_n) Z_{ac} D_n - (\bar{I}_1 + \bar{I}_2 + ... + \bar{I}_{n-1}) Z_{ac} D_{n-1} \\ & - ... - (\bar{I}_1 + \bar{I}_2 + ... + \bar{I}_i) Z_{ac} D_i \end{aligned} \tag{3.27}$$

where $\overline{V}_n$ is the voltage of the bus nearest to the CPT. Z_{ac} is the per kilometre impedance of the ac distribution line.

Equation (3.27) is simplified to

$$\overline{V}_i = \overline{V}_n - \sum_{k=i}^{n} \left[\left(\sum_{j=1}^{i} \bar{I}_j \right) Z_{ac} D_k \right]. \tag{3.28}$$

From (3.28), it can be observed that the voltage at the i^{th} bus will be lower than $\overline{V}_n$ and its magnitude depends upon current drawn by loads. On the other hand, the current direction is negative for reverse power flow, and therefore, $\overline{V}_i$ will be greater that $\overline{V}_n$. For high magnitudes of current, there will be considerable voltage drop or rise in the distribution grid.

In the proposed scheme, let $\bar{I}_{m1}, \bar{I}_{m2}, ...\bar{I}_{mn}$ are the currents injected by the DG convert-

ers 1, 2, ...n respectively, to the LVac side, as shown in Fig. 3.15. The voltage per phase at the i^{th} LVac bus will be

$$\overline{V}_{i(new)} = \overline{V}_n - \sum_{k=i}^{n}\left[\Big(\sum_{j=1}^{i}(\bar{I}_j - \bar{I}_{mj})\Big)Z_{ac}D_k\right]. \tag{3.29}$$

Using (3.28) in (3.29), we get

$$\overline{V}_{i(new)} = \overline{V}_i + \sum_{k=i}^{n}\left[\Big(\sum_{j=1}^{i}(\bar{I}_{mj})\Big)Z_{ac}D_k\right]. \tag{3.30}$$

Equation (3.30) indicates that the voltage at the i^{th} bus improves in the proposed system, as compared to the conventional system. Moreover, as reverse power flow is facilitated by the proposed LVdc line, there is no impact on LVac bus voltages for reverse power flow. Therefore, the proposed system helps in realizing better voltage regulation in the LVac distribution grid during high load and reverse power flow.

LVdc Grid Voltage Regulation

In the proposed system, as shown in Fig. 3.15, the voltage of the LVdc line is maintained by the ST. As the LVdc distribution line is connected to the dc buses of the DG converters, the voltages at the dc buses are directly regulated by the ST. This helps in reducing the control complexity of the DG converters as they need not maintain their dc bus voltage. There will be some voltage drop/rise in the LVdc line when power is taken/injected through this line. The expression for voltage at the dc bus of the i^{th} DG converter is given by

$$V_{dc(i)} = V_{dc} - \sum_{k=i}^{n}\left[\Big(\sum_{j=1}^{i}I_{dc\_j}\Big)R_{dc}D_k\right] \tag{3.31}$$

where V_{dc} is the ST LVdc link voltage and D_k is the distance between the k^{th} and $(k+1)^{th}$ dc bus.

Compared to the LVac lines, the LVdc lines are at a higher voltage and thus for the same amount of power flow, the current will be reduced in the LVdc lines. Thus, the voltage drop/rise given by (3.31) is not significant enough to affect the performance of the DG converters.

3.5 Implementation Challenges for the Proposed Meshed Hybrid Microgrid

For practical implementation of the proposed meshed hybrid microgrid, a dc distribution network has to be laid out in the distribution grid. Some of the main challenges are discussed as follows.

3.5.1 Protection

One of the major concerns in the implementation of the proposed system is the integration of protection schemes at various points of the system. With the LVdc link voltage at 1200 V, various measures have to be taken to ensure protection in situations of faults or disturbances. Protection of personnel and equipments are the two major challenges. These are discussed as follows.

Protection for Personnel

To enhance the operator safety, new dc design concepts have been suggested where manual dc disconnects are replaced with dc contactors [109]. The use of advanced connectors like multi-contact MC 4 connector and amphenol H4 connectors, compression lug studs and heavy gauge bus bars have also been proposed for use in dc grid voltages in the range of 1500 V to ensure ease of design and safety for installers and operators. For system operation and maintenance, over current protection and disconnecting means need to be made available to the operators. For high dc voltage, the safety aspects of an ST have been discussed in [110]. Double isolation or floating IT (*Isolated Terre*) earthed systems i.e. isolated or impedance-earthed neutral systems are suggested for safer operations. These techniques can be implemented in the proposed scheme to ensure safety for operators.

Protection for Equipment

Equipment protection constitutes of prevention measures for crossing specified voltage and current limits mainly during faults to prevent the equipments from getting damaged.

On detection of faults, conventionally, mechanical circuit breakers are operated to open the circuit and protect equipments present in the system. Conventional ac circuit breakers rely on the natural zero crossing of ac for proper operation. Such circuit breakers have a very low on state resistance and their effect on the efficiency of the system is negligible [111]. Mechanical circuit breakers can be implemented in the dc system, however, they will be subjected to higher stresses. Moreover, to ensure sufficient arc voltage for clearing, such breakers need to be connected in series [104]. An alternative option is to use power electronic switches to implement circuit breakers. Such breakers do not have the issues of arc extinction as faced by conventional ac breakers. However, such solid state circuit breakers have a voltage drop during ON period. This can give rise to significant losses resulting in the reduction of overall system efficiency. Hybrid circuit breakers exploit the advantages of both mechanical and solid state circuit breakers. In [112], a new topology for such a hybrid dc circuit breaker is presented which allows both normal and short circuit operations. In the proposed system, hybrid circuit breakers can be implemented in the LVdc line to ensure protection without reducing the system efficiency.

3.5.2 Cost

Another major factor is the cost of laying the LVdc line. Even though there will be initial costs involved, researches have claimed that the LVdc distribution will ensure cost saving in the long run [113]. In [114], it has been shown that due to the higher dc bus voltage, there is a reduction in copper and switchgear costs. In addition to that, a wider MPPT range and higher power density is achieved. A study has shown that higher voltage PV systems will infact reduce installation costs [115]. This is because higher voltage systems enable longer strings which reduces the number of combiner boxes in a PV plant. This also reduces the amount of wiring and thus labour costs. Therefore, ongoing research on various aspects such as installation costs, insulation and shock hazards is expected to be realized in a practical dc distribution line in the coming future.

3.5.3 Communication Requirements

One of the prime features of an ST is the communication feature [61]. In fact, it can be called as one of the distinguishing features between an SST and an ST. The proposed ST based meshed hybrid microgrid aims to exploit such improved features of an ST. Some communication aspects and challenges in an ST fed grid are presented in [116]. Here, the communication and information flow in ST is categorized into three main categories - between distributed appliances, between ST and distributed appliances and the third is between two STs or between STs and the core network.

For proper power management in the proposed meshed hybrid microgrid, there must be strong communication links between the ST and the DG converters. In practical applications, the power management algorithms require communication infrastructure for data transfer to the controller [117]. The measurement devices are used to measure input powers (e.g. load and RESs powers) which are required by controller. In [118], [119], the communication infrastructure and measurement devices useful for practical applications in distribution systems are discussed. In general, for implementing power management control, there will be a central controller and individual controller for different DG sources and loads present in the system. The communication link is used to transfer information from each controller to the central controller. In [120], IEC 61850 standard is used for communications within the distribution substation where an optimal energy management strategy is proposed for distribution system. In [121], a real-time energy management system is developed to minimize the cost of the system where data distribution service is used for communication purposes with the physical units. The real-time energy management integrates the data distribution service components for communicating the computed references to the hardware part.

3.6 Simulation Results

The proposed system is simulated in PSCAD software with two DG converters injecting power from two different PV plants. The simulation parameters are given in Table 3.2. The LVac bus 2 and 1 are at a distance of 250 m and 500 m, respectively from the ST LV converter. The per kilometer resistance and reactance of the conductors are 0.642 Ω and 0.083 Ω, respectively [122].

Table 3.2 Simulation Parameters

System Quantities	Values
LV grid voltage	0.4 kV (L-L)
ST LV converter	Power Rating = 50 kVA, V_{dc} = 1.2 kV, C_{dc} = 4700 μF, L_f = 1 mH, R_f = 0.02 Ω, C_f = 20 μF
DG converter 1	$S_{1(rated)}$ = 10 kVA, C_{dc1} = 2200 μF, L_{fm1} = 6 mH, L'_{fm1} = 68 μH, C_{fm1} = 10 μF, R_{d1} = 1 Ω
DG converter 2	$S_{2(rated)}$ = 15 kVA, C_{dc2} = 2200 μF, L_{fm2} = 4 mH, L'_{fm2} = 45 μH, C_{fm2} = 15 μF, R_{d2} = 1 Ω
dc-dc converter 1 and 2	Power Rating = 15 kW, f_s = 10 kHz, L = 1 mH, C = 1100 μF

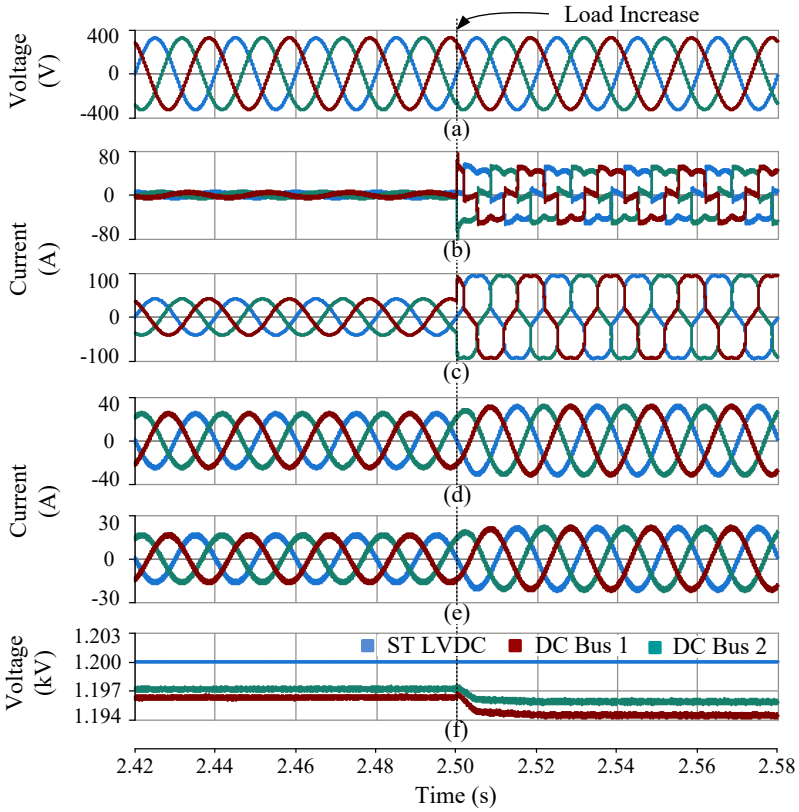

Fig. 3.19 Simulation results for load change. (a) ST LV converter voltage. (b) ST LV converter currents. (c) Total load currents (bus 1 + bus 2). (d) DG converter 1 currents. (e) DG converter 2 currents. (f) dc bus voltages.

Fig. 3.19 shows waveforms during a load change. Initially a total linear load of 20 kW was connected at LVAC bus 2. As this power is less than the total DG converter rating of 25 kW, the two DG converters share the power as per (3.2). At t = 2.5 s, the LVAC load is increased to 47 kW by switching ON a non-linear load at bus 1. Now, the DG converters inject a total of 25 kW which is their rated capacity and the deficit of 22 kW is supplied by the ST LV converter. Fig. 3.19(a) shows the ST LV converter voltage, and Fig. 3.19(b)-(e) shows the currents of the ST LV converter, load, DG converter 1 and DG converter 2, respectively. The currents of the DG converters and the ST LV

converter increase as the load current increases. Fig. 3.19(f) shows the DC bus voltages. The ST LVDC bus is maintained at 1.2 kV throughout. However, as the power drawn through the LVDC line increases, the DC bus voltage of the DG converters 1 and 2 drops to 1.195 kV and 1.196 kV, respectively due to the line resistance.

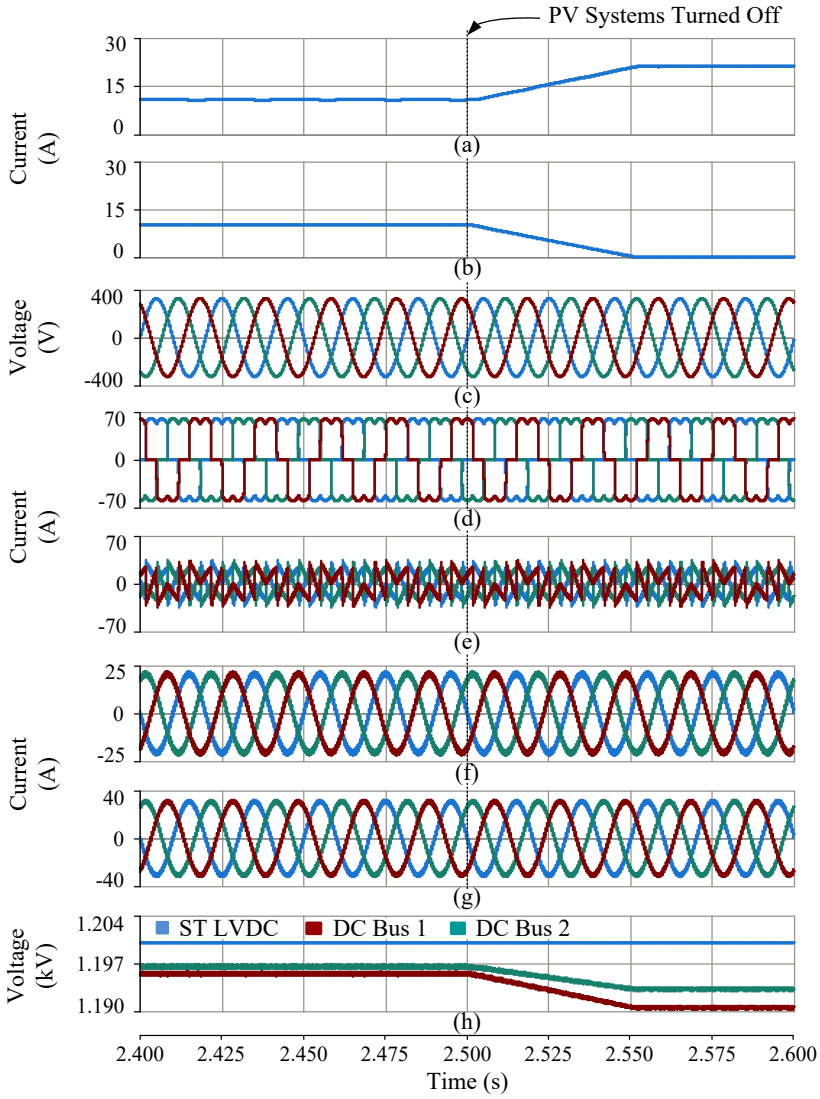

Fig. 3.20 Simulation results for absence of PV source. (a) Current drawn from ST LVdc link. (b) Total current injected by boost converters. (c) LVac voltage. (d) Total LVac load currents (bus 1 + bus 2). (e) ST LV converter currents. (f) DG converter 1 currents. (g) DG converter 2 currents. (h) dc bus voltages.

In Fig. 3.20, waveforms during sudden turn OFF of PV systems are shown. Non-linear active loads of 15 kW are connected to both LVac bus 1 and 2. Fig. 3.20(a) and (b) shows total current drawn from the ST LVdc link and total current injected by the boost converters, respectively. It is seen that once the current injected by the PV systems fall to zero, the current drawn from the proposed LVdc line increases to ensure that the current injected by the DG converters remain unchanged. Fig. 3.20(c)-(g) shows the

LVac voltage, load currents, ST LV converter currents, and the DG converter currents, respectively. These remain undisturbed during the transition. The dc bus voltages are shown in 3.20(h). As the PV systems are turned OFF, the voltages at LVdc bus 1 and 2 reduce as the power drawn through the LVdc line increases. However, these do not affect the operation of the system.

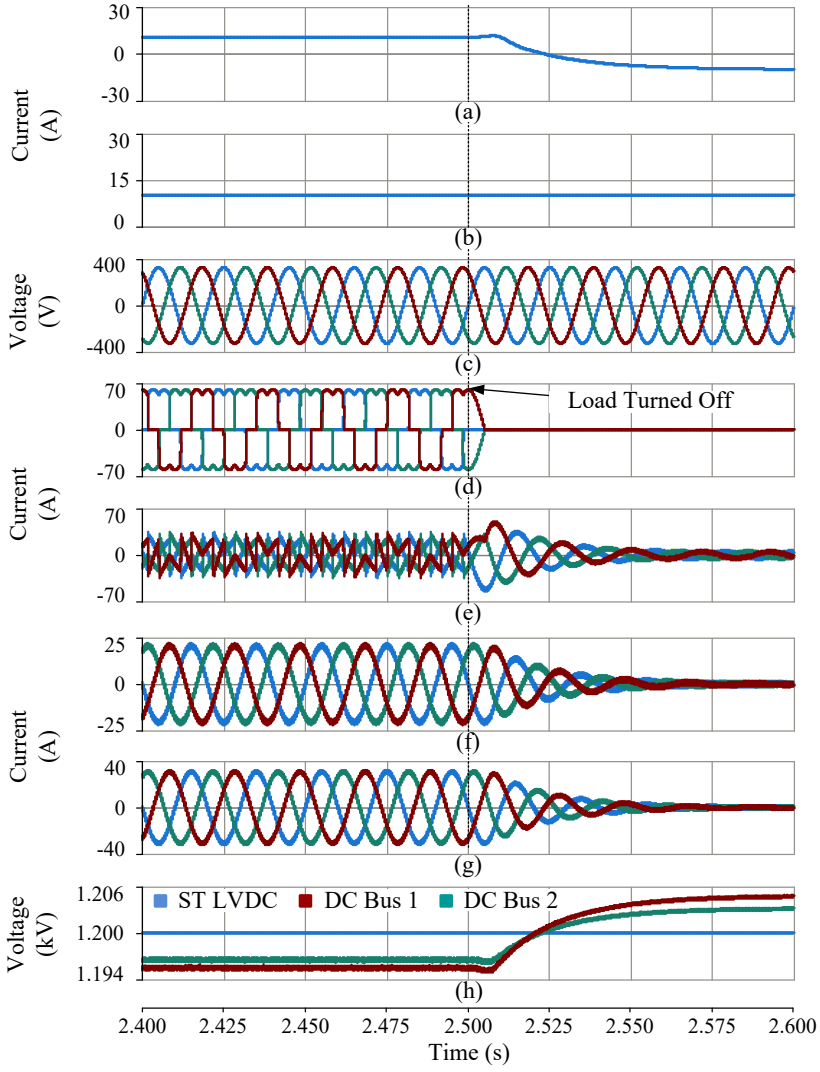

Fig. 3.21 Simulation results for reverse power flow. (a) Current drawn from ST LVdc link. (b) Total current injected by boost converters. (c) LVac voltages. (d) Total LVac load currents (bus 1 + bus 2). (e) ST LV converter currents. (f) DG converter 1 currents. (g) DG converter 2 currents. (h) dc bus voltages.

Fig. 3.21 shows the performance of the system during reverse power flow. Fig. 3.21(a) shows the total current drawn from the ST LVdc link. Fig. 3.21(b) shows the total current injected by the boost converters. Initially, the total non-linear load of 30 kW is operational. Once loads at both LVac buses are turned OFF, it is seen that the total current drawn from the proposed LVdc line becomes negative depicting reverse power flow to the ST LVdc link. The current injection from the boost converter remains constant.

Fig. 3.21(c) shows the LVac voltage. Fig. 3.21(d)-(g) shows currents of load, ST LV converter, DG converter 1, and DG converter 2, respectively. These currents reduce to zero after switching OFF the loads. Throughout the operation, the LVac voltage remains constant. Fig. 3.21(h) shows the dc bus voltages. The voltage of the dc buses 1 and 2 rise slightly during reverse power flow as the power has to flow from these buses to the ST LVdc bus which is already maintained at 1.2 kV by the ST.

Voltage variations at the two LVac buses are compared for the conventional and proposed systems. Loads are increased in steps and the per phase rms voltages at the buses 1 and 2 are shown in Fig. 3.22. The PV power injection is kept constant. It can be observed that in the proposed system, bus 1 and bus 2 have a better voltage profile as compared to conventional system. This is because the load on the LVac lines in the proposed system is lower as the LVdc line shares a part of the load power.

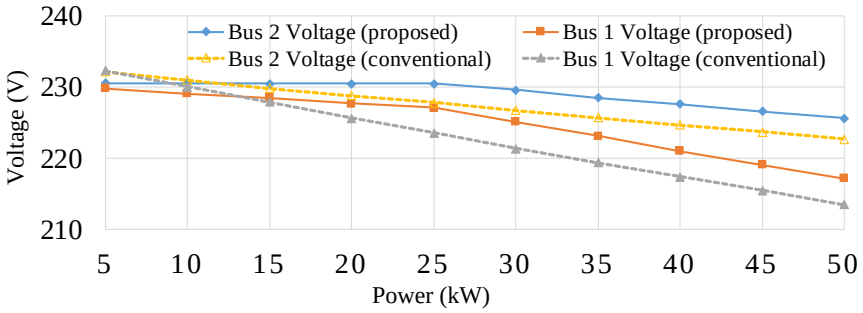

Fig. 3.22 Variation of LVac per phase rms voltage with load.

The features of the proposed system as compared to existing ST based system are given in Table 3.3. The comparison shows that the proposed system provides several features which are not possible with the existing ST based systems. Some aspects like the use of ST to control DG converter dc bus voltage, utilization of DG converters at times of unavailability of RES, lower losses during reverse power flow are possible because of the proposed configuration. These features cannot be provided with the ST based configurations existing in the literature. Moreover, the proposed system enables improved voltage regulation and meshed hybrid operation which have not been discussed in the literature with respect to ST.

Table 3.3 Features Comparison of the Proposed System with Existing ST based System.

Sl. No.	Feature	Available in literature	Proposed system
1	Control of dc bus voltage of DG converters	Controlled by the DG converter control algorithm [123]	Controlled by the ST; DG converters are not involved
2	LVac voltage regulation	Achieved by controlling the output voltage of ST [124]	In addition to ST voltage control, voltage can be improved by reducing LVac line loading
3	Line loss reduction	Not discussed with respect to ST	Achieved through meshed operation of LVac and LVdc grid enabled by ST
4	Utilization of DG converters during unavailability of DG power	Done by implementing energy storage systems [72]	Improved utilization by drawing power from LVdc line
5	ST enabled meshed operation by linking LVac and LVdc grid	Not available	Implemented in the proposed system
6	Reverse power flow in ST based system	Achieved through LVac line [92]	Achieved through LVdc line with reduced converter losses as compared to existing ST based solutions

3.7 Experimental Results

Fig. 3.23(a) shows schematic of the developed experimental setup. Fig. 3.23(b)-(d) shows photographs of ST LV converter, DG converter and dc-dc converter, respectively. The hardware parameters are given in Table 3.4. A dump load is connected at ST LVdc bus to absorb power during reverse power flow case.

Table 3.4 Hardware Parameters

System Quantities	Values
LV grid voltage	110 V (L-L)
ST LV converter	Power rating = 1 kVA, V_{dc} = 250 V, C_{dc} = 2350 μF, L_f = 20 mH, R_f= 0.5 Ω, C_f = 10 μF
DG converter	$S_{1(rated)}$ = 250 W, C_{dc1} = 2350 μF, L_{fm} = 10 mH, R_{fm} = 0.5 Ω
dc-dc converter	Power rating = 250 W, L = 10 mH, C = 10 μF, f_{sw} = 20 kHz

Fig. 3.24 shows performance of the system during a load change. Fig. 3.24(a) and (b) shows voltage and current waveforms of the ST LV converter, respectively. Fig. 3.24(c)-(f) shows the ST LVdc bus voltage, LVac load currents, DG converter bus voltage, and DG converter currents, respectively. Initially, the LVac load is 200 W. Since the load demand is less than the DG converter rating of 250 W, entire active power is supplied by the DG converter. The ST LV converter only supplies reactive and harmonic

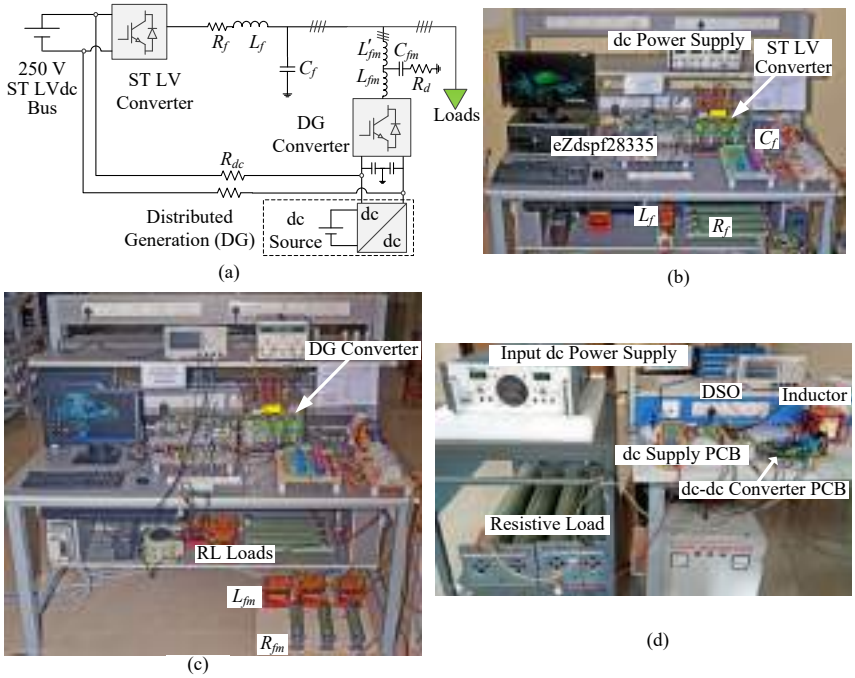

Fig. 3.23 (a) Experimental setup schematic. (b) ST LV converter. (c) DG converter. (d) dc-dc converter.

components of the load currents. The load is suddenly increased to 460 W by switching on a non-linear load. Now, the DG converter injects power at its rated value of 250 W and the remaining power is supplied by the ST LV converter. Therefore, the ST LV converter supplies active power only when the load requirement exceeds the DG converter rating. The voltage in the LVdc line drops slightly at the dc link of the DG converter, but this does not affect its operation. Moreover, the ST LV converter maintains a constant voltage on the LVac side throughout its operation.

Fig. 3.25 shows performance of the proposed system when power supplied by DG becomes zero. At the starting, a non-linear load of 300 W is connected to the LVac side. The DG converter injects active power at its rated capacity of 250 W and the balance power is fed by the ST LV converter. The DG converter receives 150 W from DG source and 100 W from LVdc line. Fig. 3.25(a) and (b) shows the current drawn from the proposed LVdc line and the current injected by the boost converter, respectively. Fig. 3.25(c) shows the LVac voltage, and it is maintained by the ST LV converter. Fig. 3.25(d)-(f) shows the load currents, ST LV currents, and DG converter currents, respectively. As the DG source is switched OFF, the current injected by it decays to zero. Subsequently, the current drawn from the LVdc line increases to ensure that the DG converter continues to operate at its rated capacity even in the absence of the DG

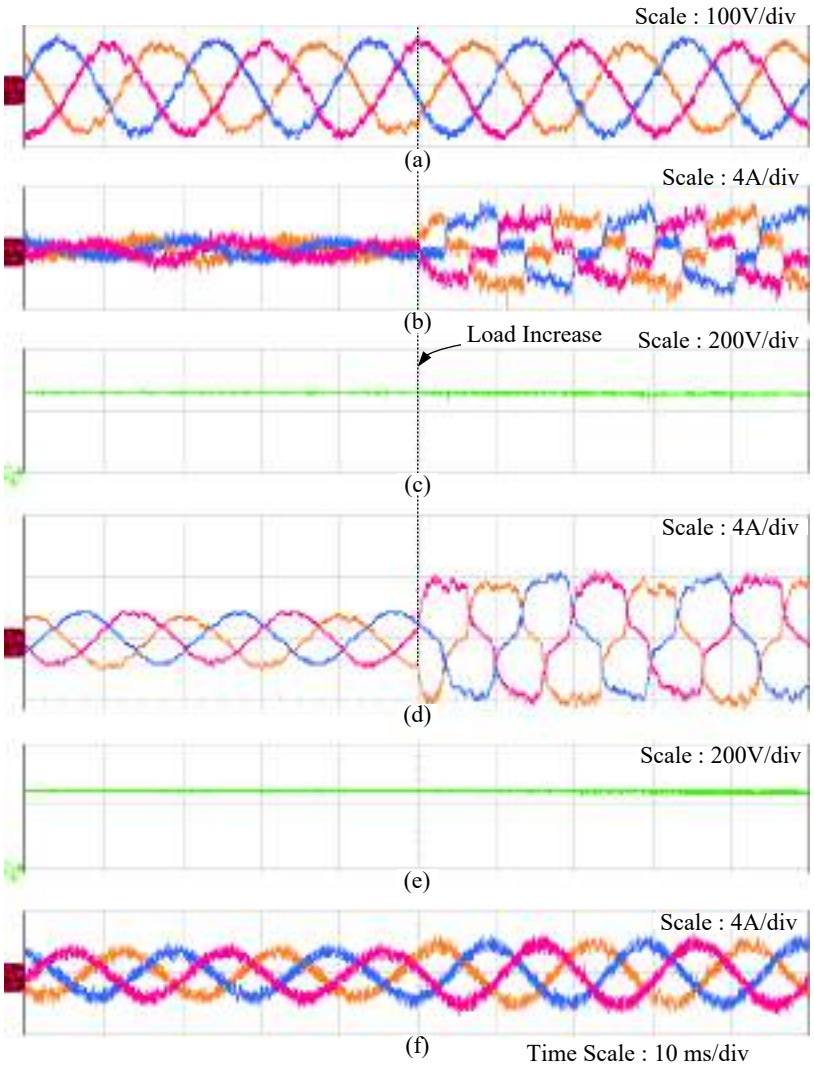

Fig. 3.24 Experimental results for load change. (a) ST LV converter voltage. (b) ST LV converter currents. (c) ST LVdc bus voltage. (d) LVac load currents. (e) DG converter dc bus voltage. (f) DG converter currents.

source. It can be seen from Fig. 3.25 that the waveforms of LVac voltage, load currents, ST LV converter currents and DG converter currents remain undisturbed during the transition.

Fig. 3.26 shows the performance during reverse power flow. A non-linear load of 300 W is connected. The DG source injects a power of 200 W. The DG converter operates at its rated power of 250 W and draws the balance power of 50 W from the LVdc line. Fig. 3.26(a) and (b) shows the current drawn from the LVdc line and the current injected by the boost converter, respectively. Fig. 3.26(c) shows the LVac voltage which is maintained by the ST LV converter. Fig. 3.26(d)-(f) shows the load currents, ST LV currents and DG converter currents, respectively. Once the load is switched OFF, current injected by the DG converter and the ST LV converter falls to zero. The boost

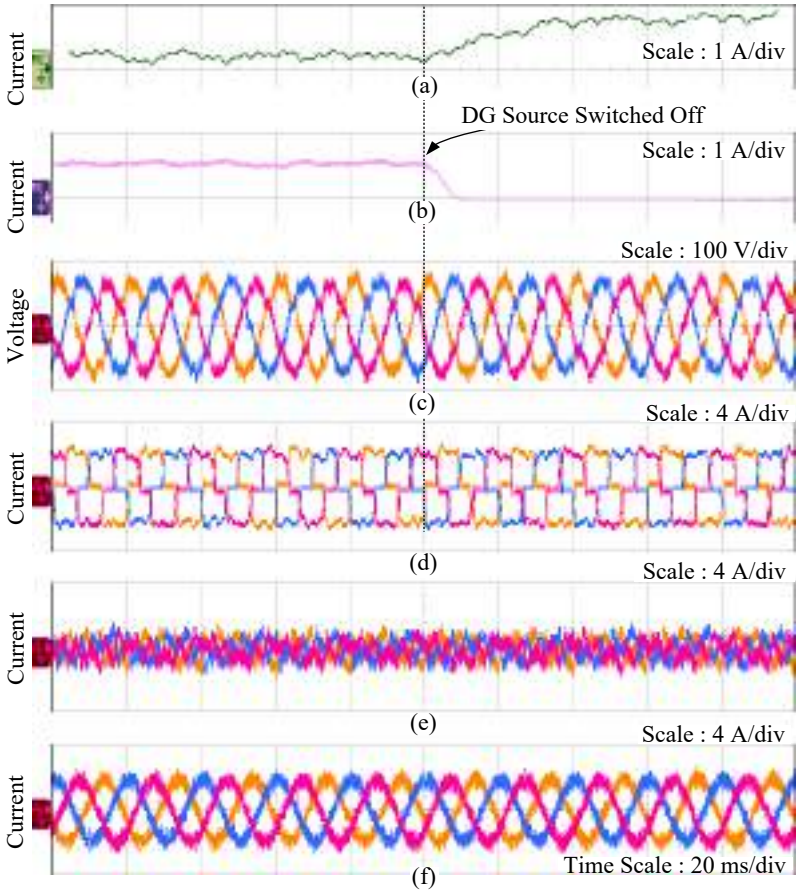

Fig. 3.25 Experimental results for absence of DG source. (a) Current drawn from proposed LVdc line. (b) Current injected by boost converter. (c) LVac voltage. (d) Load currents. (e) ST LV converter currents. (f) DG converter currents.

converter continues injecting power from the DG source. Since this power is not drawn by the DG converter, it is fed back to the ST LVdc bus through the LVdc line. It can be seen that the current in the LVdc line becomes negative.

From various results, it is observed that during load change, absence of DG source and reverse power flow, the experimental waveforms show similar behaviour as compared to the simulation waveforms. This validates performance of proposed configuration.

3.8 Summary

An ST enabled meshed hybrid distribution grid is presented in this chapter. The LVdc link of ST is proposed to connect the DG converters through an extended LVdc line. This configuration ensures that the DG converters support loads irrespective of the presence of renewable power and enhances their utilization. The line losses in proposed LVdc line are 22% as that of LVac line. During reverse power flow from the DG

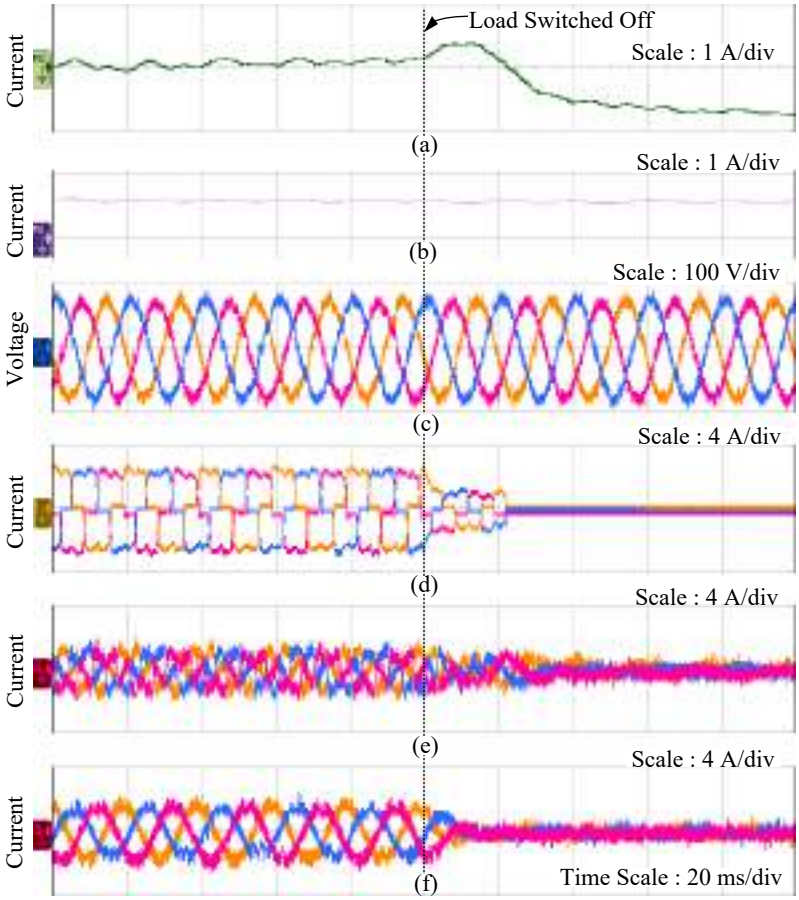

Fig. 3.26 Experimental results for reverse power flow. (a) Current drawn from proposed LVdc line. (b) Current injected by boost converter. (c) LVac voltage. (d) Load currents. (e) ST LV converter currents. (f) DG converter currents.

sources, two power conversion stages are bypassed and the efficiency at the MVac side is increased by approximately 6% in comparison to ST based microgrid. The control complexity of the DG converters is reduced as they do not need to control the dc link voltages. Moreover, the proposed system reduces loading of the LVac lines which leads to an improved LVac line voltage profile.

CHAPTER 4

ISLANDED OPERATION OF SMART TRANSFORMER BASED MESHED HYBRID MICROGRID WITH POWER LOSS MINIMIZATION

In Chapter 3, the extension of the ST LVdc bus in the distribution grid to connect the dc buses of DG converters present on the LV side is proposed. The configuration forms a meshed hybrid grid which offers more power flow paths, lower distribution line losses, lower converter losses during reverse power flow, etc. Extending the work of the last chapter, this chapter discusses the islanded operation of such a meshed hybrid microgrid. The islanded operation is achieved by switching OFF the ST MV and isolated dc-dc converters, and maintaining the LVdc bus voltage with a BESS. This enables the ST LV converter to stay operational and maintain the LVac grid voltage. The hybrid microgrid consists of renewable energy sources, EV charging stations, energy storage, etc. The battery energy storage system (BESS) is used for maintaining the LV dc bus voltage of ST. An optimal power management strategy is proposed for reducing total line losses during islanded operation.

Modern electric power systems are seeing increased integration of PV systems, wind systems, BESS, EVs, etc. [125]–[128]. Several methods are proposed to obtain improved operation of ST in the distribution grid with such integrations [89], [92], [129]. The BESS integration to the grid with the help of ST is proposed in [91]. The peak load demand is reduced with the BESS through its proper sizing. It also helps to reduce the size of the ST converters. The ST has also been used for formation and operation of microgrids. The power management for an ST based zonal microgrid is discussed in [72]. With the integration of BESS, the islanded operation of ST LV side is also proposed. However, the sizing of BESS or the power management based on SoC of the BESS is not analyzed.

The meshed operation with more power flow paths provides the possibility to optimize losses in the system. This is explored in [130], where the DG converters are optimally

controlled to incur lower losses and achieve an improved voltage profile. However, the islanded operation of the microgrid is not considered in this study.

During islanded operation of an ST based meshed hybrid microgrid, the energy stored in the LV grid needs to be controlled optimally to reduce losses and increase the operation time of LV grid. There are numerous studies in the literature which deal with the optimization and loss reduction in distribution grids. In [131], the energy demand reduction is achieved through demand response with the help of optimal scheduling of DGs and EVs. The impact of the proposed method is tested on IEEE 24 bus transmission system. In [132], a new topology of distribution network is proposed in presence of renewable energy resources for minimizing the total cost of planning while considering the power loss cost. In [133], the optimal sizing of the DG capacity is performed for effective congestion management while considering the power loss reduction. In [134], the unified power quality conditioner is used to minimize power losses in distribution system. In [135], reactive power control techniques to minimize the losses in a wind farm are discussed. In [136], the reactive power control via PV inverters is implemented for minimizing the power losses and improving the voltage profile of the system. However, in [132]–[136] the impact of energy storage devices on power loss minimization is not discussed. A communication free power loss minimization for islanded microgrids is discussed in [137] and [138] considers PV and BESS with droop optimization for loss minimization.

Moreover, aforementioned studies offer loss minimization in conventional microgrids. The loss minimization of islanded ST based meshed hybrid microgrid, utilizing the capabilities of ST and meshed operation is still unexplored.

To fill this research gap, in this chapter, an optimal power management strategy is proposed to minimize the total line loss which results in increased operation time of LV grid. The minimization of total distribution line power loss is chosen as objective function of optimization problem. The active power references of distributed generation converters and charge or discharge schedules of EVs are optimally controlled using genetic algorithm while satisfying the various constraints of the system. Further, a smart LV load shedding is also incorporated to the power management. This is activated on crossing the lower critical SoC of the BESS. It is used as a final measure to increase BESS discharge time resulting in prolonged operation of the islanded system. Simula-

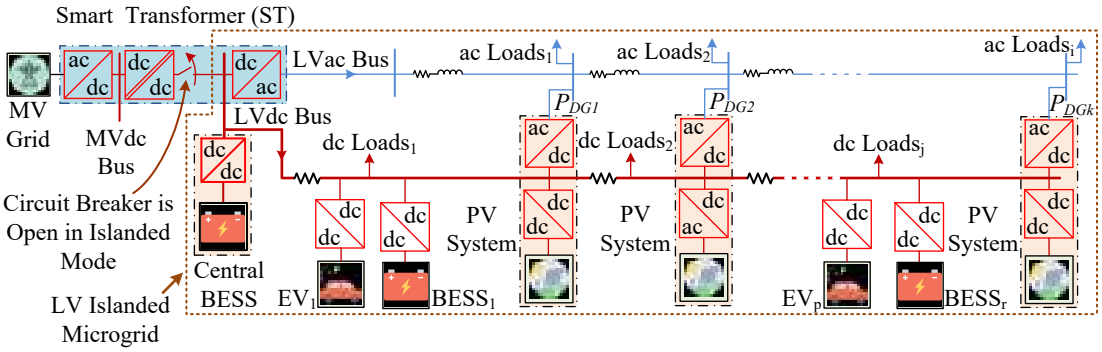

Fig. 4.1 BESS maintained ST based meshed hybrid microgrid during islanded operation.

tion and experimental results verify the performance of the proposed scheme.

4.1 Islanded Meshed Hybrid Microgrid

An ST based meshed hybrid microgrid is shown in Fig. 4.1. In this system, the ST exchanges power from the MVac side, the ST isolated dc-dc converter maintains the ST LVdc voltage and the ST LV converter maintains the ST LVac voltage. As LVdc bus is extended in the distribution line, the dc buses of the DG converters are connected to this line forming a mesh. When the LV meshed microgrid has to operate in islanded mode due to some fault or maintenance activity on the MVac side, the ST MV and isolated dc-dc converters are disconnected from the LV side with the breaker. The BESS changes over to VCM mode of operation to maintain the ST LVdc bus voltage. As the ST LVdc bus voltage is maintained constant, the ST LV converter operates undisturbed and maintains the LVac voltage. The BESS as well as EVs are connected to the LVdc line of the system. The dc-dc converters of these systems operate in CCM. The dc loads are also connected to the LVdc line at various points. The DG systems present in the distribution grid like PV or BESS inject power to the LVac side with DG converters.

4.2 Centralized Power Management Controller

The proposed meshed hybrid microgrid consists of various sources and loads. Thus, to obtain proper power balance, a centralized power management controller is proposed which takes decisions based on the balance power of the system. Subsequently, the controller delivers the information of reference power for each converter in the system.

In case the total load is higher than the total DG, the storage systems like the BESS and EVs support the loads. In case of surplus generation, the excess power is stored among the storage systems. The difference between the total load and the DG powers is the balance power (P_{bal}) of the microgrid. A positive balance power means that the storage systems will be charged, while a negative value indicates power discharge by the storage systems. The balance power expression is given by

$$P_{bal} = \sum_{i=1}^{m} P_{ac\_load_i} + \sum_{j=1}^{n} P_{dc\_load_j} - \sum_{k=1}^{o} P_{DG_k} \tag{4.1}$$

where$P_{ac_load_i}$ is the load at the i^{th} LVac bus, $P_{dc\_load_j}$ is the load at the j^{th} LVdc bus, P_{DG_k} is the power injected by the k^{th} DG plant i, j and k are integers varying from 1 to m, 1 to n and 1 to o, respectively.

An optimization algorithm ensures that the power transfer from the DG converters and each of the EVs and storage systems are such that the losses are minimum. The controller manages the power in three stages - (a) primary, (b) secondary and (c) tertiary. These power management strategies are explained as follows.

4.2.1 Primary Power Management - Source Management

In this stage, the power that has to be delivered or consumed by the BESS and EVs is computed. The LVac and LVdc buses at the ST LV converter are considered 0^{th} bus and the BESS maintaining the ST LVdc voltage is the 0^{th} BESS. The power transfer equation for the $BESS_0$ is given by

$$P_{BESS_0} = P_{bal} - \sum_{l=1}^{p} P_{EV_l} - \sum_{r=1}^{q} P_{BESS_r} \tag{4.2}$$

where P_{EV_l} is the power injected by the l^{th} EV, P_{BESS_r} is the power injected by the r^{th} BESS, l is an integer varying from 1 to p and r is an integer varying from 1 to q.

The reference power for each of the EVs and BESS are obtained from the optimization algorithm which is explained in Section 3.3.

4.2.2 Secondary Power Management - Delivery Management

In the secondary power management, the DG converter reference powers are decided. Being a meshed hybrid grid, these converters draw power from the LVdc line and thus their power injection is not dependent on the availability of DG power. It is considered that the DG converters inject only active power to the LVac grid, and the reactive and harmonic powers are supplied by the ST. The reference powers for the DG converters are also obtained from the optimization algorithm. The amount of active power that the ST LV converter has to supply into the LVac side is given by

$$P_{STLV} = \sum_{i=1}^{m} P_{ac\_load_i} - \sum_{k=1}^{o} P_{DG\_Conv_k} \tag{4.3}$$

4.2.3 Tertiary Power Management - Load Shedding

If there is a deficit of power and the BESS SoC constraints tend towards the limiting value, then load is curtailed as a last resort. This is realized with the help of the ST by controlling the LVac voltage.

When the need for load curtailment arises, the centralized controller passes the information to the ST to lower the LVac voltage (V_{LVac}) to 0.95 p.u. This information is used to disconnect the non-critical loads from the LVac grid. This is the conventional under-voltage load shedding implemented by intentional lowering of LVac voltage [139]. A critical limit of SoC ($SoC_{BESS_0}^{critical}$) is defined to start this under voltage load shedding to ensure that the centralized BESS has a prolonged discharge time in order to supply critical loads in the system. Therefore, the voltage reference for the ST LV converter can be expressed as follows.

$$V_{LVac}^{*} = \begin{cases} 0.95V_{LVac}^{nom} & \text{if} \quad SoC_{BESS_0} \leq SoC_{BESS_0}^{critical} \\ V_{LVac}^{nom} & \text{otherwise.} \end{cases} \tag{4.4}$$

The complete power management is shown in the flowchart given in Fig. 4.2.

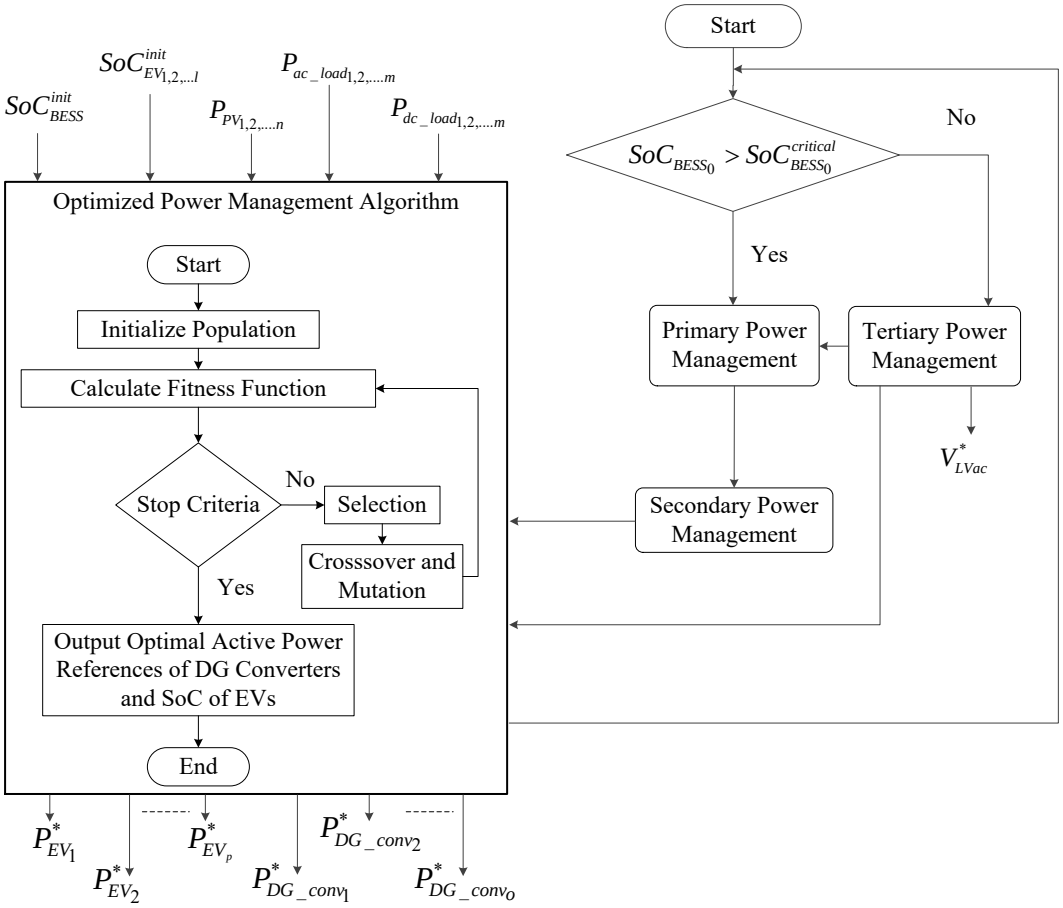

Fig. 4.2 Flowchart for power management.

4.3 Proposed Optimal Power Management Scheme

This section explains the method of determination of optimal active power references of DG converters and charge or discharge schedules of EVs ($P^o_{DG\_Conv_k}$ and $P^o_{EV_l}$). In the considered case study, the operations of BESS in the distribution grid are similar to the EVs, i.e both can act as storage systems which charge or discharge from the LVdc line working in CCM. Therefore, to simplify the analysis, only the EVs are considered.

The main goal of the proposed work is to increase the operation time of the isolated microgrid using battery energy storage and renewable energy sources present in the system. It is possible by minimizing the power losses in the distribution system. Therefore, the chosen problem is a single objective optimization problem. Accordingly, the objective function is chosen and implemented. An online optimal problem is formulated for determining $P^o_{DG\_Conv_k}$ and $P^o_{EV_l}$. The objective function and constraints are

given as follows.

$$\begin{aligned} \text{minimize } \; f = P_{loss}(t) = \textstyle\sum_{a=1}^{n_{acl}} (I_{ac}^{a}(t))^2 \times R_{ac}^{a} + \\ \sum_{b=1}^{n_{dcl}} (I_{dc}^{b}(t))^2 \times R_{dc}^{b}. \end{aligned} \tag{4.5}$$

subjected to

1. Power balance constraint given in (4.1)
2. Bus voltages constraint

$$V_{LVac}^{min} \leq V_{LVac}^{i}(t) \leq V_{LVac}^{max}; V_{LVdc}^{min} \leq V_{LVdc}^{j}(t) \leq V_{LVdc}^{max} \tag{4.6}$$

3. DG converters rating constraint

$$P_{DG\_Conv_k}(t) \leq S_{DG\_Conv_k}^{rated}. \tag{4.7}$$

4. SoC constraints of EVs

$$SoC_{EV_l}^{min} \leq SoC_{EV_l}(t) \leq SoC_{EV_l}^{max}. \tag{4.8}$$

5. SoC constraints of BESS

$$SoC_{BESS}^{min} \leq SoC_{BESS}(t) \leq SoC_{BESS}^{max}. \tag{4.9}$$

6. Charge/discharge power constraints of EVs

$$P_{EV_l}^{c}(t) \leq P_{EV_l}^{c,max}, P_{EV_l}^{d}(t) \leq P_{EV_l}^{d,max} \tag{4.10}$$

7. Charge/discharge power constraints of BESS

$$P_{BESS}^{c}(t) \leq P_{BESS}^{c,max}, P_{BESS}^{d}(t) \leq P_{BESS}^{d,max}. \tag{4.11}$$

In (4.5), a and b are ac and dc line indices. V_{LVac}^{min} and V_{LVac}^{max} are chosen as 0.95 p.u. and 1.05 p.u., respectively [33].

The considered fitness function is a non-linear function. Therefore, it is possible to solve the optimization problem with any non-linear optimization solver. The GA is a popular optimization technique used to solve the non-linear functions. Therefore, it is solved using GA solver in MATLAB [140]. The default values of GA solver are chosen for various parameters of GA, except for population size. The population size is tuned such that three different runs converges precisely to the same value and chosen as 40. The $P_{DG\_Conv_k}$ and SoC_{EV_l} are considered as control variables.

As per GA, firstly population initialization is done. Then calculation of fitness function is performed. This calculation is repeated through selection, crossover and mutation till the stop criteria is reached. This fitness function calculation requires power flow solution. For determining power flow solution, the type of buses and bus data in the distribution network are required. In the considered distribution network both LVac network and LVdc network are present. Since the ST LVac and LVdc bus voltages are maintained at 1 p.u., the ST LVac and LVdc buses are chosen as slack buses and the power flow equations are solved independently for LVac and LVdc networks. All the remaining buses are considered as load buses. The load bus power at each load bus in LVac network ($P_{lb_{ac}}$) is given in (4.12).

$$P_{lb_{ac}} = P_{ac\_load} - P_{DG\_Conv}. \tag{4.12}$$

$$Q^{i}_{lb_{ac}} = Q_{ac\_load} - Q_{DG\_Conv}. \tag{4.13}$$

The load bus power at each load bus in LVdc network ($P_{lb_{dc}}$) is given in (4.14).

$$P_{lb_{dc}} = P_{dc\_load} + P_{DG\_Conv} - P_{DG}. \tag{4.14}$$

With the help of load powers the currents drawn by each load bus in LV ac and dc network ($I_{lb_{ac}}$ and $I_{lb_{dc}}$) are calculated as given in (4.15) and (4.16), respectively.

$$I_{lb_{ac}} = \frac{P_{lb_{ac}} - jQ_{lb_{ac}}}{V_{lvac}}. \tag{4.15}$$

$$I_{lb_{dc}} = \frac{P_{lb_{dc}}}{V_{lvdc}}. \tag{4.16}$$

Using these load bus powers and currents, backward forward sweep power flow method is applied to both LVac and LVdc networks in order to obtain required power flow solution and thus, calculate the fitness function. Once fitness function is calculated, GA checks certain stop criteria options such as maximum number of generations and function tolerance. If any one of these options is satisfied, the GA stops doing iterations and provides results.

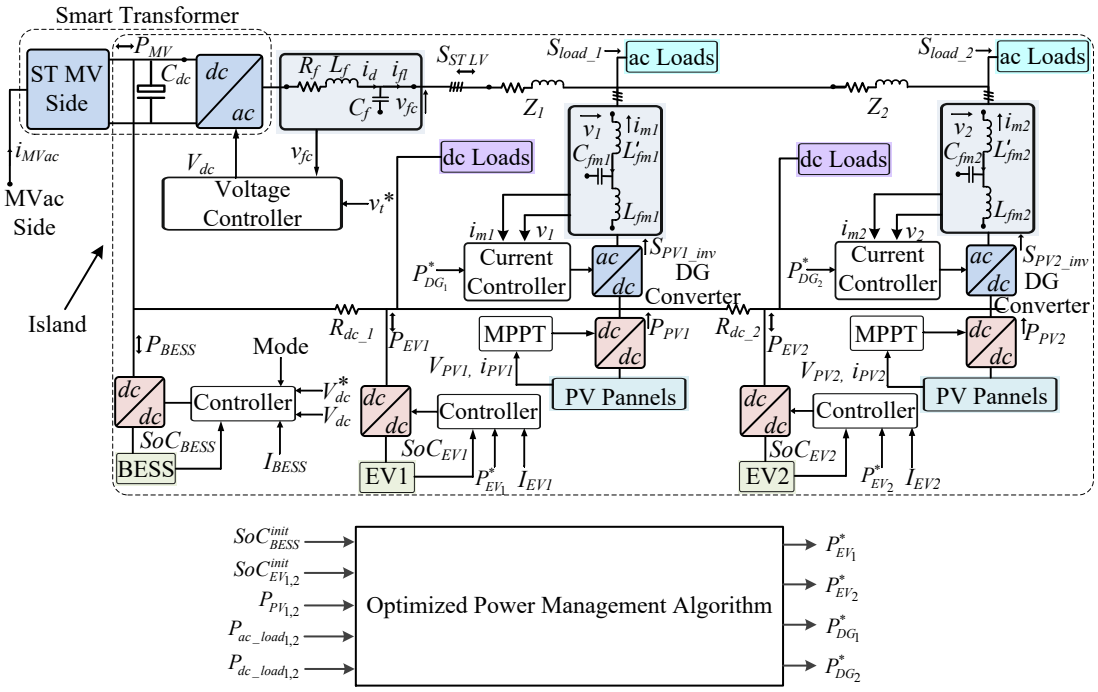

Fig. 4.3 The complete control diagram for the ST based islanded hybrid meshed microgrid.

4.4 Control Strategies

The power management algorithm in the centralized controller generates the power reference for the various converters in the system. Accordingly, the converters are controlled and operated to maintain the reference voltages and currents. The complete control diagram along with the simulation schematic considered for analysis is shown in Fig. 4.3. Two EV systems and two PV powered DG systems are considered. It is considered that EV 1 and DG 1 are at a distance of 250 m from the ST, and the EV 2 and DG 2 are at a distance of 500 m from the ST. Both these points also have ac and dc loads connected. The control strategies consist of controlling the ST LV converter, the BESS dc-dc converters, EV dc-dc converters and the DG converters. In the grid connected mode, the ST MV converter draws power at unity power factor from the MVac side while maintaining the MVdc voltage and the dc-dc converter maintains the LVdc voltage [77]. The detailed control mechanism of these two converters are explained in Chapter 3, Section 3.3.1 and 3.3.2. In the islanded mode of operation, these two converters are not operational. The control strategies for the ST LV converter and DG converter are explained in Chapter 3, Section 3.3.3 and 3.3.4, respectively. The control of the BESS dc-dc converter and the EV dc-dc converters are explained as follows.

4.4.1 BESS dc-dc Converter

The circuit diagram of the BESS dc-dc converter is shown in Fig. 4.4. The power flow direction is dependent of whether the battery needs to charge or discharge. For charging, the converter works in CCM. The reference charging current is compared with the actual battery current and the error is fed to a PI controller. The output of the PI controller is compared with a triangular wave to generate switching pulses for one switch. The other switch gets the complimentary pulse. The discharging process is also similar and the reference discharging current is maintained with the PI controller.

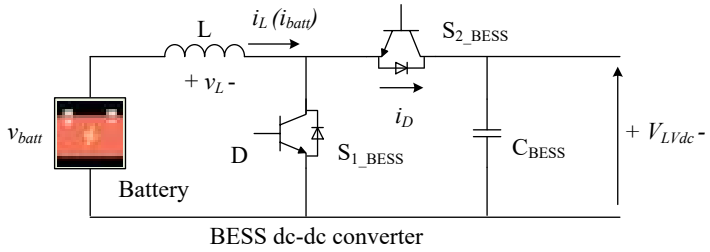

Fig. 4.4 Circuit diagram of BESS dc-dc converter.

In the islanded mode of operation, the BESS dc-dc converter is responsible for maintaining the LVdc voltage. Therefore, it operates in VCM. This also acts as the slack bus in the operation while maintaining the power balance between demand and supply in the system. If the loads cannot be supplied by the DG sources or EVs, BESS supplies the remaining power. V^*_{LVdc} is considered as the reference output voltage of the converter. By comparing the actual LVdc voltage with this, the error is obtained and it is passed through a PI controller. The PI controller output is compared with a triangular signal to generate the switching pulses [141]. The complete control strategy is shown in Fig. 4.5.

4.4.2 EV dc-dc Converter

The circuit diagram of EV dc-dc converter is shown in Fig. 4.6. The controlling action is similar to the BESS dc-dc converter in CCM mode. A current reference is given to the converter. The current references are obtained from power references which are generated by the optimal power management algorithm. The reference currents are compared with the actual currents and a PI controller is used to generate the firing pulses as per the error [141]. The control diagram of the EV dc-dc converter is also

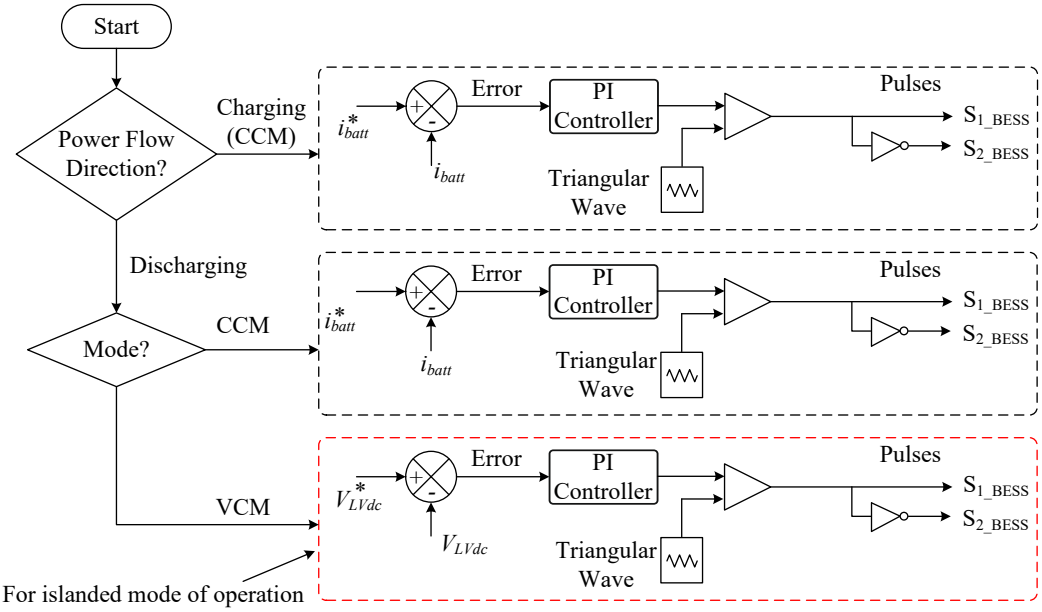

Fig. 4.5 Control strategy for BESS dc-dc converter.

shown in Fig. 4.7.

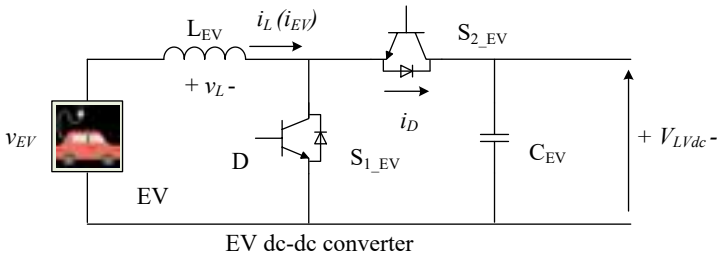

Fig. 4.6 Circuit diagram of EV dc-dc converter.

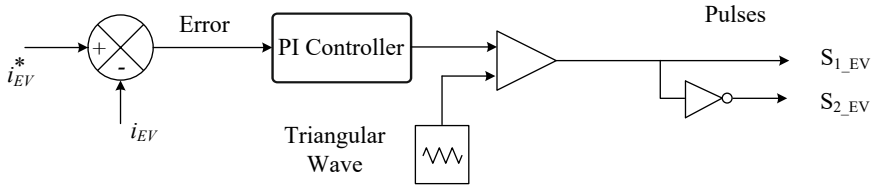

Fig. 4.7 Control strategy for EV dc-dc converter.

A comparison of the proposed work is done with the researches that are available in the literature. It is summarized in Table 4.1.

4.5 Simulation Results

The system is simulated in PSCAD software considering different scenarios. The simulation system details are given in Table 4.2.

Table 4.1 Comparison of Proposed Work with Studies Available in the Literature

Reference	Contribution	Remark
[131]	DGs and EVs participate in the optimization of losses with day-ahead scheduling approach.	Hybrid distribution system is not considered. Performance is tested on IEEE 24 bus transmission system.
[132]	Optimal network constraint-based expansion planning model is proposed along with optimal integration of intermittent RES to improve topological flexibility.	Impact of energy storage systems is not considered.
[133]	Congestion management is done with optimal DG capacity.	Hybrid distribution system is not considered. Performance is tested on standard benchmark IEEE-30 and IEEE-57 bus configurations.
[134]	Loss minimization through open unified power quality conditioner.	Impact of energy storage systems or meshed configuration is not considered.
[135]	Optimal reactive power dispatch is proposed for permanent magnet synchronous generator based wind farms to minimize losses.	Proposed method is specific for wind farms.
[136]	Optimal Volt/Var control is proposed for systems having RES with both generation and consumption capabilities	Meshed hybrid system is not considered.
[137]	Power is shared among DGs such that losses are minimum in islanded operation.	Meshed hybrid system is not considered.
[138]	Adaptive droop optimization strategy is proposed for systems with PV-BESS to minimize power losses.	Presence of energy storage is considered, but meshed hybrid system is not considered.
Proposed Work	Power loss minimization is proposed for islanded microgrid to improve system operation time. Smart load shedding is also implemented.	Considers the ST based meshed hybrid configuration. Utilizes multiple power flow paths of meshed grid and presence of energy storage as well as DG converters to optimize losses.

A total of six cases are considered for simulation. In the first two cases, loads higher than generation is considered and the load change operation is shown from Case 1 to Case 2. In the next two cases, the scenario of surplus generation is considered and a load change operation is shown in such a mode of operation. Finally, the scenario of under voltage load shedding is shown in the transition from Case 5 to Case 6. In each of the cases, the optimization algorithm which is implemented in MATLAB decides the reference powers for the EVs and the DG converters based on the system parameters. For example, in Case 1 the obtained best and mean fitness values plot of GA is shown in Fig. 4.8. The minimum value among the best fitness values i.e., 0.00824 W is the optimal power loss which is nearly zero. The obtained optimal values of $P^{o}_{DG\_Conv_k}$ and $P^{o}_{EV_l}$ are given as inputs to the PSCAD simulation to verify the control aspects of ST based meshed hybrid microgrid and resulting battery power. This process is

Table 4.2 Simulation System Details

System Quantities	Values
LV grid voltage	0.4 kV (L-L)
ST LV converter	Rating = 50 kVA, V_{DC} = 1 kV, C_{DC} = 4700 μF, L_f = 1 mH, R_f = 0.02 Ω, C_f = 20 μF
DG converter 1	$S_{1(rated)}$ = 15 kVA, C_{DC1} = 2200 μF, L_{fm1} = 6 mH, L'_{fm1} = 68 μH, C_{fm1} = 10 μF, R_{d1} = 1 Ω
DG converter 2	$S_{2(rated)}$ = 20 kVA, C_{DC2} = 2200 μF, L_{fm2} = 4 mH, L'_{fm2} = 45 μH, C_{fm2} = 15 μF, R_{d2} = 1 Ω
dc-dc converters	Rating = 15 kW, f_s = 10 kHz, L = 1 mH, C = 1100 μF
BESS dc - dc converter	Rating = 80 kW, f_s = 10 kHz, L = 1 mH, C = 100 μF
BESS	$SoC^{min}_{BESS_0}$ = 0.2, $SoC^{max}_{BESS_0}$ = 0.9, $E^{rated}_{BESS_0}$ = 400 kWh, $SoC^{critical}_{BESS_0}$ = 0.4, $P^{d,max}_{BESS_0}$ = 80 kW, $P^{c,max}_{BESS_0}$ = 80 kW
EVs 1 and 2	SoC^{min}_{EV} = 0.2, SoC^{max}_{EV} = 0.9, E^{rated}_{EV} = 40 kWh $P^{d,max}_{EV}$ = 10 kW, $P^{c,max}_{EV}$ = 10 kW

repeated while testing all the remaining cases. The power flows for these six cases are summarized in Table 4.3.

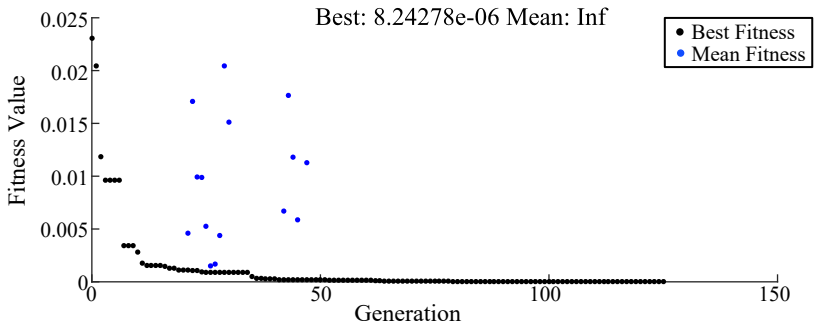

Fig. 4.8 Best and mean fitness values of GA for Case 1.

Table 4.3 Summary of Power Flows in the System

Case	LVac Bus 1 Load (kW)	LVac Bus 2 Load (kW)	LVdc Bus 1 Load (kW)	LVdc Bus 2 Load (kW)	PV 1 Power (kW)	PV 2 Power (kW)	DG 1 Power (kW)	DG 2 Power (kW)	EV 1 Power (kW)	EV 2 Power (kW)
1	15	15	5	5	14.5	18.5	14.8791	15.0599	5.308	1.608
2	25	25	5	5	14.5	18.5	15	20	5.552	6.444
3	0	0	0	0	7.2	9.3	0	0.0027	-7.228	-9.284
4	0	0	5	5	7.2	9.3	0	0.0001	-2.208	-4.296
5	25	15	15	10	0	0	15	9.9107	0	0
6	15	7.5	15	10	0	0	9.0377	3.8578	0	0

Fig. 4.9 shows the power flows during the system operation in the four cases from Case 1 to Case 4. In Case 1 and 2, the PV powers are 14.5 kW and 18.5 kW for PV 1 and PV 2, respectively. These reduce to 7.2 kW and 9.3 kW, respectively in Case 3 and Case 4. In the first two cases, the loads are higher than generation. Thus, it is seen that the EVs supply power. In the next two cases, the EVs are charged with the surplus power. The DG converters follow the reference power as obtained from the optimal algorithm.

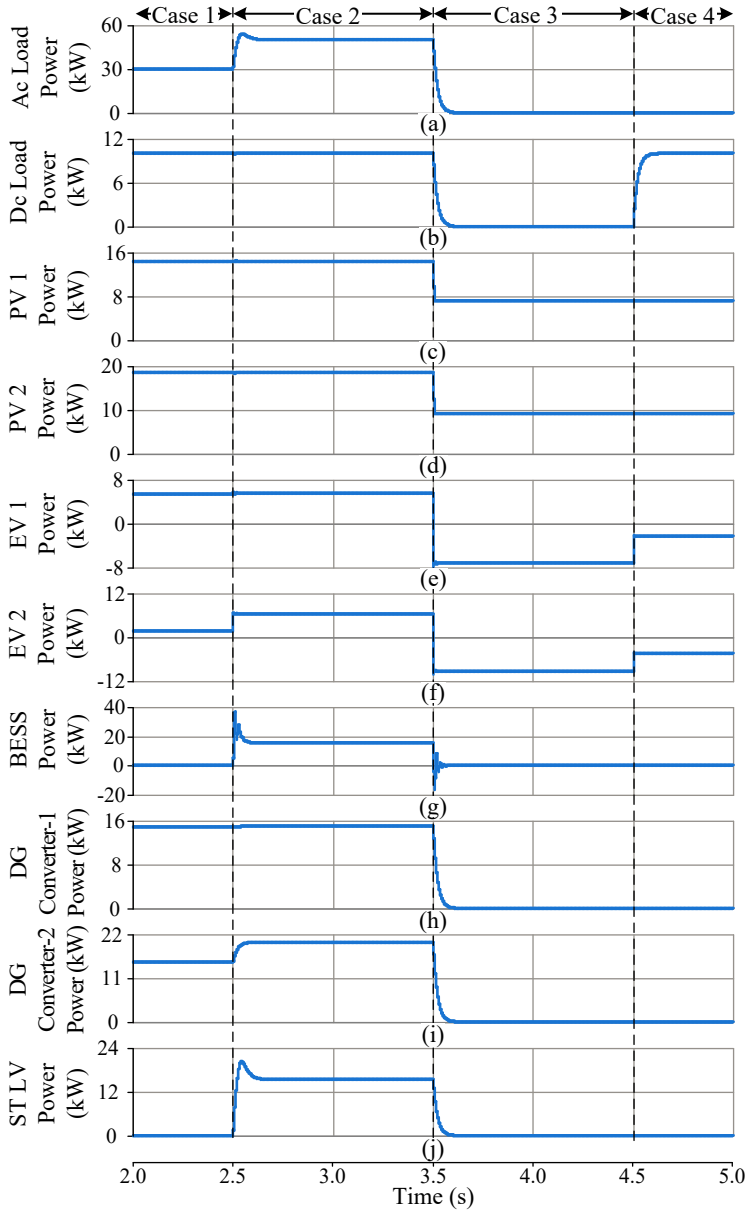

Fig. 4.9 Power flows in the system with BESS SoC within critical limits. (a) Total ac load power. (b) Total dc load power. (c) PV system 1 power. (d) PV system 2 power. (e) EV 1 power. (f) EV 2 power. (g) BESS power. (h) DG converter 1 power injection. (i) DG converter 2 power injection. (j) ST LV converter power output.

Fig. 4.10 shows the voltages and currents waveforms in the system for the transition from Case 1 to 2. The ST LVdc and ST LVac voltages are shown in Fig. 4.10(a) and (b), respectively. It can be observed that the power change does not affect these voltages. Fig. 4.10(c) and (d) shows the LVac bus 1 and LVac bus 2 load currents, respectively. The currents change as per the load data given in Table 4.3. The DG converters 1 and 2 inject currents according to the references obtained from the optimal power management algorithm and are shown in Fig. 4.10(e) and (f), respectively. The dc bus 1 and 2 voltages are shown in Fig. 4.10(g). These show minimum oscillations

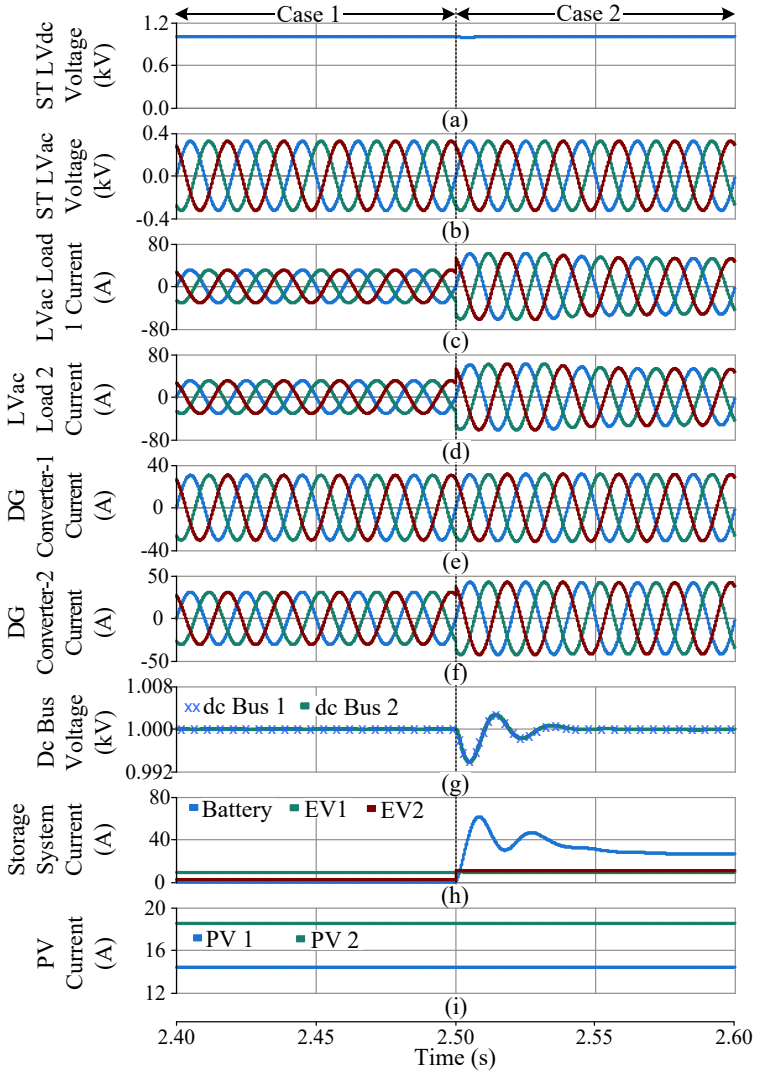

Fig. 4.10 Voltages and currents waveforms for transition from Case 1 to Case 2. (a) ST LVdc voltage. (b) ST LVac voltage. (c) LVac bus 1 load current. (d) LVac bus 2 load current. (e) DG converter 1 current. (f) DG converter 2 current. (g) The dc bus 1 and 2 voltages. (h) Storage system currents. (i) PV currents.

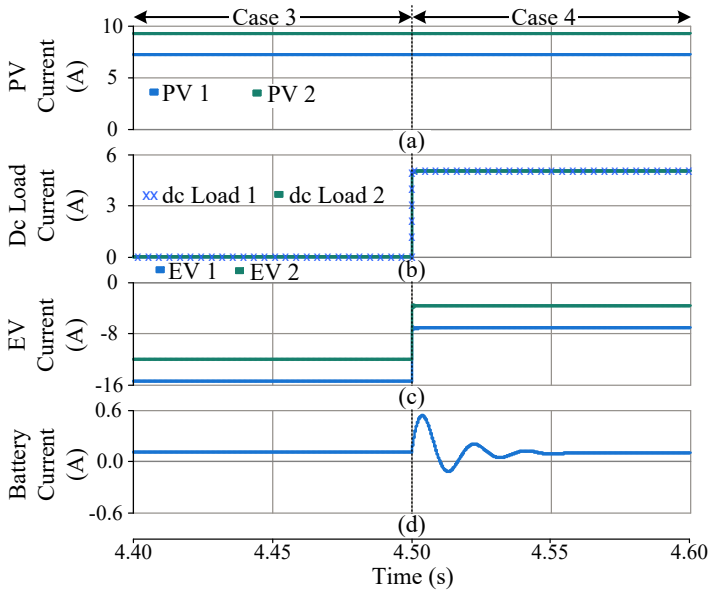

Fig. 4.11 Simulation results for load change during surplus generation. (a) PV current. (b) The dc load current. (c) EV current. (d) Battery current.

which do not affect the operation of the system. The battery and EV currents are shown in Fig. 4.10(h). These provide powers as per the given power references. The PV currents are kept constant as the PV powers are constant. These are shown in Fig. 4.10(i).

In Fig. 4.11, the currents in the system are shown for surplus generation. The transition is shown from Case 3 to Case 4. There is no ac load and the DG converters do not supply any power. The PV currents are shown in Fig. 4.11(a). These are constant as the PV powers are constant. The dc load currents are given in Fig. 4.11(b). Fig. 4.11(c) and (d) shows the EV currents and battery current, respectively. In case 3, the dc load is also zero. Thus, the entire PV power is used to charge the EVs. In Case 4, dc loads of 5 kW are added to both the dc buses. Therefore, reduced power is available for EV charging.

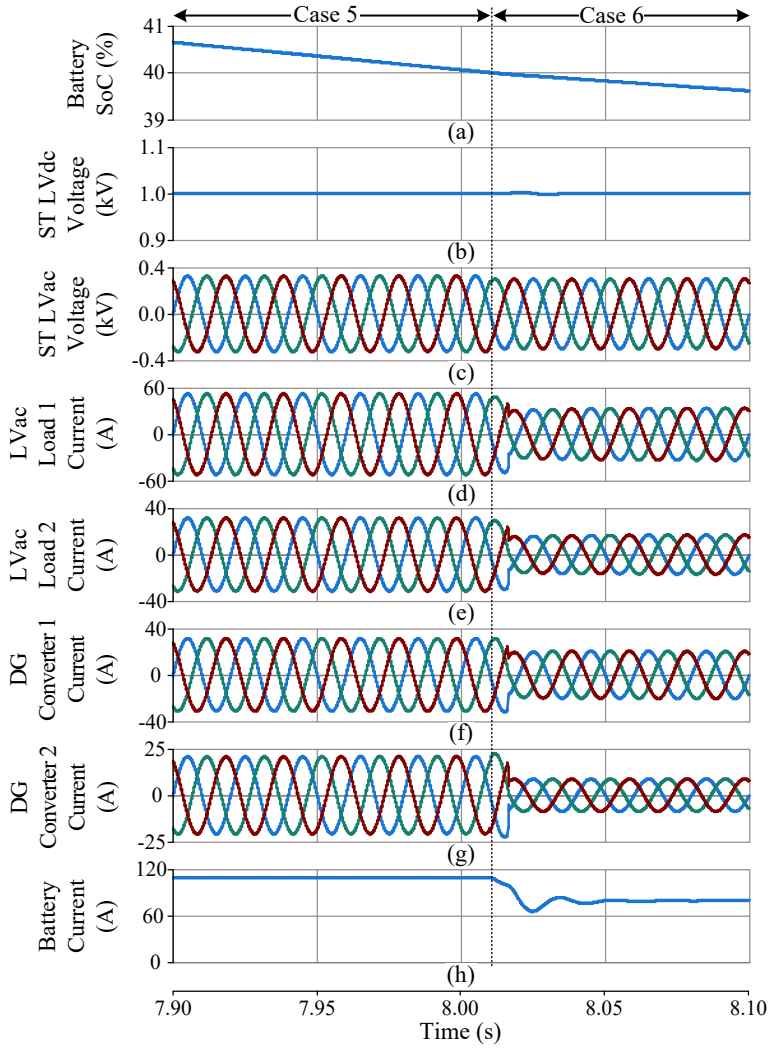

Fig. 4.12 Simulation results for under voltage load shedding. (a) Battery % SoC (b) ST LVdc voltage. (c) ST LVac voltage. (d) LVac bus 1 load current. (e) LVac bus 2 load current. (f) DG converter 1 current. (g) DG converter 2 current. (h) Battery current.

The proposed under-voltage load shedding is shown in Fig. 4.12. Fig. 4.12(a) shows the SoC of the BESS and Fig. 4.12(b) shows the ST LVdc voltage. When the SoC goes below 40%, the under voltage load shedding scheme is implemented and the LVac voltage is reduced to 0.95 p.u. This is seen in Fig. 4.12(c). This is detected at the LVac side load points and the non-critical loads are disconnected from the system. Accordingly the LVac loads reduce as seen in Fig. 4.12(d) and (e). As per the optimization algorithm, the DG converter currents also reduce. This is shown in Fig. 4.12(f) and (g). Finally, as the load is reduced, the current drawn from the battery also reduces as shown in Fig. 4.12(h). This results in a longer system run-time in the islanded mode.

To compare the performance of the proposed method with commonly used techniques, a loss comparison is done. A system is considered where power sharing by DG converters is done as per their individual ratings as considered in [97], [142]. Moreover, EV power injection is also not considered. The loss comparison for such a system with the proposed system in the six cases considered is shown in Table 4.4.

Table 4.4 Loss Comparison

Case	Power Loss in the Conventional Method [97], [142](kW)	Power Loss in the Proposed System (kW)	Power Loss Reduction (kW)
1	0.0246	≈ 0	0.02459
2	0.3186	0.2587	0.0599
3	0.1140	≈ 0	0.11399
4	0.0194	≈ 0	0.0194
5	1.3370	1.0487	0.2883
6	0.7874	0.5209	0.2665

4.6 Experimental Results

The block diagram of the complete experimental setup is shown in Fig. 4.13(a). To emulate the distribution line resistance, series resistances were added to both the ac and dc lines. The photographs of the ST LV converter, DG converter, BESS, EV system and PV system are shown in Fig. 4.13(b)-(f), respectively. The hardware parameters are given in Table 4.5.

Fig. 4.14 shows a load change operation under surplus load condition. The BESS maintains the ST LVdc voltage as shown in Fig. 4.14(a) and the ST LV converter maintains the ST LVac voltage as shown in Fig. 4.14(b). The LVdc load is kept constant at

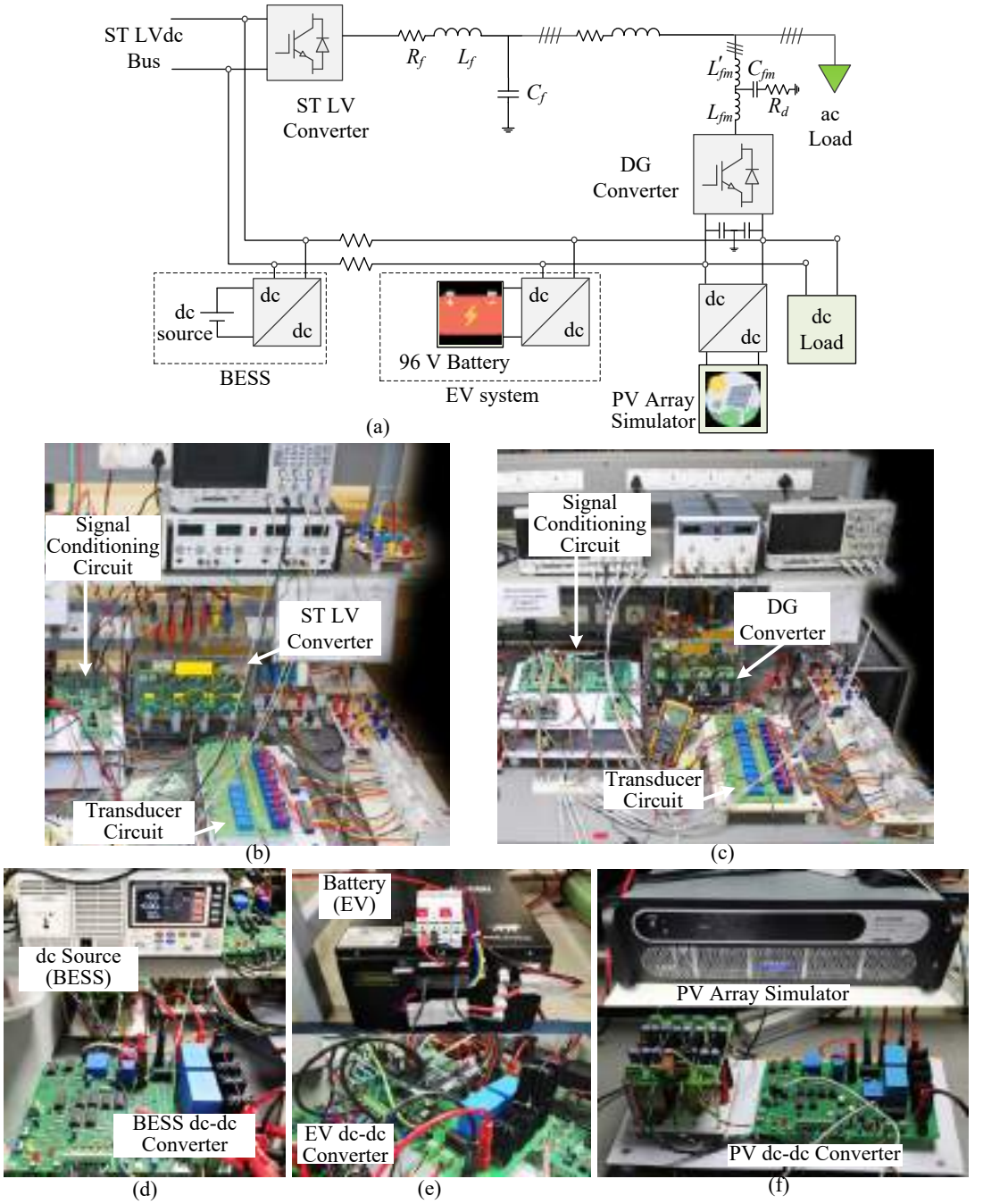

Fig. 4.13 Overview of the experimental setup. (a)Block diagram. (b) Photograph of ST LV converter. (c) Photograph of DG converter. (d) Photograph of BESS. (e) Photograph of EV system. (f) Photograph of PV system.

100 W and the LVac load is increased from 140 W to 200 W. The corresponding LVac load currents are shown in Fig. 4.14(c). The optimization algorithm decides the power reference for the DG converter and EV. The balance power is supplied by the BESS. In real-time, the optimal power management algorithm is implemented in centralized power management controller. The controller takes required inputs using communication infrastructure and provides optimal values to the respective controllers. However, in this setup, the optimal power references are given from a look up table as per the

Table 4.5 Hardware Parameters

System Quantities	Values
LV grid voltage	80 V (L-L)
ST LV converter	Rating = 1 kVA, V_{dc} = 200 V, C_{dc} = 2350 μF, L_f = 20 mH, R_f = 0.5 Ω, C_f = 10 μF
DG converter	$S_{1(rated)}$ = 1 kVA, C_{dc1} = 2350 μF, L_{fm1} = 6 mH, L'_{fm1} = 68 μH, C_{fm1} = 10 μF, R_{d1} = 1 Ω
BESS dc-dc converter	Rating = 500 W, f_s = 20 kHz, L = 13 mH, C = 10 μF
PV dc-dc converter	Rating = 500 W, f_s = 20 kHz, L = 13 mH, C = 10 μF
EV dc-dc converter	Rating = 100 W, f_s = 20 kHz, L = 13 mH, C = 10 μF
BESS source	100 V dc source
EV source	96 V lithium battery
PV source	Elgar TerraSAS PV array simulator

considered cases. Accordingly, in Case 1 to 2, the DG converter power changes from 128 W to 174 W and the corresponding currents are shown in Fig. 4.14(d). Fig. 4.14(e) shows the LVdc voltage at the DG converter and this remain unchanged throughout. With the increase in load, the power drawn from the BESS increases. Therefore, an increase in battery current is observed as shown in Fig. 4.14(f). The EV injects at its maximum capacity throughout the operation and the current is shown in Fig. 4.14(g). The PV and LVdc load currents are shown in Fig. 4.14(h) and (i), respectively. These do not change as the PV power and dc load are kept constant in this operation.

Fig. 4.15 shows a scenario of excess generation with load change operation. Only dc loads are used for this purpose. The PV source injects a constant power of 74 W. The corresponding current waveform is shown in Fig. 4.15(a). The dc load current waveform is shown in Fig. 4.15(b). Initially there is no load. Thus, the entire PV power is used to charge the EV. The EV current is shown in Fig. 4.15(c). The negative value depicts charging operation. The BESS is used to maintain the LVdc voltage only. Since no power is drawn from the BESS, the battery current is zero as shown in Fig. 4.15(d). The dc load is increased from 0 to 60 W. At this condition, the optimization algorithm ensures that the dc load draws the entire power requirement from the PV system and the balance power is fed to the EV. Therefore, there is a corresponding decrease in the EV charging current. The BESS dc-dc converter operates in grid forming mode, during the sudden load increase. Therefore, the BESS supplies the transients till the EV current settles to the new reference value. Once that condition is attained, the BESS current again settles to zero.

Fig. 4.16 shows the experimental results for under voltage load shedding. A scenario is

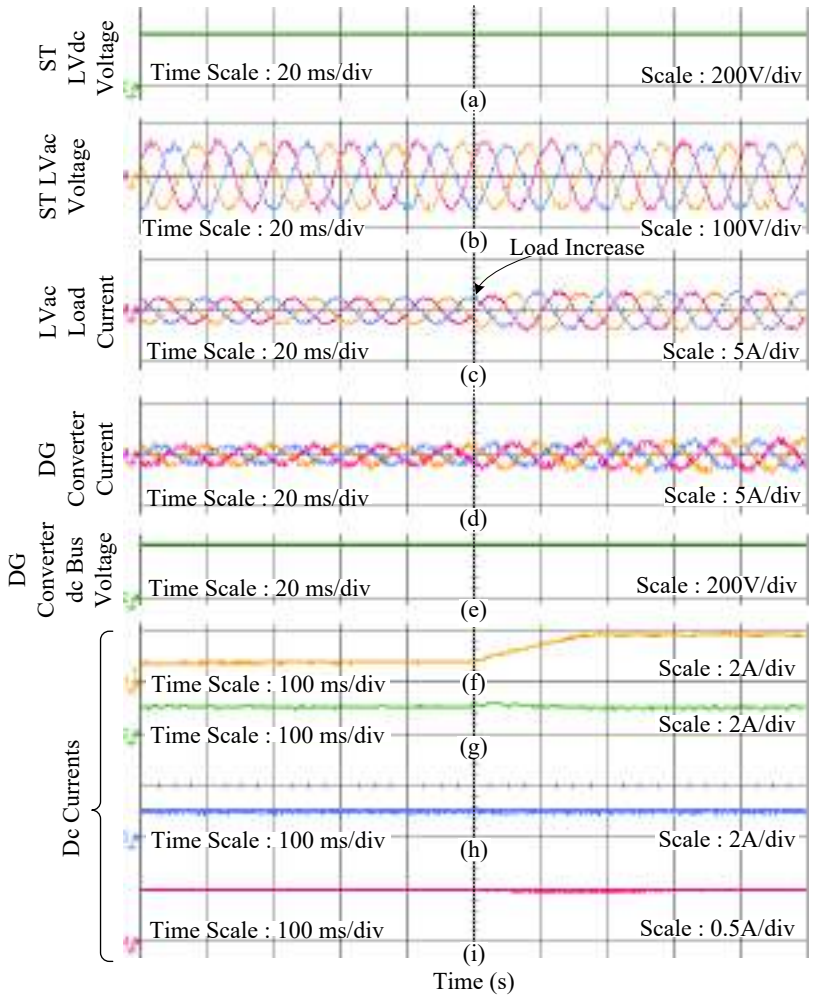

Fig. 4.14 Experimental results for load increase in surplus load condition. (a) ST LVdc voltage. (b) ST LVac voltage. (c) LVac load current. (d) DG converter current. (e) The dc bus voltage at DG converter. (f) Battery current. (g) EV current. (h) PV current. (i) dc load current.

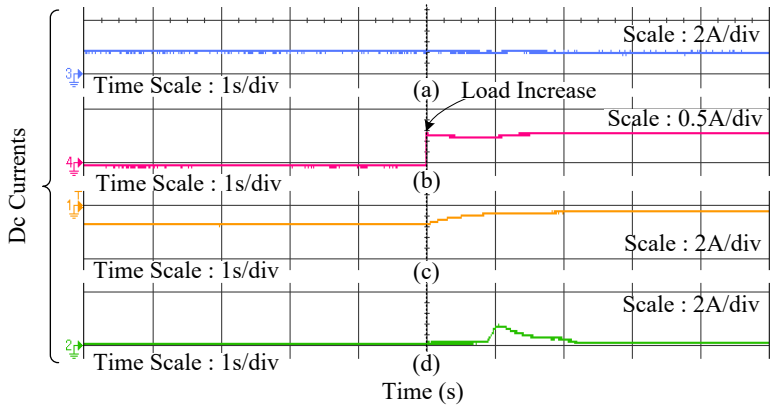

Fig. 4.15 Experimental results for load change during surplus generation. (a) PV current. (b) dc load current. (c) EV current. (d) Battery current.

considered where EV is absent, and PV and BESS are the only sources. Fig. 4.16(a)-(e) shows the ST LVdc voltage, ST LVac voltage, LVac load current, DG converter current

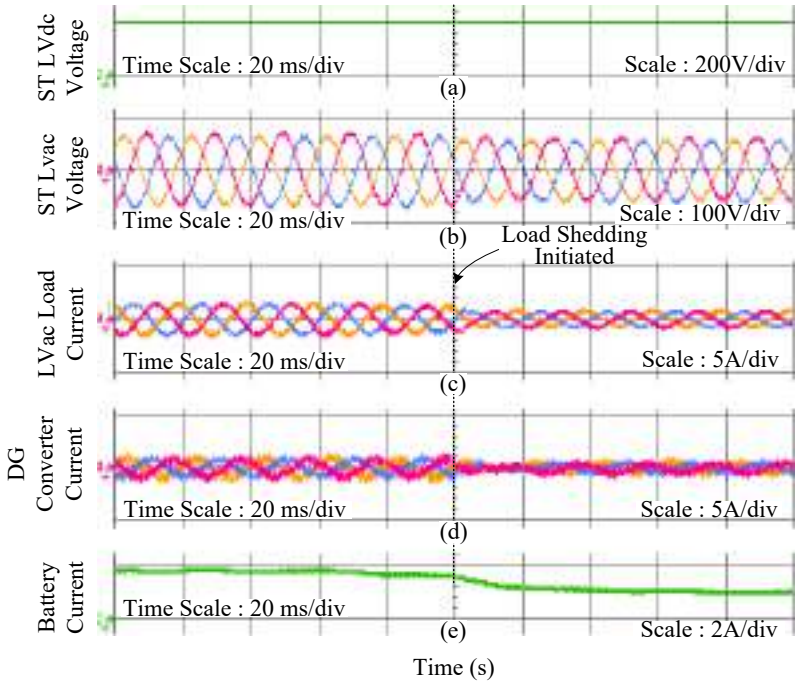

Fig. 4.16 Experimental results for under voltage load shedding. (a) ST LVdc voltage. (b) ST LVac voltage. (c) LVac load current. (d) DG converter current. (e) Battery current.

and battery current, respectively. Total LVac load in the system is 160 W. When the BESS SoC goes below the critical value, the ST reduces the LVac voltage as shown in Fig. 4.16(b). This is detected at the load point and the non-critical load of 80 W is removed from the system. The optimization algorithm accordingly decides the reference current for the DG converter in the reduced load scenario. The battery current consequently reduces. As the power drawn from the battery is reduced, longer run-time of the islanded system is achieved.

4.7 Summary

An optimal power loss minimization scheme is proposed for an ST based islanded LV meshed hybrid microgrid. Such a microgrid offers different power flow paths between the sources and loads. Based on the loading and DG power scenario, GA is used to optimally control the active power references of DG converters and charge or discharge schedules of EVs. This ensures minimum line losses in the system and helps to increase the system operation time. Moreover, a smart ST based under voltage load shedding is also incorporated into the optimization algorithm which triggers when the BESS SoC goes below the critical limit. Detailed simulation results are presented for the

various possible scenarios along with load change operations. The results obtained were compared to a system where power is shared as per the converter ratings, without the use of EVs to reduce losses. It was seen that for the six cases considered, the power loss reduction in the proposed system were respectively, 0.02459 kW, 0.0599 kW, 0.11399 kW, 0.0194 kW, 0.2883 kW and 0.2665 kW. Experimental results supporting the simulation results have been shown.

CHAPTER 5

STABILIZATION OF SMART TRANSFORMER BASED ISLANDED MESHED HYBRID MICROGRID DURING ELECTRIC VEHICLE CHARGING TRANSIENTS

Chapter 3 discusses the operation of an ST based meshed hybrid microgrid which is connected to the MVac grid through the ST. In Chapter 4, islanded operation of the meshed hybrid microgrid is discussed. The islanded operation is achieved by taking power from a BESS which maintains the LVdc voltage. Moreover, with the utilization of EVs and energy storage systems, optimal power management is achieved to reduce power loss. In the BESS maintained islanded system, BESS converter stability is important as it is responsible for maintaining both the LVdc and LVac grid. As EVs draw high power from the electric grid while charging, transients appearing from such charging can lead to system instability. This chapter investigates the stability aspects of the ST based islanded meshed hybrid microgrid when it is subjected to EV charging transients.

With the increasing focus on decentralized generation and renewable power integration, EVs and their integration to the grid have also received great importance recently [143]. For such increased integration of RES and EV in electric grid, ST has been proposed as an attractive solution [61]. Various studies have been conducted showing the utility of STs in integrating renewable sources and EVs to the grid [144], [145]. One of the key challenges in widespread deployment of EVs is the need of charging infrastructure [146], [147]. The grids have to be able to cope with the sudden increase in power demand arising from EVs. Moreover, the controllers present in the system have to be prompt to handle the power fluctuations. If not addressed properly, these fluctuations can cause stability issues especially in grids realized with the help of power electronic converters [148]. In the islanded operation of ST based meshed hybrid microgrid, the dc grid is maintained by the dc-dc converter of battery energy storage system (BESS). From the dc grid, the ST LV converter maintains the LVac voltage. Thus power fluctu-

ations appearing in the grid has to be handled by the BESS dc-dc converter. This converter is generally a bi-directional converter which works as buck converter in charging mode and as a boost converter in supplying mode [149]. The control-to-output transfer function of a boost converter has a right half plane zero (RHPZ). This makes the converter vulnerable for fast dynamic operations [150]. In the literature, several methods are proposed to eliminate the effects of the RHPZ. In [151], the RHPZ is eliminated by operating the converter in discontinuous conduction mode and in [152], output filter and magnetic coupling between inductors is used to eliminate RHPZ. However, both these methods lead to the problem of increased current stresses on the converter. The issue of current stress due to the magnetic coupling has been addressed in [153], where integrated three-winding couple inductor is proposed. However, issues of magnetic loss from leakage inductance arises in such a technology. In [150], [154]–[156], technologies like ON state energy transfer through magnetic coupling, tri-state boost converter and RC damping network are used to address the issue of RHPZ. These methods provide satisfactory operation. However, they propose change in the conventional circuitry which adds to the cost and complexity of the system. Moreover, the studies available in the literature consider the operation of a single converter. The efficacy of the technologies in coordination with other converters for grid applications have not been explored.

This chapter investigates the impact of EV charging on the overall stability of an ST based meshed hybrid microgrid during islanded mode of operation. In the islanded operation, the BESS is the primary source of power and the transients are supplied by the BESS. The RHPZ present in the BESS converter control-to-output transfer function leads to slower system response. Thus, a transient high current demand for EV charging may lead to system instability. The need for faster response of the BESS converter is initially shown through simulation and a method of voltage control by the ST is proposed to indirectly reduce loads in the system during transients to maintain the stability of the system. The proposed scheme provides a simple yet effective method to stabilize meshed islanded system in-spite of slower system dynamics. The design and stability analysis of the converters are presented to study the system performance with the proposed method. Simulation and experimental results verify the proposed control scheme.

5.1 Description of the Islanded Meshed Hybrid Microgrid

The ST based meshed hybrid microgrid is shown in Fig. 5.1. The ST draws power from the MVac grid and delivers it to the LVac grid. It consists of the ST MV converter, ST isolated dc-dc converter and the ST LV converter. The ST LVdc link is extended in the distribution grid and connected to the dc bus of the DG converter which injects power from a PV system present in the distribution grid. The maximum power is drawn from the PV panels with the help of a dc-dc converter operating in MPPT mode. The dc loads and EVs are connected to the extended ST LVdc line.

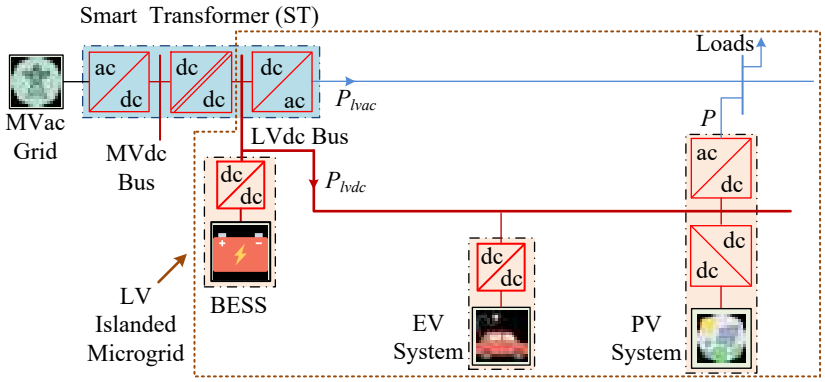

Fig. 5.1 ST based meshed hybrid microgrid.

A BESS is interfaced with the LVdc bus at the ST through a dc-dc converter. This converter operates in CCM when the system is grid connected. But in the islanded mode of operation, this converter operates in VCM and maintains the LVdc voltage. Moreover, the ST LV converter operation remains similar in both the grid connected and islanded modes.

5.2 Proposed Voltage Control Strategy for Stable Operation

The islanded operation of an ST based meshed hybrid microgrid is realized by maintaining the LVdc voltage constant using the BESS converter operating in discharging mode. The circuit diagram of the converter is shown in Fig. 5.2.

From the small signal analysis, the control to output transfer function is obtained as [157]

$$\frac{v_{LVdc}(s)}{d(s)} = \frac{v_{batt}}{1-D} \quad \frac{1-\frac{s}{\frac{(1-D)^2R}{L}}}{1+\frac{s}{(1-D)\sqrt{\frac{C}{L}}\frac{1-D}{\sqrt{LC}}}+\left(\frac{s}{\frac{1-D}{\sqrt{LC}}}\right)^2}. \tag{5.1}$$

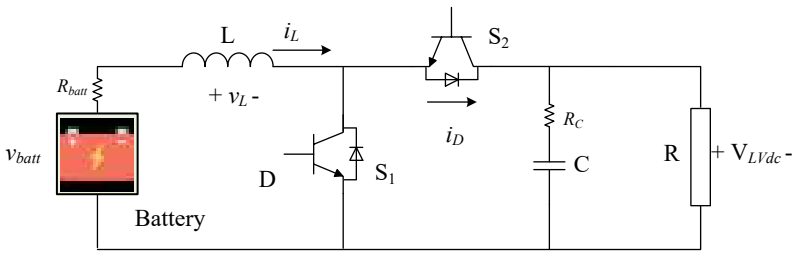

Fig. 5.2 Circuit diagram of BESS converter.

It can be seen from (5.1) that the transfer function has a zero on the right half of the s plane. This results in a 90° phase lag which leads to slow system dynamics. Therefore, owing to right half plane zero, the system's stability might be at risk in situations demanding faster response. The stability analysis for such a condition is well established in the literature [150], [157]. When the BESS output voltage is regulated with a controller, for any step increase in load on the BESS converter, the output voltage will initially decrease before the controller is able to bring it to the desired level. For large step inputs, the controller may hit the control limits which might lead the converter to lose stability. Thus, the dc microgrid grid voltage will not be maintained. In the meshed islanded microgrid, the ST LV converter maintains the LVac grid by drawing power from the LVdc bus. This means unstable dc bus voltage will also result in an unstable LVac grid. Therefore, the slower dynamic response of the BESS converter can lead to the loss of stability for the entire islanded microgrid. The reason for slower dynamics is explained as follows.

The average voltage across the converter inductor for any duty ratio D is given by

$$\begin{aligned} v_L &= (v_{batt} - i_L R_{batt})D - (V_{LVdc} - v_{batt} + i_L R_{batt})(1-D) \\ &= v_{batt} - V_{LVdc}(1-D) - i_L R_{batt} \end{aligned} \tag{5.2}$$

where v_{batt} is the BESS battery voltage, V_{LVdc} is the LVdc bus voltage, i_L is the inductor current and R_{batt} is the battery internal resistance.

The rate of change of inductor current for inductor value L is given by

$$\frac{di_L}{dt} = \frac{v_L}{L}. \tag{5.3}$$

Using (5.2) in (5.3), we get

$$\frac{di_L}{dt} = \frac{1}{L}\{v_{batt} - V_{LVdc}(1-D) - i_L R_{batt}\}. \tag{5.4}$$

For the BESS converter, the relation between inductor current and output current is

given by

$$i_L = \frac{i_{BESS}}{1-D}. \tag{5.5}$$

For a step increase in load, the inductor current has to increase accordingly. This is facilitated by the controller by changing the duty ratio of the converter. For a change in duty ratio from D_0 to D along with change of output current from I_{BESS0} to I_{BESS}, the average variation of inductor current is given by

$$\Delta i_L = \frac{I_{BESS}}{1-D} - \frac{I_{BESS0}}{1-D_0}. \tag{5.6}$$

Therefore, for the average slope of inductor current given by (5.4), the variation of average output current from I_{BESS0} to I_{BESS} will only be possible in a time duration of

$$t_{rise} = \frac{\frac{I_{BESS}}{1-D} - \frac{I_{BESS0}}{1-D_0}}{\frac{1}{L}\{v_{batt} - V_{LVdc}(1-D) - i_L R_{batt}\}}. \tag{5.7}$$

Using (5.5) in (5.7), we get,

$$t_{rise} = \frac{\frac{I_{BESS}}{1-D} - \frac{I_{BESS0}}{1-D_0}}{\frac{1}{L}\{v_{batt} - V_{LVdc}(1-D) - \frac{i_{BESS}}{1-D} R_{batt}\}}. \tag{5.8}$$

Therefore, (5.8) gives a relation for the time that is required for the duty ratio to increase from one particular value to another. In practical operations of dc-dc converters there is always a maximum and minimum limit set for the duty ratio. These are used to design the value of the time delay for the worst possible scenario where the duty ratio changes from minimum (D_{min}) to maximum (D_{max}). Therefore, (5.8) can be re-written as

$$t_{rise}^{min} = \frac{\frac{I_{BESS}^{max}}{1-D_{max}} - \frac{I_{BESS}^{min}}{1-D_{min}}}{\frac{1}{L}\{v_{batt} - V_{LVdc}(1-D_{max}) - \frac{i_{BESS}}{1-D_{max}} R_{batt}\}}. \tag{5.9}$$

The value of v_{batt} considered in this paper is 600 V, V_{LVdc} is 1 kV and I_{BESS} has a peak value of 100 A. Batteries generally have low internal resistance. For the battery considered in this paper, R_{batt} can be as low as 100 mΩ [158]. Therefore, in the denominator of the expression for t_{rise}^{min}, the term $\frac{i_{BESS}}{1-D_{max}} R_{batt}$ will relatively have a very small value and the impact of R_{batt} on t_{rise}^{min} is very small. Moreover, it is also observed that the esr of the filter capacitor has no effect on t_{rise}^{min}.

The above analysis indicates that within the ratings of a system, the system has better performance for ramp increase of load compared to step increase. Therefore, if the step load makes the system unstable, stability can be maintained by manipulating the load transition into a ramp increase with total rise time of t_{rise}^{min}.

To implement such a load manipulation in the islanded ST based meshed hybrid microgrid, the ST LV converter is used to reduce the voltage to the permissible limit of 0.9 times the nominal value. There are studies in the literature that explore the load sensitivity to voltage and the ST is suggested as a suitable tool for exploiting it to provide services in the distribution grid [159]. The active power load sensitivity to voltage is expressed as follows.

$$K_{V\_LVac} = \frac{\Delta P_{LVac}/P_{LVac}}{\Delta V_{LVac}/V_{LVac}} \tag{5.10}$$

where P_{LVac} is the LVac load power, V_{LVac} is the per phase rms voltage, ΔP_{LVac} and ΔV_{LVac} are the variations is power and voltage, respectively, of the LVac grid.

The ac loads considered in the paper are voltage dependent three phase loads, which are rated for the grid voltage of 400 V. Active power loads are considered. The load model is given by the following expression [160]

$$P = P_r \left(\frac{V}{V_r}\right)^{v_e} \left(\frac{f}{f_r}\right)^{f_e} \tag{5.11}$$

where P, V and f denote the real power, voltage and frequency. P_r is the active power demand at the rated voltage V_r and rated frequency f_r. v_e and f_e are the voltage and frequency exponents. The equation denotes that the power reduces when the voltage or frequency reduces. If the ac loads are dynamic in nature, appropriate modelling techniques have to be employed to assess the load behaviour based on change in voltage of the LVac grid. There are several methods available in the literature for modelling of dynamic loads based on measurements [161], [162].

As reduction in LVac voltage leads to the reduction of LVac load power, it reduces the overall load on the BESS. Thus, when the LVdc voltage goes below 0.9 times the nominal value due to any disturbance, the proposed voltage control is triggered. Once the LVac voltage is reduced, the voltage is again increased gradually in steps with total rise time of t_{rise}^{min}. The increment in each cycle of the control loop is based on the execution time of the controller. If T_{cd} is the time required by the controller to execute one loop, the value of LVac voltage increment in each step is given by

$$incr = 0.1 \frac{V_{LVac}^{nom} \times T_{cd}}{t_{rise}^{min}} \tag{5.12}$$

where V_{LVac}^{nom} is the nominal LVac voltage.

The overall flowchart for the proposed LVac voltage control is shown in Fig. 5.3.

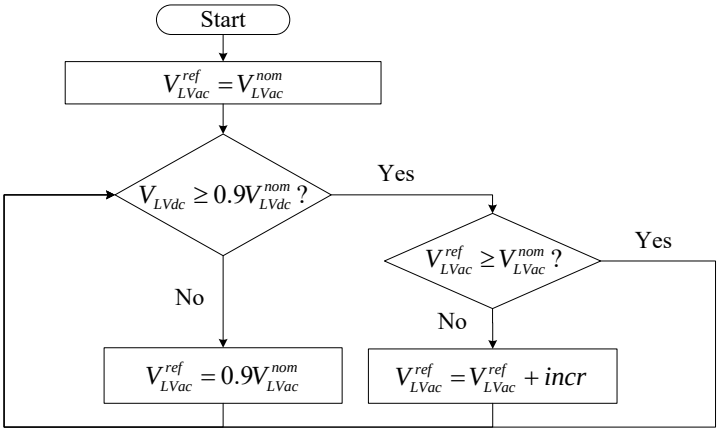

Fig. 5.3 Flowchart for the proposed LVac voltage control.

5.3 Controller Design and Stability Analysis

The overall control diagram of the complete system is shown in Fig. 5.4. The control of ST MV and ST isolated dc-dc converters are already explained in Chapter 3, Sections 3.3.1 and 3.3.2, respectively. The converters operational during the islanded mode are analyzed in detail. The controllers are designed appropriately as per the system parameters. These are explained as follows.

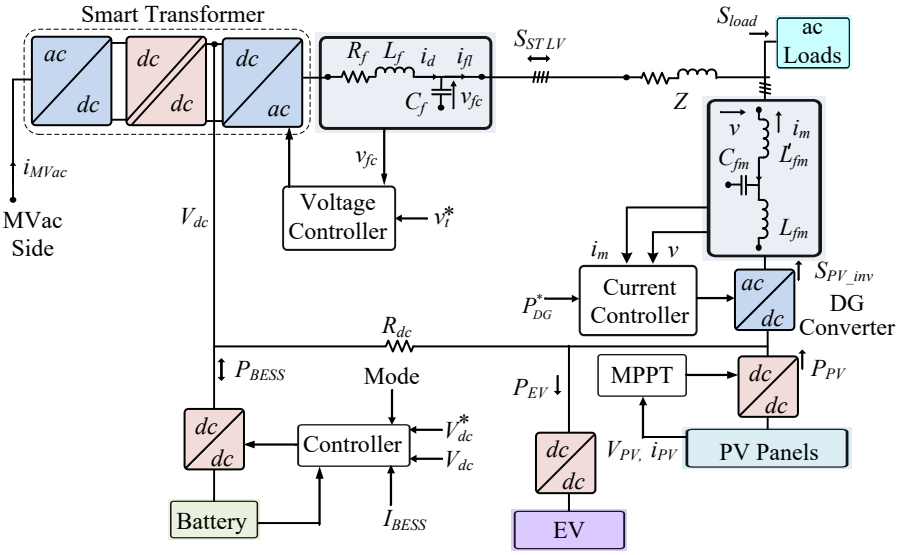

Fig. 5.4 Overall control diagram of the complete system.

5.3.1 ST LV Converter

A two-level three-phase inverter is used for the ST LV converter. It uses an *LC* filter for maintaining the three phase balanced sinusoidal voltage at the LVac line. The control

diagram is shown in Fig. 5.5. G_h^{STLV}, $G_d^{STLV}(s)$ and $H_{LC}(s)$ are the transfer functions of hysteresis gain, digital delay and *LC* filter, respectively [163]. The open loop transfer function of the ST LV converter can be expressed as

$$G_{STLV\_conv}(s) = G_h^{STLV} G_d^{STLV}(s) H_{LC}(s). \tag{5.13}$$

G_h^{STLV} is given by $\frac{1}{2h} + 0.5$, where h is the magnitude of the hysteresis band [164]. The digital delay, $G_d^{STLV}(s)$, can be expressed as [165]

$$G_d^{STLV}(s) = \frac{(1.5st_{st})^2 - 9st_{st} + 12}{(1.5st_{st})^2 + 9st_{st} + 12}, \tag{5.14}$$

where t_{st} is the sampling time.

In (5.13), H_{LC} is the *LC* filter transfer function and is given as follows.

$$H_{LC} = \frac{v_{LVac}(s)}{v_{il}(s)} = \frac{1}{L_f C_f s^2 + R_f C_f s + 1}. \tag{5.15}$$

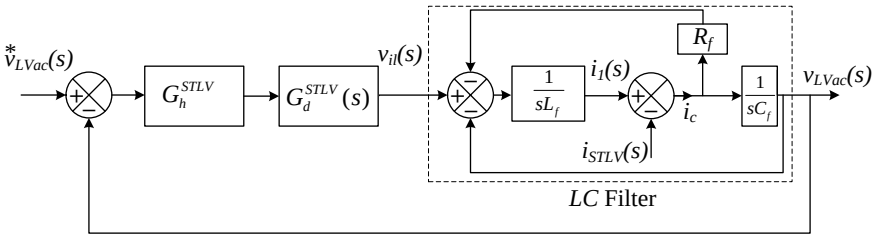

Fig. 5.5 Control diagram for ST LV converter.

Fig. 5.6 shows the Bode plot for $G_{STLV\_conv}(s)$. The inductor and capacitor create a resonance at around 400 Hz. This is damped by using the damping resistor R_f. The damped closed loop system is observed to have a gain margin of 38.5 db at 3.64 kHz and a phase margin of 52° at 502 Hz. These are sufficient to ensure stable operation. This analysis holds good for both the nominal LVdc voltage as well as during the reduced voltage as per the proposed scheme, as H_{LC} only depends on the filter and damping values.

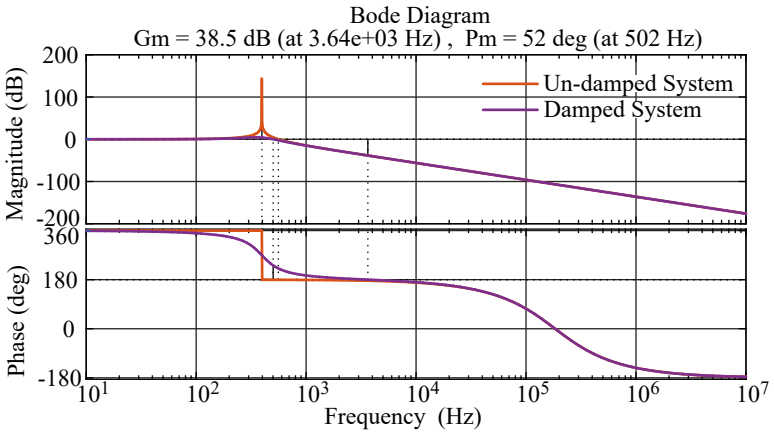

Fig. 5.6 Bode plot for ST LV converter.

5.3.2 BESS Converter

The BESS converter works in CCM in the grid connected mode. In the islanded mode, it operates in VCM to maintain the LVdc voltage. The control of BESS converter is already explained in Chapter 4, Section 4.4.1. Fig. 5.2 shows the BESS converter circuit diagram. As the converter works in VCM in islanded mode, the control-to-output voltage transfer function is analyzed for stability. Fig. 5.7 shows the block diagram for the BESS converter output voltage control. The control-to-output transfer function (G_{BESS}) is expressed in (5.1).

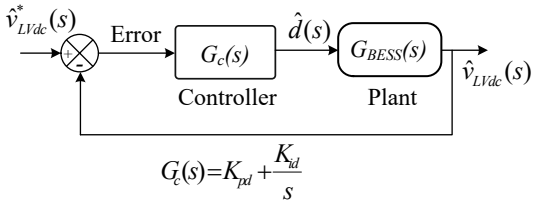

Fig. 5.7 Control block diagram of BESS.

The Bode plots for both the uncompensated and compensated system are shown in Fig. 5.8. The uncompensated system is unstable as it is seen to have a gain margin of -56.5 db at 169 Hz and a phase margin of -89.4° at 31.8 kHz. The controller is designed such that the closed loop system has a gain margin of 11.2 dB at 107 Hz and phase margin of 90.2° at 10 Hz. These indicate stable system operation.

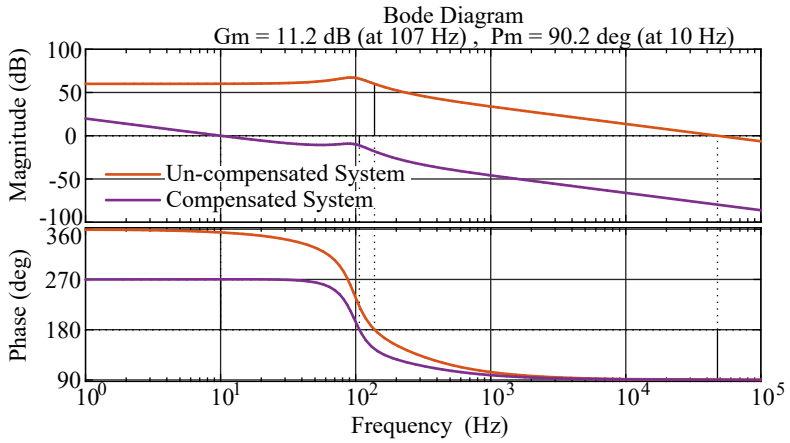

Fig. 5.8 Bode plot for control-to-output voltage transfer function of the BESS converter.

5.3.3 PV dc-dc Converter

This converter operates in MPPT mode to extract the maximum available PV power from the PV panels. The control of this converter is already explained in detail in Chapter 2, Section 2.3.5. Fig. 5.9 shows the circuit diagram of the PV dc-dc converter. Based on the MPPT algorithm, a reference PV current is obtained corresponding to maximum power and a PI controller is used to maintain the PV current as per the reference [102]. Therefore, the controller is designed with the control-to-inductor current transfer function [166]. The control block diagram is shown in Fig. 5.10.

$$G_{PV}(s) = G_{cnst}\frac{s+\omega_{zi}}{s^2+2\zeta\omega_n s+\omega_n^2}, \tag{5.16}$$

where $G_{cnst} = \frac{V_{LVdc}}{L}, \omega_{zi} = \frac{2}{RC}, \omega_n = D'\sqrt{\frac{1}{LC}}$, and $\zeta = \frac{L}{2RD'\sqrt{LC}}$

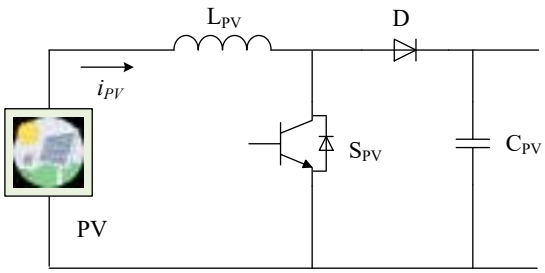

Fig. 5.9 Circuit diagram of PV dc-dc converter.

The Bode plots for control-to-inductor current transfer function of the PV dc-dc converter for both the uncompensated and compensated system are shown in Fig. 5.11. The uncompensated system is seen to have an infinite gain margin and a phase margin

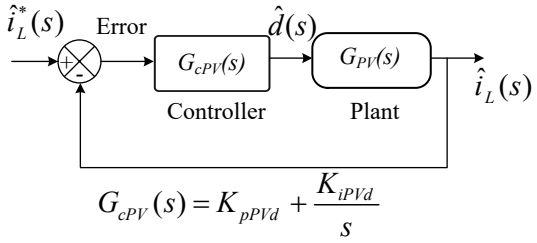

Fig. 5.10 Control block diagram of PV dc-dc converter.

of 89.7° at 16.6 kHz. The system shows stable operation. However, to obtain better system dynamics and steady-state operation in closed loop, a controller is used. The controller is designed such that the compensated closed loop system has a phase margin of 59.4° at 397 Hz and infinite gain margin.

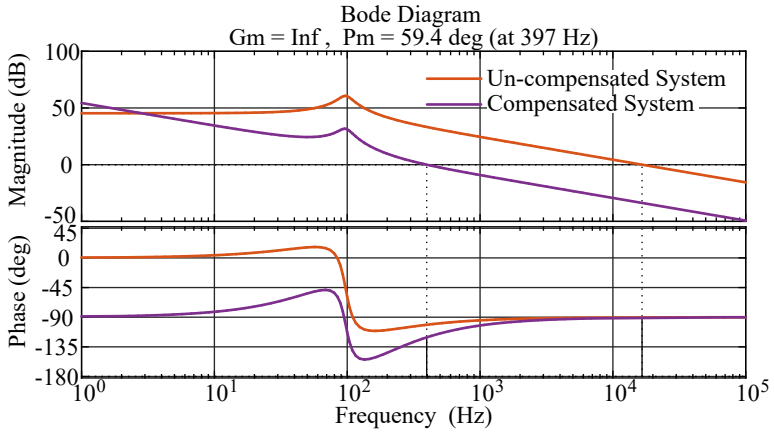

Fig. 5.11 Bode plot for control-to-inductor current transfer function of the PV dc-dc converter.

5.3.4 DG Converter

The DG converter operates in CCM and injects the reference power to the LVac grid from the LVdc bus. The control strategy for this converter is explained in detail in Chapter 3, Section 3.3.4. The converter uses an *LCL* filter. For proper operation, the design of the *LCL* filter should be accurate. The design procedure presented in [167] is considered. For the filter capacitor design, a maximum of 5% power factor variation is considered and thus, the capacitance value is taken as:

$$C_{fm} = 0.05 C_b \tag{5.17}$$

where C_b is the base capacitance.

Based on the current ripple, switching ripple attenuation and magnitude of dc link voltage, the inductor values are obtained as

$$L_{fm} = \frac{V_{LVdc}}{6 f_{sw} \Delta I_{L(max)}}. \tag{5.18}$$

$$L'_{fm} = \frac{\frac{1}{k_a} + 1}{C_{fm} \omega_{sw}^2}. \tag{5.19}$$

In (5.18) and (5.19), V_{LVdc} is the LVdc voltage, $\Delta I_{L(max)}$ is the maximum current ripple, f_{sw} is the switching frequency and k_a is the desired attenuation.

A damping resistor is connected in series with the filter capacitor to attenuate the ripple due to switching frequency. This avoids resonance and provides stable performance. The resistor value is taken as one third of the value of the filter capacitor impedance at resonant frequency (ω_{res}). Therefore,

$$R_{fm} = \frac{1}{3 \omega_{res} C_{fm}}. \tag{5.20}$$

The closed loop control diagram is shown in Fig. 5.12. The transfer function of the DG converter is given by

$$G_{DG\_conv}(s) = G_h^{DG} G_d^{DG}(s) H_{LCL}(s) \tag{5.21}$$

where G_h^{DG} is the controller transfer function, $G_d^{DG}(s)$ is the transfer function for the digital delay, and $H_{LCL}(s)$ is the transfer function of the *LCL* filter. This is expressed as follows [168].

$$H_{LCL} = \frac{i_{DG}(s)}{v_{id}(s)} = \frac{sm + 1}{s^3 n + s^2 o + sp + 1} \tag{5.22}$$

where $m = \{R_{fm} C_{fm}\}, n = \{L_{fm} L'_{fm} C_{fm}\}, o = \{R_{fm} C_{fm} (L_{fm} + L'_{fm})\}, p = \{L_{fm} + L'_{fm}\}$.

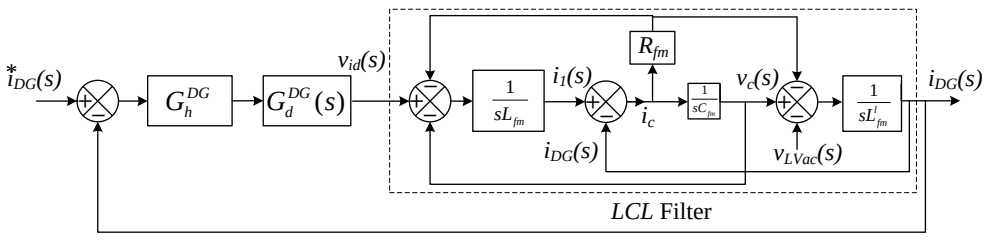

Fig. 5.12 Control diagram for DG converter.

The Bode plot for $G_{DG\_conv}(s)$ with and without the damping resistor is shown in Fig. 5.13. It is seen that the damping resistor helps to avoid the resonance at 2 kHz. Moreover, the damped system is stable with gain margin of 28.5 db at 2.19 kHz and a phase margin of 90° at 28.3 Hz.

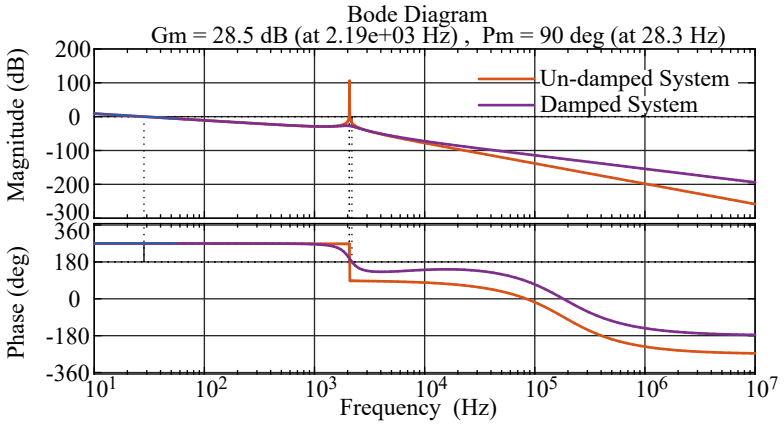

Fig. 5.13 Bode plot for DG converter.

5.4 Simulation Results

The ST based meshed hybrid microgrid is simulated in PSCAD and the impact of EV charging transients on the grid stability is explored. The ST exchanges power from the MVac and comprises of the ST MV converter, ST isolated dc-dc converter and the ST LV converter. On the LV side the meshed hybrid microgrid is interfaced. A BESS system, PV system and EV are interfaced to the ST LVdc bus. The PV system consists of a DG converter which injects the power to the LVac grid. The simulation parameters are given in Table 5.1.

Table 5.1 Simulation Parameters

System Quantities	Values
LV grid voltage	0.4 kV (L-L)
ST LV converter	Rating = 50 kVA, V_{LVdc} = 1 kV, L_f = 2 mH, R_f = 2 Ω, C_f = 100 μF
DG converter	S_{rated} = 15 kVA, L_{fm} = 5 mH, L'_{fm} = 200 μH, C_{fm} = 30 μF, R_{fm} = 1 Ω
PV dc-dc converters	Rating = 15 kW, f_s = 10 kHz, L = 1 mH, C = 1100 μF, K_{pPVd} = 0.02, K_{iPVd} = 17.74
BESS converter	Rating = 80 kW, f_s = 10 kHz, L = 0.5 mH, C = 333 μF, K_{pd} = 0.0001 , K_{id} = 0.062

Fig. 5.14(a)-(h) shows the power drawn from MVac grid, LVdc voltage, LVac voltage, LVac load current, DG converter current, EV load power, BESS power and the power

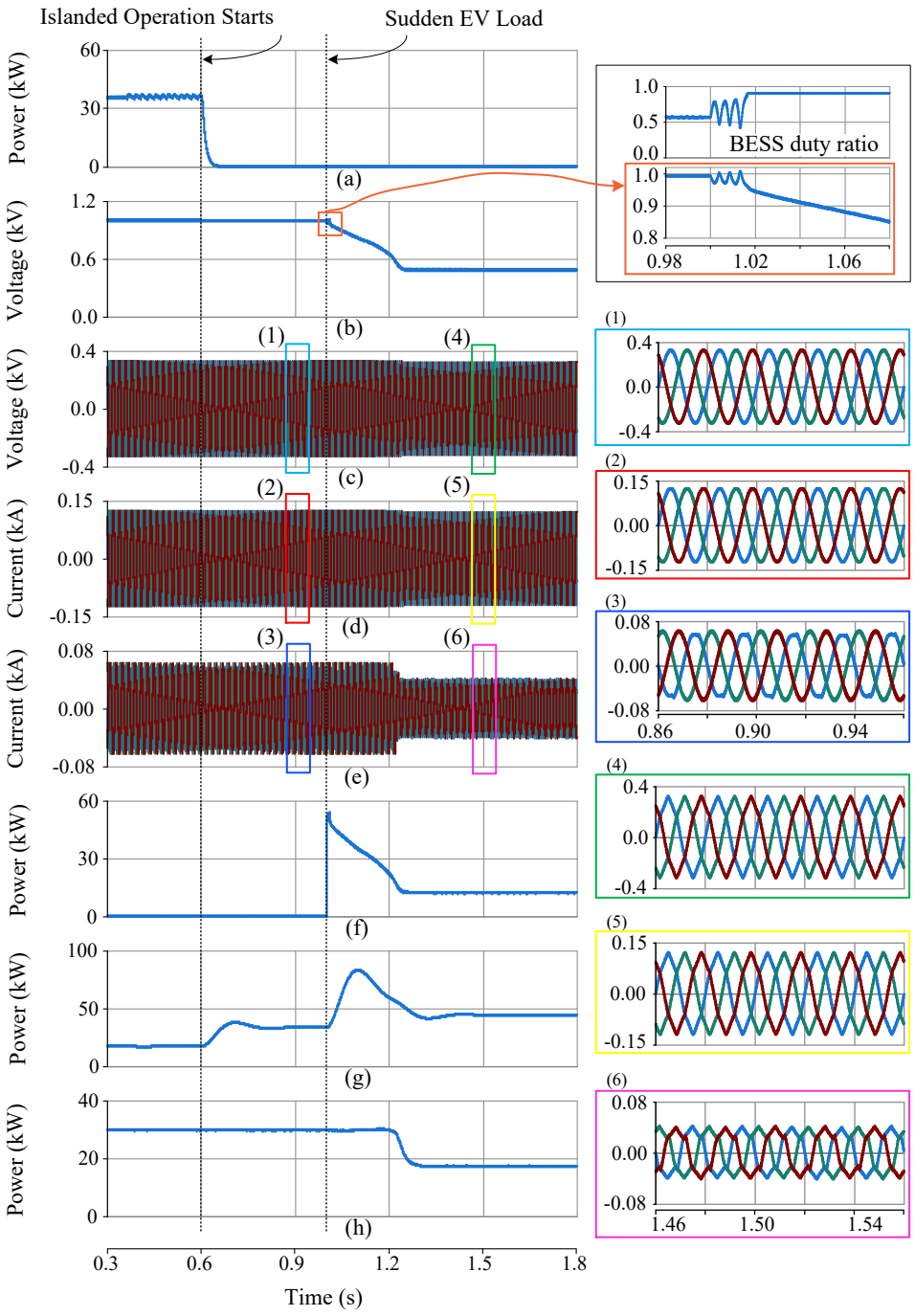

Fig. 5.14 Simulation of the sudden transient arising from EV. (a) Power drawn from MVac grid. (b) LVdc voltage. (c) LVac voltage. (d) LVac load current. (e) DG converter current. (f) EV load power. (g) BESS power. (h) Power injected by DG converter.

injected by DG converter, respectively. Initially, the system is operating in grid connected mode and all the converters of the ST are operational. The ST draws a power of 35 kW from the MVac grid. The BESS operates in CCM and injects a power of 15 kW. At t = 0.6 s, a fault is considered to occur on the MV grid and so the system is disconnected from the MV side. Consequently, the LV side islanded mode of operation starts. Therefore, the ST MV converter and the ST isolated dc-dc converter shut down and the

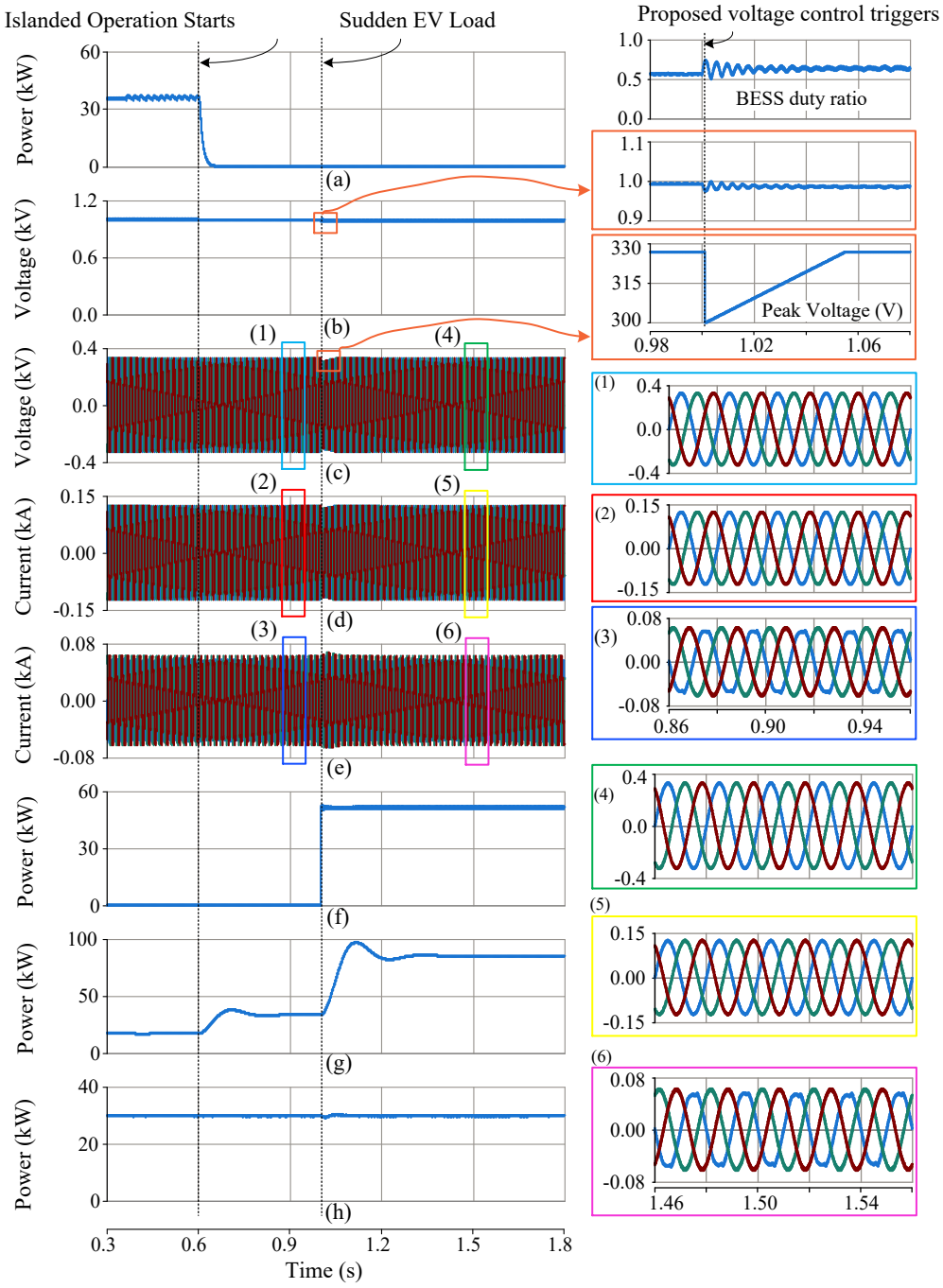

Fig. 5.15 Simulation of the sudden transient arising from EV with proposed control. (a) Power drawn from MVac grid. (b) LVdc voltage. (c) LVac voltage. (d) LVac load current. (e) DG converter current. (f) EV load power. (g) BESS power. (h) Power injected by DG converter.

MVac power becomes zero. At the same time, the BESS changes the mode of operation from CCM to VCM and starts maintaining the LVdc voltage. The power drawn from the BESS increases as it has to supply the additional power that was earlier drawn from the MVac grid. The LV side waveforms are undisturbed. At t = 1 s, a sudden EV load of 50 kW is connected to the LVdc line. It can be seen that the LVdc voltage starts oscillating and eventually the BESS converter losses stability. This is because the BESS

duty ratio also oscillates and touches the upper limit of the duty ratio range. This is as per the explanation given in Section 4.2. As the LVdc voltage reduces, the LVac voltage also gets distorted and the LVac load current is affected accordingly. As the LVac grid is not properly maintained, the power injected by the DG converter also goes down as its operation is based on the LVac voltage. Therefore, the entire microgrid becomes unstable.

Fig. 5.15 shows the simulation results with the proposed control strategy for the similar scenario as discussed above. Once the LVdc voltage goes below 0.975 p.u., it can be observed that the proposed control reduces the LVac voltage to 0.9 p.u. This enables the controller to maintain the LVdc voltage. The LVac voltage is again gradually increased back to the nominal value. The zoomed in waveform for the duty ratio of the BESS converter, LVdc voltage and peak of LVac voltage during the transition is also shown. When the LVdc voltage goes below 975 V, the proposed control mechanism reduces the reference LVac voltage to 210 V and then gradually increases it with a total rise time which is higher than t_{rise}^{min}, expressed in (5.9). This controlling action initially reduces the effective load on the LVac side when the voltages reduces. Again, when the voltage gradually increases, the BESS converter sees a ramp increase of load instead of a step increase. The duty ratio obtained from closed loop control of BESS does not oscillate and settles to a fixed value which helps to maintain the system stability. Therefore, the proposed scheme ensures a smooth transition to include the step increase in LVdc load arising from EV which would otherwise have resulted in system failure. The zoomed waveforms of the LVac voltage, LVac load current and the DG converter current show that these are properly maintained even after the EV load is added. Therefore, the proposed control scheme is able to ensure that the stability of the system is maintained.

The proposed method to addressed issue of RHPZ is compared with the methods already existing in the literature. The comparison is given in Table 5.2.

5.5 Experimental Results

The complete block diagram and photographs of the experimental setup are shown in Fig. 5.16. The system consists of the ST, BESS, DG converter and EV load at the LVdc bus. The ac loads are connected to the LVac bus. The hardware parameters of the

Table 5.2 Comparison of Proposed Method with Studies Available in the Literature

Reference	Contribution	Remark
[151]	Converter is operated in discontinuous conduction mode for RHPZ elimination.	High current stresses in the switches leads to decreased efficiency.
[152]	Uses output filter and magnetic coupling between inductors for RHPZ elimination.	Coupling inductor increases input current ripples and current stress on the converter.
[154], [155]	Tri-state boost converter topology is proposed	Extra switch and diode is added to the circuit which adds to the cost, losses and control complexity.
[153]	Magnetic coupling between inductors for RHPZ elimination. Issue of input current ripple is solved with integrated three-winding couple inductor.	Leakage inductance leads to magnetic loss, voltage/current stress on converter and electromagnetic interference issues.
[156]	RHPZ is eliminated with diode-capacitor-based step up dc-dc converter with RC damping network.	Uses additional circuit components, complicates the circuit
[150]	Forward path for energy transfer during ON period is provided through magnetic coupling.	Uses additional circuit components, complicates the circuit
Proposed Work	RHPZ is addressed by adjusting system parameters utilizing meshed hybrid configuration.	Circuit structure is not changed, no additional components used, exploits features of ST.

experimental setup are given in Table 5.3.

Table 5.3 Hardware Parameters

System Quantities	Values
LV grid voltage	80 V (L-L)
ST LV converter	Rating = 1 kVA, V_{LVdc} = 200 V, L_f = 20 mH, R_f = 0.5 Ω, C_f = 10 μF
DG converter	S_{rated} = 1 kVA, L_{fm} = 6 mH, L'_{fm} = 68 μH, C_{fm} = 10 μF, R_{fm} = 1 Ω
BESS dc-dc converter	Rating = 500 W, f_s = 20 kHz, L = 13 mH, C = 10 μF

Firstly, the system is operated in the conventional way to observe the issue arising from the transient of EV charging load. The experimental results are given in Fig. 5.17. The LVdc and LVac voltages are shown in Fig. 5.17(a) and (b), respectively. Initially, the BESS maintains the LVdc voltage at 200 V and the ST LV converter maintains the LVac voltage at 80 V line-to-line. Fig. 5.17(c) and (d) shows the LVac load currents and DG converter currents, respectively. The LVac load is initially 150 W and the DG converter is supplying 130 W. Fig. 5.17(e) and (f) shows the EV load current and BESS battery current, respectively. When the EV load of 180 W is suddenly turned ON, the LVdc voltage starts to decrease. The BESS current keeps increasing to support the load but eventually the controller is not able to keep up with the sudden load increase, and the BESS converter loses its stability. This triggers the protection circuit of the BESS

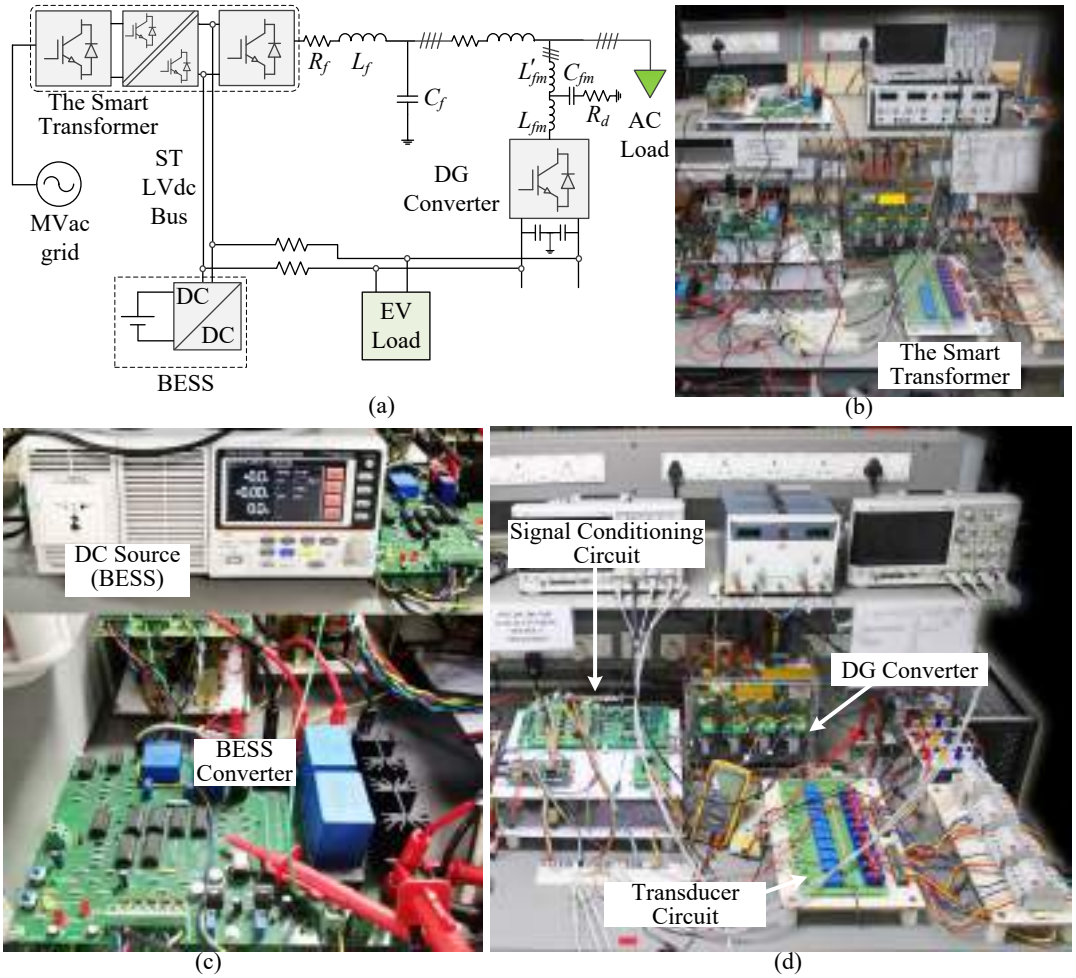

Fig. 5.16 Experimental setup. (a) Block diagram. (b) ST. (c) BESS converter. (d) DG converter.

converter and its switches are turned OFF. With the switches turned OFF permanently, the converter is unable to boost the voltage and the input voltage of 96 V from the BESS dc source is seen at the output. As a consequence, the ST LV converter is no longer able to maintain the voltage at the LVac side. This is seen in the zoomed waveforms. Similarly the LVac load current and the DG converter currents also get distorted.

Fig. 5.18 shows the waveforms during the same transient with the proposed LVac voltage control scheme. When the EV load of 180 W is turned on, the LVdc voltage starts to decrease. This is detected by the control algorithm and LVac voltage is reduced using the ST LV converter once the LVdc voltage goes below 190 V. This reduces the LVac load current and thus the overall load power reduces. This assists the BESS controller to rebuild the LVdc voltage back to the nominal value. The LVac voltage is again gradually returned back to the nominal value. Subsequently the LVac load currents increase to their initial values. To support the higher load, the BESS now supplies 3.5 A current.

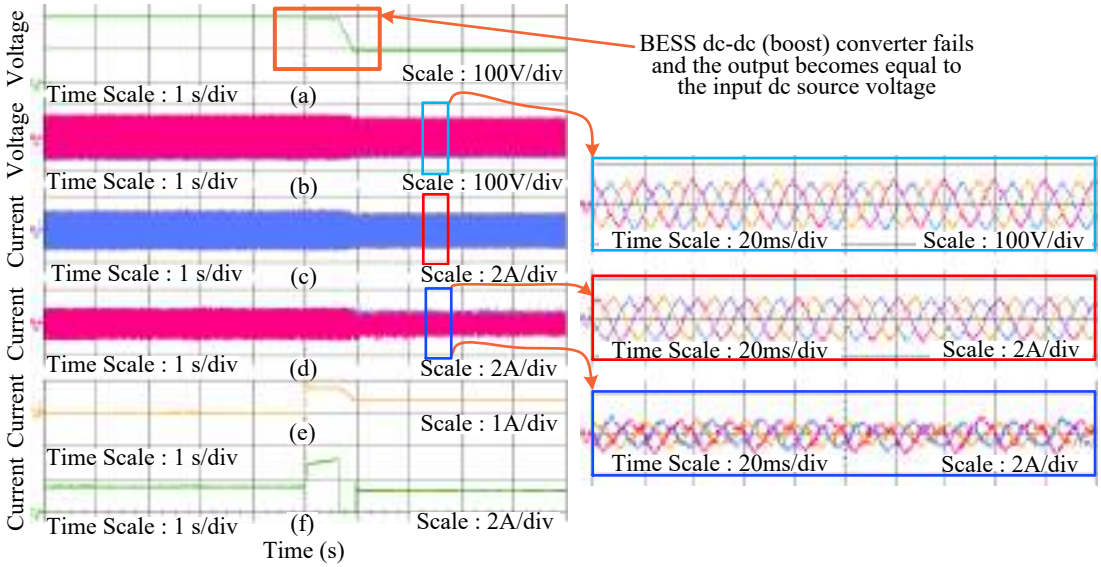

Fig. 5.17 Experimental waveforms during connection of EV charging load in conventional manner. (a) LVdc voltage. (b) LVac voltage. (c) LVac load current. (d) DG converter current. (e) LVdc load current. (f) BESS battery current.

Thus, the load increase transient is smoothened and the system shifts to the higher load without losing stability.

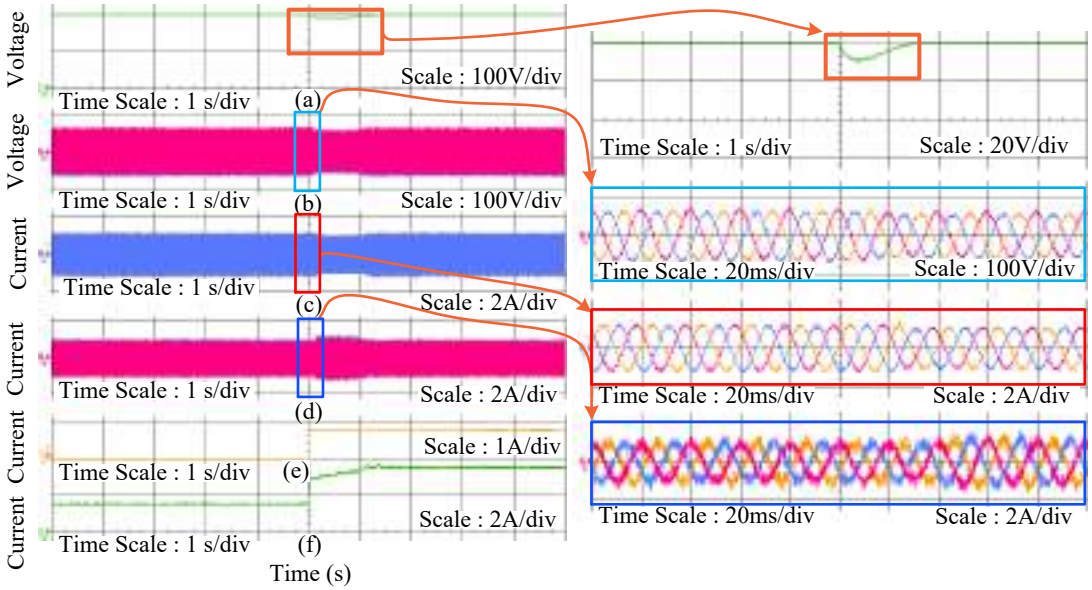

Fig. 5.18 Experimental waveforms during step EV charging load with proposed control. (a) LVdc voltage. (b) LVac voltage. (c) LVac load current. (d) DG converter current. (e) LVdc load current. (f) BESS battery current.

5.6 Summary

A method is proposed for stabilizing the ST based islanded meshed hybrid microgrid during transients occurring from EV charging transients. The ST is used to maintain the system stability by controlling the LVac voltage when the LVdc voltage goes down. This is possible as the ST forms the meshed configuration, interlinking the LVac and LVdc grids. The LVac voltage is reduced to 0.9 p.u. and gradually increased as per the limiting rate of duty ratio change. This reflects as a corresponding change in overall load of the system and helps to compensate the slower response time that a BESS converter has owing to right half zero. The controllers of the system are appropriately designed for stable operation. Initially, the system is tested with sudden EV charging transient and the loss of stability is observed. Finally, the proposed scheme for stabilizing the system during transients is implemented and the effectiveness verified through simulation and experimental results.

CHAPTER 6

PARTIAL START-UP SCHEME FOR SMART TRANSFORMER IN MESHED HYBRID ISLANDED GRID OPERATION

Chapters 4 and 5 have discussed the islanded operation of the ST based meshed hybrid microgrid. In such a case, the ST LV converter is operational while its MV converter as well as the isolated dc-dc converter are shut down. This chapter presents a step by step start-up method for these two converters of the ST to establish reconnection of the meshed hybrid LV microgrid to the MVac grid, while keeping the ST LV converter functional, such that the operation of the LV microgrid is not disturbed.

In [72], the islanded operation of ST and BESS is proposed for a zonal microgrid. However, these studies do not discuss the islanding and reclosure strategies that need to be adopted for proper transition between the islanded and grid connected modes. One of the major challenges encountered in such cases is the re-closure mechanism. Operating the LV side in islanded mode requires the ST LV converter to be operational. Moreover, the other two converters of the ST - the ST MV converter and ST isolated dc-dc converter, are turned OFF. To establish reconnection to the grid, these two converters need to be turned ON. Such power electronic converters in practice generally have bleeder resistors across the capacitor terminals to ensure that the residual capacitor voltage is discharged. This ensures safety to personnel and equipment. Therefore, turning ON such converters initially involves charging the MVdc capacitor. However, a sudden turn ON can lead to huge inrush of capacitor charging currents, leading to the breakdown of the power electronic switches.

There are several methods available in the literature for starting procedures of the ST. Most of the methods have shown starting up of the ST converters one by one in stages building up the dc link voltages while keeping the inrush current below a limit to prevent damage to the equipment. A controlled start-up of both the ST MV converter and the ST isolated dc-dc converter is done simultaneously in [169] to minimize the ST isolation

transformer inrush current. In [170], ST starting procedures are discussed for both the directions i.e. starting from MVac side to LVac side and from LVac side to MVac side. A method of reducing heavy inrush currents by charging the LVdc link from a dc source connected to the LVdc link of the ST is proposed in [171]. In the next stage, the MVdc link is charged from the LVdc link. In [172], a DAB control with long dead time is proposed to reduce inrush currents while starting the ST, and [173] proposes a novel soft start procedure where the cascaded H-bridge works as a passive rectifier and the dc-dc stage builds up the dc link voltages. However, these researches discuss the starting of the ST by charging both the dc link voltages first, and then using the ST converters for power transfer between the MVac and LVac sides.

In an ST-based LV side meshed islanded operation, the ST LVdc bus is already charged and the ST LV converter is operational, transferring power to the LVac side from the LVdc bus. Therefore, in such a scenario, a partial start-up scheme for ST is necessary which starts the ST MV converter and the ST isolated dc-dc converter without disturbing the operation of the ST LV converter during the process of reconnection to main grid. Such partial start-up will also be required when there is a fault in either ST MV converter, ST isolated dc-dc converter or MVac grid. The proposed start-up process ensures that the initial capacitor charging currents are controlled.

The proposed method involves charging the MVdc bus to 85% of the nominal value from the LVdc bus which is already energized. Next, the ST MV converter is energized to build the MVdc voltage to the nominal value. Once that is established, the power flow from the MVac grid to the LVac grid is started and the transition from islanded to grid connected mode of the meshed hybrid microgrid is established. To realize the entire starting process, a centralized controller is proposed. This controller gives the ON/OFF commands to the various converters and circuit breakers in the system as per the proposed partial start-up algorithm. Stability studies of the ST isolated dc-dc converter are carried out to ensure that the system maintains stability during the starting process. Simulation studies and experimental validation have been performed to verify the proposed starting scheme.

6.1 Description of the ST-Based Meshed Hybrid Microgrid

An ST-based hybrid distribution grid as shown in Fig. 6.1 is considered. The power exchange between the MVac and LVac sides take place through the ST MV converter, ST isolated dc-dc converter and ST LV converter. A BESS is interfaced to the ST LVdc link. In the grid connected mode, the BESS charges or discharges, working in CCM. Moreover, the ST isolated dc-dc converter maintains the LVdc grid voltage and the ST LV converter maintains the LVac grid voltage.

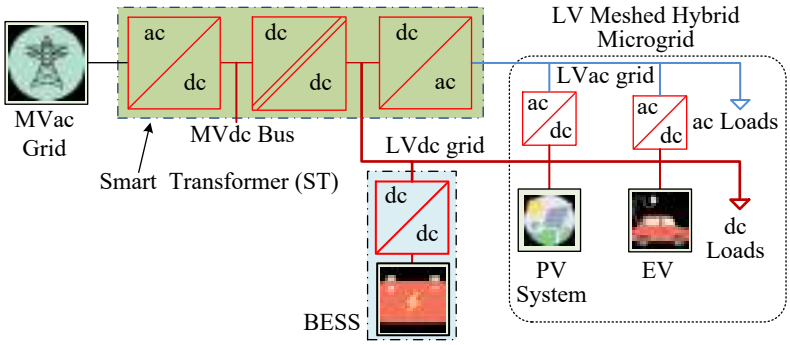

Fig. 6.1 An ST interfacing an LV meshed hybrid distribution grid to the MVac grid.

In case of islanded operation, the ST MV and ST isolated dc-dc converters are not operational and thus the BESS maintains the ST LVdc bus voltage. This also ensures that the ST LV converter maintains the LVac bus voltage in the islanded mode of operation.

6.2 Proposed Partial ST Start-up Scheme

The system operates in islanded mode by turning OFF the ST isolated dc-dc converter, and simultaneously changing the mode of operation of the BESS from CCM to VCM to maintain the LVdc voltage. Afterwards, the ST MV converter is also turned OFF. The start-up scheme allows reconnection of the LV meshed hybrid grid to the MVac side through the ST. In the start-up process, both the MVdc and LVdc buses are controlled by different converters one after the other. Thus, the proposed scheme also ensures that there is no overlap of control throughout the starting process. The start-up is done in three stages. In Stage I, the ST isolated dc-dc converter operates. In Stage II the ST MV converter operates while the ST isolated dc-dc converter is turned OFF. In Stage III, the reconnection to MVac grid is established. Detailed explanation for each stage is given as follows.

Stage I - Initial Charging of MVdc Bus through DAB

In the first stage, the MVdc bus is charged to 85% of the nominal MVdc voltage, V_{MVdc}^{nom}. This is accomplished with the ST isolated dc-dc converter. This is a DAB converter whose circuit diagram is shown in Fig. 6.2. In a DAB converter, power flow takes place because of the phase difference between the MVdc and LVdc side voltages. 85% is chosen so that majority of the charging is done by the BESS through the DAB in open loop and a margin of over 10% V_{MVdc}^{nom} is reserved for the next stage. The ideal power transfer equation for the DAB converter from the MVdc to the LVdc side is given by [174]:

$$P_{DAB} = \frac{n\delta(1-\delta)V_{MVdc}V_{LVdc}}{2f_{DAB\_sw}L_r} \tag{6.1}$$

where V_{MVdc} is the MVdc voltage, V_{LVdc} is the LVdc voltage, δ is the firing angle delay between the primary and secondary sides of the isolated dc-dc converter, n is the isolation transformer turns ratio, L_r is its leakage inductance and f_{DAB_sw} is the switching frequency of the DAB converter.

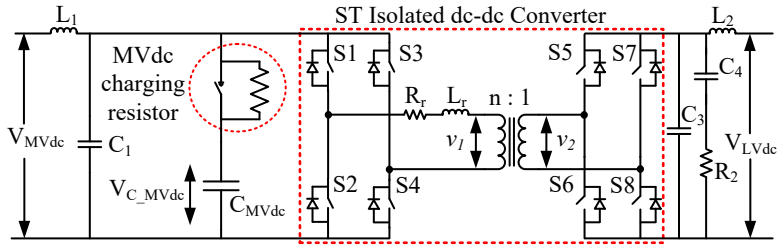

Fig. 6.2 The ST isolated dc-dc converter with MVdc charging resistor.

From (6.1), it can be observed that a negative phase shift (δ) will result in a negative power flow, meaning flow of power from the LVdc to MVdc side. However, the ST MV converter and ST isolated dc-dc converter are not operating initially and thus MVdc link voltage is zero. Therefore, (6.1) is not valid for the power flow occurring at the time of starting. Once the switching pulses to the DAB are turned ON, a square wave voltage (v_2) builds up across the secondary winding of the isolation transformer from the LVdc bus as shown in Fig. 6.2. In the ideal condition with no resistive drops, this is a square wave voltage with upper and lower limits V_{LVdc} and $-V_{LVdc}$, respectively. This voltage induces a square wave voltage (v_1) across the primary terminals of the isolation transformer. The switching of the MVdc side H-bridge further results in a steady voltage (v_{1_max}) to appear at the MVdc bus. A zero phase shift between the primary and secondary bridges should have resulted in zero voltage drop across the

leakage inductor and thus zero current. However, as soon as v_{1_max} appears at the MVdc bus, the uncharged MVdc capacitor acts as short circuit. In this case, it draws a high current from the LVdc bus. This power flow is not governed by (6.1) as it is independent of δ. Therefore, to limit this initial charging current, a charging resistor is connected in series with the MVdc capacitor for the voltage build-up, as shown in Fig. 6.2. Once the desired voltage is reached, the series resistor is disconnected. If P_{DAB}^{max} is the maximum load capacity of the DAB, then the value of charging resistor to charge the MVdc capacitor with rated load capacity of the DAB converter is given by:

$$R_{MVdc}^{charge} = \frac{(n * V_{LVdc})^2}{P_{DAB}^{max}}. \tag{6.2}$$

In (6.2), the value of n is chosen such that $n * V_{LVdc}$ is equal to V_{MVdc}^{nom}. When the MVdc voltage rises to 85% of the nominal voltage, the switching pulses to the DAB are turned OFF and the charging resistor is removed.

During the capacitor charging period, V_{C_MVdc} is governed by the capacitor charging expression and is given by:

$$V_{C\_MVdc} = V_{MVdc}\left\{1 - e^{\left(-\frac{t}{R_{MVdc}^{charge} \times C_{MVdc}}\right)}\right\} \tag{6.3}$$

where t is the time duration and C_{MVdc} is the capacitance of the MVdc capacitor.

Now, V_{C_MVdc} has to become 0.85 times V_{MVdc}^{nom}. Thus, from (6.3), we get

$$1 - e^{\left(-\frac{t}{R_{MVdc}^{charge} \times C_{MVdc}}\right)} = 0.85. \tag{6.4}$$

Further, (6.4) can be reduced to:

$$t = 1.897 \times R_{MVdc}^{charge} \times C_{MVdc}. \tag{6.5}$$

Thus, the minimum value of R_{MVdc}^{charge} is determined by (6.2). Moreover, (6.5) is used to

calculate the time required to charge the MVdc capacitor.

$$G_{oi} = \frac{\hat{v}_{LVdc}(s)}{\hat{v}_{MVdc}(s)} = \frac{rR_0 + srL_2}{\left(sC_3 + \frac{1}{R_0+sL_2} - \frac{1}{R_2+sR_2^2C_4} + \frac{1}{R_2} - zn\right)\left(\frac{1}{R_{MVdc}^{charge}+s(R_{MVdc}^{charge})^2C_{MVdc}} - sC_1 - q - \frac{1}{R_{MVdc}^{charge}}\right) - yn} \tag{6.6}$$

$$G_{od} = \frac{\hat{v}_{LVdc}(s)}{\hat{d}(s)} = \frac{R_0 + sL_2}{\left(\frac{p}{rR_2+srR_2^2C_4} - \frac{p}{rR_0+srL_2} - \frac{spC_3}{r} + \frac{pz}{r} - xn - \frac{p}{rR_2}\right)} \tag{6.7}$$

where, p, q, r x, y, z are given by the following expressions

$$p = \frac{2nV_{c3}}{R_r} - \frac{4e^{-\frac{R_r}{L_r}(1-\delta)T}}{R_r\left(e^{\frac{R_r}{L_r}T}+1\right)}.nV_{c3}, q = \frac{1}{R_r} + \frac{1}{T}.\frac{L_r}{R_r}.\frac{2\left(e^{-\frac{R_r}{L_r}T}-1\right)}{R_r\left(e^{-\frac{R_r}{L_r}T}+1\right)} \tag{6.8}$$

$$r = n.\frac{2\delta-1}{R_r} + n.\frac{1}{T}.\frac{L_r}{R_r}.\frac{2\left[e^{-\frac{R_r}{L_r}T} - 2e^{-\frac{R_r}{L_r}(1-\delta)T} + 1\right]}{R_r\left(e^{-\frac{R_r}{L_r}T}+1\right)}, x = \frac{-2V_{c1}}{R_r} + \frac{4e^{-\frac{R_r}{L_r}\delta T}}{R_r\left(e^{-\frac{R_r}{L_r}T}+1\right)}.V_{c1} \tag{6.9}$$

$$y = \frac{1-2\delta}{R_r} + \frac{1}{T}.\frac{L_r}{R_r}.\frac{2\left(e^{-\frac{R_r}{L_r}T} - 2e^{-\frac{R_r}{L_r}\delta T} + 1\right)}{R_r\left(e^{-\frac{R_r}{L_r}T}+1\right)}, z = n\left[-\frac{1}{R_r} + \frac{1}{T}.\frac{L_r}{R_r}.\frac{2\left(1-e^{-\frac{R_r}{L_r}T}\right)}{R_r\left(1+e^{-\frac{R_r}{L_r}T}\right)}\right] \tag{6.10}$$

There are schemes in the literature where the MVdc voltage is built-up with a charging resistor by drawing power from the MVac grid through the reverse diodes of the ST MV converter [170], [175]. This process of passive charging increases the MVdc capacitor voltage upto the peak of MVac voltage. In such a method, the power electronic switches cannot control the charging process upto the peak of MVac grid voltage. In the proposed method, charging starts only when the ST isolated dc-dc converter receives the firing signals. This is possible because the LVdc bus is already energized in meshed hybrid islanded operation of LV side. Thus, this method ensures continuous control on MVdc charging unlike the case for initial charging through ST MV converter.

Stage II - Final Charging of MVdc Bus Through ST MV Converter

In the second stage the ST MV converter is turned ON to charge the MVdc bus upto its nominal voltage. Stage I charges the MVdc bus to a value higher than the peak of MVac voltage. Thus, the reverse diodes of the ST MV converter do not conduct and passive charging does not occur through the ST MV converter in Stage II. The power flow only starts when firing pulses are given to the converter. A control loop is implemented to compensate the converter losses. This ensures that the power drawn from the MVac side charges the MVdc bus upto V_{MVdc}^{nom}. During this stage, the ST isolated dc-dc converter is not operational and thus the power drawn by the ST MV converter is only to charge the ST MVdc bus.

Stage III - Changeover of LVdc Control

In the third stage, the mode of operation of the BESS dc-dc converter is changed from VCM to CCM. Simultaneously, the ST isolated dc-dc converter is again turned ON by providing switching pulses to maintain the LVdc voltage. At this stage, the BESS power injection is limited to a fixed value and thus the excess power requirement of the LV side is drawn from the MVac side through the ST MV and ST isolated dc-dc converters. Thus, the system starts operating in grid connected mode. The entire flowchart of operation is shown in Fig. 6.3.

6.3 Stability Analysis for DAB Converter

In the proposed partial start-up process of the ST, the DAB converter plays a major role as the initial charging of the MVdc capacitor is done by this converter. Thus, it is important to ensure that this converter does not lose stability. The small signal average value modelling of DAB converter proposed in [176] is used to model the DAB converter. For the initial start-up process in stage I, the control variable is zero. The effective output resistance of the converter is considered as R_0 for the analysis. T is the time period of the switching pulse. Based on these, the input to output voltage transfer function is derived while considering the presence of the charging resistor in the circuit. This resistor is denoted as R_{MVdc}^{charge} and is expressed by (6.6). The Bode plot for (6.6) is

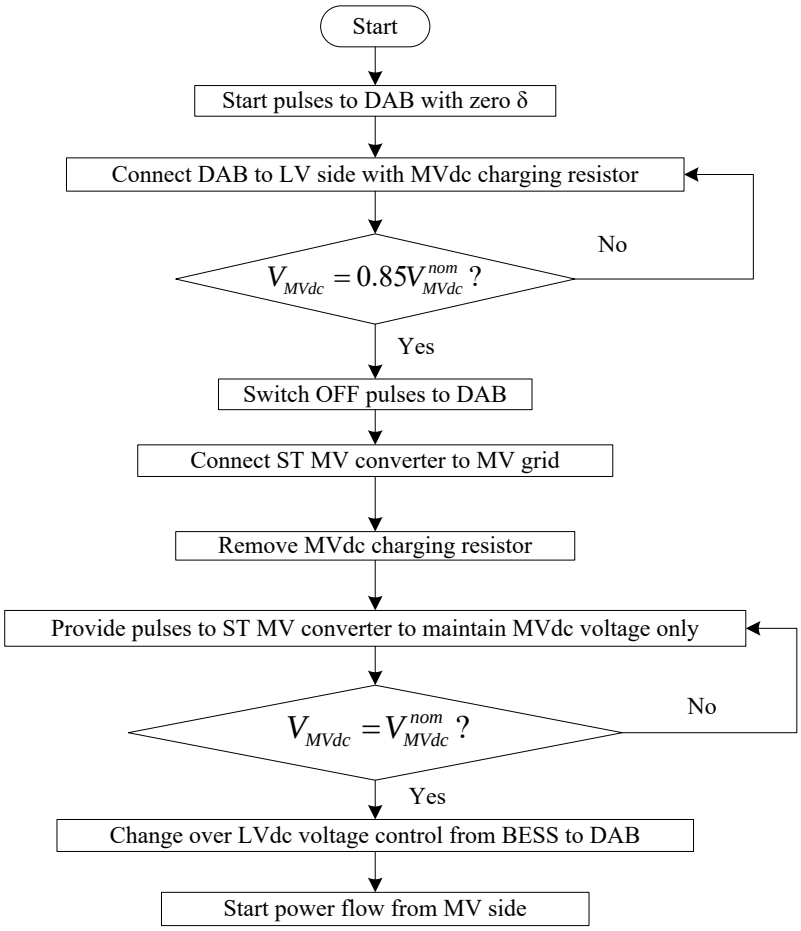

Fig. 6.3 Flowchart of partial starting operation.

given in Fig. 6.4. It is seen that the open loop system is stable with infinite gain margin and a phase margin of 52.2°.

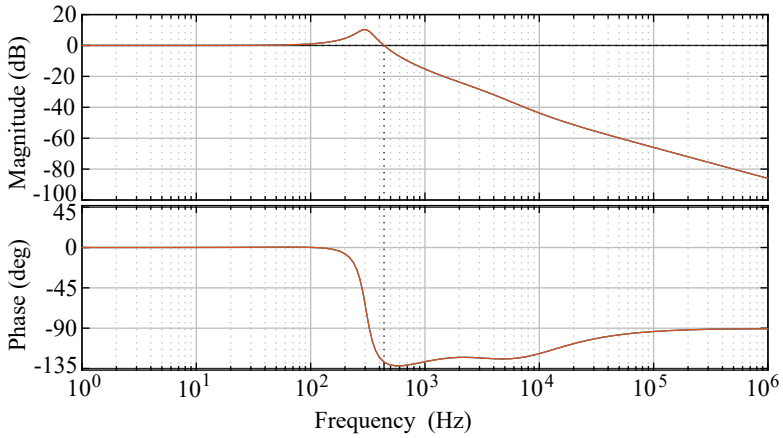

Fig. 6.4 Bode plot for input to output transfer function of the DAB converter.

The DAB converter is operated in closed loop to control the LVdc voltage in Stage III. This is done by controlling the delay angle, δ. The control-to-output transfer function is derived, and the final expression is given by (6.7) [176]. A PI controller is used as

a compensator for the system as shown in Fig. 6.5. The transfer function of the PI controller is given as follows

$$G_c(s) = K_{pd} + \frac{K_{id}}{s} \tag{6.11}$$

where K_{pd} is the proportional gain and K_{id} is the integral gain of the PI controller.

Therefore, the transfer function of the compensated system becomes

$$G(s) = G_c(s)G_{od}(s). \tag{6.12}$$

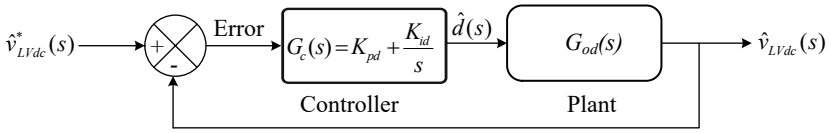

Fig. 6.5 Block diagram for the ST isolated dc-dc converter output voltage control.

The Bode plot for the uncompensated system is shown in Fig. 6.6. It is seen that the system has very small low frequency gain of about -30 db below 10 Hz. Thus, to compensate this, the PI controller is designed with the help of the loop shaping method [177] to have a phase margin of 55° at a gain crossover frequency of 2 Hz .

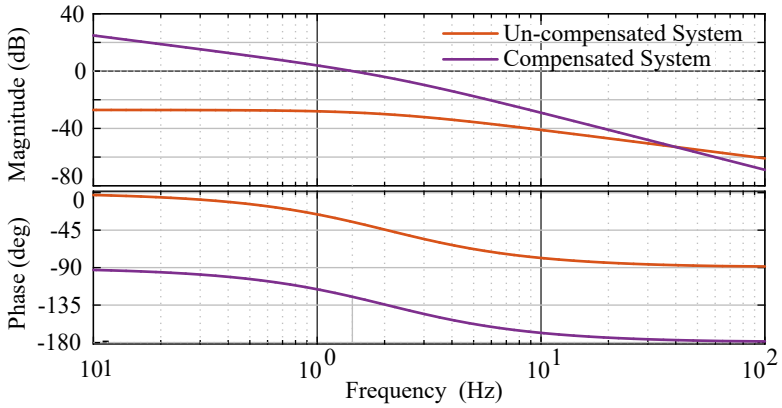

Fig. 6.6 Bode plot of control to output transfer function for both uncompensated and compensated of the DAB converter.

From the characteristic equation of the system $G(s)$, at gain cross over frequency, we get,

$$|G_c(s)G_{od}(s)| = 1, \angle G_c(s)G_{od}(s) = -180°. \tag{6.13}$$

From the Bode plot of G_{od}, the equations in (6.13) are used to calculate the values of

K_{pd} and K_{id}. Fig. 6.6 also shows the Bode plot for the compensated system. It is seen that the compensated system has infinite gain margin. Moreover, a phase margin of 57° at a gain crossover frequency of 1.38 Hz is obtained. This results in an improved stability of the system.

6.4 Control Strategies

The controlling action during the start-up of the ST is governed by a centralized controller. This controller receives the start-up command to turn ON or OFF the converters of the ST and the circuit breakers (CB). When the converters in the system get the signals from the start-up controller to operate, they perform their assigned tasks. The control mechanism for each of the controllers in the system are discussed as follows.

6.4.1 The Centralized Controller

The overall proposed starting mechanism is implemented with the centralized controller. This controller receives the start-up command and sends out seven different signals which are based on the real time value of V_{MVdc}. This is done as per the flowchart given in Fig. 6.3. The signals have a fixed value in the islanded mode. When the partial start-up scheme is initiated, the values of these signals change for each stage of operation. These are shown in Fig. 6.7. The seven output signals for this controller are as follows.

MVac CB - This is the signal for the MVac CB which connects the ST to the MVac grid. This value is “0” when the CB is OFF and “1” when it is ON.

ST LVdc CB - This is the signal for the ST LVdc CB. This breaker separates the operating part of the LV grid from the rest of the system during islanded mode of operation.

MVdc Charging Resistor CB - This is the signal for the MVdc charging resistor CB. The circuit is designed in such a manner that the MVdc resistor comes into the circuit only when this CB is OFF. A value of “0” will mean that the CB is OFF and “1” will mean that the CB is ON.

ST MV Converter ON/OFF - This is the signal which provides the switching pulses

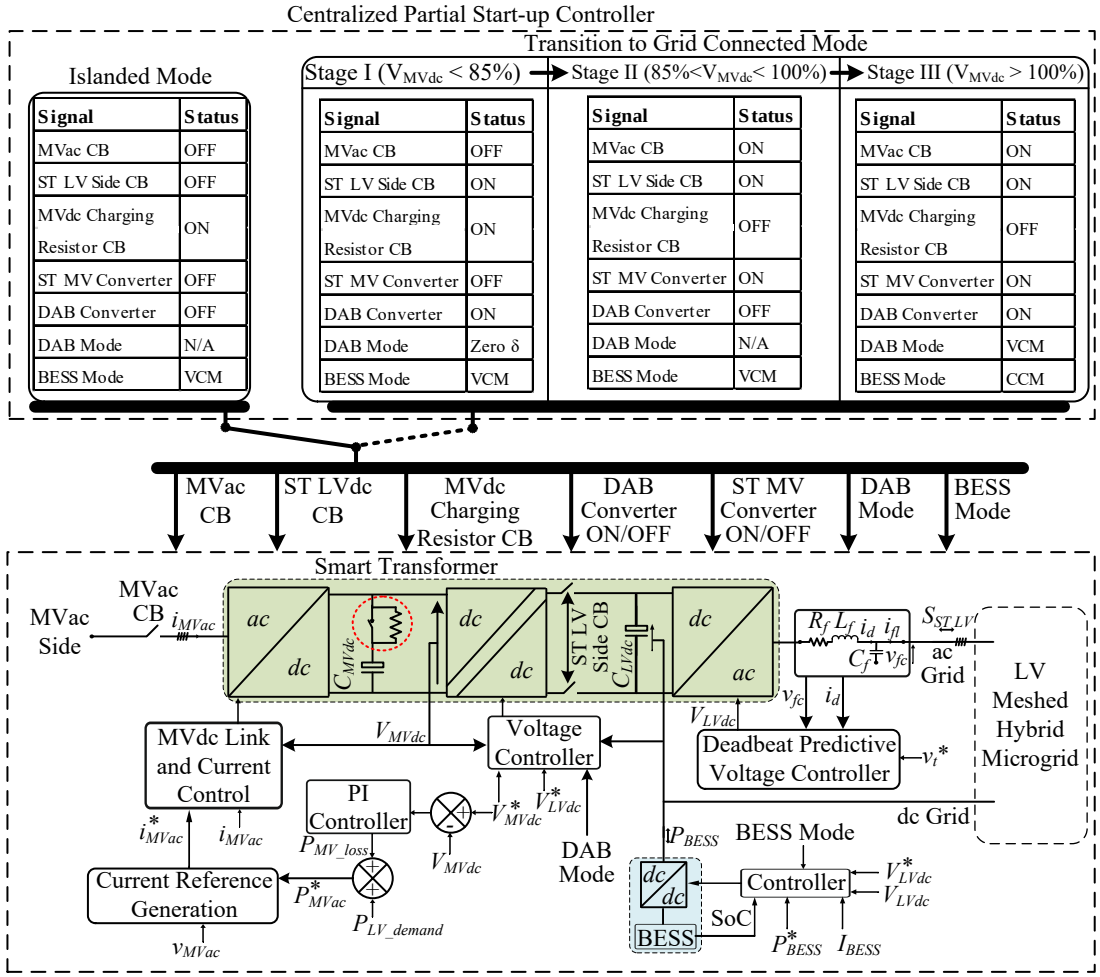

Fig. 6.7 Control diagram of the BESS integrated ST-based hybrid microgrid.

for the ST MV converter. A "0" value of this signal will mean that no pulses are given to the ST MV converter.

DAB Converter ON/OFF - This signal switches the DAB converter either ON or OFF. For a "0" value of this signal, no pulses will be given to the DAB converter. Moreover, the DAB converter will operate when this signal is "1".

DAB Mode - This signal determines the mode of operation of the DAB converter when it is ON. A "0" means open loop operation of DAB with zero angle δ and a value of "1" means closed loop operation for controlling the LVdc voltage.

BESS Mode - The BESS mode of operation is obtained from this signal. A "0" means CCM operation and "1" means VCM operation.

6.4.2 ST MV Converter

This converter exchanges power between the MVac and LV sides as per the demand or supply from the LV side. This power is denoted by P_{LV_demand}. In addition to that, it also draws the power from the MVac side to compensate the converter losses (P_{MV_Loss}). This maintains the MVdc bus voltage.

During the start-up process, the ST MV converter is used only to charge the MVdc bus. Therefore, the component P_{LV_demand} is not present in the reference power, P^*_{MVac}. Hence, P^*_{MVac} comprises of only P_{MV_loss}. Once reconnection is established to the MVac grid, P_{LV_demand} gets added to the total power reference of the ST MV converter. Based on P^*_{MVac}, the reference currents for the ST MV converter are calculated with the help of instantaneous symmetric component theory [178]. The complete control strategy for this converter is explained in Chapter 3, Section 3.3.1.

6.4.3 ST Isolated dc-dc Converter

This converter has two different modes of operation, one during the start-up process and the other mode is employed once the starting procedure is completed. During the start-up process, this converter is used to charge the MVdc capacitor upto 0.85 V^{nom}_{MVdc} by taking power from the ST LVdc link. The primary and secondary side bridges of this converter are given switching pulses with 50% duty ratio. As explained in Section 5.2, the value of the firing angle delay (δ) is zero during this mode of operation.

For transferring power from the MVdc to the LVdc side in the grid connected mode, this converter maintains the LVdc voltage. The reference LVdc voltage is compared with the actual LVdc voltage and the error is passed through a PI controller [100]. The PI controller design is explained in Section 5.3. The detailed control strategy for this converter is given in Chapter 2, Section 2.3.2.

6.4.4 SL LV Converter

This converter controls the voltage and frequency on the LVac side in both the islanded and grid connected modes. A reference voltage of 230 V per phase is maintained at a frequency of 50 Hz. The deadbeat control strategy is used to regulate the LVac voltage

[98]. This is explained in detail in Chapter 3, Section 3.3.3.

6.4.5 BESS dc-dc Converter

This converter works in CCM while operating in grid connected mode, and in VCM during islanded mode of operation. In the CCM, a current reference is obtained from the power reference which is compared with the actual output current of the converter, and the error signal is passed through a PI controller to generate switching pulses for the converter [141].

In the VCM, V^*_{LVdc} is considered as the output voltage reference of the converter. This is compared with the actual LVdc voltage. The error is passed through a PI controller and compared with a triangular signal to generate the switching pulses [141]. The BESS mode signal gives the information of whether the BESS needs to work in VCM or CCM and accordingly the corresponding reference and actual values are fed to the controller. The complete control strategy is explained in Chapter 4, Section 4.4.1.

A comparison of proposed method with ST start-up methods available in the literature is given in Table 6.1

Table 6.1 Comparison of Proposed Method with ST Start-up Methods Available in the Literature

Reference	Contribution	Remark
[169]	ST MV converter and the ST isolated dc-dc converter are started simultaneously to reduce transformer inrush currents.	Proposed method charges the LVdc link from the MV side. Scenario of already energized LVdc link is not considered.
[170]	ST starting procedures from MVac side to LVac side and from LVac side to MVac side are proposed	Scenario of already energized LVdc link is not considered.
[171]	LVdc and MVdc buses are charged from a dc source connected to LVdc bus	LV meshed grid and pre-operating ST LV converter is not considered
[172]	DAB control with long dead time is done to reduce inrush currents	Scenario of already energized LVdc link is not considered.
[173]	Cascaded H-bridge works as a passive rectifier and the dc-dc stage builds up the dc link voltages	LV meshed grid and pre-operating ST LV converter is not considered
Proposed Work	Partial start-up process builds up the MVdc voltage in stages until re-connection	ST LV converter operation and meshed LV grid is not disturbed.

6.5 Simulation Results

The proposed partial start-up scheme is simulated in PSCAD software. The ST based BESS enabled LV meshed hybrid microgrid is considered. The ST consists of the MV converter, isolated dc-dc converter and the LV converter. The ST LV side circuit breaker enables the disconnection of the ST LV converter from the other two converters of the ST - the MV converter and the isolated dc-dc converter. This enables the islanded operation. The simulation parameters are given in Table 6.2.

Table 6.2 Simulation Parameters

System Quantities	Values
MV grid voltage	11 kV (L-L)
LV grid voltage	0.4 kV (L-L)
ST MV converter	Power Rating = 1 MVA, L_{fm} = 100 mH, C_{fm} = 1 μF C_{MVdc} = 1350 μF
ST isolated dc-dc converter	Power Rating = 1 MW, f_s = 1 kHz, V_{MVdc} = 20 kV
ST LV converter	Power Rating = 1 MVA, V_{LVdc} = 1 kV, C_{LVdc} = 4700 μF, L_f = 1 mH, C_f = 20 μF
BESS dc-dc converter	Power Rating = 1.5 MW, f_s = 10 kHz, L = 1 mH, C = 100 μF

The various signals received from the centralized start-up controller are shown in Fig. 6.8. The MVdc charging resistor CB signal, DAB ON/OFF and ST MV converter ON/OFF signals are shown in Fig. 6.8(a)-(c), respectively. Fig. 6.8(d) and (e) show the signals for the modes of operation of the DAB and the BESS, respectively. Fig. 6.8(f) shows the MVdc voltage and Fig. 6.8(g) shows the LVdc voltage. Initially, the BESS is operating in VCM maintaining the LVdc voltage, and the ST MV and DAB converters are OFF. To replicate practical systems, bleeder resistors have been used to ensure that there is no residual voltage when the system is turned OFF. Therefore, before the start-up, the MVdc voltage is zero. At t = 0 s, the MVdc charging resistor is connected and the DAB converter gets the firing pulses with zero value of angle δ. This is seen in Fig 6.8(a) and (b). Next, at t = 0.5 s, the start-up process is initiated by closing the ST LVdc CB and providing pulses to the DAB converter. Consequently, the MVdc voltage starts building up across the MVdc capacitor. It can be seen that the LVdc voltage is maintained constant throughout the start-up process. There are small oscillations in the LVdc voltage during the transitions from Stage I to Stage II and from Stage II to Stage III, but these do not affect the operation of the system.

The system voltages and currents for the transition from Stage I to Stage II and Stage

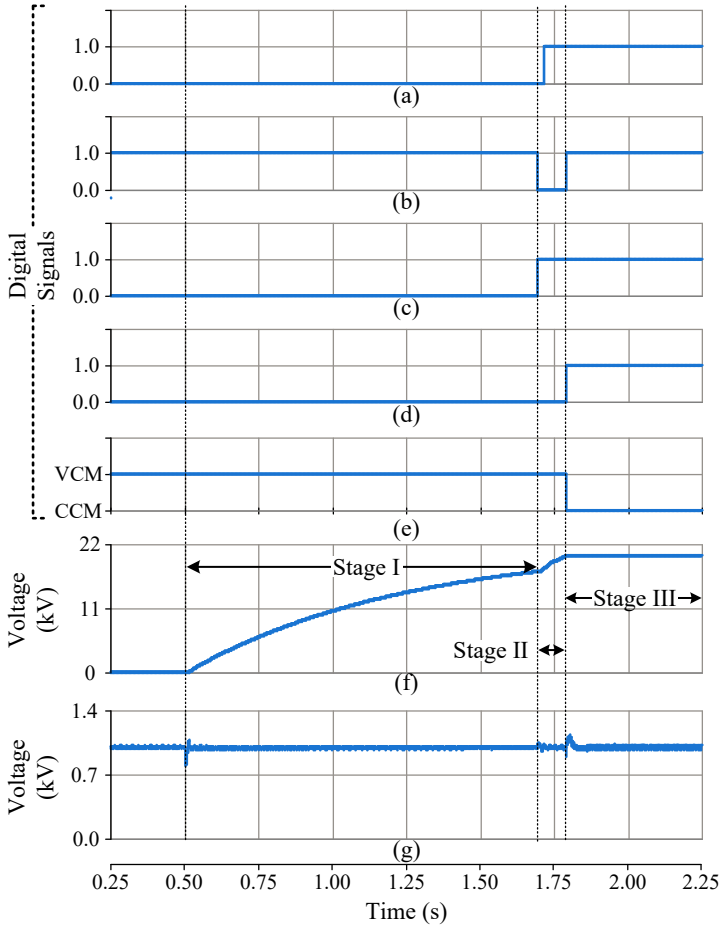

Fig. 6.8 Signals of centralized controller and ST dc voltages. (a) MVdc charging resistor CB signal. (b) DAB converter ON/OFF signal. (c) ST MV converter ON/OFF signal. (d) DAB mode signal. (e) BESS mode signal. (f) MVdc voltage (g) LVdc voltage

II to Stage III are shown in Fig. 6.9. Fig. 6.9(a)-(d) shows the MVac voltage, MVac current, LVac voltage and LVac current, respectively. The ST MV converter is connected to the MVac grid when the MVdc voltage reaches 85% of nominal MVdc voltage as shown in Fig. 6.9(e). The system draws MVac current first for fully charging the MVdc bus and then to supply power to the LV side. The LVac voltages and currents remain undisturbed during the transition. The corresponding LVdc voltage waveform is shown in Fig. 6.9(f).

The power flows in the system are shown in Fig. 6.10. The meshed hybrid microgrid draws a total power of 0.5 MW. A power of 0.4 MW is drawn by the LVac grid and 0.1 MW is drawn by the LVdc grid. This is shown in Fig. 6.10(a) and (b), respectively. These remain undisturbed during the transition from islanded to grid connected mode. Fig. 6.10(c) and (d) shows the power supplied by the BESS and the power delivered by the DAB, respectively. The MVdc capacitor starts charging by drawing power from

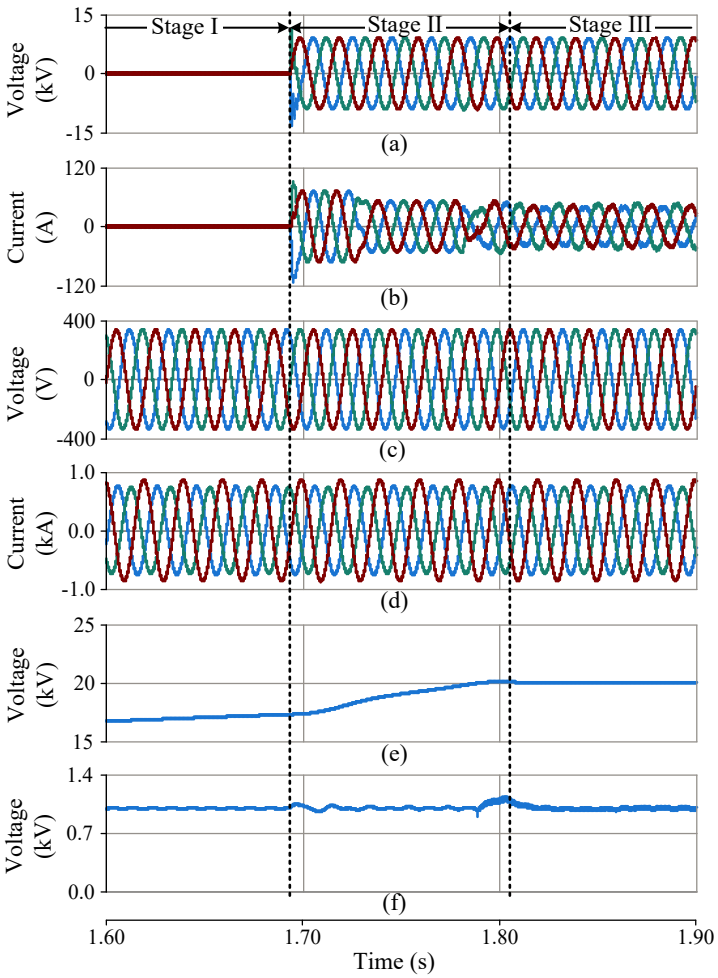

Fig. 6.9 Voltage and current waveforms for transition from Stage I to Stage II and Stage II to Stage III. (a) MVac voltage. (b) MVac current. (c) LVac voltage. (d) LVac current. (e) MVdc voltage. (f) LVdc voltage.

the BESS. This power is delivered through the DAB converter. As the power flows in the reverse direction through the DAB, there is a corresponding increase of DAB power in the negative direction. As the capacitor charging currents decays, there is a corresponding decrease in power flow. On reaching 85% of MVdc nominal value, the MVac converter starts drawing power from the MVac side. This can be seen in Fig. 6.10(e). With the completion of the starting process, all the powers settle down to steady-state values. In the grid connected mode, the BESS is used to limit the power drawn from the MVac side to 0.4 MW. This results in the BESS supplying a power of 0.1 MW.

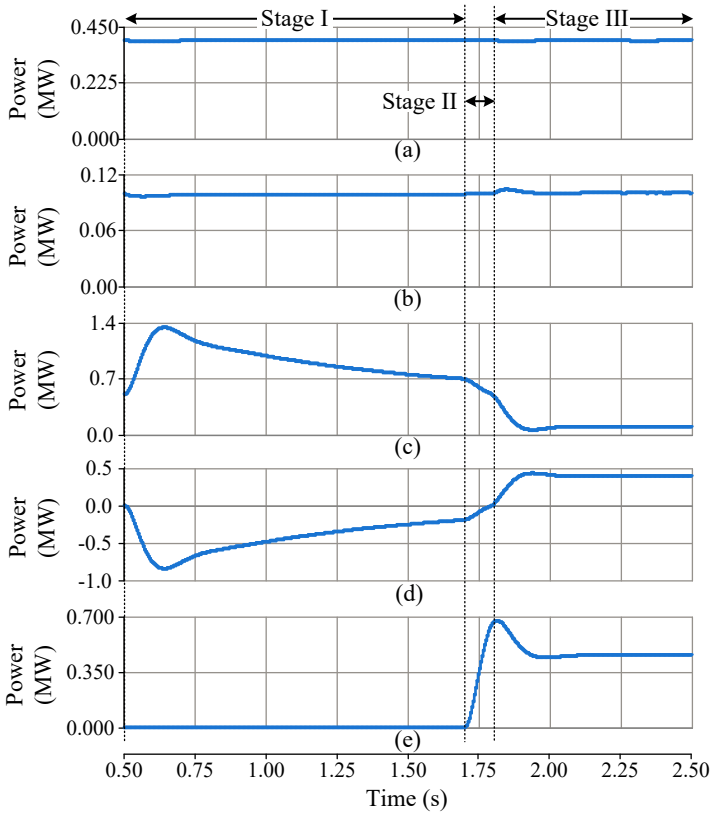

Fig. 6.10 Power flow curves. (a) LVac load power. (b) LVdc load power. (c) BESS power output. (d) ST dc-dc converter/DAB power output. (e) Power drawn from MVac side.

6.6 Experimental Results

The experimental setup block diagram is given in Fig. 6.11 (a). The three stages of the ST are developed with appropriate sensors for voltage and current measurements. Moreover, protection schemes are implemented to stop firing pulses in case of over current or over voltage faults. The ST MV converter and the ST isolated dc-dc converter/DAB setups are shown in Fig. 6.11(b). The BESS is realized with a dc source and a dc-dc converter. The ST LV converter and the BESS dc-dc converter setups are shown in Fig. 6.11(c). The hardware parameters are given in Table 6.3.

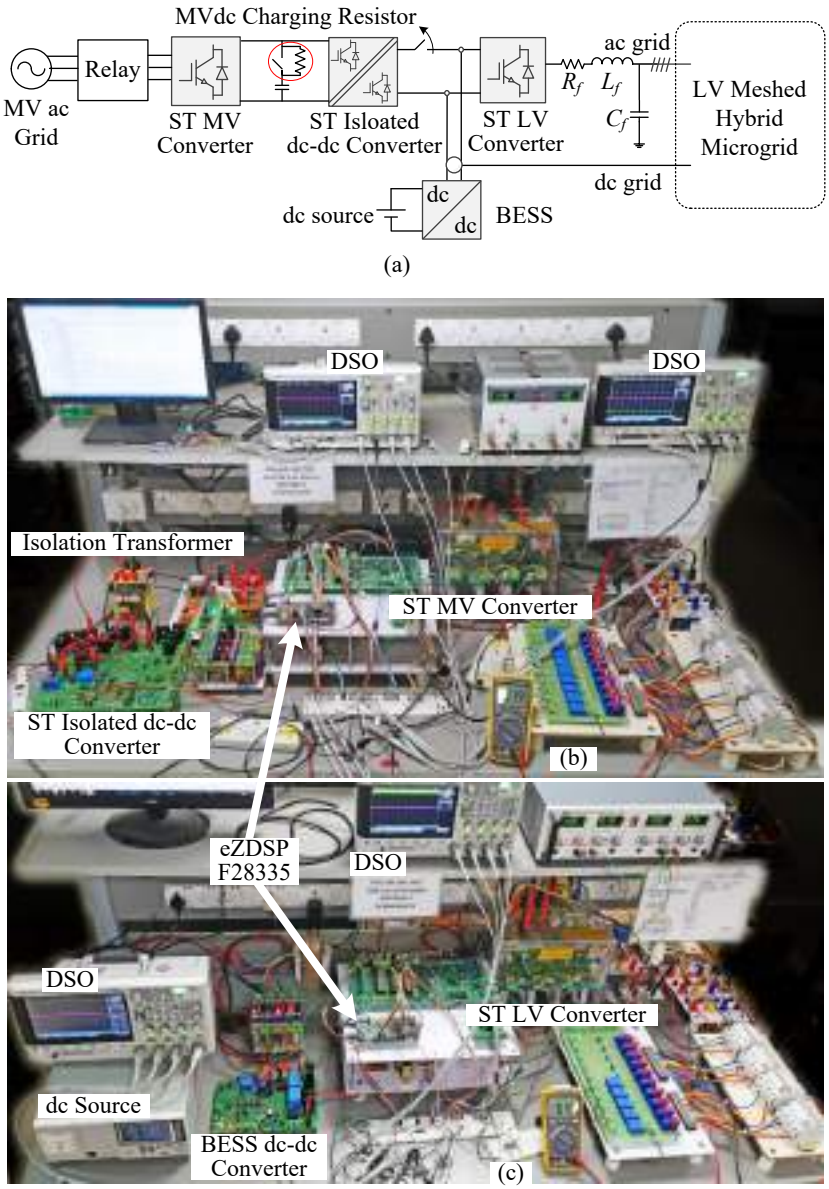

Fig. 6.11 (a) Experimental setup block diagram. (b) Photograph of ST MV converter and ST isolated dc-dc converter/DAB. (c) Photograph of ST LV converter and BESS dc-dc converter.

Table 6.3 Hardware Parameters

System Quantities	Values
MV grid voltage	120 V (L-L)
LV grid voltage	90 V (L-L)
ST MV converter	Power Rating = 1 kVA, L_{fm} = 20 mH, C_{fm} = 10 μF C_{MVdc} = 2350 μF
ST isolated dc-dc converter	Power Rating = 1.5 kW, f_s = 20 kHz, V_{MVdc} = 240 V
ST LV converter	Power Rating = 1 kVA, V_{LVdc} = 180 V, C_{LVdc} = 2350 μF, L_f = 20 mH, C_f = 10 μF
BESS dc-dc converter	Power Rating = 500 W, f_s = 20 kHz, L = 13 mH, C = 10 μF

The start-up controller signals along with the dc link voltages are given in Fig. 6.12. The

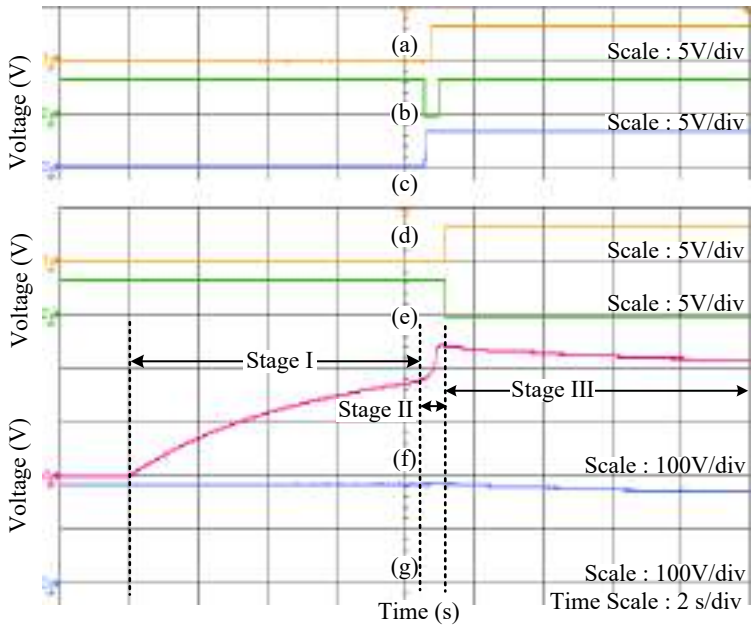

Fig. 6.12 Signals of centralized controller and ST dc voltages during partial start-up. (a) MVdc resistor CB signal. (b) DAB converter ON/OFF signal. (c) ST MV converter ON/OFF signal. (d) DAB mode signal. (e) BESS mode signal. (f) MVdc voltage. (g) LVdc voltage.

MVdc charging resistor CB signal is shown in Fig. 6.12(a). Initially, the DAB converter is ON and ST MV converter is OFF as shown in Fig. 6.12(b) and (c), respectively. The DAB mode of operation is in open loop where angle δ is set to zero. This is shown by the "low" value in DAB mode shown in Fig. 6.12(d). The BESS mode signal is "high", depicting VCM operation as shown in Fig. 6.12(e). The ST LV side CB is closed manually and immediately the MVdc voltage starts rising as shown in Fig. 6.12(f). When the CB gets a "high" signal, it operates and the charging resistor gets disconnected from the circuit. This occurs after the ST MVdc voltage reaches 85% of the nominal MVdc voltage. At this point the DAB converter turns OFF and the ST MV converter turns ON to charge the MVdc bus to the nominal value of 240 V. Once that voltage level is reached, the DAB converter again turns ON. Simultaneously, the BESS changes its mode of operation from VCM to CCM and the system starts working in grid connected mode.

Fig. 6.13 shows the voltages, currents and power flows in the system for the complete start-up process till the system attains steady-state operation. Once the MVdc voltage reaches 85% of 240 V, the MVac side CB closes and the ST MVac voltage appears. This is shown in Fig. 6.13(a). A zoomed in waveform is also shown together. When the ST MV converter gets the firing pulses, it starts drawing current to charge the MVdc

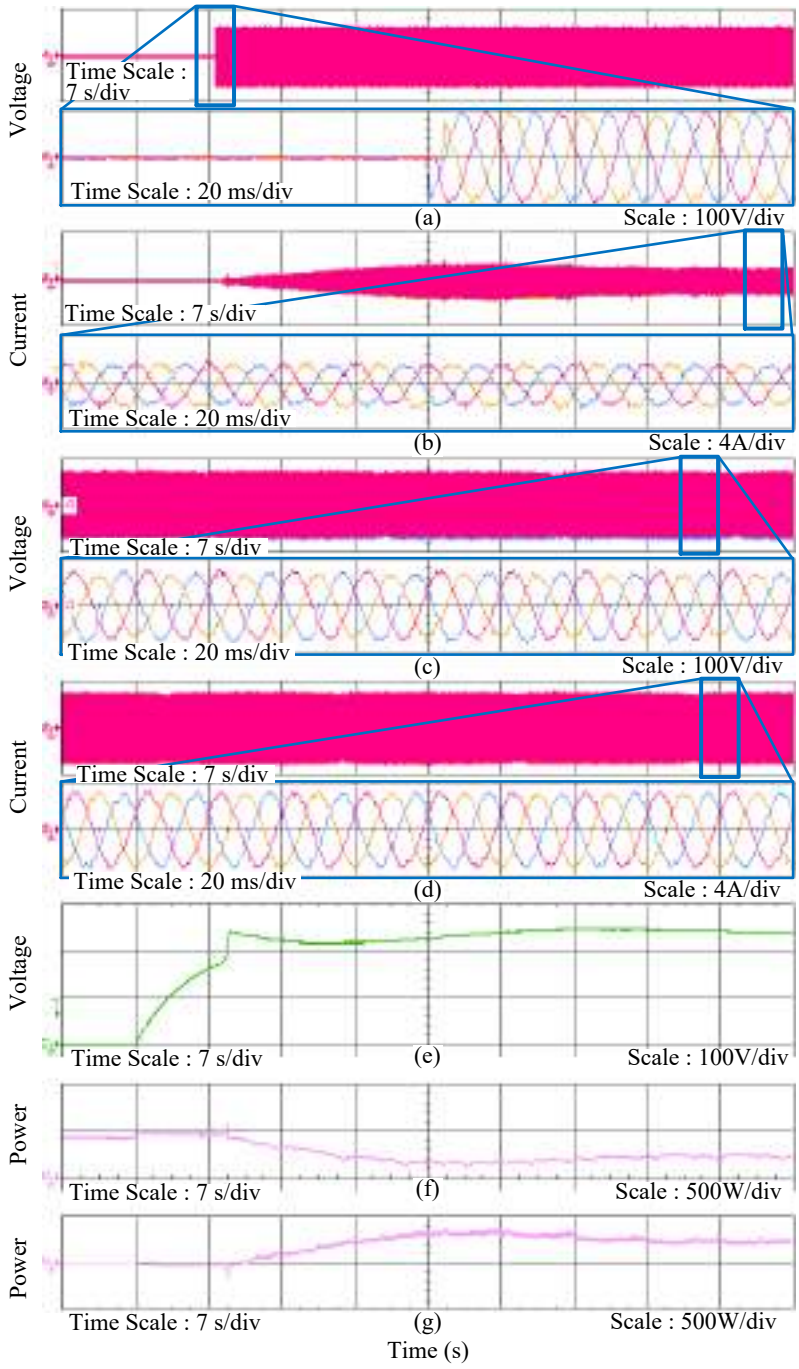

Fig. 6.13 Experimental results from partial start-up to steady-state operation. (a) ST MVac voltage. (b) MVac current. (c) LVac voltage. (d) LVac current. (e) MVdc voltage. (f) BESS power output. (g) ST isolated dc-dc converter/DAB power output.

capacitors. The current drawn from the MVac side is shown in Fig. 6.13(b). The LVac voltages and currents are shown in Fig. 6.13(c) and (d), respectively. These remain unaffected during the entire start-up transition, showing the uninterrupted operation of the LV side. The BESS power output is shown in Fig. 6.13(f). The total load in the system is 420 W and initially the BESS completely supplies this power through the ST LV converter. For the initial build-up of MVdc voltage to 85%, the charging

power is also supplied by the BESS. Thus, the BESS power output increases during the initial charging stage. In Stage II, when the ST MV converter charges the MVdc capacitors, the BESS power injection comes down due to the decrease in capacitor charging current as the voltage builds up across the capacitor. In the grid connected mode, it injects a fixed power of 200 W by operating in CCM. The ST isolated dc-dc converter power output is shown in Fig. 6.13(g). When the start-up is initiated, the power is negative as there is reverse power flow to charge the MVdc capacitor. Next the power output becomes zero during the period when the ST MV converter charges the MVdc capacitors. Finally, in the grid connected mode, the balance load power of 220 W which is not supplied by the BESS, is drawn from the MVac side by the ST isolated dc-dc converter.

6.7 Summary

A three stage partial start-up scheme is proposed for an ST in meshed hybrid islanded grid operation. The start-up procedure ensures that the ST MV converter and the ST isolated dc-dc converter start smoothly to connect LVdc grid to the MVac grid without disturbing the operation of the ST LV converter. Both the ST isolated dc-dc converter and ST MV converter are used to build up the MVdc voltage to the nominal value. The capacitor charging is achieved by limiting the charging current to prevent over currents. Initial charging through the ST isolated dc-dc converter ensures that the passive charging through ST MV converter reverse diodes is avoided. The developed stability criteria for the ST isolated dc-dc converter ensures its stable operation during the start-up. The simulation and experimental results verify the feasibility of the proposed scheme.

CHAPTER 7

CONCLUSIONS

7.1 SUMMARY

Electric power systems are changing due to the increasing interest on renewable energy sources (RES), decentralized generation, energy storage systems, etc. This has led to various challenges in the electric grid which are currently being addressed with various devices and technologies. Moreover, in recent times there is an increase in dc sources and loads in the grid. This has led to the existence of hybrid grids. Hybrid grids pose various challenges like power management, grid interlinking, microgrid formations, stability issues, etc. Generally, interlinking converters are used to interconnect the ac and dc grids to form hybrid grids. Therefore, with time, there is an increasing need of different power converters for specific applications in the electric grid. This has led researchers to look for solutions which can overcome several grid issues and requirements.

Researchers have proposed the solid state transformer (SST) as a very promising solution that address several issues in the modern power system. With additional control and communication features incorporated to an SST, the capabilities of an SST increase manyfolds. Such a device is termed as smart transformer (ST). The three stage ST has been suggested as the most suitable candidate for utilization in the distribution grid. It comprises of the medium voltage (MV) converter that converts MVac to MVdc, the isolated dc-dc converter which steps down the MVdc to low voltage (LV) dc and an LV converter which converts the LVdc to LVac. Since the ST comprises of power electronic converters, they can be individually controlled to improve the power flow in the grid. Further, with the presence of dc links, an ST can be used to interface various RES, and also be used as a device that forms hybrid grids.

This thesis explores the operation of an ST in the hybrid LV microgrid. The ST based meshed hybrid microgrid had been proposed by extending the ST LVdc link in the distribution grid and connecting to the dc buses of the distributed generation (DG) converters

already present in the system. The proposed system ensures maximum utilization of DG converters, reduction in size of ST LV converter, reduction of distribution losses, lower converter losses during reverse power flow, reduced complexity of control algorithms and improved LVac line voltage profile.

The islanded operation of the proposed ST-based meshed hybrid microgrid is investigated and improved power management strategies for optimal power loss reduction is proposed. A BESS maintains the LVdc voltage in the islanded mode, and the ST LV converter maintains the LVac voltage. In such islanded operation, the LV side can operate even when the MV side has some fault. Moreover, intentional MV side shutdown for maintenance is possible without disturbing the operation of the LV grid. As the islanding is done at the LVdc link of the ST, the challenge of synchronization during reclosure does not arise. The optimal power management algorithm proposed for reduced loss ensures longer operation time of the system. A method of smart under voltage load shedding enabled by ST is also proposed to ensure longer operation time of critical loads in the system.

With the recent interest in EVs, it is certain that the EVs will become very popular in the near future. Along with it, there will be issues of EVs charging which will draw high power from the electric grid. In the proposed ST based meshed hybrid microgrid, such charging transients can lead to system instability especially during islanded operation. One common stability issue is due to the right half plane zero (RHPZ) that is inherently present in the control-to-output transfer function of BESS converter. RHPZ results in slower system response and makes the system unsuitable for high load transients. For such scenarios in the islanded ST based meshed hybrid microgrid, stability studies have been conducted and a control algorithm is proposed to ensure that such an islanded system does not lose stability during EV charging transients.

Finally, a step-by-step start-up procedure is proposed to re-connect the islanded ST based meshed hybrid microgrid back to the MVac grid. The ST LV converter is operational in the islanded mode of operation and the reconnection to MVac grid is done by turning ON the remaining two converters of the ST namely the MV and isolated dc-dc converter. Therefore, this start up scheme for the ST is named as the partial start-up scheme. The scheme ensures start-up of the ST isolated dc-dc converter and the ST MV converter without affecting the operation of the LV grid. Both the ST isolated dc-dc

converter and ST MV converter are used to build up the MVdc voltage. The MVdc capacitor charging is achieved by limiting the charging current to prevent over currents.

The simulation study in this thesis has been conducted in PSCAD/EMTDC software. To practically validate the theoretical findings in a real time hardware prototype, an experimental setup has been developed. Following are the major contributions of this thesis.

- An ST based meshed hybrid microgrid is proposed by extending the ST LVdc bus and connecting to the dc buses of DG converters present in the LV distribution grid. The system performance is compared with the existing topologies to bring out the advantages.
- Islanded operation of such a microgrid is explored along with the integration of EV and BESS. Optimal power loss minimization is done to reduce the line losses during the islanded operation to improve operation time.
- EV charging transients are analyzed and a method is proposed utilizing the meshed hybrid configuration to mitigate the transients and improve stability of the islanded system.
- Reconnection of the islanded system to the MVac grid through a step-by-step partial ST start-up scheme is proposed. The scheme ensures that the LV grid operation is undisturbed during the start-up process.
- An experimental prototype has been developed in the laboratory. All the proposed control algorithms and operation methods are validated in both simulation and experimental environments.

7.2 SCOPE FOR FUTURE WORK

This thesis has proposed the ST based meshed hybrid microgrid. With parallel existence of ac and dc grids, the meshed system provides attractive advantages of loss reduction, improved converter utilization, multiple power flow paths, etc. This further needs to be explored in terms of economic viability and cost estimates to modify existing distribution grids in the proposed manner. There are also aspects like dc distribution, protection,

circuit breakers which will be inherent aspects and components of the proposed system. These will need detailed studies for practical implementation.

The ST based islanded operation enables islanding at the LVdc link. In this thesis, aspects like islanding detection, anti-islanding schemes, safety measures, etc. have not been discussed. In the proposed meshed hybrid microgrid, such aspects will play an important role. These may be investigated for improved operation and feasibility.

A method is proposed to minimize line losses to achieve improved operation time during islanded mode of operation of the ST based meshed hybrid microgrid. However, the converter losses are not considered in the analysis. Moreover, the analysis is done with the active power loads only. The inclusion of converter losses and reactive power loads in the minimization algorithm can further improve the system optimization for real world implementation. Research also needs to be done on the real-time implementation of the proposed optimization method in actual grid conditions.

An aspect of stability has been analyzed in one of the chapters and a method is proposed to stabilize the BESS dc-dc converter during EV charging transients. Various such situations may arise in the meshed hybrid microgrid in the islanded as well as grid connected modes, where converter and system stability may be jeopardized. Moreover, as there are multiple power electronic converters in the system, there is the possibility of intentional as well as unintentional interaction of one converter with another. These opens the doors for a completely new area of research.

APPENDIX A

EXPERIMENTAL SETUP DETAILS

Various power converter setups along with auxiliary circuits and components were developed in the laboratory to verify the operations proposed in this thesis. In addition to that, digital controllers were used for controlling the various converters. This was done by programming and operating the controllers from a host computer. Fig. A.1 shows the schematic of the overall control layout that is used for controlling each power converter in the experimental setup. The various sections and components of the experimental setup are explained as follows.

A.1 Power Converters

A.1.1 ST MV Converter

The ST MV converter is realized with a SEMIKRON voltage source converter. All the voltages and currents necessary for monitoring and control were sensed with a 20 channel transducer circuit fabricated in the laboratory. The signals from the transducer circuit were fed to a 16 channel signal conditioning circuit to make them suitable for the analogue to digital converter (ADC) of the ezDSP-F28335 digital controller which was used to control the converter. A photograph of the setup is shown in Fig. A.4.

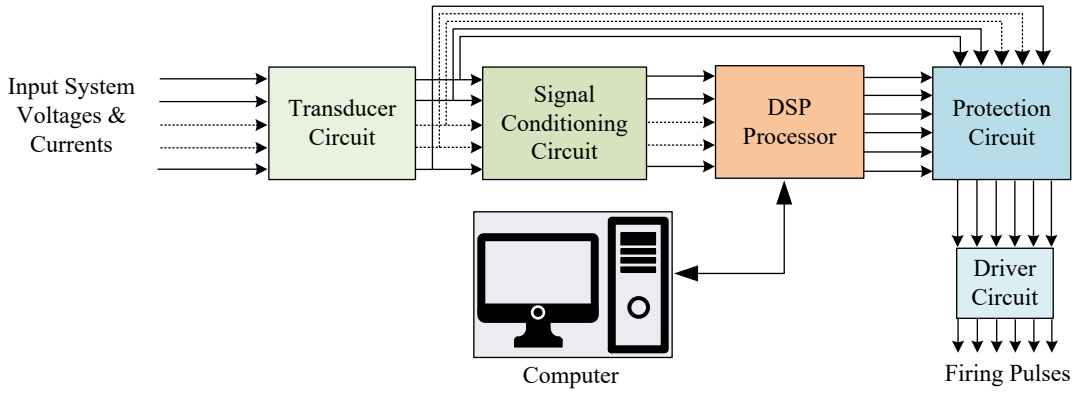

Fig. A.1 Controller layout of the experimental setup.

A.1.2 ST Isolated dc-dc Converter

For the ST isolated dc-dc converter, a DAB converter was developed with a power rating of 1.5 kW. The circuit consists of eight IGBTs, four on the primary and four on the secondary side with a high frequency isolation transformer in between. The PCB was designed with sensors, protection and delay generation circuits for the proper operation of the converter. A photograph of the setup is shown in Fig. A.5.

A.1.3 ST LV Converter

The SEMIKRON voltage source converter is used as the ST LV converter which draws power from the LVdc bus, maintained by the ST isolated dc-dc converter. A photograph of the setup is shown in Fig. A.6.

A.1.4 Bi-directional dc-dc Converter

To interface BESS to the distribution grid, a bi-directional dc-dc converter rated at 650 W was designed and developed as part of the experimental prototype in the laboratory. The converter was coupled with sensors for voltage and current measurement to enable closed loop operation. Protection circuits were also included to protect the converter against over currents and over voltages. The PCB was designed and developed and the system was operated with an ezDSP-F28335 digital controller. A similar PCB was also used in the EV setup which was realized with a dc source and dump load. Fig. A.7 shows the photograph of the BESS and EV system where the bi-directional dc-dc converter is used.

A.2 Auxiliary Circuits

A.2.1 Transducer Circuits

To measure the voltages and currents at various points of the setup, Hall Effect transducers were used. These need a separate circuitry based on the gain factor. The LV 55P was used to sense the voltages and the LA 25P was used to sense the currents. A pho-

tograph of the circuit with 10 individual voltage and current sensing channels is shown in Fig. A.9(a).

A.2.2 Signal Conditioning Circuits

For feeding the sensed signals into the digital controller, further conditioning of the signals needs to be done to match with the specifications of the ADC pins of the digital controller. This is done with a signal conditioning circuit which consists of operational amplifiers used for scaling and level shifting. Fig. A.9(b) shows a PCB which contains a 16 channel signal conditioning circuit.

A.2.3 Protection Circuits

The protection circuit ensures that the system can be shutdown in case of an undesired event of over-voltage or over-current. It is realized with operational amplifiers used as comparators to compare the actual sensed signal with a set reference. Digital circuits are used to combine the compared values from different sensors, and ensure that the firing pulses are turned OFF in case any of the sensed signals goes over the respective reference.

A.2.4 Blanking Circuits

The blanking circuits are used to create a dead band between the top and bottom switches of each leg in the power electronic converters. They ensure that the turn OFF time of the switch does not lead to switch turn ON overlap in that same leg, which may otherwise lead to short circuit.

A.2.5 Relay Circuits

This circuit is used to physically connect or disconnect a part of the system with the help of the digital controller. The signal from the controller is amplified with the help of transistors to drive the coil of the relay for each phase. Fig. A.10(c) shows the photograph of the controller operated relay circuit.

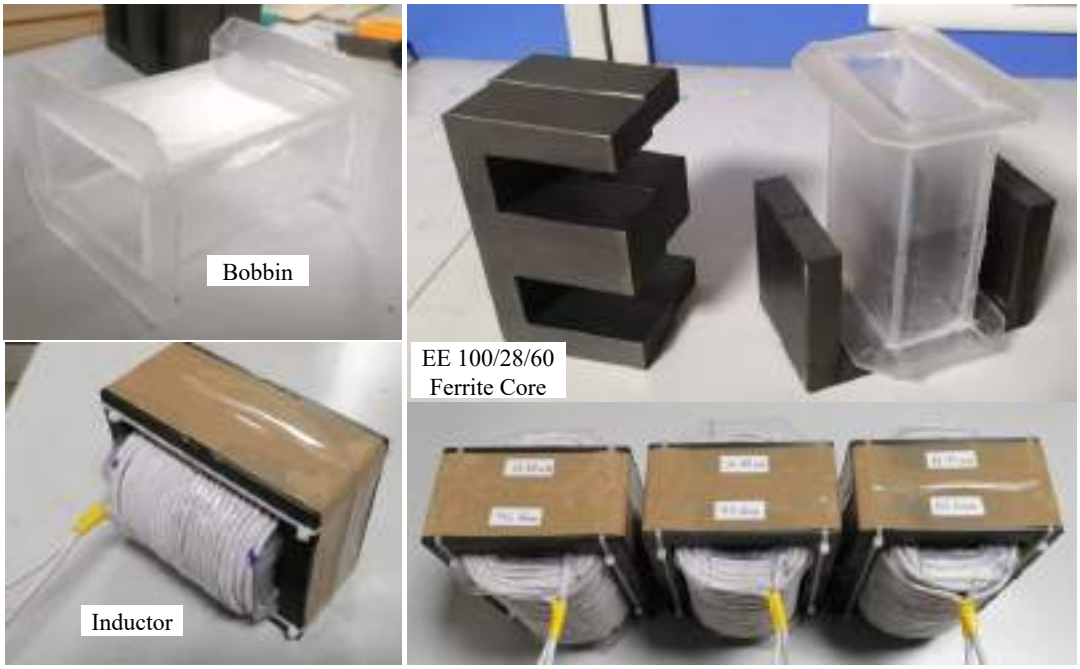

Fig. A.2 Photograph of inductor constructed in the laboratory.

A.3 Construction of Inductors

The design process of an inductor is based on three specifications namely (a) the inductance value, (b) the current rating and (c) the operating frequency.

Inductance is given as the number turns squared, divided by the reluctance. This is expressed as [179]

$$L = \frac{N^2}{\mathscr{R}} \tag{A.1}$$

where L is the inductance, N is the number of turns and $\mathscr{R}$ is the reluctance.

Reluctance is expressed as

$$\mathscr{R} = \frac{\frac{l_m}{\mu_r} + l_g}{\mu_0 A_c} \tag{A.2}$$

where l_m is the mean magnetic length, l_g is the air gap length, A_c is the area of cross section, μ_o is the permeability of free space and μ_r is the relative permeability of the core material. Based on these, the various components and their specifications needed for the inductor are decided as follows.

A.3.1 Selection of Wire

The selection of wire for the inductor windings is based on the current rating and the switching frequency. As the switching frequency increases, due to the appearance of skin effect, the effective cross sectional area of the conductor reduces. This provides an added resistance to the flow of current. The American wire gauge (AWG) chart shows the maximum current that can flow for various cross sectional area of the conductor. The chart also gives information regarding the maximum frequency the wire can handle maintaining 100% skin depth. As the cross sectional area of a conductor increases, its current rating increases. However, the maximum frequency for 100% skin depth decreases. Thus, in order to make a winding with high current rating, working at high frequency, a bundled conductor is made consisting of insulated strands. Such a wire is called a Litz wire. In a Litz wire, the individual strands are selected based on the maximum frequency requirement. Based on the current rating of each strand, an appropriate number of strands are used so that the total rated current of the inductor can flow.

A.3.2 Selection of Core

The size of the inductor core is determined by the number of turns of the wire that needs to be accommodated in the core. From equations (A.1) and (A.2) it is seen that the number of turns again depends upon the size and material of the core used. Thus, a specific core is selected with an arbitrary air gap and the number of turns required is calculated. Based on the cross sectional area of the Litz wire, an estimate is made if the required number of turns will fit in the core window area available. In case the core cannot accommodate the windings, a bigger size of core is selected.

Before finalizing the core, the calculation for flux density in the core must be done to ensure that during operation, the magnetization of the core does not exceed the saturation magnetization (B_s). The maximum flux density is given by

$$B_{max} = \frac{LI_{max}}{NA_c} \tag{A.3}$$

where I_{max} is the maximum current that can flow through the inductor.

To maintain the saturation limits, B_{max} must be less than B_s. If this criterion is not

met, the air-gap length is increased and the number of turns is recalculated. In case the number of turns is more than what the core can accommodate, the core size is further increased.

Finally, a trade-off is made amongst the various parameters mentioned above to arrive at the optimum size of the core.

A.3.3 Construction of Bobbin

Toroidal cores are generally wound directly. However, for other types of core like EE, EI, CI, etc., the windings are generally done on a bobbin before inserting the bobbin into the core. The bobbin material is usually an insulating material strong enough to house the windings.

A.3.4 Winding and Assembly

The Litz wire is wound carefully on the bobbin with the number of turns calculated and bobbin is inserted into the core. The airgap of the core is adjusted as per the calculation. Finally, with some binding material like glue or tape, the cores are fixed together.

A.3.5 Specifications of Inductors Constructed in the Lab

The design specifications of the inductor are given in Table A.1. The specifications of the Litz wire used are given in Table A.2. The core and bobbin specifications are given in Table A.3.

Table A.1 Inductor Specifications

Parameter	Values
Inductance	13 mH
Current Rating	5 A
Frequency	50 kHz

Table A.2 Specifications of Litz Wire

Parameter	Values
AWG	23
Diameter of each strand	0.57404 mm
Maximum current capacity of each strand	0.729 A
Maximum frequency for 100% skin depth	53 kHz
Total number of strands	15

Table A.3 Specifications of Core and Bobbin

Parameter	Values
Core material	Ferrite
Core size	Stack of two EE 100/60/28
Effective magnetic path length (l_m)	274 mm
Effective magnetic cross section (A_c)	1470 mm^2
Effective relative permeability (μ_r)	1930
Bobbin material	2 mm thick acrylic sheet

A.3.6 Testing and Comparison

The inductors were used as filters for a grid connected inverter in the existing experimental setup. Fig. A.3 shows a comparison of the inverter currents using purchased inductors and the ones designed in the laboratory. With the purchased inductors, the current waveforms are seen to have spikes as shown in Fig. A.3 (a). However, the reference currents are properly maintained with the inductors developed in the laboratory as shown in Fig. A.3 (b).

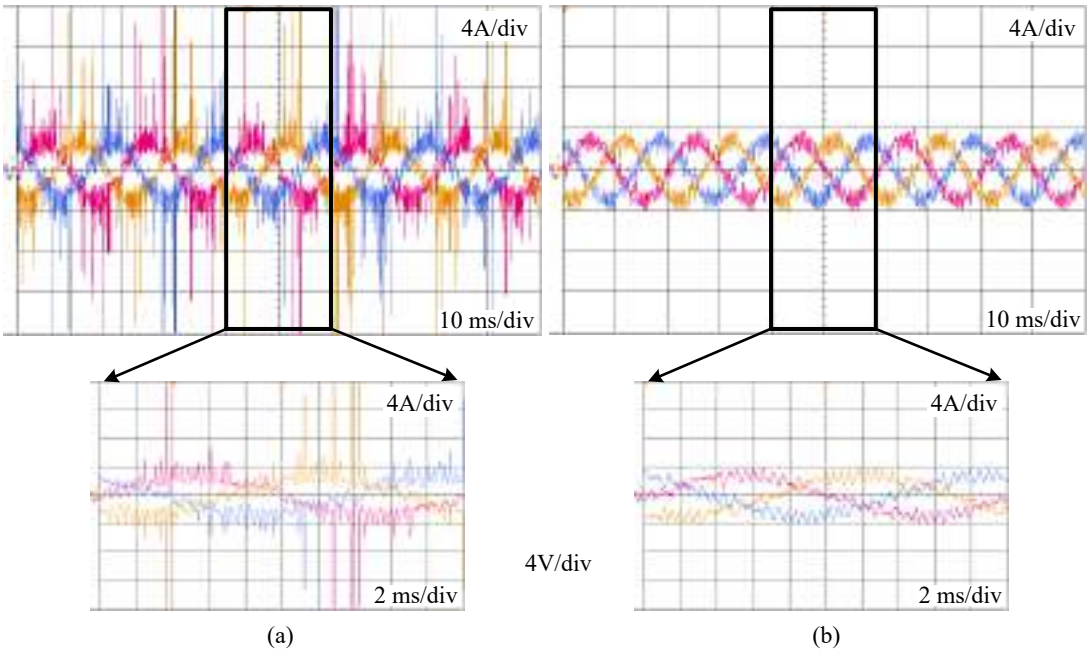

Fig. A.3 Comparison of current waveforms. (a) Purchased inductors. (b) Inductors designed in the laboratory.

A.4 PHOTOGRAPHS OF THE SETUP

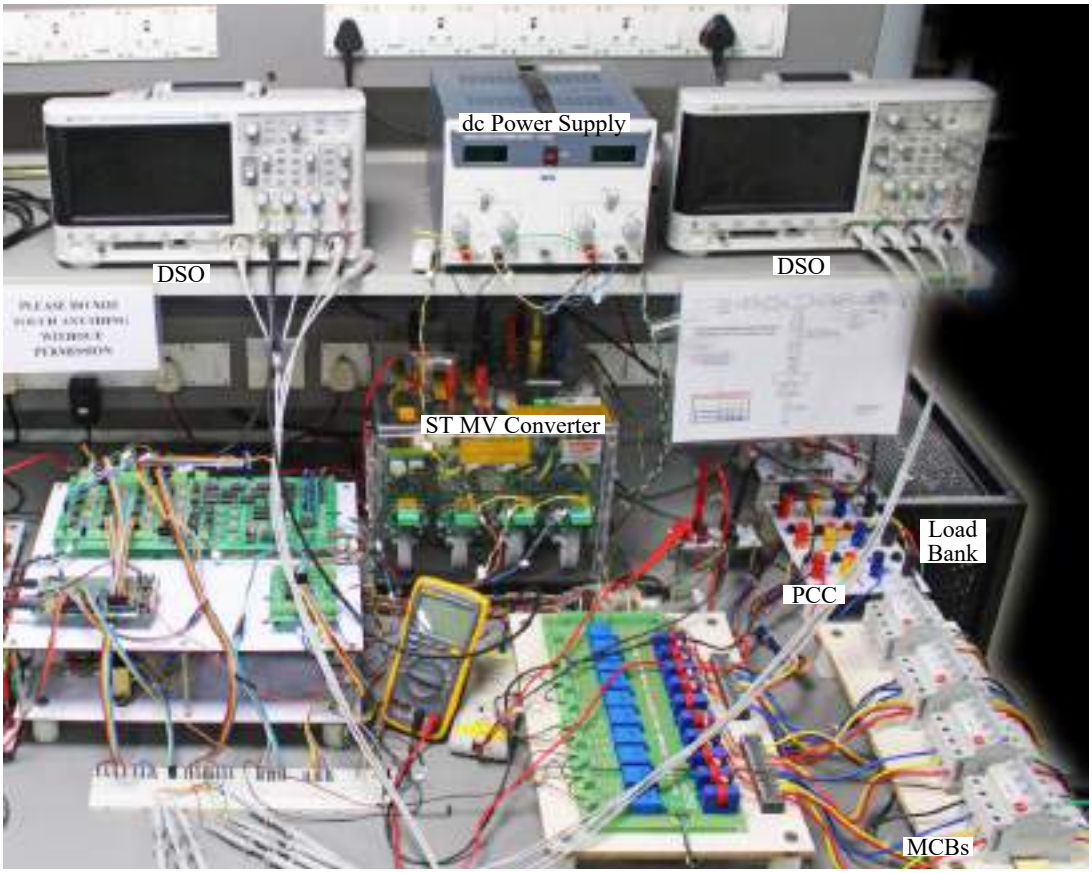

Fig. A.4 Experimental setup for ST MV converter.

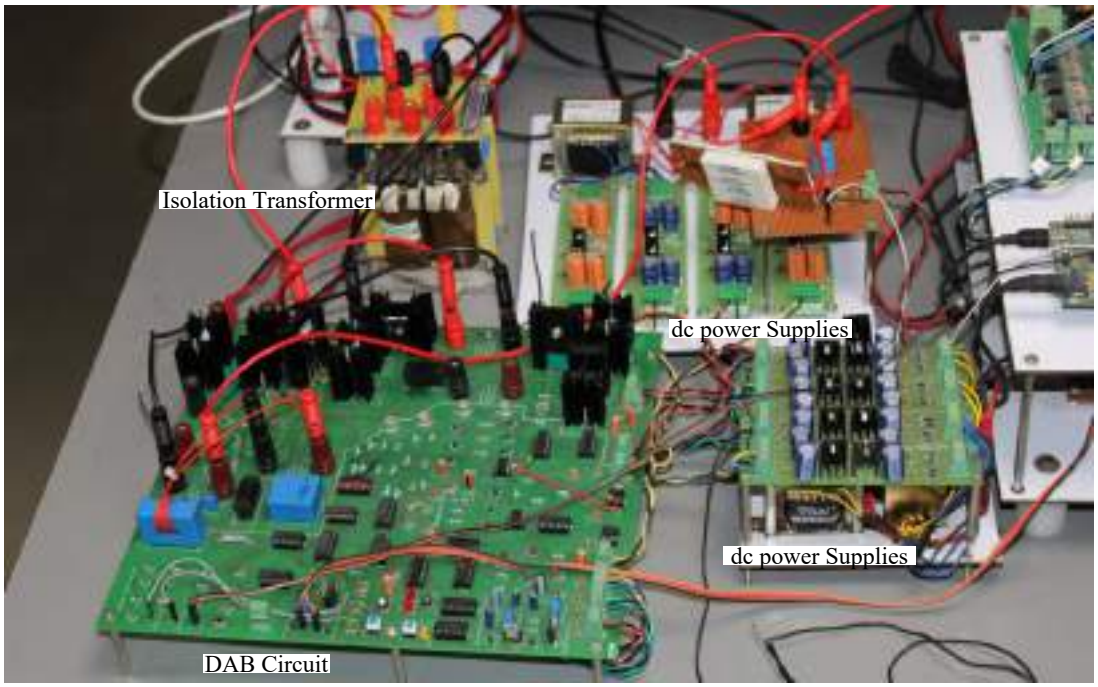

Fig. A.5 Experimental setup for ST isolated dc-dc converter.

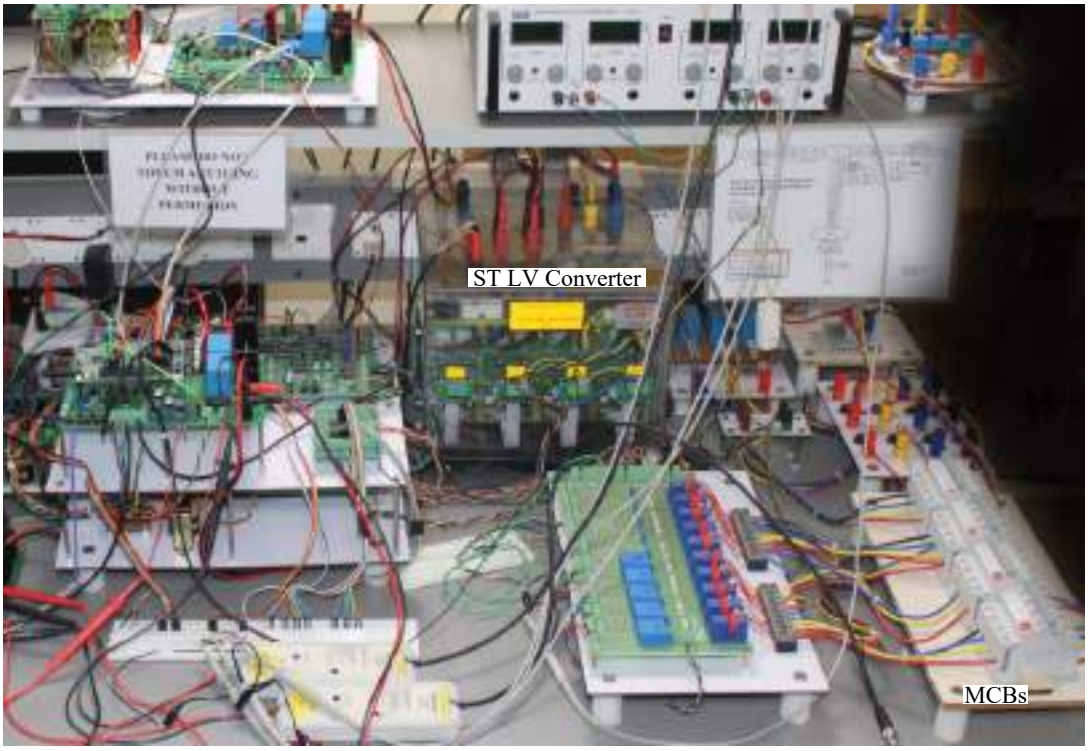

Fig. A.6 Experimental setup for ST LV converter.

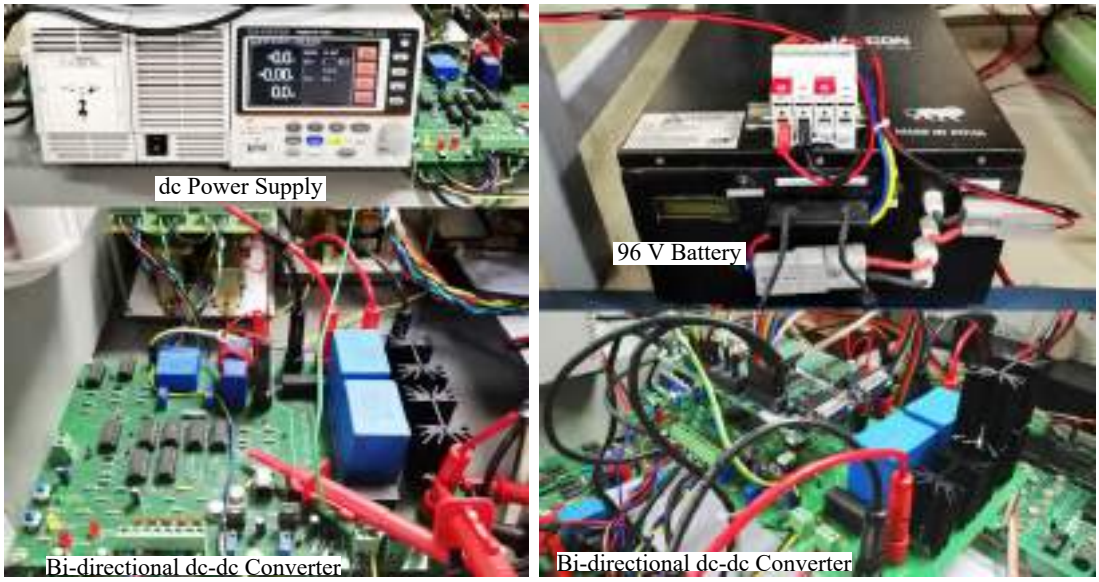

(a) (b)

Fig. A.7 Experimental setup. (a) BESS. (b) EV.

Fig. A.8 Experimental setup for PV system.

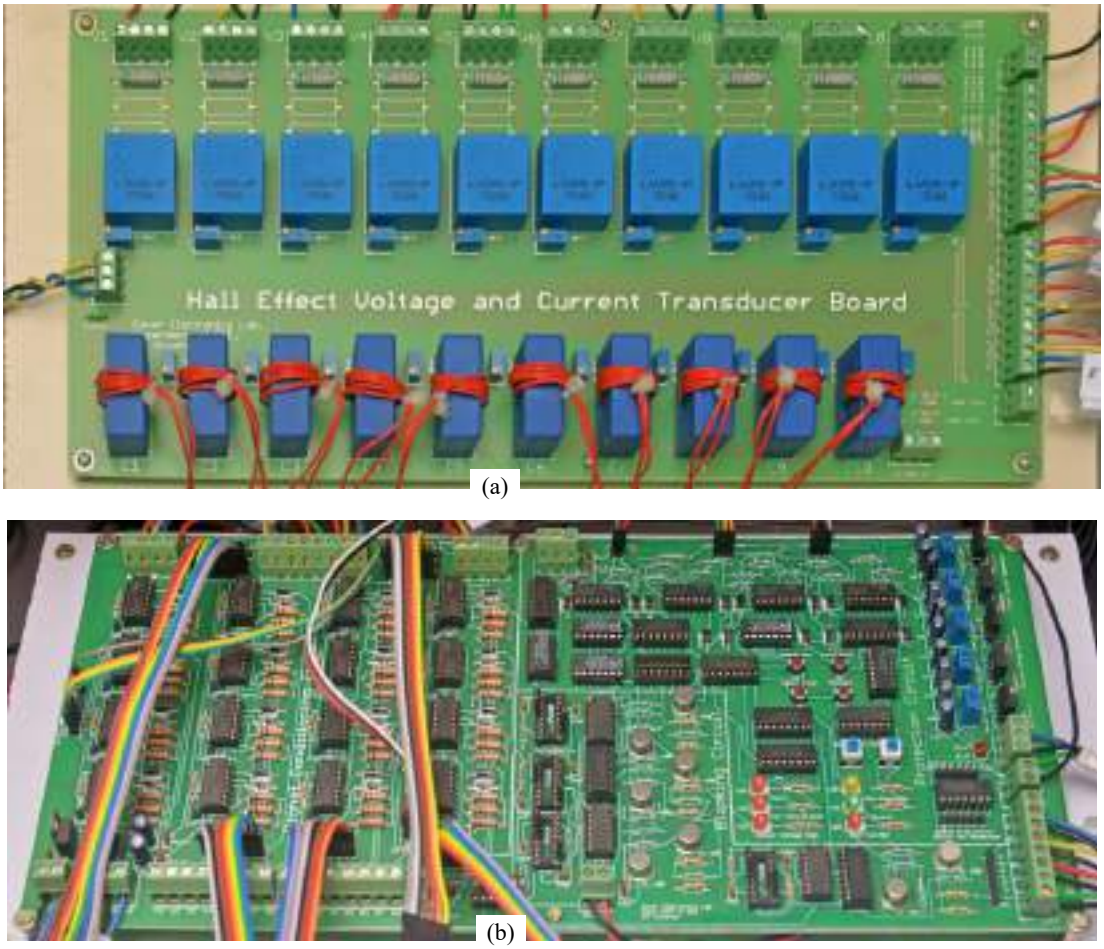

Fig. A.9 Photograph. (a) Transducer circuit board. (b) Signal conditioning, protection and blanking circuit board.

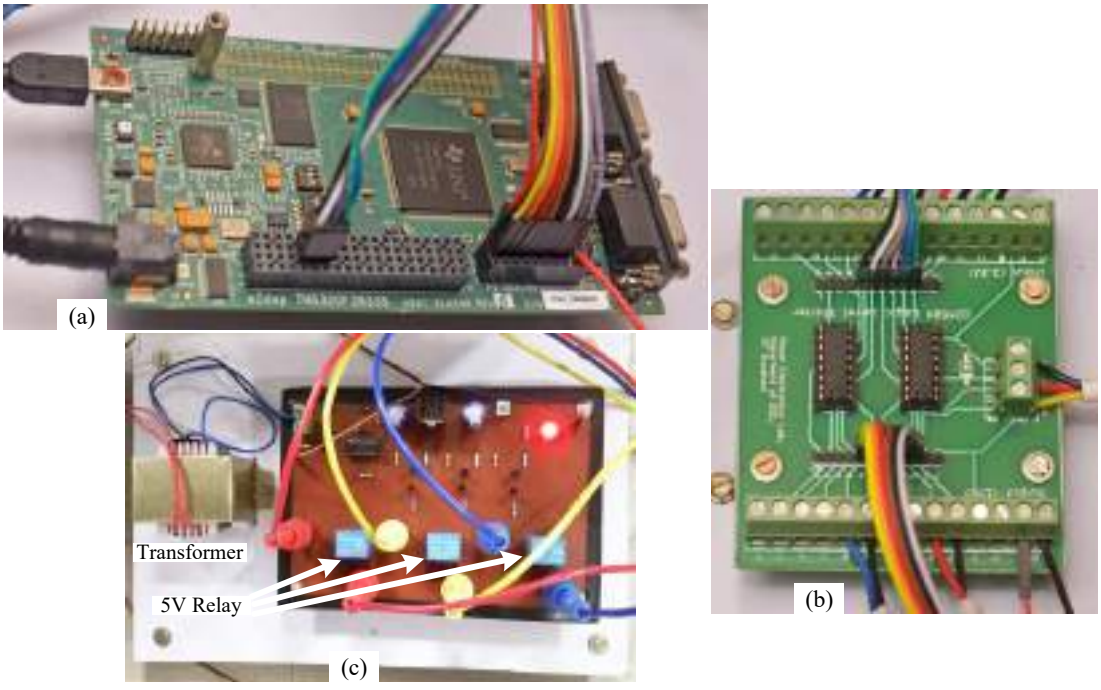

Fig. A.10 Photograph. (a) eZDSP28335 controller. (b) Level shifter circuit. (c) Controller operated relay circuit.

REFERENCES

[1] K. Hassmann, "Electric power generation," *Proceedings of the IEEE*, vol. 81, no. 3, pp. 346–354, 1993.

[2] A. H. Frampton, "Hydroelectric power plants," *Electrical Engineering*, vol. 65, no. 4, pp. 151–159, 1946.

[3] M. R. Hannah Ritchie and P. Rosado, "Energy," *Our World in Data*, 2020.

[4] A. Joshi, "Share of Solar Rises to 13.2% of India's Total Installed Power Capacity," *Mercom India Clean Energy News and Insights*, vol. 2, no. 3, p. 35, May 2022.

[5] S. Rahman and A. de Castro, "Environmental impacts of electricity generation: a global perspective," *IEEE Transactions on Energy Conversion*, vol. 10, no. 2, pp. 307–314, 1995.

[6] R. M. Elavarasan, G. Shafiullah, S. Padmanaban, N. M. Kumar, A. Annam, A. M. Vetrichelvan, L. Mihet-Popa, and J. B. Holm-Nielsen, "A Comprehensive Review on Renewable Energy Development, Challenges, and Policies of Leading Indian States With an International Perspective," *IEEE Access*, vol. 8, pp. 74 432–74 457, 2020.

[7] Irena.org. (2021, Mar) "Renewable capacity highlights". [Online]. Available: https://www.irena.org/-/media/Files/IRENA/Agency/Publication/2021/Apr/IRENA_-RE_Capacity_Highlights_2021.pdf?la=en&hash=1E133689564BC40C2392E85026F71A0D7A9C0B91

[8] H. Abu-Rub, M. Malinowski, and K. Al-Haddad, "Challenges of the Current Energy Scenario: The Power Electronics Contribution," in *Power Electronics for Renewable Energy Systems, Transportation and Industrial Applications*, 2014, pp. 27–49.

[9] X. Liang, "Emerging Power Quality Challenges Due to Integration of Renewable Energy Sources," *IEEE Transactions on Industry Applications*, vol. 53, no. 2, pp. 855–866, 2017.

[10] V. T. Tran, M. R. Islam, D. Sutanto, and K. M. Muttaqi, "Mitigation of Solar PV Intermittency Using Ramp-Rate Control of Energy Buffer Unit," *IEEE Transactions on Energy Conversion*, vol. 34, no. 1, pp. 435–445, 2019.

[11] C. Eisenhut, F. Krug, C. Schram, and B. Klockl, "Wind-Turbine Model for System Simulations Near Cut-In Wind Speed," *IEEE Transactions on Energy Conversion*, vol. 22, no. 2, pp. 414–420, 2007.

[12] P. Denholm, E. Ela, B. Kirby, and M. Milligan, "Role of energy storage with renewable electricity generation," *Office of Scientific and Technical Information (OSTI)*, 2010.

[13] X. Liang and C. Andalib Bin-Karim, “Harmonics and Mitigation Techniques Through Advanced Control in Grid-Connected Renewable Energy Sources: A Review,” *IEEE Transactions on Industry Applications*, vol. 54, no. 4, pp. 3100–3111, 2018.

[14] R. Langella, A. Testa, J. Meyer, F. MÃűller, R. Stiegler, and S. Z. Djokic, “Experimental-Based Evaluation of PV Inverter Harmonic and Interharmonic Distortion Due to Different Operating Conditions,” *IEEE Transactions on Instrumentation and Measurement*, vol. 65, no. 10, pp. 2221–2233, 2016.

[15] H. Hu, Q. Shi, Z. He, J. He, and S. Gao, “Potential Harmonic Resonance Impacts of PV Inverter Filters on Distribution Systems,” *IEEE Transactions on Sustainable Energy*, vol. 6, no. 1, pp. 151–161, 2015.

[16] R. K. Varma, S. A. Rahman, T. Vanderheide, and M. D. N. Dang, “Harmonic Impact of a 20-MW PV Solar Farm on a Utility Distribution Network,” *IEEE Power and Energy Technology Systems Journal*, vol. 3, no. 3, pp. 89–98, 2016.

[17] “Supraharmonics,” *HyTEPS*. [Online]. Available: https://hyteps.com/power-quality/supraharmonics/

[18] Learning Electrical Engineering. [Online]. Available: https://www.electricalengineeringtoolbox.com/2017/01/basics-of-harmonics-in-electrical.html

[19] A. S. Alsharafi, A. H. Besheer, and H. M. Emara, “Primary Frequency Response Enhancement for Future Low Inertia Power Systems Using Hybrid Control Technique,” *Energies*, vol. 11, no. 4, 2018.

[20] X. Chen, Y. Hou, S.-C. Tan, C.-K. Lee, and S. Y. R. Hui, “Mitigating Voltage and Frequency Fluctuation in Microgrids Using Electric Springs,” *IEEE Transactions on Smart Grid*, vol. 6, no. 2, pp. 508–515, 2015.

[21] Y.-S. Kim, E.-S. Kim, and S.-I. Moon, “Frequency and Voltage Control Strategy of Standalone Microgrids With High Penetration of Intermittent Renewable Generation Systems,” *IEEE Transactions on Power Systems*, vol. 31, no. 1, pp. 718–728, 2016.

[22] S. Vlahinić, D. Franković, V. Komen, and A. Antonić, “Reactive Power Compensation with PV Inverters for System Loss Reduction,” *Energies*, vol. 12, no. 21, 2019.

[23] Globalweathercorp.com. (2021, Jul.) "What is global horizontal irradiance (GHI) and why does it matter?". [Online]. Available: https://blog.globalweathercorp.com/global-horizontal-irradiance-solar-panel-efficiency

[24] Solargis.com. "Solar historical time series & TMY 1-minute solar radiation data". [Online]. Available: https://solargis.com/products/evaluate/overview

[25] D. T. Ton and M. A. Smith, “The U.S. Department of Energy’s Microgrid Initiative,” *The Electricity Journal*, vol. 25, no. 8, pp. 84–94, 2012.

[26] P. Villenueve, “Concerns generated by islanding [electric power generation],” *IEEE Power and Energy Magazine*, vol. 2, no. 3, pp. 49–53, 2004.

[27] A. Woyte, R. Belmans, and J. Nijs, "Testing the islanding protection function of photovoltaic inverters," *IEEE Transactions on Energy Conversion*, vol. 18, no. 1, pp. 157–162, 2003.

[28] S. Ranade, N. Prasad, S. Omick, and L. Kazda, "A study of islanding in utility-connected residential photovoltaic systems. I. Models and analytical methods," *IEEE Transactions on Energy Conversion*, vol. 4, no. 3, pp. 436–445, 1989.

[29] S. Ranade, N. Prasad, S. Omick, and L. Kazda, "A study of islanding in utility-connected residential photovoltaic systems. II. Case studies," *IEEE Transactions on Energy Conversion*, vol. 4, no. 3, pp. 446–452, 1989.

[30] F. Blaabjerg, R. Teodorescu, M. Liserre, and A. Timbus, "Overview of Control and Grid Synchronization for Distributed Power Generation Systems," *IEEE Transactions on Industrial Electronics*, vol. 53, no. 5, pp. 1398–1409, 2006.

[31] J. Kwon, S. Yoon, and S. Choi, "Indirect Current Control for Seamless Transfer of Three-Phase Utility Interactive Inverters," *IEEE Transactions on Power Electronics*, vol. 27, no. 2, pp. 773–781, 2012.

[32] S. W. Lee, S. B. Byun, W. S. Kim, J. K. Lee, and K. D. Choi, "Design of a Single Phase 33 MVA HTS Transformer With OLTC," *IEEE Transactions on Applied Superconductivity*, vol. 17, no. 2, pp. 1939–1942, 2007.

[33] X. Liu, A. Aichhorn, L. Liu, and H. Li, "Coordinated Control of Distributed Energy Storage System With Tap Changer Transformers for Voltage Rise Mitigation Under High Photovoltaic Penetration," *IEEE Transactions on Smart Grid*, vol. 3, no. 2, pp. 897–906, 2012.

[34] M. Bahadornejad and N.-K. C. Nair, "Intelligent Control of On-Load Tap Changing Transformer," *IEEE Transactions on Smart Grid*, vol. 5, no. 5, pp. 2255–2263, 2014.

[35] G. R. Chandra Mouli, P. Bauer, T. Wijekoon, A. Panosyan, and E.-M. Bärthlein, "Design of a Power-Electronic-Assisted OLTC for Grid Voltage Regulation," *IEEE Transactions on Power Delivery*, vol. 30, no. 3, pp. 1086–1095, 2015.

[36] A. A. A. Ismail, H. Alsuwaidi, and A. Elnady, "Automatic Voltage Stabilization Using IGBT Based on Load Tap Changer With Fault Consideration," *IEEE Access*, vol. 9, pp. 72 769–72 780, 2021.

[37] T. Aziz and N. Ketjoy, "Enhancing PV Penetration in LV Networks Using Reactive Power Control and On Load Tap Changer With Existing Transformers," *IEEE Access*, vol. 6, pp. 2683–2691, 2018.

[38] T.-T. Ku, C.-H. Lin, C.-S. Chen, and C.-T. Hsu, "Coordination of Transformer On-Load Tap Changer and PV Smart Inverters for Voltage Control of Distribution Feeders," *IEEE Transactions on Industry Applications*, vol. 55, no. 1, pp. 256–264, 2019.

[39] J. de Oliveira Quevedo, F. E. Cazakevicius, R. C. Beltrame, T. B. Marchesan, L. Michels, C. Rech, and L. Schuch, "Analysis and Design of an Electronic On-Load Tap Changer Distribution Transformer for Automatic Voltage Regulation," *IEEE Transactions on Industrial Electronics*, vol. 64, no. 1, pp. 883–894, 2017.

[40] C. Kumar and M. K. Mishra, "A Multifunctional DSTATCOM Operating Under Stiff Source," *IEEE Transactions on Industrial Electronics*, vol. 61, no. 7, pp. 3131–3136, 2014.

[41] A. Ghosh and G. Ledwich, *Power quality enhancement using custom power devices*. Springer Science & Business Media, 2012.

[42] S. Sannigrahi, S. R. Ghatak, and P. Acharjee, "Coordinated Planning of Distribution System With RES, DSTATCOM, and Protective Devices," *IEEE Transactions on Industry Applications*, vol. 57, no. 4, pp. 4294–4305, 2021.

[43] B. Singh, M. Kandpal, and I. Hussain, "Control of Grid Tied Smart PV-DSTATCOM System Using an Adaptive Technique," *IEEE Transactions on Smart Grid*, vol. 9, no. 5, pp. 3986–3993, 2018.

[44] K. K. Prasad, H. Myneni, and G. S. Kumar, "Power Quality Improvement and PV Power Injection by DSTATCOM With Variable DC Link Voltage Control from RSC-MLC," *IEEE Transactions on Sustainable Energy*, vol. 10, no. 2, pp. 876–885, 2019.

[45] S. Choi, B. Li, and D. Vilathgamuwa, "Dynamic voltage restoration with minimum energy injection," *IEEE Transactions on Power Systems*, vol. 15, no. 1, pp. 51–57, 2000.

[46] N. Abas, S. Dilshad, A. Khalid, M. S. Saleem, and N. Khan, "Power Quality Improvement Using Dynamic Voltage Restorer," *IEEE Access*, vol. 8, pp. 164 325–164 339, 2020.

[47] H. Fujita and H. Akagi, "The unified power quality conditioner: the integration of series- and shunt-active filters," *IEEE Transactions on Power Electronics*, vol. 13, no. 2, pp. 315–322, 1998.

[48] S. Devassy and B. Singh, "Design and Performance Analysis of Three-Phase Solar PV Integrated UPQC," *IEEE Transactions on Industry Applications*, vol. 54, no. 1, pp. 73–81, 2018.

[49] J. Jipping and W. Carter, "Application and experience with a 15 kV static transfer switch," *IEEE Transactions on Power Delivery*, vol. 14, no. 4, pp. 1477–1481, 1999.

[50] H. Mokhtari, S. Dewan, and M. Iravani, "Analysis of a static transfer switch with respect to transfer time," *IEEE Transactions on Power Delivery*, vol. 17, no. 1, pp. 190–199, 2002.

[51] G. Putrus, N. Jenkins, and C. Cooper, "A static fault current limiting and interrupting device," in *IEE Colloquium on Fault Current Limiters - A Look at Tomorrow*, London, UK, 8 June, 1995, pp. 5/1–5/6.

[52] N. Eghtedarpour and E. Farjah, "Power Control and Management in a Hybrid AC/DC Microgrid," *IEEE Transactions on Smart Grid*, vol. 5, no. 3, pp. 1494–1505, 2014.

[53] P. C. Loh, D. Li, Y. K. Chai, and F. Blaabjerg, "Autonomous Operation of Hybrid Microgrid With AC and DC Subgrids," *IEEE Transactions on Power Electronics*, vol. 28, no. 5, pp. 2214–2223, 2013.

[54] S. M. Malik, X. Ai, Y. Sun, C. Zhengqi, and Z. Shupeng, "Voltage and frequency control strategies of hybrid AC/DC microgrid: a review," *IET Generation, Transmission & Distribution*, vol. 11, no. 2, pp. 303–313, 2017.

[55] X. Shen, D. Tan, Z. Shuai, and A. Luo, "Control Techniques for Bidirectional Interlinking Converters in Hybrid Microgrids: Leveraging the advantages of both ac and dc," *IEEE Power Electronics Magazine*, vol. 6, no. 3, pp. 39–47, 2019.

[56] F. Nejabatkhah and Y. W. Li, "Overview of Power Management Strategies of Hybrid AC/DC Microgrid," *IEEE Transactions on Power Electronics*, vol. 30, no. 12, pp. 7072–7089, Dec. 2015.

[57] P. C. Loh, D. Li, Y. K. Chai, and F. Blaabjerg, "Autonomous Control of Interlinking Converter With Energy Storage in Hybrid AC-DC Microgrid," *IEEE Transactions on Industry Applications*, vol. 49, no. 3, pp. 1374–1382, 2013.

[58] S. Peyghami, H. Mokhtari, and F. Blaabjerg, "Autonomous Operation of a Hybrid AC/DC Microgrid With Multiple Interlinking Converters," *IEEE Transactions on Smart Grid*, vol. 9, no. 6, pp. 6480–6488, 2018.

[59] W. Mcmurray, "Power converter circuits having a high frequency link," U.S. Patent 3517300, June 1970.

[60] D. Dujic, C. Zhao, A. Mester, J. K. Steinke, M. Weiss, S. Lewdeni-Schmid, T. Chaudhuri, and P. Stefanutti, "Power Electronic Traction Transformer-Low Voltage Prototype," *IEEE Transactions on Power Electronics*, vol. 28, no. 12, pp. 5522–5534, 2013.

[61] M. Liserre, G. Buticchi, M. Andresen, G. D. Carne, L. F. Costa, and Z. X. Zou, "The Smart Transformer: Impact on the Electric Grid and Technology Challenges," *IEEE Industrial Electronics Magazine*, vol. 10, no. 2, pp. 46–58, June 2016.

[62] X. She, A. Q. Huang, and R. Burgos, "Review of Solid-State Transformer Technologies and Their Application in Power Distribution Systems," *IEEE Journal of Emerging and Selected Topics in Power Electronics*, vol. 1, no. 3, pp. 186–198, 2013.

[63] R. Peña Alzola, G. Gohil, L. Mathe, M. Liserre, and F. Blaabjerg, "Review of modular power converters solutions for smart transformer in distribution system," in *2013 IEEE Energy Conversion Congress and Exposition*, Denver, CO, USA, 15-19 Sep., 2013, pp. 380–387.

[64] P. E. M. Coloma, J. R. E. Castro, C. R. B. Fuentes, and J. A. R. Carrasco, "Cascaded H-Bridge Converters Based on Current-Source Inverters: Analysis, Design, and Application on AC Drives," in *Recent Developments on Power Inverters*, A. Saghafinia, Ed. Rijeka: IntechOpen, 2017, ch. 3. [Online]. Available: https://doi.org/10.5772/intechopen.68525

[65] R. De Doncker, D. Divan, and M. Kheraluwala, "A three-phase soft-switched high-power-density DC/DC converter for high-power applications," *IEEE Transactions on Industry Applications*, vol. 27, no. 1, pp. 63–73, 1991.

[66] L. M. Cúnico and A. L. Kirsten, "Improved ZVS Range for Three-Phase Dual-Active-Bridge Converter With Wye-Extended-Delta Transformer," *IEEE Transactions on Industrial Electronics*, vol. 69, no. 8, pp. 7984–7993, 2022.

[67] S. Bandyopadhyay, Z. Qin, and P. Bauer, "Decoupling Control of Multiactive Bridge Converters Using Linear Active Disturbance Rejection," *IEEE Transactions on Industrial Electronics*, vol. 68, no. 11, pp. 10 688–10 698, 2021.

[68] R. Gao, I. Husain, F. Wang, and A. Q. Huang, "Solid-state transformer interfaced PMSG wind energy conversion system," in *2015 IEEE Applied Power Electronics Conference and Exposition (APEC)*, Charlotte, NC, USA, 15-19 Mar., 2015, pp. 1310–1317.

[69] R. Gao, X. She, I. Husain, and A. Q. Huang, "Solid-State-Transformer-Interfaced Permanent Magnet Wind Turbine Distributed Generation System With Power Management Functions," *IEEE Transactions on Industry Applications*, vol. 53, no. 4, pp. 3849–3861, 2017.

[70] T. Liu, X. Yang, W. Chen, Y. Xuan, Y. Li, L. Huang, and X. Hao, "High-Efficiency Control Strategy for 10-kV/1-MW Solid-State Transformer in PV Application," *IEEE Transactions on Power Electronics*, vol. 35, no. 11, pp. 11 770–11 782, 2020.

[71] X. She, A. Q. Huang, S. Lukic, and M. E. Baran, "On Integration of Solid-State Transformer With Zonal DC Microgrid," *IEEE Transactions on Smart Grid*, vol. 3, no. 2, pp. 975–985, 2012.

[72] A. Agrawal, C. S. Nalamati, and R. Gupta, "Hybrid DC-AC Zonal Microgrid Enabled by Solid-State Transformer and Centralized ESD Integration," *IEEE Transactions on Industrial Electronics*, vol. 66, no. 11, pp. 9097–9107, 2019.

[73] S. Hambridge, A. Q. Huang, and R. Yu, "Solid State Transformer (SST) as an energy router: Economic dispatch based energy routing strategy," in *2015 IEEE Energy Conversion Congress and Exposition (ECCE)*, Montreal, QC, Canada, 20-24 Sep., 2015, pp. 2355–2360.

[74] Z.-X. Zou, G. De Carne, G. Buticchi, and M. Liserre, "Smart Transformer-Fed Variable Frequency Distribution Grid," *IEEE Transactions on Industrial Electronics*, vol. 65, no. 1, pp. 749–759, 2018.

[75] G. De Carne, G. Buticchi, M. Liserre, and C. Vournas, "Frequency-Based Overload Control of Smart Transformers," in *2015 IEEE Eindhoven PowerTech*, Eindhoven, Netherlands, 29 June - 2 July, 2015, pp. 1–5.

[76] H. Zhan, C. Wang, Y. Wang, X. Yang, X. Zhang, C. Wu, and Y. Chen, "Relay Protection Coordination Integrated Optimal Placement and Sizing of Distributed Generation Sources in Distribution Networks," *IEEE Transactions on Smart Grid*, vol. 7, no. 1, pp. 55–65, Jan. 2016.

[77] L. F. Costa, G. D. Carne, G. Buticchi, and M. Liserre, "The Smart Transformer: A solid-state transformer tailored to provide ancillary services to the distribution grid," *IEEE Power Electronics Magazine*, vol. 4, no. 2, pp. 56–67, June 2017.

[78] R. Zhu, G. Buticchi, and M. Liserre, “Investigation on Common-Mode Voltage Suppression in Smart Transformer-Fed Distributed Hybrid Grids,” *IEEE Transactions on Power Electronics*, vol. 33, no. 10, pp. 8438–8448, 2018.

[79] E. Csanyi. (2016, Jun.) "4 Main Types of Distribution Feeder Systems to Recognize". [Online]. Available: https://electrical-engineering-portal.com/4-main-types-distribution-feeder-systems

[80] W. Chen, X. Zhu, L. Yao, G. Ning, Y. Li, Z. Wang, W. Gu, and X. Qu, “A Novel Interline DC Power-Flow Controller (IDCPFC) for Meshed HVDC Grids,” *IEEE Transactions on Power Delivery*, vol. 31, no. 4, pp. 1719–1727, 2016.

[81] J. Sau-Bassols, E. Prieto-Araujo, O. Gomis-Bellmunt, and F. Hassan, “Series Interline DC/DC Current Flow Controller for Meshed HVDC Grids,” *IEEE Transactions on Power Delivery*, vol. 33, no. 2, pp. 881–891, 2018.

[82] O. Gomis-Bellmunt, J. Sau-Bassols, E. Prieto-Araujo, and M. Cheah-Mane, “Flexible Converters for Meshed HVDC Grids: From Flexible AC Transmission Systems (FACTS) to Flexible DC Grids,” *IEEE Transactions on Power Delivery*, vol. 35, no. 1, pp. 2–15, 2020.

[83] L. Mackay, E. Vandeventer, and L. Ramirez-Elizondo, “Circulating Net Currents in Meshed DC Distribution Grids: A Challenge for Residual Ground Fault Protection,” *IEEE Transactions on Power Delivery*, vol. 33, no. 2, pp. 1018–1019, 2018.

[84] J. Zhou, Y. Liu, Z. Kang, and Z. Jiang, “Economic and Stable Operation of Meshed MTDC/AC Grid as Affected by the Spatiotemporal Complementarities of Geographically Dispersed Wind Generation,” *IEEE Access*, vol. 10, pp. 22 556–22 567, 2022.

[85] M. Yilmaz and P. T. Krein, “Review of the Impact of Vehicle-to-Grid Technologies on Distribution Systems and Utility Interfaces,” *IEEE Transactions on Power Electronics*, vol. 28, no. 12, pp. 5673–5689, Dec. 2013.

[86] A. Hussain, C.-H. Kim, and A. Mehdi, “A comprehensive review of intelligent islanding schemes and feature selection techniques for distributed generation system,” *IEEE Access*, vol. 9, pp. 146 603–146 624, 2021.

[87] J. D. Watson, N. R. Watson, and B. Das, “Effectiveness of power electronic voltage regulators in the distribution network,” *IET Generation, Transmission and Distribution*, vol. 10, no. 15, pp. 3816–3823, 2016.

[88] R. Zhu and M. Liserre, “Requirements for smart transformer,” in *PCIM Europe 2019; International Exhibition and Conference for Power Electronics, Intelligent Motion, Renewable Energy and Energy Management*, Nuremberg, Germany, 7-9 May, 2019, pp. 1–8.

[89] X. Yu, X. She, X. Zhou, and A. Q. Huang, “Power Management for DC Microgrid Enabled by Solid-State Transformer,” *IEEE Transactions on Smart Grid*, vol. 5, no. 2, pp. 954–965, Mar. 2014.

[90] X. Yu, X. She, X. Ni, and A. Q. Huang, "System Integration and Hierarchical Power Management Strategy for a Solid-State Transformer Interfaced Microgrid System," *IEEE Transactions on Power Electronics*, vol. 29, no. 8, pp. 4414–4425, Aug. 2014.

[91] C. Kumar, R. Zhu, G. Buticchi, and M. Liserre, "Sizing and SOC Management of a Smart-Transformer-Based Energy Storage System," *IEEE Transactions on Industrial Electronics*, vol. 65, no. 8, pp. 6709–6718, Aug. 2018.

[92] G. D. Carne, G. Buticchi, Z. Zou, and M. Liserre, "Reverse Power Flow Control in a ST-Fed Distribution Grid," *IEEE Transactions on Smart Grid*, vol. 9, no. 4, pp. 3811–3819, July 2018.

[93] A. Gupta, S. Doolla, and K. Chatterjee, "Hybrid AC-DC Microgrid: Systematic Evaluation of Control Strategies," *IEEE Transactions on Smart Grid*, vol. 9, no. 4, pp. 3830–3843, July 2018.

[94] S. Mohamed, M. F. Shaaban, M. Ismail, E. Serpedin, and K. A. Qaraqe, "An Efficient Planning Algorithm for Hybrid Remote Microgrids," *IEEE Transactions on Sustainable Energy*, vol. 10, no. 1, pp. 257–267, Jan. 2019.

[95] E. Aprilia, K. Meng, M. Al Hosani, H. H. Zeineldin, and Z. Y. Dong, "Unified Power Flow Algorithm for Standalone AC/DC Hybrid Microgrids," *IEEE Transactions on Smart Grid*, vol. 10, no. 1, pp. 639–649, Jan. 2019.

[96] Y. Yan, L. Xiang, and W. Dianfeng, "Integrated Solutions for Photovoltaic Grid Connection: Increasing the Reliability of Solar Power," *IEEE Power and Energy Magazine*, vol. 12, no. 2, pp. 84–91, 2014.

[97] J. M. Guerrero, L. Hang, and J. Uceda, "Control of Distributed Uninterruptible Power Supply Systems," *IEEE Transactions on Industrial Electronics*, vol. 55, no. 8, pp. 2845–2859, 2008.

[98] C. Kumar and M. K. Mishra, "Operation and Control of an Improved Performance Interactive DSTATCOM," *IEEE Transactions on Industrial Electronics*, vol. 62, no. 10, pp. 6024–6034, 2015.

[99] J. Riedel, D. G. Holmes, B. P. McGrath, and C. Teixeira, "Active Suppression of Selected DC Bus Harmonics for Dual Active Bridge DC-DC Converters," *IEEE Transactions on Power Electronics*, vol. 32, no. 11, pp. 8857–8867, Nov. 2017.

[100] S. Falcones, R. Ayyanar, and X. Mao, "A DC-DC Multiport-Converter-Based Solid-State Transformer Integrating Distributed Generation and Storage," *IEEE Transactions on Power Electronics*, vol. 28, no. 5, pp. 2192–2203, May 2013.

[101] O. Wasynezuk, "Dynamic Behavior of a Class of Photovoltaic Power Systems," *IEEE Transactions on Power Apparatus and Systems*, vol. PAS-102, no. 9, pp. 3031–3037, 1983.

[102] C. Li, Y. Chen, D. Zhou, J. Liu, and J. Zeng, "A High-Performance Adaptive Incremental Conductance MPPT Algorithm for Photovoltaic Systems," *Energies*, vol. 9, no. 4, 2016.

[103] M. Starke, L. M. Tolbert, and B. Ozpineci, "AC vs. DC distribution: A loss comparison," in *2008 IEEE/PES Transmission and Distribution Conference and Exposition*, Chicago, IL, USA, 21-24 Apr., 2008, pp. 1–7.

[104] E. Rodriguez-Diaz, F. Chen, J. C. Vasquez, J. M. Guerrero, R. Burgos, and D. Boroyevich, "Voltage-Level Selection of Future Two-Level LVdc Distribution Grids: A Compromise Between Grid Compatibiliy, Safety, and Efficiency," *IEEE Electrification Magazine*, vol. 4, no. 2, pp. 20–28, 2016.

[105] "IEC 60038," *IEC Standard Voltages*, Edition 7.0, June, 2009.

[106] B. Ooi, J. Dixon, A. Kulkarni, and M. Nishimoto, "An integrated AC drive system using a controlled-current PWM rectifier/inverter link," *IEEE Transactions on Power Electronics*, vol. 3, no. 1, pp. 64–71, 1988.

[107] M. K. Mishra and K. Karthikeyan, "An Investigation on Design and Switching Dynamics of a Voltage Source Inverter to Compensate Unbalanced and Nonlinear Loads," *IEEE Transactions on Industrial Electronics*, vol. 56, no. 8, pp. 2802–2810, 2009.

[108] A. Q. Huang, "Medium-Voltage Solid-State Transformer: Technology for a Smarter and Resilient Grid," *IEEE Industrial Electronics Magazine*, vol. 10, no. 3, pp. 29–42, Sep. 2016.

[109] C. Crowell. (2017) "1,500-volt systems to trend in 2017: Here's what you need to know". [Online]. Available: https://solarbuildermag.com/news/2017-year-1500-volt-systems-take-off-heres-need-know/

[110] A. Emhemed, G. Burt, K. Smith, P. Black, A. Kazerooni, and A. Donoghue, "Protection and earthing requirements of lv ac and dc distribution networks interfaced by a smart transformer," in *25th International Conference on Electricity Distribution*, June Madrid, Spain, 3-6 June, 2019, pp. 3–6.

[111] M. Landry, O. Turcotte, and F. Brikci, "A Complete Strategy for Conducting Dynamic Contact Resistance Measurements on HV Circuit Breakers," *IEEE Transactions on Power Delivery*, vol. 23, no. 2, pp. 710–716, Apr. 2008.

[112] R. Lazzari and L. Piegari, "Design and Implementation of LVDC Hybrid Circuit Breaker," *IEEE Transactions on Power Electronics*, vol. 34, no. 8, pp. 7369–7380, Aug. 2019.

[113] T. Hakala, T. LÃd'hdeaho, and P. JÃd'rventausta, "Low-voltage dc distributionâĂŤutilization potential in a large distribution network company," *IEEE Transactions on Power Delivery*, vol. 30, no. 4, pp. 1694–1701, 2015.

[114] E. Serban, M. Ordonez, and C. Pondiche, "Dc-bus voltage range extension in 1500 v photovoltaic inverters," *IEEE Journal of Emerging and Selected Topics in Power Electronics*, vol. 3, no. 4, pp. 901–917, 2015.

[115] S. Moskowitz, "The Next Opportunity for Utility PV Cost Reductions: 1,500 Volts DC." Greentech Media, May 2015. [Online]. Available: https://www.greentechmedia.com/articles/read/the-next-opportunity-for-utility-pv-cost-reductions-1500-volts-dc#gs.xqoulr

[116] Z.-X. Zou, G. Buticchi, and M. Liserre, "Control and communication in the smart transformer-fed grid," in *2016 IEEE 21st International Conference on Emerging Technologies and Factory Automation (ETFA)*, 2016, pp. 1–9.

[117] S. U. Jeon, J. Noh, S. Kang, and J.-W. Park, "Practical power management of pv/ess integrated system," *IEEE Access*, vol. 8, pp. 189 775–189 785, 2020.

[118] S. H. M. S. Andrade, G. O. Contente, L. B. Rodrigues, L. X. Lima, N. L. Vijaykumar, and C. R. L. FrancÃłs, "A smart home architecture for smart energy consumption in a residence with multiple users," *IEEE Access*, vol. 9, pp. 16 807–16 824, 2021.

[119] S. Ahmadzadeh, G. Parr, and W. Zhao, "A review on communication aspects of demand response management for future 5g iot- based smart grids," *IEEE Access*, vol. 9, pp. 77 555–77 571, 2021.

[120] W. Shi, X. Xie, C.-C. Chu, and R. Gadh, "Distributed optimal energy management in microgrids," *IEEE Transactions on Smart Grid*, vol. 6, no. 3, pp. 1137–1146, 2015.

[121] F. Z. Harmouch, A. F. Ebrahim, M. M. Esfahani, N. Krami, N. Hmina, and O. A. Mohammed, "An optimal energy management system for real-time operation of multiagent-based microgrids using a t-cell algorithm," *Energies*, vol. 12, no. 15, 2019.

[122] J. Rocabert, A. Luna, F. Blaabjerg, and P. Rodriguez, "Control of Power Converters in AC Microgrids," *IEEE Transactions on Power Electronics*, vol. 27, no. 11, pp. 4734–4749, Nov. 2012.

[123] Q. Ye, R. Mo, and H. Li, "Multiple Resonances Mitigation of Paralleled Inverters in a Solid-State Transformer (SST) Enabled AC Microgrid," *IEEE Transactions on Smart Grid*, vol. 9, no. 5, pp. 4744–4754, Sep. 2018.

[124] X. Gao, F. Sossan, K. Christakou, M. Paolone, and M. Liserre, "Concurrent Voltage Control and Dispatch of Active Distribution Networks by Means of Smart Transformer and Storage," *IEEE Transactions on Industrial Electronics*, vol. 65, no. 8, pp. 6657–6666, Aug. 2018.

[125] S. Harasis, H. Abdelgabir, Y. Sozer, M. Kisacikoglu, and A. Elrayyah, "A Center of Mass Determination for Optimum Placement of Renewable Energy Sources in Microgrids," *IEEE Transactions on Industry Applications*, vol. 57, no. 5, pp. 5274–5284, 2021.

[126] S. X. Chen, H. B. Gooi, and M. Q. Wang, "Sizing of Energy Storage for Microgrids," *IEEE Transactions on Smart Grid*, vol. 3, no. 1, pp. 142–151, 2012.

[127] R. Manojkumar, C. Kumar, S. Ganguly, and J. P. S. Catalão, "Optimal Peak Shaving Control Using Dynamic Demand and Feed-In Limits for Grid-Connected PV Sources With Batteries," *IEEE Systems Journal*, vol. 15, no. 4, pp. 5560–5570, 2021.

[128] X. Wang and Q. Liang, "Energy Management Strategy for Plug-In Hybrid Electric Vehicles via Bidirectional Vehicle-to-Grid," *IEEE Systems Journal*, vol. 11, no. 3, pp. 1789–1798, 2017.

[129] E. I. Pool-Mazun, J. J. Sandoval, P. N. Enjeti, and I. J. Pitel, "An Integrated Solid-State Transformer With High-Frequency Isolation for EV Fast-Charging Applications," *IEEE Journal of Emerging and Selected Topics in Industrial Electronics*, vol. 1, no. 1, pp. 46–56, 2020.

[130] C. Kumar, R. Manojkumar, S. Ganguly, and M. Liserre, "Impact of Optimal Control of Distributed Generation Converters in Smart Transformer Based Meshed Hybrid Distribution Network," *IEEE Access*, vol. 9, pp. 140 268–140 280, 2021.

[131] F. K. Abo-Elyousr, A. M. Sharaf, M. M. F. Darwish, M. Lehtonen, and K. Mahmoud, "Optimal scheduling of DG and EV parking lots simultaneously with demand response based on self-adjusted PSO and k-means clustering," *Energy Sci. Eng.*, 2022.

[132] S. Zhou, Y. Han, P. Yang, K. Mahmoud, M. Lehtonen, M. M. Darwish, and A. S. Zalhaf, "An optimal network constraint-based joint expansion planning model for modern distribution networks with multi-types intermittent rers," *Renewable Energy*, vol. 194, pp. 137–151, 2022.

[133] Prashant, M. Sarwar, A. S. Siddiqui, S. S. M. Ghoneim, K. Mahmoud, and M. M. F. Darwish, "Effective transmission congestion management via optimal dg capacity using hybrid swarm optimization for contemporary power system operations," *IEEE Access*, vol. 10, pp. 71 091–71 106, 2022.

[134] S. Lakshmi and S. Ganguly, "An on-line operational optimization approach for open unified power quality conditioner for energy loss minimization of distribution networks," *IEEE Transactions on Power Systems*, vol. 34, no. 6, pp. 4784–4795, 2019.

[135] N. Wang, J. Li, W. Hu, B. Zhang, Q. Huang, and Z. Chen, "Optimal reactive power dispatch of a full-scale converter based wind farm considering loss minimization," *Renewable Energy*, vol. 139, pp. 292–301, 2019.

[136] V. Sarfi and H. Livani, "Optimal volt/var control in distribution systems with prosumer ders," *Electric Power Syst. Research*, vol. 188, p. 106520, 2020.

[137] S.-Y. Shieh, T. Ersal, and H. Peng, "Power Loss Minimization in Islanded Microgrids: A Communication-Free Decentralized Power Control Approach Using Extremum Seeking," *IEEE Access*, vol. 7, pp. 20 879–20 893, 2019.

[138] N. Vazquez, S. S. Yu, T. K. Chau, T. Fernando, and H. H.-C. Iu, "A Fully Decentralized Adaptive Droop Optimization Strategy for Power Loss Minimization in Microgrids With PV-BESS," *IEEE Transactions on Energy Conversion*, vol. 34, no. 1, pp. 385–395, 2019.

[139] C. Taylor, "Concepts of undervoltage load shedding for voltage stability," *IEEE Transactions on Power Delivery*, vol. 7, no. 2, pp. 480–488, 1992.

[140] W. K. A. Najy, H. H. Zeineldin, and W. L. Woon, "Optimal Protection Coordination for Microgrids With Grid-Connected and Islanded Capability," *IEEE Transactions on Industrial Electronics*, vol. 60, no. 4, pp. 1668–1677, 2013.

[141] S. Lu, L. Wang, T. Lo, and A. V. Prokhorov, "Integration of Wind Power and Wave Power Generation Systems Using a DC Microgrid," *IEEE Transactions on Industry Applications*, vol. 51, no. 4, pp. 2753–2761, 2015.

[142] D. Das, V. M. Hrishikesan, C. Kumar, and M. Liserre, "Smart Transformer-Enabled Meshed Hybrid Distribution Grid," *IEEE Transactions on Industrial Electronics*, vol. 68, no. 1, pp. 282–292, Jan. 2021.

[143] A. Y. Saber and G. K. Venayagamoorthy, "Plug-in Vehicles and Renewable Energy Sources for Cost and Emission Reductions," *IEEE Transactions on Industrial Electronics*, vol. 58, no. 4, pp. 1229–1238, 2011.

[144] R. Zhu, G. D. Carne, F. Deng, and M. Liserre, "Integration of Large Photovoltaic and Wind System by Means of Smart Transformer," *IEEE Transactions on Industrial Electronics*, vol. 64, no. 11, pp. 8928–8938, Nov. 2017.

[145] A. C. Nair and B. G. Fernandes, "Solid-State Transformer Based Fast Charging Station for Various Categories of Electric Vehicles With Batteries of Vastly Different Ratings," *IEEE Transactions on Industrial Electronics*, vol. 68, no. 11, pp. 10 400–10 411, 2021.

[146] C. Liu, K. T. Chau, D. Wu, and S. Gao, "Opportunities and Challenges of Vehicle-to-Home, Vehicle-to-Vehicle, and Vehicle-to-Grid Technologies," *Proceedings of the IEEE*, vol. 101, no. 11, pp. 2409–2427, 2013.

[147] S. Habib, M. M. Khan, F. Abbas, L. Sang, M. U. Shahid, and H. Tang, "A Comprehensive Study of Implemented International Standards, Technical Challenges, Impacts and Prospects for Electric Vehicles," *IEEE Access*, vol. 6, pp. 13 866–13 890, 2018.

[148] A. Tuckey and S. Round, "Grid-Forming Inverters for Grid-Connected Microgrids: Developing "good citizens" to ensure the continued flow of stable, reliable power," *IEEE Electrification Magazine*, vol. 10, no. 1, pp. 39–51, 2022.

[149] H.-L. Do, "Nonisolated Bidirectional Zero-Voltage-Switching DC-DC Converter," *IEEE Transactions on Power Electronics*, vol. 26, no. 9, pp. 2563–2569, 2011.

[150] B. Poorali and E. Adib, "Right-Half-Plane Zero Elimination of Boost Converter Using Magnetic Coupling With Forward Energy Transfer," *IEEE Transactions on Industrial Electronics*, vol. 66, no. 11, pp. 8454–8462, 2019.

[151] J. Sun, D. Mitchell, M. Greuel, P. Krein, and R. Bass, "Averaged modeling of pwm converters operating in discontinuous conduction mode," *IEEE Transactions on Power Electronics*, vol. 16, no. 4, pp. 482–492, 2001.

[152] J. Calvente, L. Martinez-Salamero, H. Valderrama, and E. Vidal-Idiarte, "Using magnetic coupling to eliminate right half-plane zeros in boost converters," *IEEE Power Electronics Letters*, vol. 2, no. 2, pp. 58–62, 2004.

[153] Y. Gu, D. Zhang, and Z. Zhao, "Input/output current ripple cancellation and rhp zero elimination in a boost converter using an integrated magnetic technique," *IEEE Transactions on Power Electronics*, vol. 30, no. 2, pp. 747–756, 2015.

[154] K. Viswanathan, R. Oruganti, and D. Srinivasan, “Dual-mode control of tri-state boost converter for improved performance,” *IEEE Transactions on Power Electronics*, vol. 20, no. 4, pp. 790–797, 2005.

[155] B. Akin, “An Improved ZVT-ZCT PWM DC-DC Boost Converter With Increased Efficiency,” *IEEE Transactions on Power Electronics*, vol. 29, no. 4, pp. 1919–1926, 2014.

[156] Y. Zhang, J. Liu, Z. Dong, H. Wang, and Y.-F. Liu, “Dynamic Performance Improvement of Diode-capacitor-Based High Step-up DC-DC Converter Through Right-Half-Plane Zero Elimination,” *IEEE Transactions on Power Electronics*, vol. 32, no. 8, pp. 6532–6543, 2017.

[157] R. W. Erickson and D. Maksimovic, *Fundamentals of Power Electronics*, 2nd ed. Springer, 2001.

[158] Hioki.com. "Why is it Important to Measure Battery’s Internal Resistance?". [Online]. Available: https://www.hioki.com/global/learning/electricity/internal-resistance.html

[159] G. D. Carne, G. Buticchi, M. Liserre, and C. Vournas, “Load Control Using Sensitivity Identification by Means of Smart Transformer,” *IEEE Transactions on Smart Grid*, vol. 9, no. 4, pp. 2606–2615, July 2018.

[160] L. M. Korunović, J. V. Milanović, S. Z. Djokic, K. Yamashita, S. M. Villanueva, and S. Sterpu, “Recommended parameter values and ranges of most frequently used static load models,” *IEEE Transactions on Power Systems*, vol. 33, no. 6, pp. 5923–5934, 2018.

[161] D. P. Stojanović, L. M. Korunović, and J. Milanović, “Dynamic load modelling based on measurements in medium voltage distribution network,” *Electric Power Systems Research*, vol. 78, no. 2, pp. 228–238, 2008.

[162] B.-K. Choi, H.-D. Chiang, Y. Li, H. Li, Y.-T. Chen, D.-H. Huang, and M. Lauby, “Measurement-based dynamic load models: derivation, comparison, and validation,” *IEEE Transactions on Power Systems*, vol. 21, no. 3, pp. 1276–1283, 2006.

[163] Z. Zou, G. Buticchi, and M. Liserre, “Analysis and Stabilization of a Smart Transformer-Fed Grid,” *IEEE Transactions on Industrial Electronics*, vol. 65, no. 2, pp. 1325–1335, Feb. 2018.

[164] R. R. Chan, Y. Lee, S. D. Sudhoff, and E. L. Zivi, “Evolutionary Optimization of PowerElectronics Based Power Systems,” *IEEE Transactions on Power Electronics*, vol. 23, no. 4, pp. 1907–1917, 2008.

[165] Q. Zhang, M. Mao, G. Ke, L. Zhou, and B. Xie, “Stability problems of PV inverter in weak grid: a review,” *IET Power Electronics*, vol. 13, no. 11, pp. 2165–2174, 2020.

[166] B. Bryant and M. Kazimierczuk, “Small-signal duty cycle to inductor current transfer function for boost PWM DC-DC converter in continuous conduction mode,” in *2004 IEEE International Symposium on Circuits and Systems (ISCAS)*, vol. 5, Vancouver, BC, Canada, 23-26 May, 2004, pp. V–V.

[167] M. Liserre, F. Blaabjerg, and S. Hansen, "Design and control of an LCL-filter-based three-phase active rectifier," *IEEE Transactions on Industry Applications*, vol. 41, no. 5, pp. 1281–1291, 2005.

[168] A. Reznik, M. G. Simões, A. Al-Durra, and S. M. Muyeen, "*LCL* Filter Design and Performance Analysis for Grid-Interconnected Systems," *IEEE Transactions on Industry Applications*, vol. 50, no. 2, pp. 1225–1232, 2014.

[169] X. Liu, H. Li, and Z. Wang, "A Start-Up Scheme for a Three-Stage Solid-State Transformer With Minimized Transformer Current Response," *IEEE Transactions on Power Electronics*, vol. 27, no. 12, pp. 4832–4836, 2012.

[170] M. Saeed, J. M. Cuartas, A. Rodriguez, M. Arias, and F. Briz, "Energization and Start-Up of CHB-Based Modular Three-Stage Solid-State Transformers," *IEEE Transactions on Industry Applications*, vol. 54, no. 5, pp. 5483–5492, 2018.

[171] K. Mainali, S. Madhusoodhanan, A. Tripathi, D. Patel, and S. Bhattacharya, "Start-up scheme for solid state transformers connected to medium voltage grids," in *2015 IEEE Applied Power Electronics Conference and Exposition (APEC)*, Charlotte, NC, USA, 15-19 Mar., 2015, pp. 1014–1021.

[172] X. Zhang, Y. Xu, A. Siddique, Y. Long, and X. Xiao, "A Microprocessor Resource-Saving Dual Active Bridge Control for Startup and Restart of Three-Stage Modular Solid-State Transformer," *IEEE Transactions on Power Delivery*, vol. 35, no. 3, pp. 1443–1454, 2020.

[173] S. Pugliese, G. Buticchi, R. A. Mastromauro, M. Andresen, M. Liserre, and S. Stasi, "Soft-Start Procedure for a Three-Stage Smart Transformer Based on Dual-Active Bridge and Cascaded H-Bridge Converters," *IEEE Transactions on Power Electronics*, vol. 35, no. 10, pp. 11 039–11 052, 2020.

[174] A. Rodriguez, A. Vázquez, D. G. Lamar, M. M. Hernando, and J. Sebastián, "Different Purpose Design Strategies and Techniques to Improve the Performance of a Dual Active Bridge With Phase-Shift Control," *IEEE Transactions on Power Electronics*, vol. 30, no. 2, pp. 790–804, 2015.

[175] H. Dehghani Tafti, C. Shuyu, K. Ravi Kishore, G. Farivar, H. L. Yeo, V. Sriram, J. Pou, and A. Tripathi, "Control of active front-end rectifier of the solid-state transformer with improved dynamic performance during precharging," in *2017 Asian Conference on Energy, Power and Transportation Electrification (ACEPT)*, Singapore, 24-26 Oct., 2017, pp. 1–6.

[176] K. Zhang, Z. Shan, and J. Jatskevich, "Large- and Small-Signal Average-Value Modeling of Dual-Active-Bridge DC-DC Converter Considering Power Losses," *IEEE Transactions on Power Electronics*, vol. 32, no. 3, pp. 1964–1974, 2017.

[177] J. M. Diaz, R. Costa-Castello, and S. Dormido, "Closed-Loop Shaping Linear Control System Design: An Interactive Teaching/Learning Approach [Focus on Education]," *IEEE Control Systems Magazine*, vol. 39, no. 5, pp. 58–74, 2019.

[178] C. Kumar, Z. Zou, and M. Liserre, "Smart transformer-based hybrid grid loads support in partial disconnection of MV/HV power system," in *2016 IEEE Energy Conversion Congress and Exposition (ECCE)*, Milwaukee, WI, USA, 18-22 Sep, 2016, pp. 1–8.

[179] R. W. Erickson and D. Maksimović, *Fundamentals of power electronics*, 2nd ed. Dordrecht, Netherlands: Springer, 2001.

LIST OF PAPERS BASED ON THESIS

PUBLICATIONS IN REFEREED JOURNALS

- Published
  1. Dwijasish Das, Rampelli Manojkumar, Chandan Kumar and Sanjib Ganguly "Power Loss Minimization in Smart Transformer Enabled Low Voltage Islanded Meshed Hybrid Microgrid," *IEEE Access*, vol. 10, pp. 123259-123270, Nov. 2022.
  2. Dwijasish Das, Chandan Kumar, "Partial Startup Scheme for Smart Transformer in Meshed Hybrid Islanded Grid Operation," *IEEE Transactions on Industry Applications*, vol. 58, no. 1, pp. 142-151, Jan.-Feb. 2022.
  3. Dwijasish Das, Hrishikesan VM, Chandan Kumar, Marco Liserre, "Smart Transformer Enabled Meshed Hybrid Distribution Grid", *IEEE Transactions on Industrial Electronics*, vol. 68, no. 1, pp. 282-292, Jan. 2021.

- Submitted
  1. Dwijasish Das, Chandan Kumar, Marco Liserre, "Stabilization of Smart Transformer Based Islanded Meshed Hybrid Microgrid During Electric Vehicle Charging Transients", *IEEE Journal of Emerging and Selected Topics in Industrial Electronics* (under review).

PUBLICATIONS IN REFEREED CONFERENCES

1. Dwijasish Das, Manojkumar Rampelli, Chandan Kumar, Sanjib Ganguly, "Optimal Power Management for Islanded Operation of ST-based Meshed Hybrid LV Microgrid", *IEEE Energy Conversion Congress Exposition Asia (ECCE ASIA), 2021*, Singapore, May 24-27, 2021.

2. Dwijasish Das, Chandan Kumar, "Partial Start-up Scheme for ST to Reconnect to MV Grid from LV Side Islanded Operation", *9th IEEE International Conference on Power Electronics, Drives and Energy systems (PEDES)*, MNIT Jaipur, India, 16-17 Dec. 2020.

3. Dwijasish Das, Hrishikesan VM, Chandan Kumar, "BESS-PV Integrated Islanded Operation of ST-based Hybrid Microgrid", *2020 IEEE 9th International Power Electronics and Motion Control Conference (IPEMC 2020-ECCE Asia)*, Nanjing, China, Nov. 29-Dec 2, 2020.

4. Dwijasish Das, Hrishikesan VM, Chandan Kumar, "Smart Transformer-based Hybrid LVAC and LVDC Interconnected Microgrid," *4th IEEE Southern Power Electronics Conference (SPEC)*, Singapore, Dec. 2018.

5. Dwijasish Das and Chandan Kumar, "Operation and control of smart transformer based distribution grid in a microgrid system," *National Power Electronics Conference (NPEC)*, Pune, India, Dec. 2017, pp. 135-140.